UNIVERSITY OF SOUTHAMPTON

Methods for Increased Energy and Flux in High Harmonic Generation

by

Thomas J. Butcher

Thesis for the
degree of Doctor of Philosophy

in the
Faculty of Physical and Applied Sciences
Optoelectronics Research Centre

March 2012

UNIVERSITY OF SOUTHAMPTON

ABSTRACT

FACULTY OF PHYSICAL AND APPLIED SCIENCES
OPTOELECTRONICS RESEARCH CENTRE

Doctor of Philosophy

by Thomas J. Butcher

High harmonic generation (HHG) is a nonlinear light matter interaction that results in the generation of high order harmonics of a driving optical field. It is routinely used to generate coherent short wavelength radiation in the soft x-ray and extreme ultraviolet (XUV) regimes. HHG-based XUV sources require a highly intense driving pulse to be focused into a target gas typically within a gas cell, gas jet or hollow capillary. They can be used for a variety of applications, one of which is nanoscale imaging. The work presented in this thesis focuses on the development of two high flux HHG sources for use in tabletop nanoscale imaging; a capillary based HHG system using a Ti:Sapphire based laser and a gas cell based HHG system using an Yb-doped fibre laser.

The manufacture and use of a 7 cm hollow core capillary in HHG is described. The propagation of the pump pulse is modelled using a new nonlinear propagation model and compared to experimental results. The pulse is found to undergo pulse self-compression using a new regime of high ionisation pulse compression. The pulse is observed to reduce in length from 53 fs to 28 fs, with post compression reducing this further to 15 fs. The XUV spectrum from the 7 cm capillary is measured and its dependence on gas pressure discussed using calculations of the XUV transmission within the capillary. Using the observations made of the 7 cm capillary a new more efficient 4.5 cm capillary is designed and manufactured. Comparison between the two capillaries shows an increase in flux of the new capillary design of more than an order of magnitude, with a calculated value of 5.3×10^{12} ph $harm^{-1}$ s^{-1} cm^{-2}, one of the highest in the world.

A gas cell is used in the Yb-doped fibre laser based HHG source and the XUV signal is measured using an XUV photodiode. The XUV signal is characterised by measuring its dependence on focal position, gas pressure and pump laser power. A novel method of increasing the flux by twisting of a second lens outside the vacuum chamber is discovered and was found to double the measured signal. The maximum flux for this fibre laser based HHG source is calculated and found to be 2.2×10^{12} ph s^{-1}, the highest measured for a fibre based HHG source.

Contents

List of Figures

DECLARATION OF AUTHORSHIP

I, Thomas John Butcher, declare that the thesis entitled "Methods for Increased Energy and Flux in High Harmonic Generation" and the work presented in it are my own. I confirm that:

- this work was done wholly or mainly while in candidature for a research degree at this University;
- where any part of this thesis has previously been submitted for a degree or any other qualification at this University or any other institution, this has been clearly stated;
- where I have consulted the published work of others, this is always clearly attributed;
- where I have quoted from the work of others, the source is always given. With the exception of such quotations, this thesis is entirely my own work;
- I have acknowledged all main sources of help;
- where the thesis is based on work done by myself jointly with others, I have made clear exactly what was done by others and what I have contributed myself;

Signed: _____

Date: _____

Acknowledgements

It is safe to say this thesis would not exist without the help and support of many people who deserve thanks for getting me this far.

Bill Brocklesby, my supervisor, for putting up with all my inane questions to begin with and teaching me not only to question everything that I assume to be true but to take a step back from time to time and look at the big picture.

Jeremy Frey, for his advice, guidance and unequalled enthusiasm for new results, both the interesting and the expected.

Peter Horak, for the work he has done explaining theoretically the results I've observed and his help and advice in understanding pulse propagation.

Jonathan Price, for the many hours of work he has put into making the fibre laser system that we used and for being such good company whilst we hunted for XUV signals.

The people that came before me, Matt Praeger, Ed Rogers, Ben Mills and James Grant-Jacob, for answering my questions and making me feel welcome. Those following in my footsteps, Aaron Parsons, Patrick Anderson and Rachel Card, for asking the awkward questions about things I take for granted and for accepting my answers.

Richard Chapman, a fellow researcher and tea drinker, for all the tea breaks, chats and discussions that helped pass the slow times and occasionally led to some interesting new research ideas.

Jess Butcher, my sister, for all of the early morning phone calls to get me up and writing, I think the conclusion of this thesis would be put back somewhat if not for her cheerful phone calls. Thanks for putting up with the grumpy tired brother.

Helen Rogers, my better half, for her support during my writing up and for looking interested when I spent 'another' ten minutes telling her about the exciting things I was looking at. Thank you for all you've done.

Finally the rest of my family, for all the support they've been over the years and the past couple of months whilst they avoided asking that forbidden question ... "How's the thesis going?".

"Light thinks it travels faster than anything, but it is wrong. No matter how fast light travels, it finds the darkness has always got there first, and is waiting for it "

Terry Pratchett

Chapter 1

Introduction

The advent of the laser in 1960 [1] heralded a new era in the exploration of light matter interactions. This was rapidly followed in 1961 by the work of Franken et al [2], who showed for the first time nonlinear light matter interactions by demonstrating second harmonic generation from a ruby laser line. From that first experiment the field of nonlinear optics was born, growing to a huge field that studies the nonlinear interaction between light and matter. Harmonic generation is one result of the nonlinear response of a material to an applied optical field and is used in many areas of science and technology to generate coherent beams at different frequencies.

During the early nineties two models were produced [3,4] to describe a process by which one could generate high order harmonics, producing a coherent beam of electromagnetic radiation with wavelengths in the extreme ultraviolet (XUV) range. This process was named high-harmonic generation (HHG) [5,6]. Since its discovery the limit of HHG has been pushed to energies of 3.5 keV, corresponding to sub nanometre wavelengths [7]. There are many uses for this short wavelength coherent beam, one of which is nanoscale imaging, the driving force behind this work.

The following introductory sections will describe the motivation for the research carried out; a brief introduction to possible x-ray sources, HHG, a description of the laser sources and generation geometries used to produce HHG in this thesis.

1.1 Motivation - tabletop nanoscale imaging

1.1.1 Non-optical nanoscale imaging

The diffraction limit [8] necessitates the use of X-ray / XUV radiation if one desires nanoscale imaging using optical techniques. There are alternative methods for nanoscale imaging that have their own advantages and disadvantages.

Electron microscopy [9,10] is the most commonly used imaging method for the nanoscale regime. Scanning electron microscopy (SEM) uses an accelerated electron beam to probe a surface, the ultimate resolution of an SEM being set by the energy of the electrons in the beam. In practice focusing and collecting the electrons places a different limit on the resolution; even so, resolutions in the nanometer regime are commonplace. SEM typically requires a conducting surface to avoid charge build up on the sample, thus limiting the samples one can observe. It is possible to coat non-conductive samples with gold allowing a larger variety of samples to be imaged, however, this process can fundamentally change the structure of the object. SEMs are widely used in the applied and biological sciences to provide high resolution images including manmade structures, animals and even bacteria.

In transmission electron microscopy [11] (TEM) the transmission of a high energy electron beam through a sample is used to map the structure within, requiring very thin samples due to the strong interaction of the electron with the atoms of the sample. The different interactions of the electrons with the sample have lead to a multitude of different imaging techniques. These include bright field imaging, where the absorption or transmission of the electrons produces an image of the sample; dark field or diffraction contrast imaging, where Bragg scattering from crystal planes is used to study a sample's structure; and phase contrast imaging, where the complex phase of the transmitted electron waves is affected by interaction with the sample. The versatility of TEM imaging has lead to them being routinely used in many areas of research.

Other methods exist for probing the nanoscale regime that do not use electromagnetic radiation, including atomic force microscopy, scanning tunnelling microscopy and focused ion beam technology. X-ray microscopy can complement this current range of imaging techniques. It is non-invasive although not always non-destructive, due the potential for generating a Coulomb explosion [12] of the sample. However, the short timescale of the pulses allows information to be extracted prior to this. It can be used on non-conducting samples and the wavelength of the probe can be adjusted to increase the contrast of certain elements. For example radiation between 3 - 5 nm, known as the water window [13], has very low absorption in water but high absorption by carbon; as such one could use this to image organic material in solution, a feat not possible with other techniques.

1.1.2 X-ray / XUV sources

HHG is not the only source of X-ray / XUV radiation generated for experimental purposes. Large installations exist that already produce hard and soft x-rays. Examples include Synchrotron sources such as Diamond [14] at the Rutherford Appleton Laboratory near Oxford and free electron lasers (FELs) such as FLASH [15] situated in Hamburg.

Synchrotrons are particle accelerators that use accelerated electrons to generate high energy x-ray radiation. Charged particles that undergo radial acceleration emit Synchrotron radiation, whose energy is dependent on the energy of the particle and the bend radius. In a Synchrotron, electrons are accelerated to high energies and emit radiation by the use of bending magnets, wigglers and undulators. Bending magnets and wigglers produce broadband radiation, whereas the period of the oppositely poled magnetic fields in an undulator is such that the electrons emit radiation in narrow bands.

FELs generate x-rays using a linear particle accelerator and operate on the principle of self-amplified stimulated emission. An electron bunch is accelerated along the length of the FEL, typically hundreds of meters, to energies up to 1 GeV in the case of FLASH. At this point the electrons pass through a long undulator. Initially they emit incoherently, however due to interactions between the electrons and the emitted radiation they undergo micro-bunching, forming bunches separated by a distance equal to a single wavelength. At this point the electrons emit in phase and produce a coherent beam of radiation. The wavelength of the emitted radiation can be tuned by adjusting the strength of the magnetic field in the undulator or the energy of the initial electrons.

Although these are very bright high energy sources, they are also built on a huge scale and cost hundreds of millions of pounds to build and run.

Examples of smaller sources include x-ray lasers and laser plasma sources. X-ray lasers typically use multi-joule pulses focused to a narrow line on a solid target [16], generating a plasma column of highly charged ions that acts as a single-pass amplifier. The lasing line depends on the material used but can range from 3 - 50 nm [17]. The lifetime of the excited states in x-ray lasers is very short, as a result these sources are used as single-pass amplifiers for a coherent HHG seed beam or produce a weakly coherent beam of amplified spontaneous emission.

Laser plasma sources use a high energy pulse typically focused to intensities ranging from $10^{16} - 10^{18}\ Wcm^{-2}$ on a target. The plasma generated by the pulse emits radiation in the hard [18] and soft x-ray regimes [19] due to the relaxation of the hot electrons generated within the plasma. The emission of these sources can either be broadband thermal emission from the hot electrons or from emission lines; for example the K_α [20] emission line for an electron transition between the 2p or second L shell to the 1s or innermost K shell. In both cases the emission is into 2π steradians producing two experimental issues, collection of the radiation and protecting optics from the ablated material.

1.1.2.1 Basics of HHG

HHG occurs when an intense driving laser field is incident on an atom. The highly intense field can distort the Coulomb potential of the atom to such an extent that a potential barrier is created and a valence electron can tunnel through the barrier into

free space. In free space the electron is accelerated by the driving field and follows a trajectory that can cause it to recombine with the parent ion. The kinetic energy gained by the electron during its acceleration is emitted as a high-energy photon. This process can be modelled semi-classically and quantum mechanically. It is known as the three-step model [3, 4, 21] and will be discussed in more detail in Section 2.1.

Unlike the x-ray laser, the laser plasma source and the Synchrotron, HHG produces an intrinsically coherent beam, which is important for many experiments including far field optical imaging. In addition to this the HHG process generates a few femtosecond long pulse train of attosecond pulses in sync with the fundamental pulse, enabling pump probe experiments [22] and the exploration of ultrashort dynamics [23].

1.1.3 Uses of a coherent XUV beam

Microscopy in the XUV can be achieved using objective lenses such as zone plates [24]; however, a technique for imaging in the soft x-ray / XUV regime without the need for objective lenses, known as coherent diffractive imaging (CDI), is becoming increasingly popular. In CDI the scattered light transmitted through a sample is collected on a charge coupled device (CCD) camera and the phase information is retrieved using an iterative algorithm [25–27]. Using this method sub 30 nm resolutions have recently been demonstrated by Seaberg et al [28] using a capillary based HHG source producing 13 nm radiation. Current phase retrieval algorithms require the diffracted image from single harmonics, however a new method has been developed that can use multiple wavelength diffracted images [29], increasing the number of photons available from the HHG spectrum. In 2007 the CDI technique was extended by Rodenburg et al [30] to allow imaging of extended objects with x-ray resolution using a technique known as ptychography.

HHG typically uses pulses of a few tens of femtoseconds to generate attosecond bursts of XUV within an envelope of a few tens of femtoseconds. It has been shown that single attosecond pulses can be generated using polarisation gating [31], where the front and back of the pulse are circularly polarised, in which the field does not return the accelerated electron to the parent ion and thus cannot produce HHG. The result is a single attosecond XUV pulse. The attosecond pulses have high intensities and may therefore prove useful in examining the nonlinear response of materials in the XUV region [32, 33]. This area has not yet been well explored but offers exciting new challenges.

One of the limits of any imaging technique is the signal-to-noise ratio (SNR). To improve the SNR one can increase the integration time, which for current HHG systems ranges from minutes to tens of minutes. Development of a high flux HHG source would reduce this time making scanning microscopy and ptychography in the XUV possible. The exploration of nonlinearity in the XUV regime requires high intensities and therefore

high flux coupled with short pulses. A high flux HHG source is more likely to observe nonlinearity in the XUV regime. Both of these areas of research require high flux levels in the XUV and improving the wavelength or flux of the generated harmonics would allow for higher resolution imaging. This is the driving force behind the work shown in this thesis.

1.2 A table-top XUV source

Two HHG sources have been developed in the course of this thesis. The conventional system uses a Ti:Sapphire chirped pulse amplifier (CPA) that can produce 3 mJ, 40 fs pulses at a repetition rate of 1 kHz. The second system is a fibre based CPA that has been designed and built by Dr Jonathan Price within the Optoelectronics Research Centre [34,35]. The use of fibres allows higher average powers and thus higher repetition rates for a given pulse energy (16.6 kHz or 33.3 kHz) at 1055 nm with 380 fs pulse lengths. The next two sections will briefly describe each of these systems.

1.2.1 Ti:Sapphire based CPA system

The main system shown in Figure 1.1 was supplied by Spectra Physics. A Tsunami Ti:Sapphire oscillator is pumped by a frequency doubled (532 nm) diode pumped solid state (DPSS) neodymium yttrium vanadate (Nd:YVO_4) Millennia laser. The oscillator produces 35 fs pulses centred at 790 nm running with an average power of 450 mW at a repetition rate of 79 MHz. Upon entering the Spitfire Pro CPA the seed pulses are stretched by a grating stretcher to ~200 ps in length, after which a Pockels cell is used to select a pulse for amplification. This pulse enters the regenerative amplifier cavity of the amplifier. The Ti:Sapphire crystal in the amplifier is dual end pumped by a 17 W Positive Light 'Evolution' frequency doubled DPSS Nd:YLF laser. The Evolution runs at a 1 kHz repetition rate and produces 5 ns pulses. The seed pulse completes 13 round trips within the cavity before being switched out by a second Pockels cell. It is passed through a telescope before passing through a grating compressor where the pulse length is reduced to 40 fs. The output pulse has an energy up to 3 mJ with a central wavelength of 790 nm. The CPA runs at a repetition rate of 1 kHz.

The pulse length can be adjusted by changing the path length within the compressor. The output power of the laser can be adjusted by changing the current supplied to the diodes of the Evolution. The change in pump power reduces the gain at each pass through the Ti:Sapphire crystal resulting in more round trips to achieve high power. The pulse is still switched out after 13 passes and thus has an energy which is dependant on the pump power. There is no change to the pulse length, allowing control over the power and thus intensity of the laser pulse.

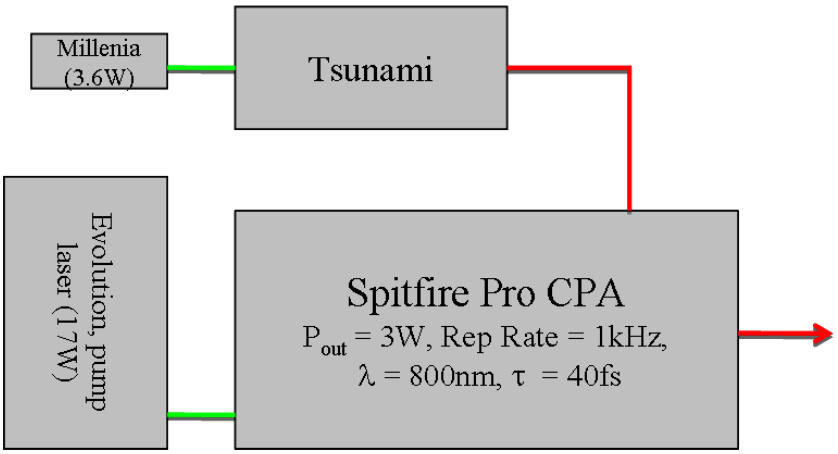

Figure 1.1: Spectra Physics CPA system for HHG. Comprises two 1064nm diode pumped lasers (Millenia, Evolution), Ti:Sapphire seed laser (Tsunami),and a regenerative cavity based CPA (Spitfire Pro).

1.2.2 Fibre laser based CPA system

The ytterbium-doped fibre CPA used in the experiments discussed in Chapter 6 was developed by Dr Jonathan Price. It is based on a single-pass CPA design using Yb doped optical fibre as the gain medium. A fibre oscillator produces 150 fs pulses at 50 MHz. The output beam is coupled through an electro-optic modulator (EOM) which reduces the repetition rate to 100 kHz. The pulses are then stretched in a bulk grating stretcher to approximately 1 ns and coupled back into a series of core pumped fibre preamplifiers that raise the power to 0.1 W. The repetition rate is reduced twice more using acousto-optic modulators (AOM) to 33.3 kHz and finally 16.6 kHz. Two cladding pumped final amplifiers, one after each AOM raise the pulse energy further still. The amplifiers are all pumped by electrically driven continuous wave 975 nm diode lasers coupled into the amplifier fibres. The amplified pulses are compressed in a bulk stretcher down to 450 fs with an energy of $\sim 99\mu$J centred at 1055 nm. A schematic of the laser design produced by Dr Price is shown in Figure 1.2. In addition to this a phase only pulse shaper was installed after the grating stretcher to mitigate some of the effects of the nonlinear propagation in the final amplifiers. A genetic algorithm used the feedback from a 2 photon detector to reduce the pulse length from 450 fs to 380 fs.

1.2.3 Laser diagnostics

Diagnostics are carried out using a 2% beamsplitter to direct a portion of the beam into a frequency resolved optical gating device (FROG) [36] and an in house M^2 meter.

The M^2 is a measure of beam quality [37], which affects how a beam focuses. A perfect Gaussian beam has an $M^2 = 1$. The M^2 can be measured by recording the spot size of the beam at regular intervals through a focus. The variation of the spot size through the

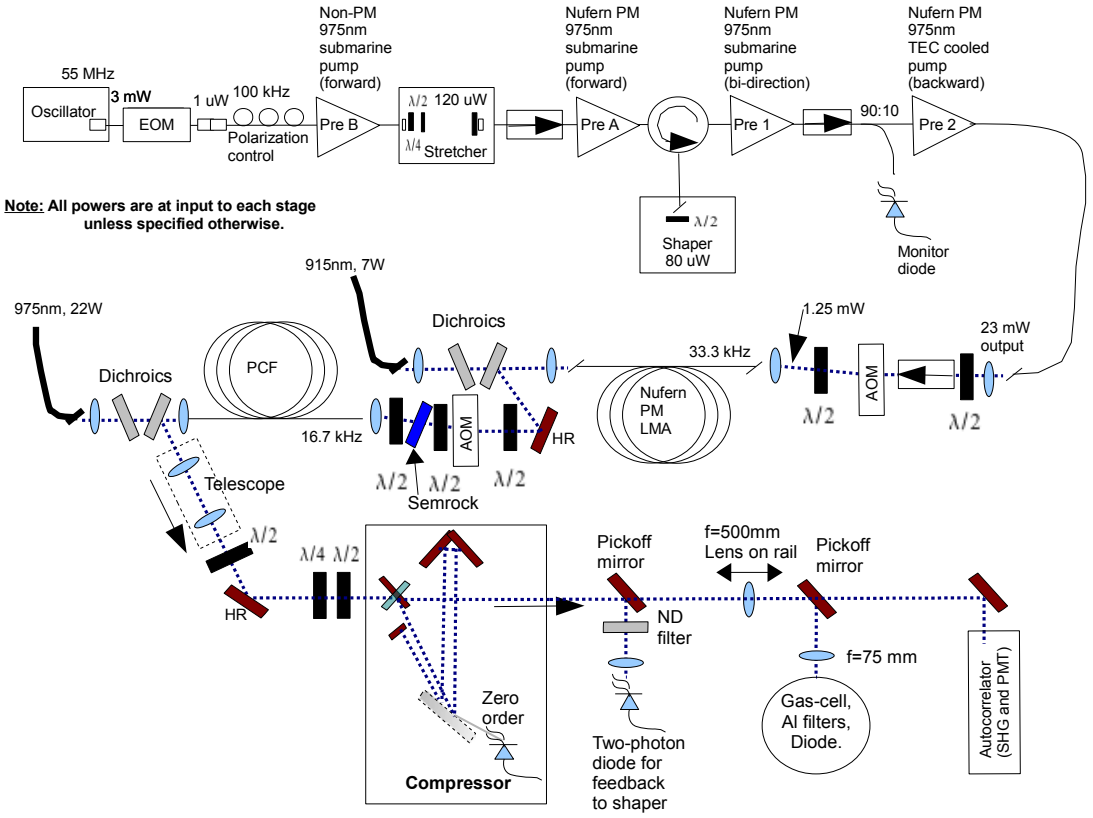

Figure 1.2: Schematic of the CPA based fibre laser currently under development as a source for HHG.

focus is determined by the M^2 and so the M^2 can be calculated by fitting the measured values. Knowledge of the M^2 and thus the focal spot size is important for efficient coupling into a capillary, as discussed in Section 2.3.4.

FROG is a method of ultrashort pulse measurement that uses frequency-resolved autocorrelation. The pulse is gated with a variably delayed replica of itself inside a nonlinear crystal. The resulting spectrogram is recorded on a spectrometer. The spectrogram is the set of spectra at all temporal slices of the pulse. As the gate function is not known in FROG an iterative Fourier transform algorithm is used to find the pulse intensity and phase. Various types of beam geometries can be used for FROG [38] but the one employed here is based on second harmonic generation (SHG). The FROG used in this work is a Swamp Optics GRENOUILLE 8-20. It is a simplified version of the SHG FROG [39], a comparison of the two is shown in Figure 1.3 taken from the Swamp Optics Grenouille tutorial.

In standard SHG FROG a delay line is used to generate the variable delay between the pulse and the gate, in the Grenouille this is replaced by a Fresnel biprism. When a beam hits a Fresnel biprism it is split into two beams that are crossed at a given angle. The crossing of the beams within a nonlinear crystal allows single shot measurements of the pulse to be made, as the time delay between the two pulses depends on the

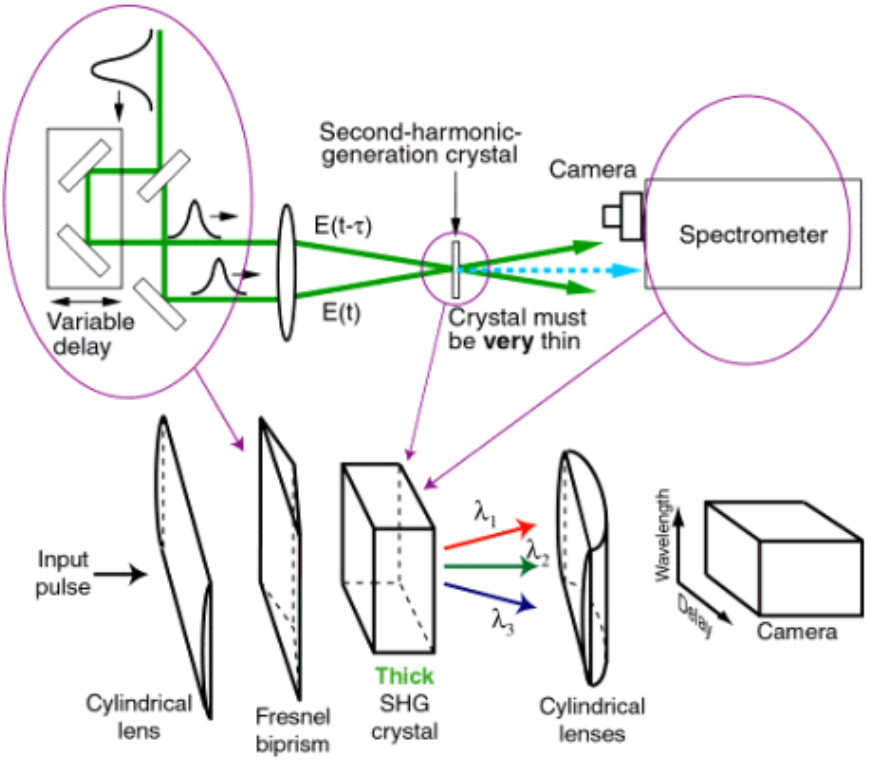

Figure 1.3: TOP:Schematic of a standard SHG FROG setup comprising a beamsplitter, delay line, focussing optic and spectrometer. BOTTOM: Schematic of the Grenouille design that uses a Fresnel biprism and thick nonlinear crystal to replace the delay line and spectrometer respectively. (Image taken from Swamp optics: http://www.swampoptics.com/tutorialsGRENOUILLE.htm)

horizontal position within the crystal. The use of a thick nonlinear crystal acts as a low resolution spectrometer [39]. The thick crystal has a small phase-matching bandwidth, so the phasematched wavelength that it produces varies with angle. The cylindrical lens used to focus the beam into the crystal means that in the vertical direction the second harmonic spectrum produced is spatially resolved. Two final cylindrical lenses image the resultant vertical angle (wavelength) to the vertical position on a camera and the position in the crystal (time delay) to the horizontal position on the camera. The Grenouille used here is capable of measuring 20 fs pulse lengths.

For very short pulses with large bandwidths dispersion within the Grenouille can artificially lengthen a pulse. As a result for short wavelengths one must back propagate through the first cylindrical lens, the Fresnel biprism and nonlinear crystal itself. The thickness of these components was measured and produce a second order dispersion of 220 fs^2. The dispersion of these components is used in Chapter 4 to calculate the actual length of an output pulse from a capillary.

1.2.4 Generation Geometries

HHG is typically achieved using a gas as the target medium.The noble gases, helium, neon, argon and xenon are typically used [40] although the use of molecular gases has also been studied [41,42]. Figure 1.4 shows the three basic geometries used in gas based HHG. The top two are free space geometries with no external guiding of the beam. The beam is focused through either a gas jet or cell. Free space geometries benefit from high transmission and ease of alignment.

The capillary waveguide geometry allows an increased interaction length and more control over phase-matching conditions using the waveguide structure itself. Alignment of this geometry is more difficult and losses are higher.

Both types of HHG geometry have their benefits and the group is continuing to work with both to determine which is ultimately more useful. The work discussed in the first three experimental Chapters uses capillary based HHG whilst the reduced space and complexity in the fibre laser lab necessitates the use of a more compact gas cell approach as is shown in Chapter 6.

1.3 Thesis aims

The basics of HHG, the motivation behind a high flux tabletop XUV source and the laser systems and basic geometries employed within the group have been discussed. Based on these, the main aims of this thesis are:

- To study pump pulse propagation within short hollow core capillaries to improve the XUV flux and energy of capillary based HHG.
- To create a high flux HHG source using a Yb doped fibre CPA laser, leading to a new generation of high flux, compact XUV sources.

The first three Chapters of this thesis focus on capillary based HHG. Chapter 3 begins with an introduction to short hollow core capillary manufacture and discusses some of the initial observations made when coupling high intensity pulses into an argon filled capillary. It then uses the nonlinear propagation model described in Section 2.4 to examine the effects on the pump pulse in the frequency domain whilst testing and improving the accuracy of the model itself.

Chapter 4 extends this work into the time domain and compares the experimentally measured output pulse to the theoretical equivalent for a range of input powers and pressures. The results lead to another improvement in the way the model is applied and the pump pulse is found to undergo self compression, which is discussed before moving

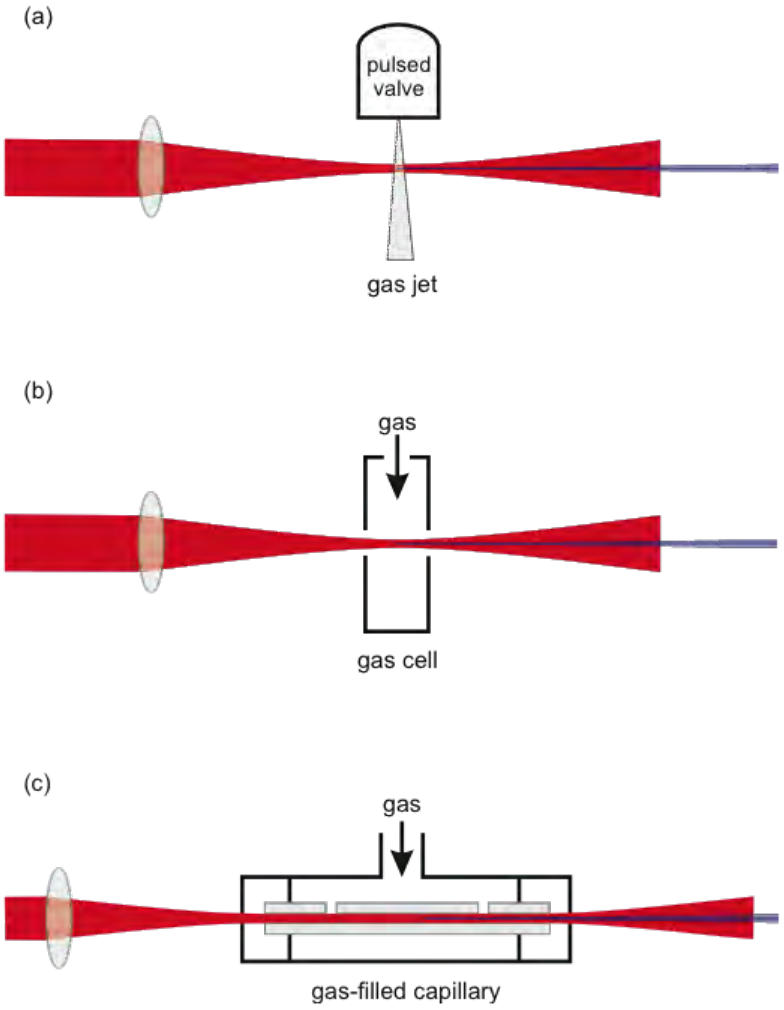

Figure 1.4: Schematic of the three geometries commonly used in HHG. A gas jet (a), a gas cell (b) or a capillary waveguide (c).

onto the XUV spectra generated. The measured XUV spectra for a range of pressures is studied and their dependance on pressure is discussed.

In Chapter 5 a new capillary is designed and manufactured based on observations and analysis of the previous two chapters. The model is used to help design a higher flux capillary by maximising the nonlinear mode coupling, discussed later, that occurs during the pump pulse propagation. This leads to a shorter more effective capillary that boasts a much greater flux.

Chapter 6 leaves capillary based HHG using bulk lasers for gas cell HHG using an Yb doped fibre CPA laser. Experiments are carried out using a compact xenon filled gas cell setup and an XUV photodiode to generate and detect an XUV signal. The dependence of this signal on pressure, power and focal position are explored to maximise the XUV flux, which is then calculated and compared to the flux of the newly designed capillary from Chapter 5.

Chapter 2

Background and Theory

The four experimental chapters within this thesis are separated into two distinct areas, the first covering pulse propagation and HHG using hollow core capillaries, the second focusing on HHG using a high repetition rate fibre laser system. The theory required to understand the drive behind them will be discussed in the following sections. The first section will describe the theory behind HHG, looking at both the semi classical and quantum mechanical (QM) models. These two subsections will explain the source of the high harmonics and what predictions can be made based on experimental conditions. Efficient harmonic conversion requires a coherent growth of the harmonic signal during propagation of the field, which is discussed in the phase-matching section. This will explain the basics of phase-matching and how the conversion efficiency can be improved within the limits of the experiment. The third section concentrates on the theory required to understand the pump pulse propagation. It will be separated out into four sections, discussing the nonlinear, dispersive and ionisation induced effects on propagation, ending with a brief description of capillary based propagation. Due to the complexity of the propagation within the capillary the theory associated with this work has been developed by Dr Peter Horak in conjunction with the Ultrafast X-ray Group. The propagation model, which is based on a multimode generalised nonlinear Schrödinger equation (MM-NLSE) will be briefly described. All theoretical data related to the pump pulse propagation within the capillary was calculated by Dr Horak in conjunction with myself.

2.1 High harmonic generation

Two models are currently used in the field to explain the HHG process. The semi-classical model treats the driving field and the ionised electron classically, whereas the

QM model uses the time dependent Schrödinger equation to model the electron wavefunction within a soft Coulomb potential. The following two sections will describe the basics of these models, the predictions they make and the limitations that are seen.

2.1.1 Semi-classical model

The semi classical model conceived by Corkum [3] treats the single atom response to a high intensity electric field, summarised in Figure 2.1. As the intensity of the field increases its potential distorts the Coulomb potential of the atom allowing a valence electron to tunnel through the barrier created by these two potentials. The ionised electron appears in free space with zero initial velocity and is accelerated by the driving laser field. The trajectory that the electron follows can be modelled classically and has a finite probability of returning the electron to the parent ion. During the course of its trajectory the electron gains kinetic energy which can be released as an extreme ultraviolet (XUV) photon if the electron recombines with its parent ion.

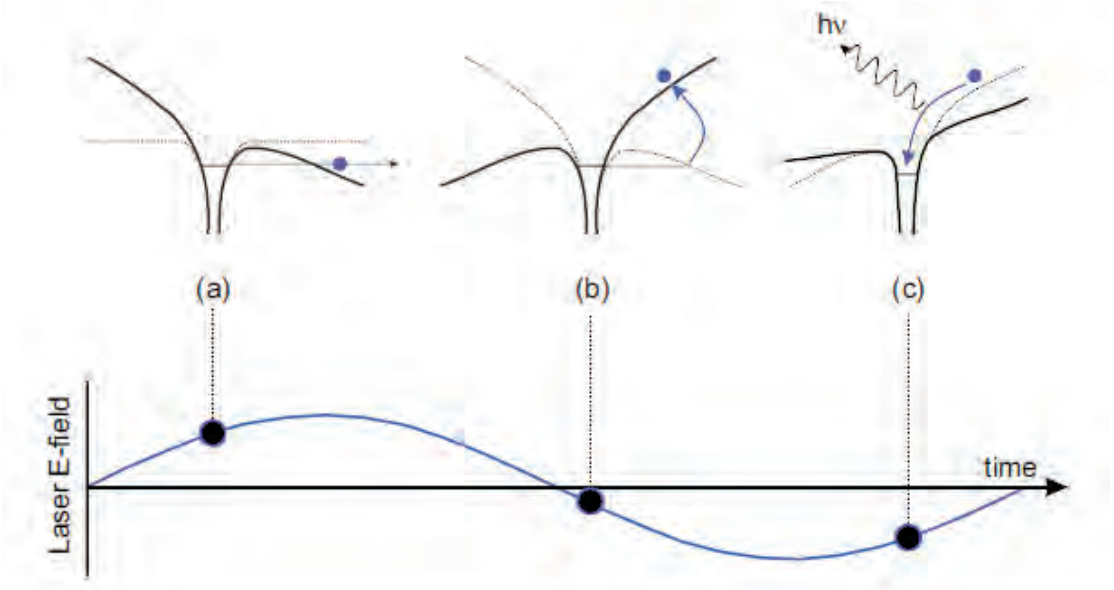

Figure 2.1: Three-step model of HHG. (a) Driving field distorts Coulomb potential allowing electron to tunnel out and accelerate in driving field (b) Field reverses accelerating electron back towards parent ion. (c) Electron recombines with ground state, emitting photon.

The classical trajectory of the electron can be calculated by modelling an electron under the influence of a sinusoidal driving field $E = E_0 \sin(\omega t)$. Using the assumption that the electron has zero velocity at time $t = t_0$ and a position of $x = 0$ at time $t = t_1$ and $t = t_0$ one can calculate the position, velocity and acceleration of the electron using Newton's

second law.

$$x = \frac{eE_0}{m\omega}\left(\frac{1}{\omega}\left(\sin(\omega t_0) - \sin(\omega t)\right) + (t - t_0)\cos(\omega t_0)\right) \tag{2.1}$$

$$\dot{x} = \frac{eE_0}{m\omega}\left(\cos(\omega t_0) - \cos(\omega t)\right) \tag{2.2}$$

$$\ddot{x} = \frac{eE_0}{m}\sin(\omega t) \tag{2.3}$$

where e, m are the charge and mass of an electron respectively, E_0 is the electric field amplitude and ω is the angular frequency. t_0 is the release time and t_1 is the return time of the ionised electron.

The trajectory that an ionised electron will take depends strongly on the phase of the driving field at the moment of ionisation. Using equation 2.1 the electron trajectories for four release times (t_0) within the optical cycle were modelled and shown in Figure 2.2. The ionised electron will only return to the parent ion if it is released when the phase of the driving field is between $\frac{\pi}{2}$ and π or $\frac{3\pi}{2}$ and 2π, these are shown by the green and light blue trajectories. In other cases the electron is accelerated away from the ion, shown by the dark blue and red trajectories. The arrows indicate the velocity of the returning electrons. The electron released at $\frac{\pi}{2}$ returns with zero velocity, whilst the electron released at $\frac{8\pi}{5}$ returns with almost maximum velocity. Recombination can only occur every half optical cycle, which produces a series of XUV intensity spikes in the time domain. The Fourier transform of this is a spectrum comprised of a series of harmonics of the fundamental driving frequency. As the XUV spikes occur twice each optical cycle in the time domain, only even or odd harmonics can be generated. The alternate XUV emissions occur with a π phase shift with respect to each other resulting in odd harmonics.

It is possible to use the classical electron velocity from this model to calculate the maximum, or cutoff energy that an emitted photon can have [43]. The return velocity can be calculated by replacing t with t_1 in equation 2.2, from which the return energy can be calculated. Figure 2.3 shows the electron return energy as a function of the travelling time $\tau = t_1 - t_0$. This gives a cutoff energy of

$$E_{cutoff} = 3.17U_p + I_p \tag{2.4}$$

where I_p is the ionisation potential of the atom and U_p is the ponderomotive potential of the electron and is given by

$$U_p = \frac{e^2E_0^2}{4m\omega^2} \tag{2.5}$$

The ponderomotive potential is the average kinetic energy imparted to a charged particle by a sinusoidal electric field.

An electron that returns to the ion with an energy less than $3.17U_p$ can take two possible trajectories. These are known as the long and short trajectories. The harmonic emitted

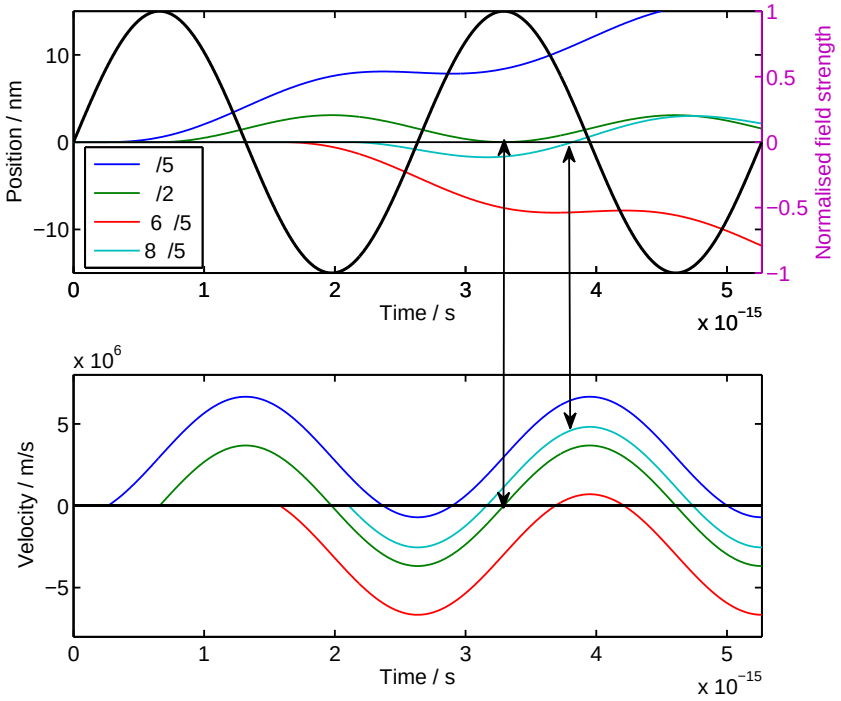

Figure 2.2: Electron trajectories for four different release times. The top figure shows the electron position, the bottom the velocoity. The solid black line is the driving field, the thinner coloured lines represent different electron trajectories. The electron position only returns to zero and hence can recombine if it is ionised at certain phases of the driving field. The arrows show the velocity of the two returning electrons at the point where they can recombine.

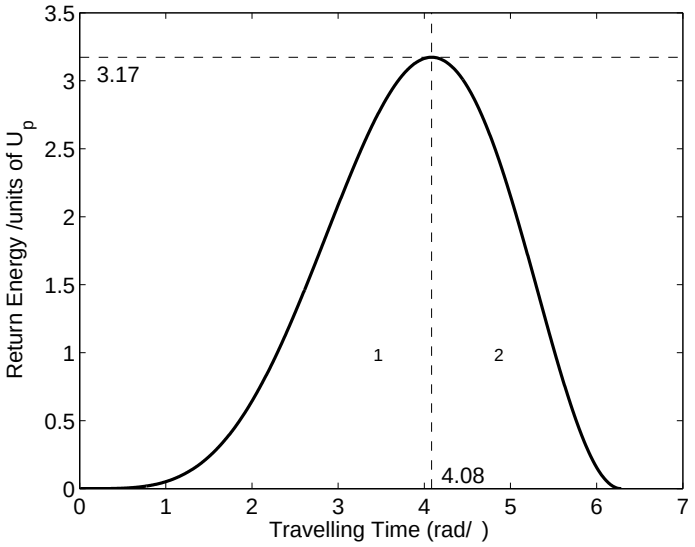

Figure 2.3: Return energy of electron as a function of the travelling time. The energy is given in units of the ponderomotive potential of the electron. The maximum return energy occurs at a travelling time of 4.09 rads/ω. Trajectories with travelling times less than this are known as short trajectories 'τ_1' those greater are called long trajectories 'τ_2'.

in each case has the same energy but has acquired a different phase due to the differing time the electron spent under acceleration by the driving field. This is the 'atomic phase' and will be discussed further in Section 2.2.

The harmonic spectrum produced by HHG contains three distinct regions, shown in figure 2.4, the perturbative, the plateau and the cutoff regions. The position of the cutoff region is defined by equation 2.4 and contains the highest energy harmonics. Between the perturbative and cutoff regions there is an equal probability that an electron will return with any energy up to the cutoff and so a plateau is observed.

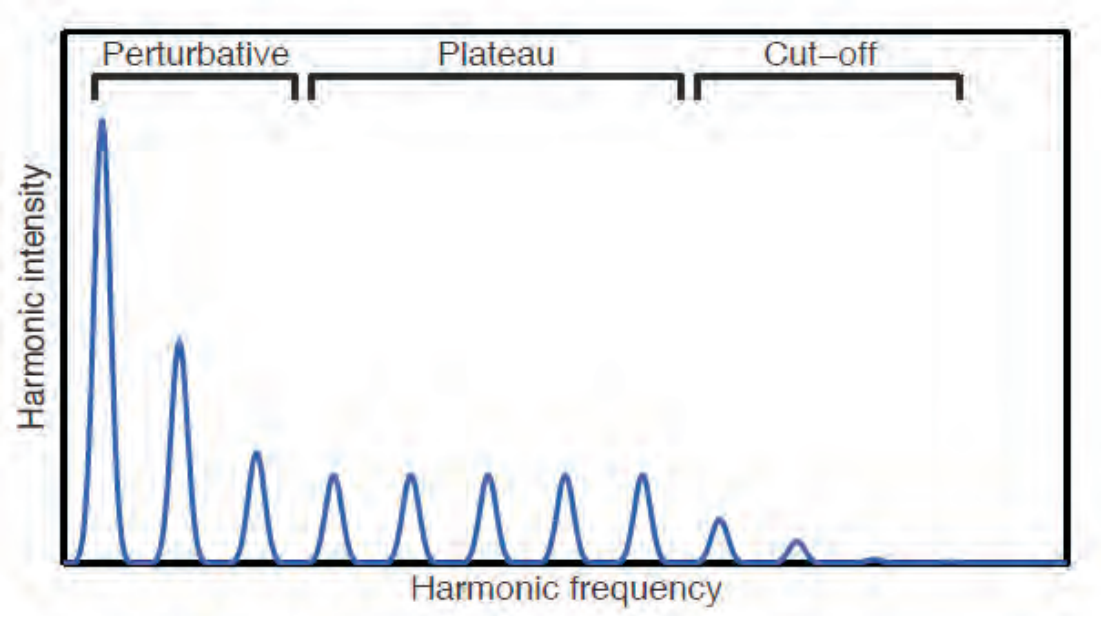

Figure 2.4: High harmonic spectrum shows a perturbative region with harmonics of highest intensity. Following a rapid decrease of intensity is the plateau region, an area of constant intensity. The spectrum ends in a cut-off region, which has the highest generated harmonics.

The semi-classical model detailed thus far can predict the electron trajectories and the cutoff energy, however, it does not explain the recombination process nor where the nonlinearity in this harmonic generation system exists. To answer these questions one requires a QM model of HHG [4].

2.1.2 Quantum Mechanical Model

The treatment of the driving field in this model remains classical, the difference exists in the treatment of the electron. In the previous section the electron was treated as a classical particle in free space under the influence of a driving field. The QM model treats it as an electron wavefunction within a soft Coulomb potential. The model described in the following pages is a simplified version of the real situation. The driving field is linearly polarised and so a 1-D atomic potential is used instead of the full 3-D atomic potential.

This is appropriate for this case but would require changing to predict the effects of elliptically polarised fields. In addition the atom is modelled as a single electron bound within a soft Coulomb potential that is scaled to provide the appropriate first ionisation level for the atom in question; in the case of argon it is 15.76 eV. The time dependent Schrödinger equation (TDSE) is used to calculate the change of the wavefunction over time.

$$i\hbar\frac{\partial}{\partial t}\left|\psi,t\right\rangle = \hat{H}\left|\psi,t\right\rangle \tag{2.6}$$

where $|\psi,t\rangle$ is the electron wavefunction at time t and $\hat{H}$ is the Hamiltonian operator which will be described later. To calculate the change of the wavefunction in time one can use a Taylor expansion of $|\psi,t_0+t\rangle$. The Taylor expansion is not a stable propagator, however, as will be discussed the final propagation uses the Crank-Nicholson [44] scheme to produce stable a result. The Taylor expansion of $|\psi,t_0+t\rangle$ is given as

$$\left|\psi,t_0+t\right\rangle = \left|\psi,t_0\right\rangle + (t-t_o)\frac{\partial}{\partial t}\left|\psi,t_0\right\rangle + \cdots \tag{2.7}$$

One can substitute into this using equation 2.6 to give

$$\left|\psi,t_0+t\right\rangle \simeq \left|\psi,t_0\right\rangle - \frac{i}{\hbar}(t-t_o)\hat{H}\left|\psi,t_0\right\rangle \tag{2.8}$$

Factorising this produces a time propagation operator that can be used in this approximation

$$\left|\psi,t_0+t\right\rangle = \left[\hat{I}-\frac{i}{\hbar}(t-t_o)\hat{H}\right]\left|\psi,t_0\right\rangle \tag{2.9}$$

where $\hat{I}$ is the identity operator. To use the time propagator one must know how to apply the Hamiltonian. In this case the Hamiltonian is given as

$$\hat{H} = -\frac{\hbar^2}{2m}\frac{\partial^2}{\partial x^2} + V(x) \tag{2.10}$$

where m is mass of an electron and $V(x)$ is given by

$$V(x) = -\frac{e^2}{4\pi\varepsilon_0}\frac{1}{\sqrt{\alpha_0^2+x^2}} + eEx \tag{2.11}$$

where e is charge of an electron, ε_0 is the permittivity of free space, a_0 is the Bohr radius and x is the distance from the atom. The first term is the soft Coulomb potential of the atom. A soft Coulomb potential is used to avoid generating singularities in the numerical simulation. If the Bohr radius is used as in equation 2.11 the first ionisation level is ~ 19 eV. This is changed to fractions of the Bohr radius to scale the first ionisation level to the atom in question, in the case of argon the first ionisation level is at 15.76 eV. This and the initial ground state wavefunction of the outer valence electron are shown in

Figure 2.5. The second term is the potential exerted on the electron by the driving field, E. Both of these terms are simple to use in numerical simulation, the more complicated term is the second order partial differential in space.

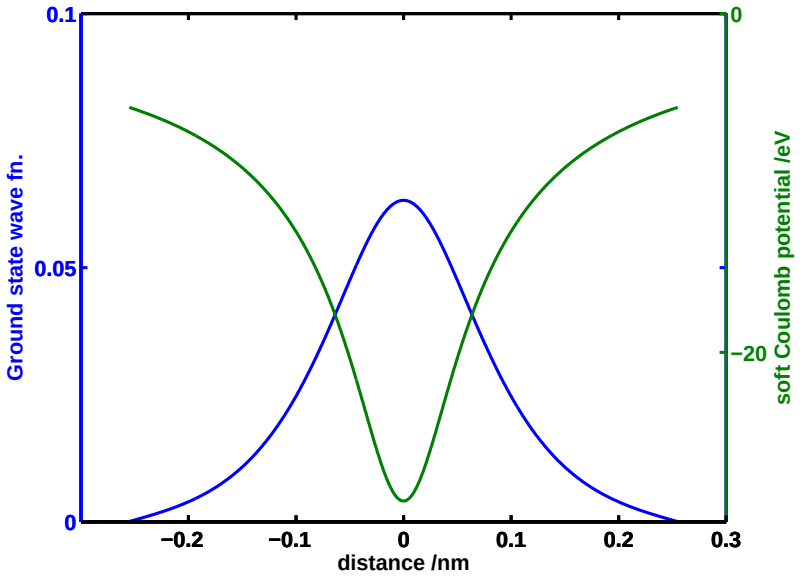

Figure 2.5: The ground state electron wavefunction (blue line) within the soft Coulomb potential (green line).

To calculate $\frac{\partial^2}{\partial x^2}$ one can again turn to a Taylor expansion, written as

$$|\psi, x_0 + x\rangle = |\psi, x_0\rangle + \Delta x \frac{\partial}{\partial x} |\psi, x_0\rangle + \Delta x^2 \frac{\partial^2}{\partial x^2} |\psi, x_0\rangle + \dots \tag{2.12}$$

where $\Delta x = x_0 + x$. It is possible to write out a similar expansion for $|\psi, x_0 - x\rangle$

$$|\psi, x_0 - x\rangle = |\psi, x_0\rangle - \Delta x \frac{\partial}{\partial x} |\psi, x_0\rangle + \Delta x^2 \frac{\partial^2}{\partial x^2} |\psi, x_0\rangle + \dots \tag{2.13}$$

If equations 2.12 and 2.13 are added together one can rearrange the result to obtain

$$\frac{\partial^2}{\partial x^2} |\psi, x_0\rangle \simeq \frac{|\psi, x_0 - x\rangle - 2\,|\psi, x_0\rangle + |\psi, x_0 + x\rangle}{\Delta x^2} \tag{2.14}$$

Therefore if one knows the wavefunction for all x one can calculate $\frac{\partial^2 \psi}{\partial x^2}$ by differencing. Within the numerical model this is achieved by multiplying the wavefunction by a tri-diagonal matrix constructed from the above equation. From here on to simplify the nomenclature $|\psi, x_i, t_n\rangle$ will be written as ψ_n^i. With this equation 2.14 becomes

$$\frac{\partial^2 \psi_n^i}{\partial x^2} = \frac{\psi_n^{i+1} - 2\psi_n^i + \psi_n^{i-1}}{\Delta x^2} \tag{2.15}$$

By substituting this into equation 2.10 the full form of the time propagation of the wavefunction shown in equation 2.9 can be written as

$$\psi_{n+1}^{i} = \psi_{n}^{i} - \frac{i\Delta t}{\hbar}\left(-\frac{\hbar^2}{2m}\left(\frac{\psi_{n}^{i+1} - 2\psi_{n}^{i} + \psi_{n}^{i-1}}{\Delta x^2}\right) + V(x)\psi_{n}^{i}\right) \tag{2.16}$$

This is known as the 'forward time central step' scheme (FTCS), an equivalent of this can be written propagating in the opposite direction to calculate ψ_{n-1}^{i}, known as the 'backward time central step' (BTCS). Neither of these propagation schemes are stable when used individually, however it has been shown that the average of the two is stable. This is known as the Crank-Nicholson [44] scheme and is used to propagate the wavefunction forward in time. Using this, the final equation used to calculate the time propagation steps of the electron wavefunction is

$$\psi_{n+1} = \left(\hat{I} + \frac{i\Delta t}{2\hbar}\hat{H}\right)^{-1}\left(\hat{I} - \frac{i\Delta t}{2\hbar}\hat{H}\right)\psi_{n} \tag{2.17}$$

where $\hat{I}$ is the identity operator. An example of the results produced by this numerical simulation is shown in Figure 2.6. This shows a 7 fs driving pulse (black line) incident on a single atom. The colourmap is log plot of the probability distribution of the electron wavefunction in time and space. The x-axis shows the time whilst the y-axis shows the distance from the centre of the atom. A function is applied to the wavefunction that reduces it to zero at spatial boundaries to prevent unreal reflections in the simulation. The soft Coulomb potential combined with that of the driving field creates a potential barrier that the classical electron can tunnel through. Here the electron is modelled as a wavefunction and so a portion of this wavefunction may tunnel through the barrier and be accelerated away from the centre of the soft Coulomb potential along similar trajectories to those described in the semi-classical model, Figure 2.6. This can be seen in Figure 2.6 in the form of sinusoidal like ripples in the probability distribution. The greatest proportion of the probability density remains bound with the atom at the centre, however an unbound portion of the wavefunction propagates out into free space and can be seen to return to the core later.

The returning unbound portion of the wavefunction acquires a different frequency to the bound part at the origin due to acceleration by the driving field, resulting in interference between the two. This interference causes a dipole oscillation at the beat frequency of the bound and unbound portions of the wavefunction. The oscillating dipole generates the XUV field and its response to the driving field is highly nonlinear. In the model the expectation value of the position of the electron wavefunction, $\langle x \rangle$, can be calculated. The second derivative with respect to time of this expectation value gives an acceleration which is assumed to be equal to the field generated by the oscillating dipole. This acceleration is calculated every few time steps within the numerical simulation to produce the new XUV field. The time derivative of the expectation value of an operator can be

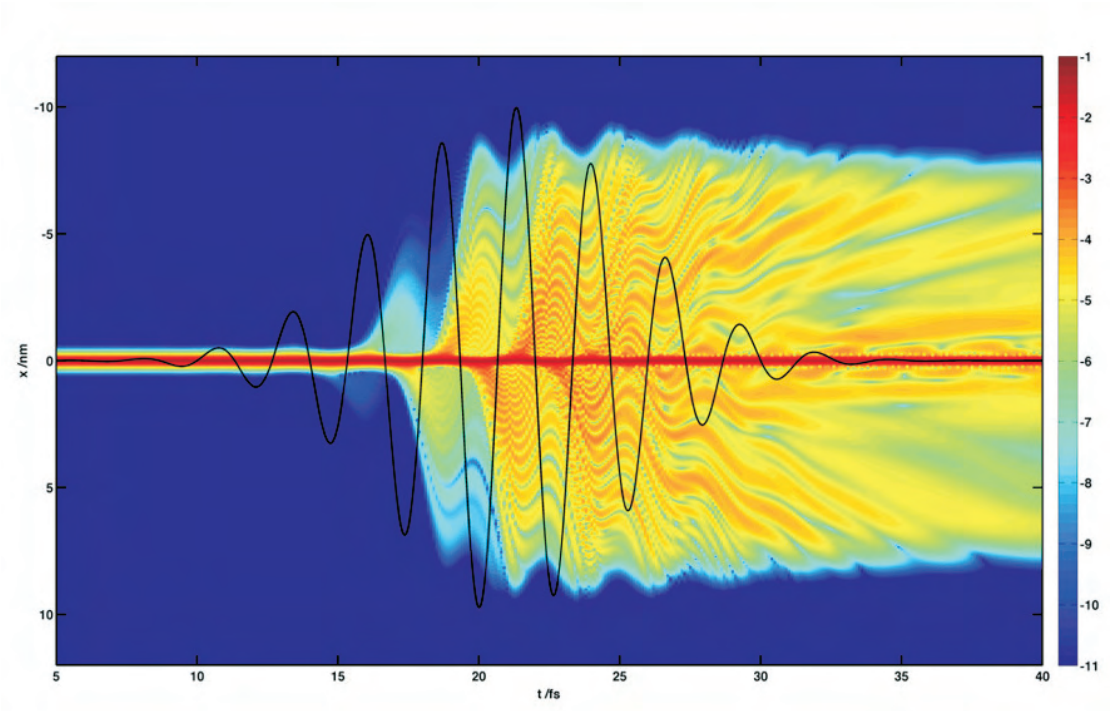

Figure 2.6: Plot of the probability distribution of the electron wavefunction in time and space. The solid black line represents a 7 fs driving pulse. The colour map is a $\log_{10}$ plot of the probability density of the wavefunction. The greatest density remains at the core, areas of high probability density propagate away and return to the nucleus in similar trajectories to those in the semi-classical model.

written as

$$\frac{\partial}{\partial t}\left\langle \hat{A} \right\rangle = \left\langle \frac{\partial \hat{A}}{\partial t} \right\rangle + \frac{i}{\hbar}\left\langle \left[\hat{H}, \hat{A}\right] \right\rangle \tag{2.18}$$

Most operators are time independent and thus $\left\langle \frac{\partial \hat{A}}{\partial t} \right\rangle = 0$. Using equation 2.18 the acceleration of the dipole and hence XUV field can be calculated as

$$\frac{\partial^2}{\partial t^2}\langle \hat{x} \rangle = -\frac{1}{\hbar}\left\langle \left[\hat{H}, \left[\hat{H}, x\right]\right] \right\rangle \tag{2.19}$$

The electric field of the generated XUV is proportional to this dipole acceleration. The temporal field calculated from Figure 2.6 is shown in Figure 2.7. The field has had the lower frequency components filtered to show the high frequency XUV field. The Fourier transform of the temporal field is shown in Figure 2.8 and is the expected spectrum from an ensemble of single atoms. The plateau and cutoff regions are clearly visible. Harmonics cannot be seen before the cutoff region due to interference between the XUV fields of the long and short trajectories.

The initial coding for this simulation was carried out by Dr W.S Brocklesby. The simulation is written in Matlab and C and is being used by the group to understand the

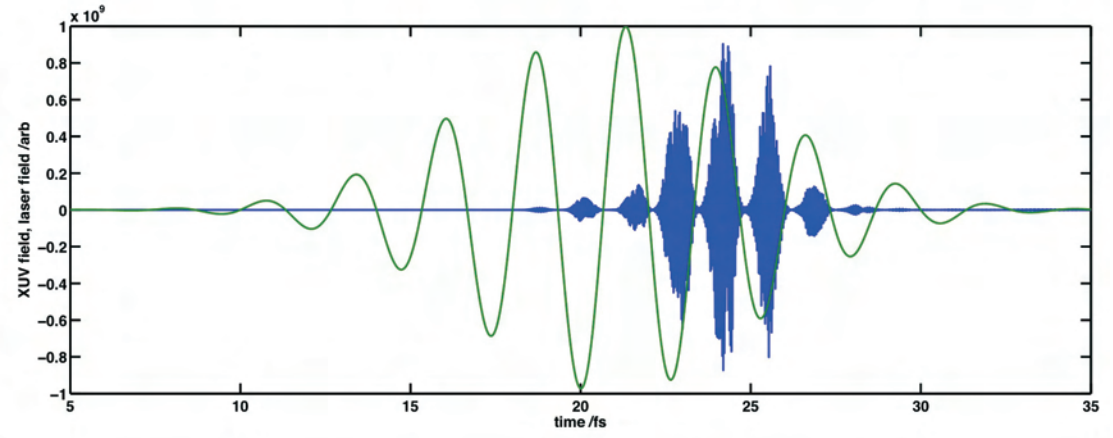

Figure 2.7: Electron acceleration driven by a 7 fs pulse. The green line represents the 7 fs driving pulse, the blue line indicates the XUV field which is the electron acceleration. This is obtained by removing the lower frequency components from the dipole oscillation.

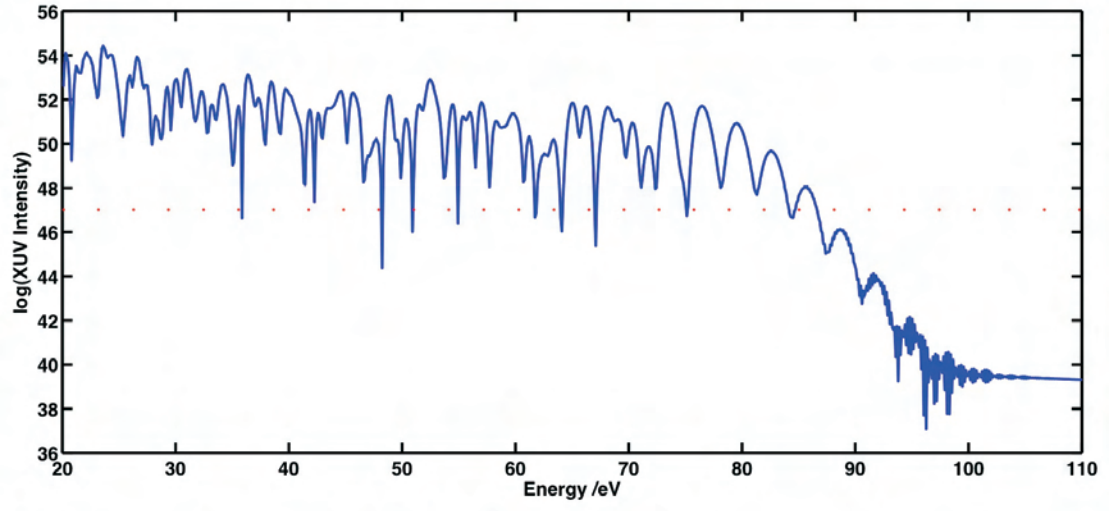

Figure 2.8: XUV spectrum produced by HHG using a 7 fs driving pulse. The spectrum is the Fourier transform of the XUV field shown in Figure 2.7. The harmonics at the cut-off are visible between 80 and 90 eV.

HHG process more fully. In the future the model will be used to predict HHG in the short hollow core capillaries used in this thesis. I have begun this work already but it is still at an early stage.

2.2 Phase-matching

For any nonlinear optical conversion process to be efficient it is necessary to have coherent emission from a large number of atoms. As the driving laser field propagates through the generation medium a harmonic field is produced that co-propagates with it. For the induced harmonic field to build in intensity over the entire generation region its

phase velocity must be equal to that of the fundamental driving field, i.e. it must be phasematched. This is shown schematically in Figure 2.9.

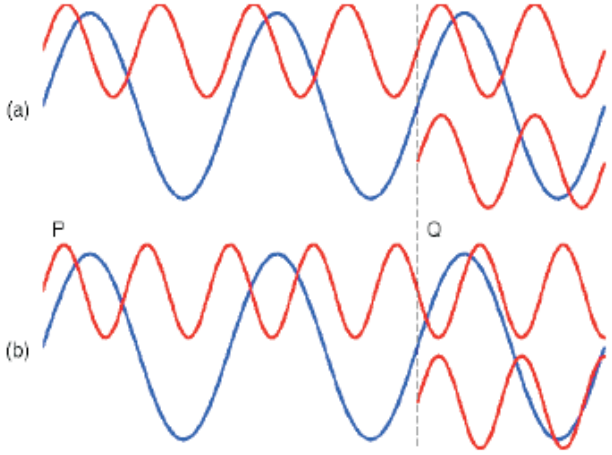

Figure 2.9: Schematic of basic phase-matching for second harmonic generation. (a) Harmonic produced at Q is in phase with that produced at P, constructive interference builds up the signal. (b) Harmonic produced at Q is out of phase with that produced at P, therefore they interfere destructively and the signal is reduced.

Consider the electric field vector of the fundamental driving field $E_f \propto e^{i(k_f x - \omega_f t)}$, and that of the harmonic $E_q \propto e^{i(k_q x - q\omega_f t)}$. The phase mismatch between the two, Δk, must be reduced to zero for perfect phase-matching.

$$\Delta k = k_q - q k_f = 0 \tag{2.20}$$

The phase mismatch between the fundamental and harmonic fields depends on dispersion from the neutral gas atoms Δk_{dis} , the free electrons Δk_{fe}, geometrical effects Δk_{ge} due to focusing conditions and the method of generation and the atomic phase Δk_{at}. These terms must be balanced for effective phase-matching

$$\Delta k = \Delta k_{dis} + \Delta k_{fe} + \Delta k_{geo} + \Delta k_{at} = 0 \tag{2.21}$$

Equation 2.21 would produce perfect phase-matching in which the driving field and harmonic remain in phase over an infinite distance. In practise it is rare that $\Delta k = 0$, nonetheless phase-matching over the generation length is possible. A useful measure for this is the coherence length, which is the distance over which the phase mismatch equals π.

$$L_{coh} = \frac{\pi}{\Delta k} \tag{2.22}$$

When the phase mismatch equals π newly generated harmonics will interfere destructively with previously generated ones, so L_{coh} indicates the length over which the coherent growth of the harmonic field occurs. Figure 2.10 shows the harmonic build up for perfect phase-matching (blue) imperfect phase-matching (green) and quasi-phase-matching (red). In quasi-phase-matching (QPM) techniques the harmonic field is generated for a single coherence length followed by an equal distance of no generation and repeated. This allows the harmonic field to grow over a length greater than the coherence length. The increase in yield is equal to the number of QPM regions created. In HHG this is achieved by either varying the pulse intensity [45] or the gas density [46].

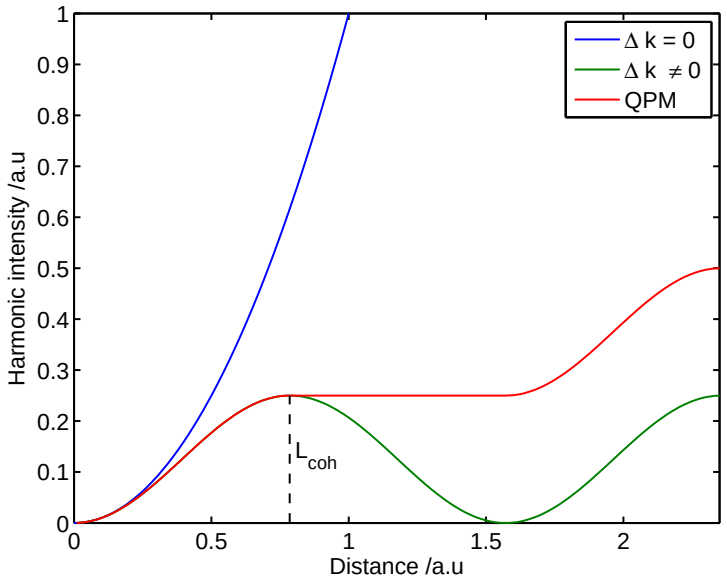

Figure 2.10: Plot of harmonic generation during propagation. Perfect phase-matching occurs when $\Delta k = 0$ (blue line), when $\Delta k \neq 0$ (green line) the coherence length is given by equation 2.22 and shown by the dashed line. QPM is shown in red where the harmonic signal is increased in alternating regions.

2.2.1 Gas and free electron phase-matching contributions

HHG is inextricably linked to ionisation; as a result free electrons are produced in all HHG experiments and the fundamental and harmonic fields propagate within a partially ionised gas. The refractive index of the plasma for the fundamental can be written as

$$n_{fe} = \left(1 - \frac{\omega_p^2}{\omega_0^2}\right)^{\frac{1}{2}} \tag{2.23}$$

where ω_0 is the angular frequency of the driving field and ω_p is the plasma frequency. This is a function of the free electron density N_e and is given by

$$\omega_p = \left(\frac{e^2 N_e}{m\varepsilon_0}\right)^{\frac{1}{2}} \tag{2.24}$$

where the free electron density $N_e = P\eta N_a$ depends on pressure, P in atmospheres (atm), the ionisation fraction, η and the number density of atoms at 1 atm N_a. From equation 2.20 we can write the phase mismatch due to the free electrons as

$$\Delta k = k_q - qk_0 \tag{2.25}$$

$$\Delta k_{fe} = \frac{2\pi q}{\lambda_0} . \frac{1}{2} \frac{\omega_p^2}{\omega_0^2} \tag{2.26}$$

$$\Delta k_{fe} = \frac{\pi q \omega_p^2}{\lambda_0 \omega_0^2} \tag{2.27}$$

The free electron coherence length L_{fe} is then given as

$$L_{fe} = \frac{2\pi c \omega_0}{q\omega_p^2} \tag{2.28}$$

Two approximations exist that can been made with respect to the contribution to the refractive index from the ionised gas. The first is that the ions have a refractive index of 1 and therefore do not contribute to the phase mismatch [47], the second, used here assumes that the ionisation has no effect on the refractive index [48], i.e. the refractive index of the ions is the same as the neutral atoms. The refractive index of a partially ionised gas can be written as

$$n = 1 + P\left(\delta(\lambda) + n_2 I\right) \tag{2.29}$$

where $\delta = \Re(n) - 1$, n_2 is the nonlinear refractive index and I is the intensity of the driving pulse. From this the propagation constant can be written as

$$k \approx \frac{2\pi}{\lambda} + \frac{2\pi P \delta(\lambda)}{\lambda} + n_2 I P \tag{2.30}$$

where the terms correspond respectively to vacuum, neutral gas dispersion and nonlinear refractive index. From this point on the nonlinear refractive index term will be left out as it is small compared to the other terms. Using equation 2.20 the phase mismatches corresponding to the neutral and ionised gas can be written as

$$\Delta k_{dis} = q k_f (n(\lambda_q) - n(\lambda_f)) \tag{2.31}$$

$$\Delta k_{dis} = \frac{q 2\pi P}{\lambda_f} \left[\delta(\lambda_f) - \delta(\lambda_q)\right] \tag{2.32}$$

where P is the pressure in atm. Using equations 2.31 and 2.22 the coherence length of the gas is

$$L_{dis} = \frac{\pi\lambda_f}{q2\pi P}\frac{1}{[\delta(\lambda_f) - \delta(\lambda_q)]} \tag{2.33}$$

The coherence lengths of both the gas and free electrons are inversely proportional to the harmonic order q and the gas pressure P. The high harmonics shown in later chapters range from the 17th to the 31st harmonic order. It is important to note that as the harmonic order is increased the coherence length and thus the length over which HHG can occur will decrease. HHG therefore becomes very inefficient for higher values of q unless the phase mismatches are balanced. The phase mismatch due to the free electrons is proportional to the ionisation fraction. As a result if the ionisation fraction is kept low equation 2.27 becomes negligible and the phase-matching can be treated linearly; this is known as the neutral gas limit. The above equations show that the total phase mismatch is affected by the gas pressure and harmonic order. Only the free electron contribution depends on the ionisation fraction and hence the pulse intensity, which provides a degree of control over the total phase mismatch.

2.2.2 Geometrical phase-matching contributions

The geometrical phase mismatch depends on the generation conditions. Within a capillary the geometrical phase mismatch is caused by the waveguiding properties of the capillary itself. The driving field is subject to its effect which will be discussed in the following section, however due to the short wavelength of the harmonics they are not affected by it. As a result changes to the structure of the waveguide can be used to balance the phase mismatch. The coherence length in this case is given by [49]

$$L_{wg} = \frac{4\pi^2}{u_{nm}^2}\frac{a^2}{q\lambda_0} \tag{2.34}$$

where u_{nm} is the Bessel function and a is the bore radius. As with the gas and free electron dispersion terms, the waveguide phase mismatch and hence coherence length is dependent on the harmonic order q. This can be reduced by increasing the inner capillary bore radius a as the coherence length scales with the square of the bore radius. Whilst one could increase q by an order of magnitude for an increase in radius of just $\sqrt{10}$, the subsequent reduction in pulse intensity will similarly reduce the cutoff. This is a method that could only be used in conjunction with a very high intensity laser system.

In free space focusing geometries, such as gas cell or jet HHG, there is no waveguide to provide a phase mismatch. In these cases the curved wavefront of a focused Gaussian

field undergoes a phase shift given by [50]

$$\phi(r,z) = arg\left[\frac{1}{2(z_0+iz)}\exp\left(-\frac{k_f r^2}{2(z_0+iz)}\right)\right] \tag{2.35}$$

where r is the radial distance, z is the longitudinal distance and z_0 is the Rayleigh length. To illustrate how phase shift can affect the phase-matching it is useful to look at the phase change on-axis known as the Gouy phase, which can be written as [51]

$$\phi_G = \arctan\left(\frac{z}{z_0}\right) \tag{2.36}$$

The propagation vector due to the on-axis Gouy phase is then given by

$$k_G = \frac{d\phi_G}{dz} \tag{2.37}$$

$$k_G = \frac{z_0}{z^2+z_0^2} \tag{2.38}$$

Equation 2.20 therefore gives

$$\Delta k_G = \frac{qz_0}{z^2+q^2z_0^2} - \frac{qz_0}{z^2+z_0^2} \tag{2.39}$$

The term due to the harmonic propagation vector is neglected as it can be approximated by $\frac{1}{qz_0} \approx 0$. Therefore the phase mismatch and coherence length due to the Gouy phase are given by

$$\Delta k_G = -\frac{qz_0}{z^2+z_0^2} \tag{2.40}$$

$$L_{Gouy} = \frac{\pi(z^2+z_0^2)}{qz_0} \approx \frac{\pi z_0}{q} \tag{2.41}$$

The Gouy coherence length is proportional to the Rayleigh range [49], this makes it more dominant for shorter focal length systems such as in the fibre laser HHG system described in Chapter 6. It is worth noting that the Gouy phase mismatch shown in equation 2.40 is also dependent on the relative position with respect to the focus. This means that its contribution to the total phase mismatch changes with z, resulting in different phase-matching conditions through the focus. This is observed in Chapter 6 where the phase-matching for a gas cell based HHG system is calculated using the atomic and Gouy phase contributions.

2.2.3 Atomic phase contribution

The atomic phase is an intrinsic phase of the harmonic, dependent on the trajectory of the ionised electron mentioned in Section 2.1.1. The atomic phase is given by the

integral of the quasi classical action of the electron [52]

$$\phi_{at} = \frac{S(t_0, t_1)}{\hbar} + q\omega t_1 \tag{2.42}$$

where ϕ_{at} is the phase of the emitted harmonic and

$$S(t_0, t_1) = \int_{t_0}^{t_1} \left(\frac{m_e v(t)^2}{2} + I_p \right) \mathrm{d}t \tag{2.43}$$

where t_0 and t_1 are the tunnelling and return times of the electron.

The classical action is a function of the kinetic energy the electron acquires from the driving field due to the time spent in the continuum. As the electron wavefunction is accelerated the phase of the driving field continues to change. The unbound portion of the wavefunction undergoes a frequency shift equal to the kinetic energy gained due to travelling in the continuum. When it returns to the core, the phase difference is due to the frequency shift the accelerated portion has acquired and the travelling time spent in the continuum. As such the long and short trajectories provide different phase shifts for a given harmonic and thus can vary differently for a given pulse intensity. This is shown in Figure 2.11 which shows the atomic phase calculated for the long (blue) and short (red) trajectories as a function of the intensity. The dependence on the driving

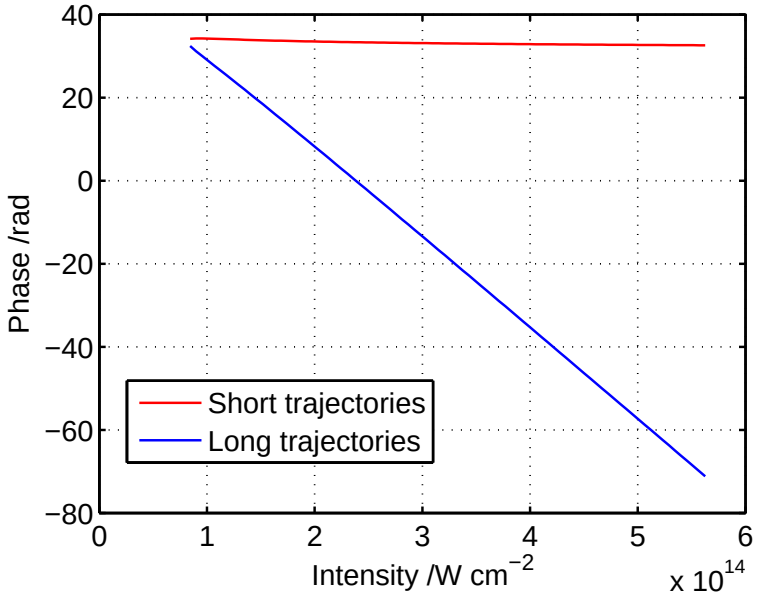

Figure 2.11: Atomic phase contribution from the short (red) and long (blue) electron trajectories as a function of the pulse intensity. The dependence of both long and short trajectories is linear with pulse intensity, however the long trajectories have a stronger dependence.

field intensity is found to be almost linear [52] for both long and short trajectories. The intensity of the pulse varies across the beam therefore the atomic phase contribution generates a curved wavefront. The dependence of the long trajectories is much greater

than the short trajectories leading to a higher divergence of the subsequently generated harmonics. As a result after significant propagation the short trajectory harmonics dominate those created by the long trajectories.

It is important to note at this point that the atomic phase scales with intensity but not with the harmonic number as in the previous three cases. At higher harmonics the contribution from this term will become negligible compared to the free electron and geometrical contributions.

It was shown previously in equations 2.4 and 2.5 that the maximum energy a harmonic photon can have is proportional to the intensity of the driving field. Therefore to generate higher harmonics an increase in the intensity of the driving field is required. At first this appears to simply require tighter focusing, however, the ionisation fraction will increase with the field intensity, decreasing L_{fe}. In addition the Gouy coherence length L_{Gouy} scales with the square of the focal length. The best method for increasing the intensity is pulse compression. A few cycle pulse has a very steep leading edge resulting in a higher intensity for low ionisation fractions. In this way higher harmonics can be generated whilst maintaining long coherence lengths, allowing the harmonics more time to build up and increase the total yield.

This is the driving force behind part of this project, to create a pulse compression system that can reduce the current pulse length of 40 - 45 fs down to sub-10fs.

2.3 Pulse propagation

Propagation of an optical field within a medium results in a polarisation of the medium. For large optical field strengths the response of the bound electrons within the medium is anharmonic leading to nonlinear contributions to the total polarisation **P**. The general relation for the polarisation of a medium is then

$$\mathbf{P} = \varepsilon_0 \left(\chi^{(1)}.\mathbf{E} + \chi^{(2)}.\mathbf{EE} + \chi^{(3)}.\mathbf{EEE} + \ldots \right) \tag{2.44}$$

where ε_0 is the permittivity of free space and $\chi^{(j)}\,(j = 1, 2, \ldots)$ is the jth order susceptibility. The first order susceptibility, $\chi^{(1)}$, is the dominant contributor to **P** and is responsible for the linear refractive index and absorption of a material. The second order, $\chi^{(2)}$, leads to nonlinear effects such as second harmonic and sum frequency generation. The third order susceptibility, $\chi^{(3)}$, gives rise to temporal effects such as self phase modulation (SPM) and self steepening, as well as spatial effects such as Kerr self focusing. Centrosymmetric media such as gases have zero contributions from the second order susceptibility, $\chi^{(2)}$, and so it will not contribute further, higher terms in the material polarisation **P** will also be neglected as they are small compared to $\chi^{(1)}$ and $\chi^{(3)}$.

2.3.1 Nonlinear propagation effects

In a low pressure monatomic gas the response of the medium to a pulse can be approximated to instantaneous. This assumes, due to its increased mass the response of the nucleus is long compared to timescale of the pulse, and so does not contribute to the field. In this case the nonlinear polarisation $\mathbf{P}_{NL}$ can be related to the electric field $\mathbf{E}(\mathbf{r},t)$ by [53]

$$\mathbf{P}_{NL}(\mathbf{r},t) = \varepsilon_0 \chi^{(3)} \vdots \mathbf{E}(\mathbf{r},t)\mathbf{E}(\mathbf{r},t)\mathbf{E}(\mathbf{r},t) \tag{2.45}$$

where the electric field of the pulse $\mathbf{E}(\mathbf{r},t)$ can be written as a product of a slowly varying envelope and a fast oscillating term.

$$\mathbf{E}(\mathbf{r},t) = E(\mathbf{r},t)\exp i(\mathbf{kr} - \omega_0 t) \tag{2.46}$$

$E(\mathbf{r},t)$ is the slowly varying field amplitude, $\mathbf{k}$ is the propagation constant of the field discussed in the phase-matching section, $\mathbf{r}$ is the the vector representing the Cartesian coordinates (x,y,z), ω_0 is the central angular frequency of the pulse spectrum and t is time. Substituting this term into the nonlinear polarisation, equation 2.45, produces a term that oscillates at ω_0 and one that oscillates at $3\omega_0$. The third harmonic term can be ignored in this case as it requires specific phase-matching, leaving the polarisation amplitude equal to

$$P_{NL}(\mathbf{r},t) \approx \varepsilon_0 \varepsilon_{NL} E(\mathbf{r},t) \tag{2.47}$$

where ε_{NL} is the nonlinear contribution to the dielectric constant and is defined as

$$\varepsilon_{NL} = \frac{3}{4}\chi^{(3)}_{xxxx}|E(\mathbf{r},t)|^2 \tag{2.48}$$

The dielectric constant of the material is now given as

$$\varepsilon(\omega) = 1 + \tilde{\chi}^{(1)}_{xx}(\omega) + \varepsilon_{NL} \tag{2.49}$$

The inclusion of ε_{NL} to the dielectric constant results in an intensity dependance of the complex refractive index of the material, usually written as

$$\tilde{n} = n_0 + n_2|E(\mathbf{r},t)|^2 \tag{2.50}$$

where n_0 is the linear part of the refractive index and n_2 is the nonlinear refractive index given by

$$n_2 = \frac{3}{8n_0}\Re(\chi^{(3)}_{xxxx}) \tag{2.51}$$

It is the intensity dependance of the refractive index of the material that gives rise to nonlinear effects, therefore at low pulse intensities the contribution from the nonlinear refractive index becomes negligible and the pulse propagates linearly. One can calculate the significance of the nonlinear effects during propagation using the nonlinear length

L_{NL}. This is a measure of the distance over which nonlinear effects become important and cannot be ignored. For a Gaussian beam it is given as

$$L_{NL} = \frac{c}{n_2 I_0 \omega_0} \tag{2.52}$$

where c is the speed of light in vacuum and I_0 is the peak intensity of the pulse.

For the Ti:Sapphire laser system used in this thesis, 2.5 mJ, 43 fs, spot size $w = 4$ mm, the peak intensity is $I_0 = 1.09{\times}10^{15}\ Wm^{-2}$. The nonlinear refractive index of air is approximately $n_2 = 5{\times}10^{-23}\ m^2W^{-1}$ which gives a nonlinear length of the unfocused pulse propagating through air of $L_{NL} = 2.3$ m. This is a good indication that propagation of the pulse prior to and following the focus of the HHG system is linear. Conversely at the focus of the main beamline the spot size $w_0 = 48$ μm, resulting in a nonlinear length of $L_{NL} = 333$ μm. The strongest nonlinear effects that arise due to the $\chi^{(3)}$ response a material are SPM, self-steeping and Kerr self-focusing. The first two effects act to broaden the pulse spectrum and will be discussed first.

The instantaneous angular frequency within a pulse is given by

$$\omega(t) = -\frac{\mathrm{d}\phi}{\mathrm{d}t} \tag{2.53}$$

where ϕ is the phase of the pulse shown in equation 2.46. The phase has two components, kz, where it is assumed the pulse is propagating in the z direction and hence $\mathbf{r} \rightarrow z$ and $\omega_0 t$. The spatial term kz has a temporal dependence due to equation 2.50 and can be separated into two parts, which produces

$$\phi = -\omega_0 t + \frac{n_0 \omega_0 z}{c} + \frac{n_2 \omega_0 z I(t)}{c} \tag{2.54}$$

where z is the distance travelled by the pulse in time t and $I(t)$ is the intensity distribution of the pulse. The temporal variation of the intensity leads to a temporal variation of the phase. After propagating a distance z this produces a frequency shift away from ω_0 of $\mathrm{d}\omega$. The instantaneous frequency is then

$$\omega(t) = \omega_0 - \mathrm{d}\omega \tag{2.55}$$

where $\mathrm{d}\omega$ is given by

$$\mathrm{d}\omega = \frac{\omega_0 n_2 z}{c} \frac{\mathrm{d}I(t)}{\mathrm{d}t} \tag{2.56}$$

Figure 2.12 shows the variation of $\mathrm{d}\omega$ through the pulse. As the pulse propagates new frequencies will be generated. SPM generates new frequencies symmetrically about the central frequency of the pulse. The leading edge of the pulse generates red shifted frequencies whilst blue shifted frequencies are generated at the trailing edge, resulting in a positive chirp. The chirp increases with propagation distance as new frequencies are generated.

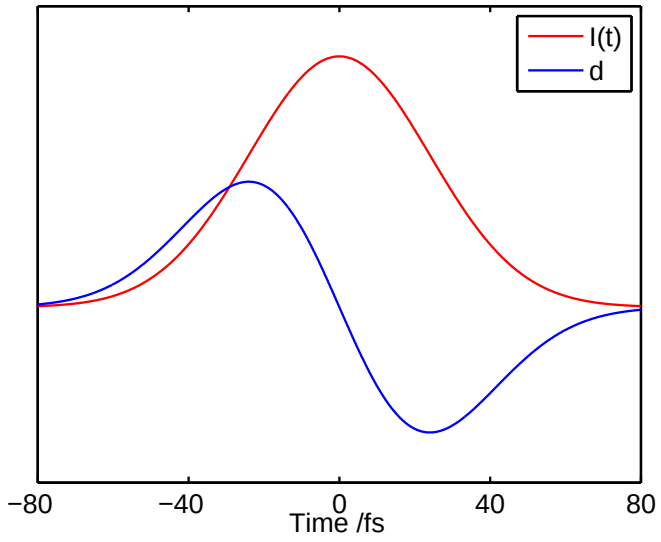

Figure 2.12: Instantaneous frequency shift of an initially unchirped pulse that has experienced SPM. The blue line indicates the intensity distribution of the pulse, the red line shows the frequency shift dω through the pulse.

Self-steepening, like SPM, is caused by the shape of the intensity distribution in time $I(t)$. In SPM the shape of the pulse leads to certain frequencies generated at the leading and trailing edges of the pulse, brought about by the change in ϕ with time. Self-steeping occurs due to the high intensity of the centre of the pulse with respect to the wings. Equation 2.50 shows that the material refractive index is increased by $n_2|E|^2$. At the peak of the pulse the increase in refractive index is greater than that at the wings, therefore the peak sees a higher refractive index and so propagates more slowly. As the pulse propagates the peak of the pulse shifts backward with respect to the wings, effectively steepening the trailing edge. This results in a large frequency shift away from ω_0 as shown by equation 2.56. As this larger shift occurs at the trailing edge of the pulse only, the result is an asymmetric spectrum with a large blue shift.

These effects are routinely used in pulse compression where the pulse bandwidth is increased by SPM and self-steepening before being recompressed [54]. The compression is required to remove the positive chirp of the pulse induced by the SPM. The method of recompressing a pulse will be discussed in the following section.

The spatial analogue to SPM is Kerr self-focusing where at high intensities the nonlinear refractive index contribution leads to a change in the refractive index of the material due to the spatial distribution of the beam. In the same way that a Gaussian pulse has a high intensity at the centre with gradually lower intensity in the wings so too does a Gaussian beam in space. As a result an intense pulse propagating through a material will see a convex refractive index profile, with a higher refractive index on axis. The pulse therefore undergoes self-focusing shown schematically in Figure 2.13. Self-focusing can only overcome diffraction if the initial power P_{in} of the pulse is sufficient; this is

given by the critical power P_{cr} [55]

$$P_{cr} = \frac{3.77\lambda_0^2}{8\pi n_0 n_2} \tag{2.57}$$

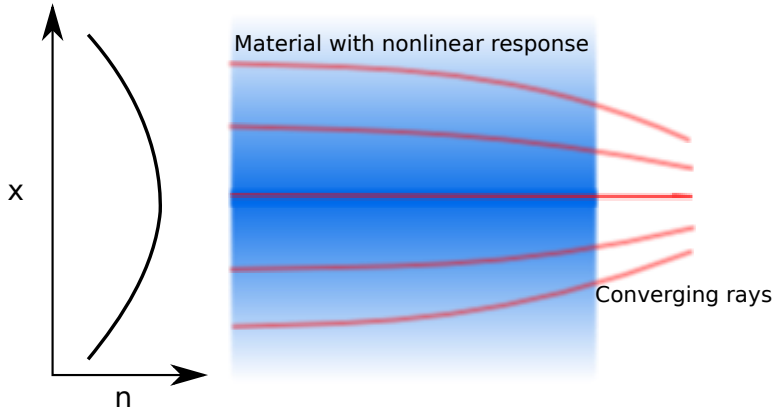

Figure 2.13: Schematic of Kerr self-focusing. The refractive index profile is indicated by the graph. The rays (red lines) propagating through the material converge due to the convex refractive index profile induced by the intensity dependence of the nonlinear refractive index.

2.3.2 Dispersive propagation effects

The nonlinear effects described in the previous section are time domain effects. The dispersive effects that affect a propagating pulse are more easily described in the frequency domain. The Fourier transform of the pulse propagating in the direction z is defined as

$$\tilde{E}(\mathbf{r}, \omega - \omega_0) = \int_{-\infty}^{\infty} E(\mathbf{r}, t) \exp i[kz - (\omega - \omega_0)t] dt \tag{2.58}$$

Separating the variables allows this to be written as

$$\tilde{E}(\mathbf{r}, \omega - \omega_0) = F(x, y)\tilde{A}(z, \omega - \omega_0) \exp i(k(\omega)z) \tag{2.59}$$

where $F(x, y)$ is the modal distribution, $\tilde{A}(z, \omega - \omega_0)$ is the slowly varying envelope and $k(\omega)$ is the frequency dependent propagation constant. The modal distribution depends on the boundary conditions of the wave equation used to describe the propagation. In free space a Gaussian distribution is often used, in a capillary waveguide this cannot be used due to the capillary walls. Gaussian fields extend to infinity whilst in a perfect waveguide the field goes to zero at the boundary. Marcatili and Schmeltzer showed that this is a good approximation in hollow capillary waveguides [56], where the field reduces to near zero. As a result propagation within a capillary occurs as an ensemble of

Bessel modes. The basic theory of capillary coupling and propagation will be discussed in Section 2.3.4.

The complex phase of the electric field in the frequency domain is known as the spectral phase. In equation 2.59 the spectral phase takes the form of $k(\omega)z$. To understand how the pulse changes with propagation $k(\omega)$ can be expanded in a Taylor series about the central frequency ω_0

$$k(\omega) = k + k' \frac{\omega - \omega_0}{1!} + k" \frac{(\omega - \omega_0)^2}{2!} + \dots \tag{2.60}$$

where k is the propagation constant in vacuum $k = \frac{2\pi}{\lambda_0}$. The second term relates to the group velocity at which the envelopes propagates and the third term is the group velocity dispersion (GVD). The GVD represents the spreading out of the pulse envelope as it propagates. This is due to the frequency dependence of the group velocity for the individual components comprising the pulse. The GVD can be positive or negative and leads to a chirp of the pulse, so called because the variation of frequency within the pulse is linear with time. Normal dispersion produces a positively chirped pulse that has red components at the leading edge of the pulse and blue components at the rear. In nonlinear propagation the combination of SPM and normal dispersion causes the chirp to increase more rapidly. GVD is given in units of $\mathrm{f}s^2m^{-1}$ and is well documented for most materials. Given the frequency dependance of the phase velocity, pulses with a larger spectral bandwidth will lengthen more rapidly due to the greater difference in phase velocity between the extremes. For example, consider a pulse propagating through 1 cm of fused silica, GVD = 36 $\mathrm{f}s^2mm^{-1}$. A 10 fs Gaussian pulse centred at 800 nm passing through this would be stretched to ∼100 fs where as a 40 fs pulse would only increase in length to ∼47 fs. The total group delay dispersion (GDD) that affects the pulse is given by the product of the material GVD and the propagation distance. In this case the GDD = 360 $\mathrm{f}s^2$.

Higher-order dispersion effects do not lengthen the pulse as dramatically as the second order dispersion but act to change the pulse shape. Third order dispersion causes an asymmetry in the spectral phase across the pulse which in the time domain gives rise to a pre or post pulse depending on its sign. The majority of higher order dispersion effects are neglected as they are small compared to the first and second orders. However, some of the later experimental results do show pre and post pulses which are likely due to third order dispersion effects.

An initially positively chirped pulse, such as that produced by SPM, can be recompressed by applying an equal amount of negative chirp. A pulse with a flat spectral phase, i.e. one that has no second order or above dispersion applied to it, is said to be transform limited. The length of a transform limited pulse is defined by its spectral bandwidth.

For a Gaussian pulse this relation is

$$\Delta\tau = \frac{2ln2}{\pi\Delta\nu} \approx \frac{0.441}{\Delta\nu} \tag{2.61}$$

where $\Delta\tau$ is the full width at half maximum (FWHM) intensity of the pulse in time and $\Delta\nu$ is the FWHM of the spectral intensity of the pulse. The two are inversely proportional so one requires a large bandwidth to produce a short pulse. The aim of a pulse compression scheme is to produce a pulse with a large bandwidth as close to its transform limit as possible. This is not simple as very few materials exist that have anomalous dispersion, capable of applying negative GVD. The three most common methods are grating compressors [57], prism compressors [58] and chirped mirrors [59]. The first two are used within lasers themselves and can apply thousands of fs^2 of negative GDD by spatially separating the frequency components and propagating them different distances to remove the second order dispersion. Post compression systems that are used to further compress a commercially purchased laser do not require such large amounts of GDD and so use chirped mirrors. These mirrors consist of a graded Bragg grating, alternating layers of two different refractive indices. The graded thickness of the layers allows different wavelengths to propagate different thicknesses within the mirror surface. Longer wavelengths propagate more deeply and so upon reflection have travelled a longer path length than the shorter wavelength components, applying negative dispersion.

The previous two sections have described the effects on a pulse propagating through a general material. In the case of HHG this material is a gas, in Section 2.2 the ionisation of the gas was mentioned with respect to the phase mismatch a free electron plasma induced between the fundamental and the harmonics. The ionisation of the gas and the resulting plasma affect the propagating pulse in other ways, which will be discussed in the following section.

2.3.3 Ionisation-induced propagation effects

Ionisation of a gas by a high intensity laser can be achieved by two methods; multiphoton ionisation (MPI), where two or more photons are simultaneously absorbed by the atom to free an electron, and tunnelling ionisation, where the Coulomb potential of the atom is distorted by the electric field so that quantum mechanical tunnelling through the barrier is possible. The ionisation process can be described by two models; Keldysh theory [60] and ADK theory [61]. Doubt has been cast over the accuracy of the ADK model in a comprehensive review of Keldysh theory by Popov in 2004 [62]. To know whether MPI or tunnelling ionisation is the dominant effect in the following experiments, one can use the Keldysh parameter γ which is the ratio of the optical frequency to the tunnelling frequency [62]

$$\gamma = \left(\frac{I_p}{2U_p}\right)^{\frac{1}{2}} \tag{2.62}$$

where I_p is the ionisation potential of the atom in question and U_p is the ponderomotive potential given in equation 2.5. Tunnelling ionisation is the dominant effect when $\gamma < 1$ whereas MPI is the dominant effect when $\gamma > 1$. All of the experiments carried out in this thesis have a Keldysh parameter of $\gamma < 1$ and so tunnelling ionisation is used to model the ionisation.

The ionisation rate is given by [62]

$$W(\mathbf{r},t) = W_0\kappa^2\sqrt{\frac{3}{\pi}}C_{\kappa l}^2 2^{2n^*}F(\mathbf{r},t)^{1.5-2n^*}\exp\left(-\frac{2}{3F(\mathbf{r},t)}\right) \tag{2.63}$$

where κ^2 is the ratio of the ionisation potential I_p to the ionisation potential for hydrogen $I_H = 13.6eV$, $W_0 = m_e e^4/\hbar^3$, $F(\mathbf{r},t) = E(\mathbf{r},t)/(\kappa^3 E_a)$ is the reduced electric field where E_a is the atomic unit of field intensity and $E(\mathbf{r},t)$ is the real electric field. $C_{\kappa l}$ is an asymptotic coefficient that for singly ionised argon is given as 0.95, whilst n^* is the principal quantum number, which in the same case is given as 0.929. These are given to an accuracy of 3-10 %. This ionisation rate is included in the MM-NLSE propagation model shown in Section 2.4 to describe pump pulse propagation within a short hollow core capillary.

The effect of ionisation on the refractive index of the gas, shown in equation 2.29, is a reduction in the refractive index proportional to the number density of the electrons. The greater the ionisation the greater the reduction in refractive index. This leads to an intensity dependent refractive index profile following the spatial distribution of the beam. For a beam with a Gaussian spatial distribution the refractive index at the centre of the beam is smallest, increasing gradually with radius. The refractive index profile a pulse would see in this case is similar to a concave lens, leading to a divergence of the beam, Figure 2.14. This is complicated by the fact that the beam generates this refractive index profile as it propagates, leading to two significant effects.

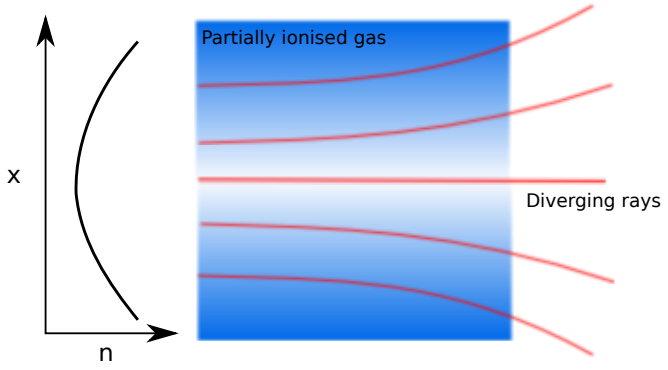

Figure 2.14: Schematic of plasma defocusing. The refractive index profile is indicated by graph. The rays (red lines) propagating through the partially ionised gas diverge due to the concave refractive index profile induced by the free electron plasma.

The ionisation is caused by the leading edge of the pulse, generating the new refractive index profile. The trailing edge of the pulse is then defocused as it passes through the new plasma induced refractive index. In Section 2.3.1 the nonlinear process of SPM was discussed. It was shown in equation 2.56 that blue shifted frequency components are generated by SPM at the trailing edge of the pulse. The divergence of the trailing edge of the pulse results in these blue shifted components being defocused, leaving the on axis pulse with a steeper trailing edge that acts in combination with the nonlinear self-steepening effect. A second effect is the change in refractive index with time. Ionisation is a nonlinear effect and thus increases rapidly with intensity. This leads to a rapid increase in the ionisation and consequently a rapid decrease in the refractive index with respect to time. It was shown in equation 2.53 that the frequency is the time derivative of the phase. The rapid change in refractive index with time leads to a rapid change in the phase with time, generating large changes in the instantaneous frequency, broadening the spectrum. The free electron contribution to spectral broadening is greater than the nonlinear contribution in the presence of high ionisation.

2.3.4 Propagation in a capillary waveguide

The majority of the work discussed in this thesis focuses on pump pulse propagation and HHG in a capillary waveguide. As a result an understanding of how a pulse propagates within a capillary is necessary. The spatial distribution of the output of a laser can be most simply described by the basis set of Hermite Gaussian modes, where the M^2 of the beam is a measure of how close to the fundamental transverse mode TEM_{00} the beam profile is. Gaussian modes have no spatial boundary condition and so in theory stretch to infinity, although the energy decays exponentially off-axis.

In a capillary, the Gaussian spatial distribution cannot exist due to the boundary conditions enforced by the capillary wall. The electric field reduces to near zero beyond the capillary wall. The eigenmodes that satisfy this condition are known as Bessel modes and were first reported by Marcatili and Schmeltzer [56]. As such the Gaussian laser distribution must be coupled into this new set of Bessel modes. To know how this can be achieved one must first look at which modes exist within the capillary. The laser is linearly polarised therefore the pulse will excite only linearly polarised modes within the capillary, these are the hybrid EH_{nm} modes given by

$$E_{y,nm} = J_{n-1}\left(u_{nm}\frac{r}{a}\right) cos([n-1]\theta + \phi) \tag{2.64}$$

$$E_{x,nm} = J_{n-1}\left(u_{nm}\frac{r}{a}\right) sin([n-1]\theta + \phi) \tag{2.65}$$

where E_x and E_y are the electric field components in the x and y directions, J_p is the p^{th} order Bessel function of the first kind, u_{nm} is the mth root $J_{n-1}(u_{nm}) = 0$, ϕ is an arbitrary constant and a is the capillary radius. These modes are linearly polarised for

the case $n = 1$. The laser is linearly polarised in only one direction and so the EH_{1m} modes that propagate within the capillary and are given as

$$E_{y,1m} = J_0\left(u_{1m}\frac{r}{a}\right) \tag{2.66}$$

$$E_{x,1m} = 0 \tag{2.67}$$

The intensity distribution of the first two modes, EH_{11} and EH_{12} are shown in Figure 2.15. The complex propagation constant for the EH_{nm} modes γ_{nm} is given by

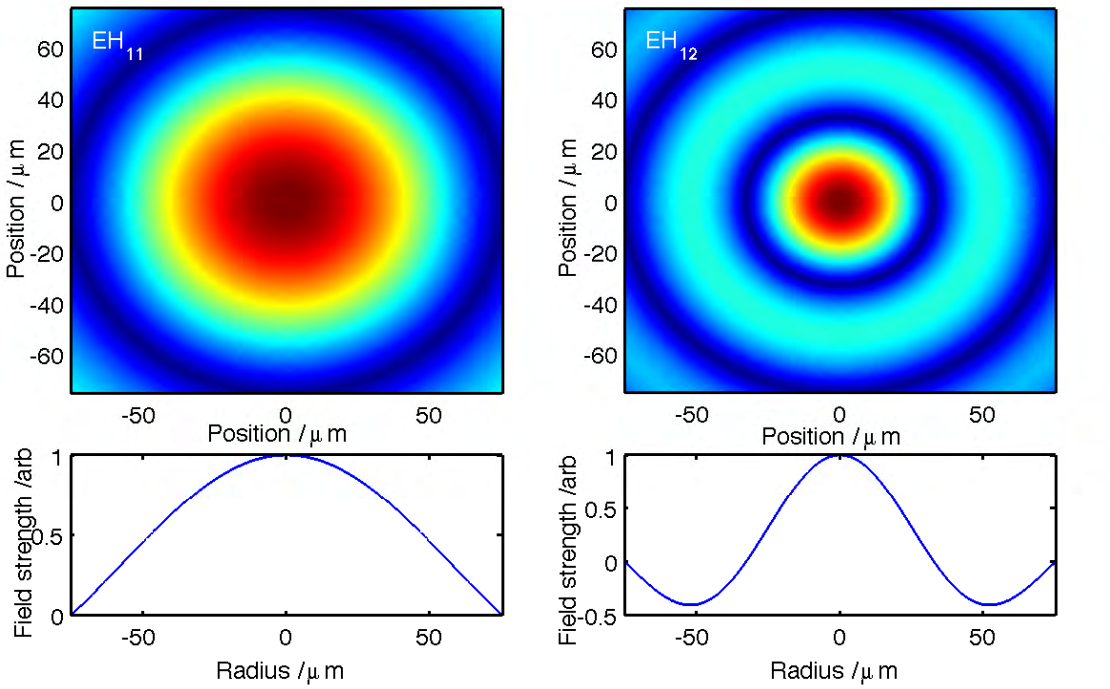

Figure 2.15: Intensity (top) and field (bottom) distributions for the first two EH_{1m} modes

$$\gamma_{nm} = \beta_{nm} + i\alpha_{nm} \tag{2.68}$$

where β_{nm} and α_{nm} are the propagation and attenuation constants respectively and are given as [56]

$$\beta_{nm} = k_0\left[1 - \frac{1}{2}\left(\frac{u_{nm}\lambda}{2\pi a}\right)^2\right] \tag{2.69}$$

$$\alpha_{nm} = \left(\frac{u_{nm}}{2\pi}\right)^2 \frac{\lambda^2}{a^3}\left(\frac{\frac{1}{2}(\nu^2+1)}{\sqrt{\nu^2-1}}\right) \tag{2.70}$$

where k_0 is the propagation constant in a free space vacuum and ν is the refractive index of the dielectric comprising the capillary waveguide. The attenuation coefficient α_{nm} scales with u_{nm}^2, this results in more lossy higher order modes. The lowest order mode EH_{11} is therefore the least lossy and the most suitable mode to couple into. The

beam in free space is approximated by a perfect Gaussian mode (TEM_{00}) whilst the propagation within the capillary requires Bessel modes. The power coupling efficiency of converting the TEM_{00} mode to each of the EH_{1m} modes, η_m, can be calculated using the overlap integral [63]

$$\eta_m = \frac{\left[\int_0^a \exp(-r^2/w^2) J_0\left(u_{1m}\frac{r}{a}\right) r dr\right]^2}{\int_0^\infty \exp(-2r^2/w^2) r dr \int_0^a J_0^2\left(u_{1m}\frac{r}{a}\right) r dr} \tag{2.71}$$

where r is the radius and w is the Gaussian beam spot size. The power coupling efficiency for the first five EH_{1m} modes plotted as a function of spot size to capillary radius is shown in Figure 2.16. The optimum coupling efficiency to the EH_{11} modes occurs for a ratio of $w/a = 0.64$ shown by the vertical dotted line. In this case 98.1% of the power is transferred into the EH_{11}, 0.5% to the EH_{12} and the remainder to the higher order modes.

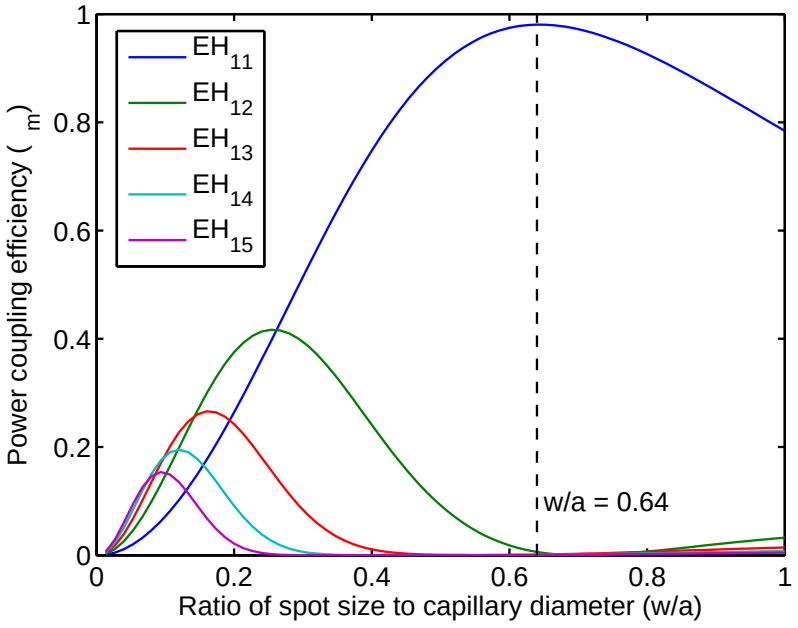

Figure 2.16: Coupling efficiency, η_m, from a TEM_{00} Gaussian beam in to the first five EH_{1m} Bessel modes of the capillary. η is given as a function of the ratio between the Gaussian beam width w and the capillary radius a. Optimum coupling exists for a ration of $w/a = 0.64$.

2.4 Nonlinear propagation model

The previous section described the various processes that occur during the propagation of an intense ($> 10^{13}\ Wcm^{-2}$) pulse through gaseous media. These include dispersive, nonlinear and ionisation effects. The ultimate goal of this work, to produce an efficient high yield XUV source, requires not only the ability to understand the relevant processes,

but also to predict them and make changes to the system as required. In short, an accurate model of the pump pulse propagation is needed.

Modal propagation within a hollow capillary waveguide is similar to that of a fibre, both have an inner core with a given refractive index surrounded by a cladding layer of a different refractive index. Dr Peter Horak, a theorist within the Optoelectronics Research Centre, University of Southampton has developed a model to describe the propagation of ultrashort pulses in fibres [64]. Building on this work in conjunction with the Ultrafast X-ray Group he has adapted that model to include ionisation effects and thus make it capable of modelling the high intensity propagation observed in capillary based HHG. The following three experimental chapters use this model to predict the pump pulse propagation in an effort to improve the HHG process. In Chapters 3 and 4 the model was tested against experimental results to both gain an understanding of its limitations and improve its accuracy. Following this the model was used to help design a new capillary, shown in Chapter 5, that boasts improved XUV flux over the original design. All theoretical modelling of the pump pulse propagation used in this thesis was carried out by Dr Horak and his student Patrick Anderson. The experimental data measuring, analysis and comparison to the theory, as well as the development of the capillary design were conducted by myself.

The following section will describe briefly the nonlinear propagation model and how it relates to the processes previously discussed in this chapter.

Pulse propagation within single-mode fibres is routinely modelled using a generalised nonlinear Schrödinger equation (NLSE) to describe the evolution of the pulse's electric field amplitude envelope as it propagates [53, 65]. At high powers large diameter core fibres are required leading to multimode propagation. The basic NLSE framework was extended to allow for arbitrary mode numbers, polarisations, tight mode confinements and ultrashort pulses [64]. It is this adapted model that is further extended and used to model propagation within the capillary [66].

The model starts with an optical pulse similar to that shown in equation 2.46

$$\mathbf{E}(\mathbf{r},t) = E(\mathbf{r},t)\exp[i(\beta_0\mathbf{r} - \omega_0 t)] \tag{2.72}$$

where $E(\mathbf{r},t)$ is the slowly varying complex electric field amplitude and $\exp[i(\beta_0\mathbf{r} - \omega_0 t)]$ describes the carrier wave. In this case the free space propagation constant k_0 is replaced by β_0, the propagation constant in the fundamental fibre mode. The electric field amplitude can then be expanded into a superposition of the individual spatial modes, $p = 0, 1, 2\ldots$, within the capillary and a modal envelope $A_p(z,t)$

$$E(\mathbf{r},t) = \sum_p \frac{\mathbf{F}_p(x,y)}{\left[\int dxdy|\mathbf{F}_p|^2\right]^{1/2}} A_p(z,t) \tag{2.73}$$

where $\mathbf{F}_p(x, y)$ is the discrete transverse fibre mode profile for mode p, in this case EH_{1p}. Using this formalism the multimode generalised nonlinear Schrödinger equation (MM-NLSE) is given by [66]

$$\frac{\partial A_p}{\partial z} = \mathcal{D}\{A_p\} + \mathcal{N}\{A_p\} + \mathcal{N}_{pl}\{A_p\} + \mathcal{L}_{ion}\{A_p\} \tag{2.74}$$

where the individual terms describe the dispersion, nonlinearity, plasma nonlinearity and ionisation losses respectively. The dispersive term $\mathcal{D}\{A_p\}$ includes the Taylor expansion of the propagation constant from equation 2.60. This include the effects of first, second, third order dispersion etc, and is given by

$$\begin{aligned}\mathcal{D}\{A_p\} = i(\beta_0^{(p)} - \Re[\beta_0^{(0)}])A_p - (\beta_1^{(p)} - \Re[\beta_1^{(0)}])\frac{\partial A_p}{\partial t} \\ + i\sum_{n\geq 2}\frac{\beta_n^{(p)}}{n!}\left(i\frac{\partial}{\partial t}\right)^n A_p\end{aligned} \tag{2.75}$$

where p denotes the mode number and $\beta_n^{(p)} = \partial^n \beta^{(p)}/\partial\omega^n$. The first and second terms are contributions from the first and second terms in the spectral phase from equation 2.60, the third term accounts for all greater terms, including second order dispersion responsible for positive chirping of the pulse.

The nonlinear term $\mathcal{N}\{A_p\}$ includes both SPM and self-steepening effects and is given by

$$\mathcal{N}\{A_p\} = i\frac{n_2\omega_0}{c}\left(1 + \frac{i}{\omega_0}\frac{\partial}{\partial t}\right)\sum_{l,m,n} S^K_{plmn} A_l A_m A^*_n \tag{2.76}$$

where n_2 is the nonlinear refractive index given by equation 2.51 and S^K_{plmn} is the mode overlap integral. The first and second terms describe SPM and self-steepening respectively. Raman effects can be included within the model but have been neglected due to the monatomic nature of the medium. The model also accounts for Kerr self-focusing, briefly mentioned in Section 2.3.1. This is the spatial analogy to SPM and produces the opposite effect to plasma defocusing. The refractive index is greater for high intensities, equation 2.50, and so the spatial centre of the beam sees a greater refractive index than the wings, such an effect leads to self-focusing of the beam.

The ionisation effects discussed in Section 2.3.3 lead to the addition of two terms to the standard NLSE propagation model. The ionisation rate is calculated using equation 2.63 from which the fraction of neutral $N(\mathbf{r}, t)$ atoms and thus the free electron density ($N_e(\mathbf{r}, t)$) can be calculated. $\mathcal{N}_{pl}\{A_p\}$ describes the self-steepening induced by the nonlinear coupling of the trailing edge of the beam to higher order modes. It is given by

$$\mathcal{N}_{pl}\{A_p\} = -\left(1 - \frac{i}{\omega_0}\frac{\partial}{\partial t}\right)\frac{i}{2}k_0\int dxdy\frac{\mathbf{F}_p(x, y)^* \cdot E(\mathbf{r}, t)}{[\int dxdy|\mathbf{F}_p|^2]^{1/2}}\frac{\omega_{pl}(\mathbf{r}, t)^2}{\omega_0^2} \tag{2.77}$$

The nonlinear coupling to higher order modes leads to an increase in loss as discussed in the previous section. In addition to this, one must account for loss due to the ionisation process itself [67]. This ionisation induced loss is the final term in equation 2.74 and is written as

$$\mathcal{L}_{ion}\{A_p\} = -\frac{1}{2}\int dxdy \frac{\mathbf{F}_p(x,y)^* \cdot E(\mathbf{r},t)}{[\int dxdy|\mathbf{F}_p|^2]^{1/2}} \frac{PN(\mathbf{r},t)W(\mathbf{r},t)I_p}{|E(\mathbf{r},t)|^2} \tag{2.78}$$

where P is the pressure in atm, $W(\mathbf{r},t)$ is the ionisation rate and I_p is the ionisation potential of the gas. Thus equation 2.74 describes the evolution of a pump pulse within a capillary in the presence of ionisation by quantum tunneling. Propagation of the field within the model is accomplished using the symmetrised split step Fourier method [53] with an extension to include the nonlinear plasma and ionisation loss terms.

Using the data from the model it is possible to generate the spatial distribution of the pulse in both the temporal and spectral domains at any point within the capillary. An example of this is shown in Figure 2.17. Knowledge of the pulse at all points within the capillary will enable the QM high harmonic generation process to be calculated at every point within the capillary and the subsequently generated XUV beam to be predicted. This work is underway but has not been included in this thesis as it is in its early stages.

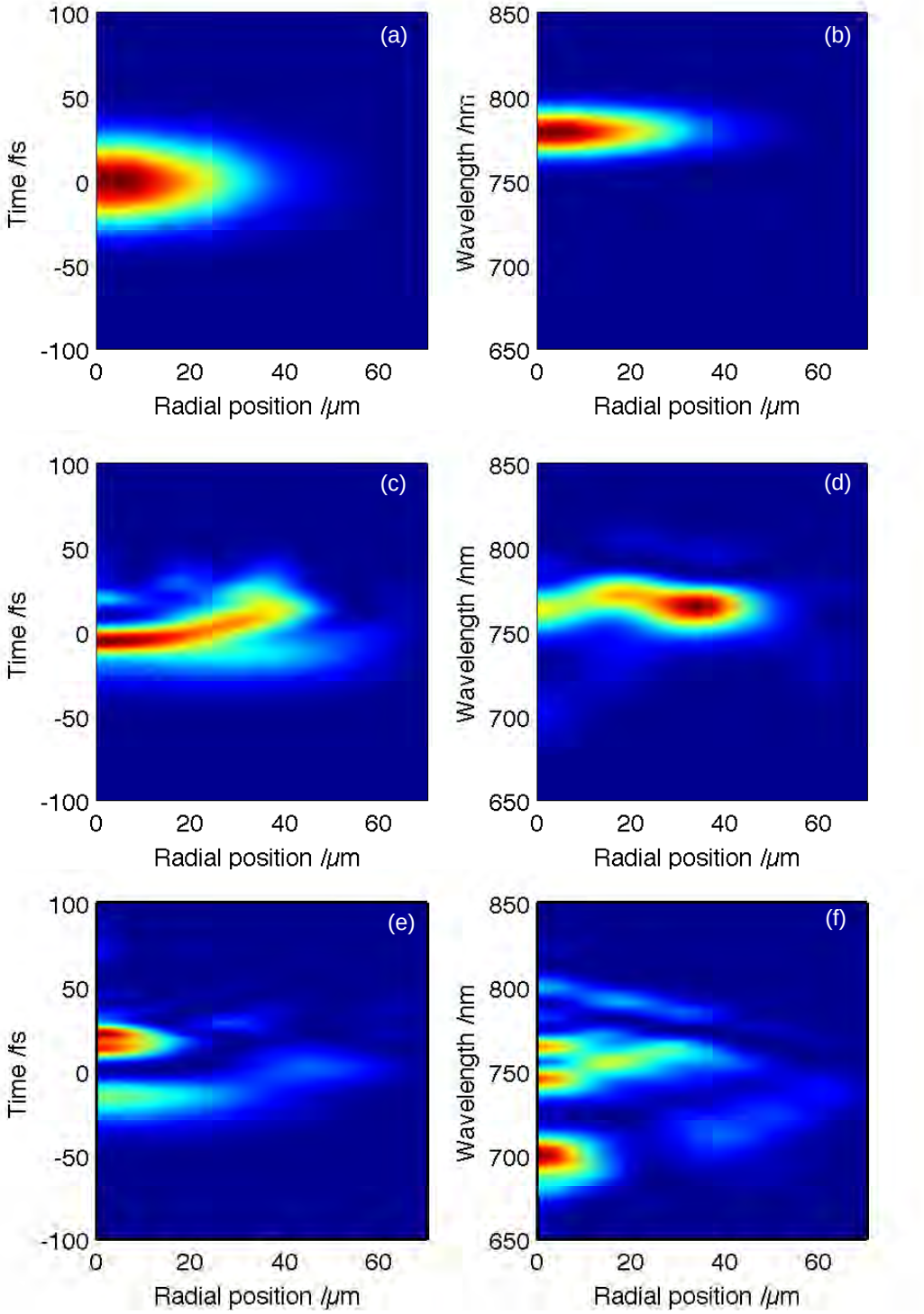

Figure 2.17: Example of the spatio-temporal (left) and spatio-spectral (right) data that can be modelled using equation 2.74. Here a 0.805 mJ, 53 fs, 800 nm, pump pulse is propagated down a 7 cm capillary held at 150 mbar of argon, see Chapter 4. The pulse is shown at the beginning (a,b), middle (c,d) and end (e,f) of the capillary. The intensity colour-map is plotted on a normalised linear scale.

Chapter 3

Capillary manufacture and pump pulse analysis

The first part of this chapter describes the methods used to fabricate the capillaries that have been used in this thesis. These include cleaving the capillary to the correct length, ensuring the end faces are flat and polished, and creation of the gas inlets by laser drilling through the capillary wall. Examples of cleaving and the final results for all are shown. This is followed by the approach used to effectively couple into capillaries at low power to avoid damage and maintain the capillary. Once aligned the laser power is increased and images of the capillary and its ring structured output, for 805 mW input power and 150 mbar gas pressure, are shown and the nonlinear and plasma effects discussed. The modal ring structure of the output beam leads on to the second section of the chapter where analysis of the propagation is studied. Three experiments were carried out to begin testing of the model described in Section 2.4, which was developed by Dr Peter Horak in conjunction with the Ultrafast X-ray Group. The experiments shown here fall under two categories, direct measurement of the spatio-spectral output of the pump laser and indirect measurement by imaging of the argon ion fluorescence within the capillary.

3.1 Capillary fabrication and laser coupling

This section will describe the fabrication of the 7 cm capillary focusing on the cleaved, polished ends and the gas inlets. The approach used to efficiently couple the pump pulse into the capillary will be discussed as will the initial observations of the pump pulse propagation. The capillaries used for all of the experiments within this report are of the same general design. They were purchased as 30 cm long cleaved, unpolished capillaries which required cleaving to the correct length, polishing, drilling and mounting such that the target gas could flow in through holes drilled into the walls, and out at

both ends. The outer diameter is 1.6 mm whilst the inner diameter is 150 μm. The original capillary design, shown in Figure 3.1, was 7 cm long with holes drilled 2 and 5 cm from the front of the capillary. Chapter 5 looks at a new capillary design based on the observations made of its predecessor, the methods for producing the new capillary were the same as those presented here.

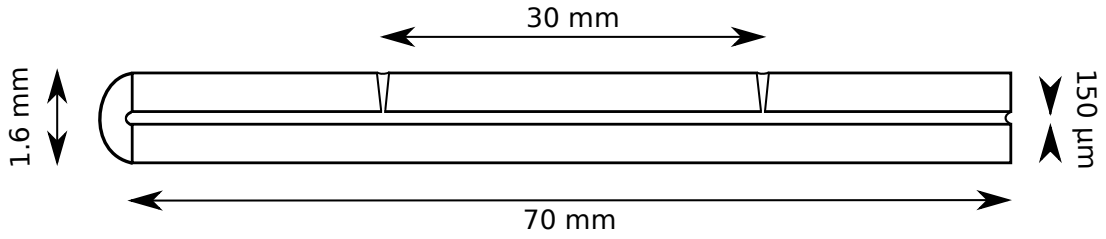

Figure 3.1: Schematic of 7 cm capillary. The capillary is 1.6 mm in diameter with an inner bore diameter of 150 μm. Gas inlets passing through the capillary wall are positioned at 2 and 5 cm along the capillary length.

3.1.1 Cleaving and polishing

The 30 cm capillaries had to be cleaved to produce a capillary of the desired length, in this case 7 cm. To do this a score was cut into the capillary using a ceramic fibre cleaver to set the position of the cleave. A small amount of de-ionised water was placed over the score mark which can propagate through the wall and cause the capillary to break more easily. The capillary was cleaved by holding the capillary on both sides of the score line, which was faced away from the holder, and pulled along the length of the capillary whilst gently bending it so that the score line was on the apex of the bend. Very little pressure was required, too much would cause the capillary to cleave unevenly and leave behind a large protrusion on one side of the cleave, known as a hackle. The capillary cleaved without much force or bend radius, and it was noted that these cases produced much better cleaves. Figure 3.2 shows two examples, the left is a cleanly cleaved capillary end while the right shows a poor cleave. In both cases the left hand side was at the apex of the bend used to cleave the capillary. The hackle in the capillary end is almost always present even for well cleaved capillaries. The right cleave is less desirable due to the crack facing the hackle at the core. This crack propagates a few mm in and thus is difficult to remove by polishing, if it is left in place it can make initial coupling more difficult by changing the scattering pattern on the front of the capillary which is used for alignment. In addition to that it can act as a scattering centre similar to the gas inlets shown later and thus reduce the total coupling efficiency.

Once a capillary of the correct length with two good cleaves was produced it was polished. The polishing pads used were standard fibre polishing pads and come in a variety of particle roughness. For this work 12, 9, 3, 1 and 0.3 μm pads were used. A custom mount was made to hold the capillary vertically upright whilst allowing its weight to

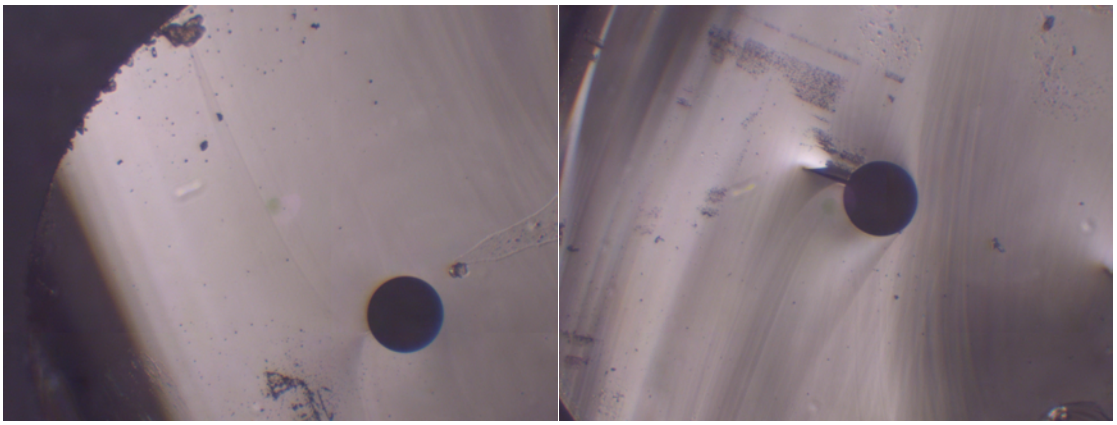

Figure 3.2: Microscope images of two cleaves made in a capillary. The left image is an example of a good cleave, where stress was minimised. The right image is an example of a poor cleave where a stress fracture has formed at the inner bore.

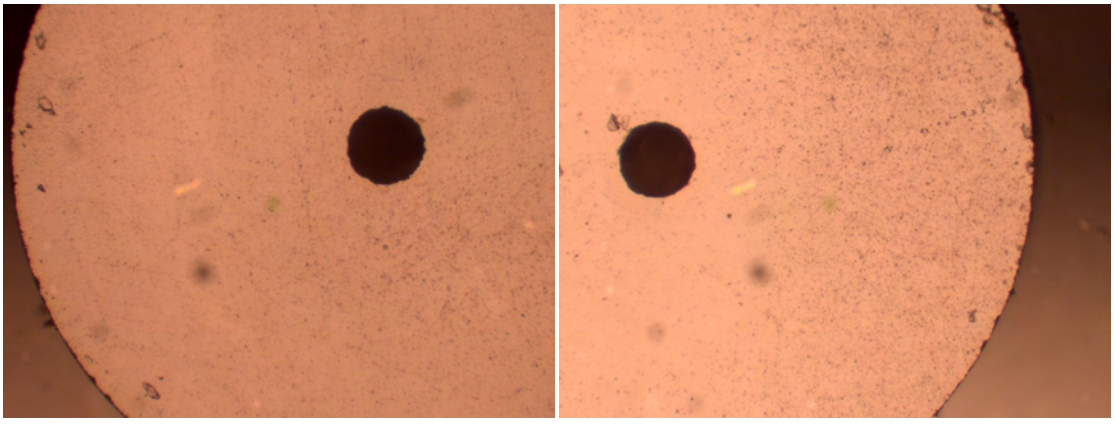

Figure 3.3: Microscope images of the final capillary end faces. Both have been polished to a to a surface roughness of < 300 nm.

push it into the polishing pad. The pads were wetted with de-ionised water and polishing fluid for the 0.3 μm graded pad. A figure of eight pattern was used to polish the capillary ends as this scours the surface in all directions, preventing the build up of ridges. The roughest (12 μm) polishing pad was used first and after 20 figure eights the capillary end was checked under a microscope. The 12 μm features scatter light well, so under a light the entire surface of the capillary end appears dull. This first stage can take some time depending on the quality of the cleave and how flat the end is. Once past the largest size 20 iterations of the figure eight was sufficient to remove the large features from the previous pad. At the smallest size the finished capillary end appeared flat and reflected light well, as any features were 300 nm or smaller. Figure 3.3 shows the final two ends used in the 7 cm capillary. The image is taken using a standard 20x microscope objective with lighting from below. The ends are flat with a roughness of less than 300 nm, any small features seen were removed in an acetone bath.

The acetone bath was necessary to remove grit and fused silica from within the capillary forced inside during the polishing process. This took several attempts and also required

blowing air through to help remove larger pieces.

Once the capillary was cleaved and polished the gas inlets were produced.

3.1.2 Gas inlets and mounting

Inlet holes always scatter the pump beam to a certain extent as they are much larger than the wavelength of the pump pulse and therefore in the vicinity of the hole change the waveguide. The size of the holes and the surrounding damage to the waveguide structure determines the amount of scatter. In this work the majority of loss within the capillary at zero pressure is attributed to scatter from these holes. The scatter can be seen due to SPM within the fused silica at the scattering centres broadening the spectrum. The diameter of the capillary bore (150 μm) means that mechanical production of the inlet holes was difficult. The smallest drill bits available were 300 μm and drilling into such a small circular glass structure was difficult. In addition, a 300 μm diameter drill bit would produce a large hole in the 150 μm waveguide. As a result laser drilling was used to create the gas inlets.

A suitable mount was designed and built to hold the capillary vertically in the main beamline at the focus of the lens. The spot size at the focus was approximately 50 μm with a Rayleigh range of 9.8 mm, well in excess of the total capillary diameter. The mount comprised two translation stages to allow movement of the capillary perpendicular to the laser beam axis. Initial placement of the capillary was carried out at low power, 10 - 20 mW, so that the beam could be seen but not damage the capillary. The cylindrical nature of the capillary meant that the transmission through the capillary produced a distinctive pattern, symmetrical about the capillary axis. Alignment to the core was carried out by adjusting the capillary position within the beam to produce a perfectly symmetric transmission pattern. When the laser power was increased the overall shape of the pattern was maintained, with a dark central region appearing where the laser ablated the fused silica leaving highly scattering remains. The capillary was moved within the beam to increase the size of this dark region and use of the translation stage micrometers gave an indication of the width of the hole being drilled.

It is important to note two things here.

- The hole size at the surface was much larger than that at the core, for example a 200 μm hole width on the surface translated to 40-70 μm at the core.
- The transmission pattern did not provide an indication of how far through the drilling had gone. This was gauged by trial and error on practice runs beforehand.

Using the laser with a pulse energy of 1 mJ, 60 seconds at a single height was sufficient to drill through to the core. This was achieved by moving the capillary laterally, leaving

it in a single place for long periods of time did not work as the ablated material was not removed from within the capillary wall and blocked further penetration. Lateral movement of the capillary allows the laser to dislodge this and penetrate further.

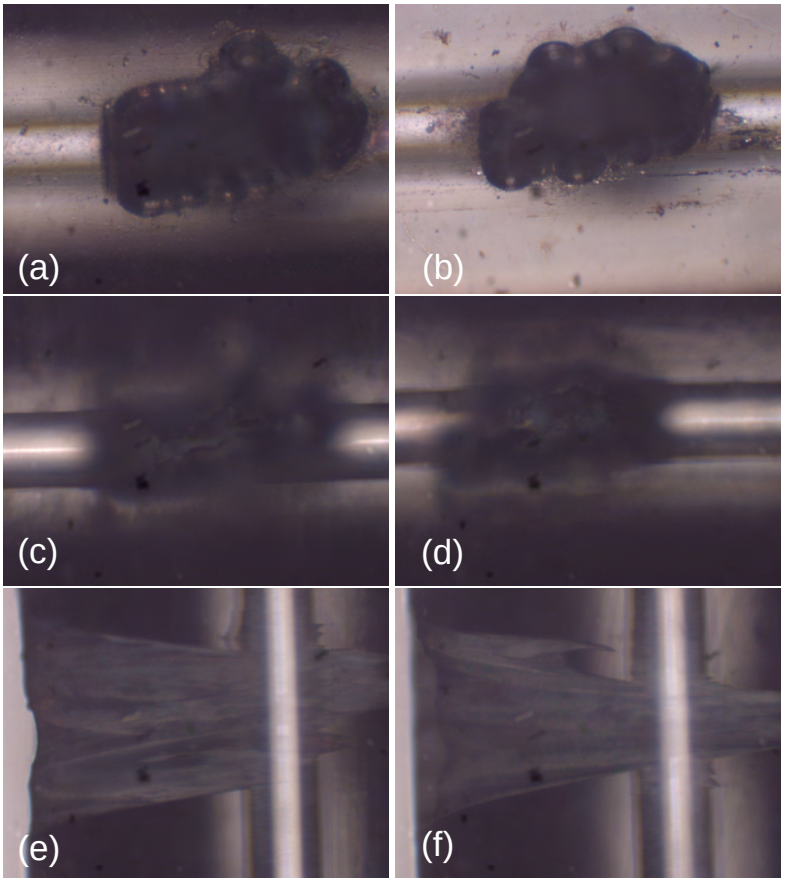

Figure 3.4: Microscope images of gas inlet holes laser drilled through the capillary wall. The top images show the outer surface of the first (left) and second (right) gas inlets. The focus is translated through to the core for the middle image. The hole passing through to the open core can be seen in the centre of each image. The bottom image shows a side view of each gas inlet. The holes at the core are on the order of 50 μm wide.

The holes at the core were on the order of 150-200 μm in length and 50 μm wide and can be seen in Figure 3.4. The top images show the first (a) and second (b) gas inlets at the surface of the capillary, the inner bore can be seen in soft focus travelling through the dark holes. Images (c) and (d) are focused 800 μm into the capillary; the core can be seen in sharper focus and the holes are visible as the lighter areas within the central dark region. Side images of the two inlets are shown in (e) and (f). In both cases the laser has drilled through the far side of the core and into the opposite wall. This is caused by the long Rayleigh length of the beam (9.8 mm). To avoid this in future work a lens with a Rayleigh length of less than 150 μm could be used, however this would make drilling to the core more difficult. Further work on this is required.

After drilling and checking the gas inlets the capillary was cleaned in an ultrasonic bath using both de-ionised water and acetone to remove internal debris. Air was blown through the capillary to ensure that none of the four holes were blocked in any way. The capillary was mounted within a glass T-piece shown in Figure 3.5.

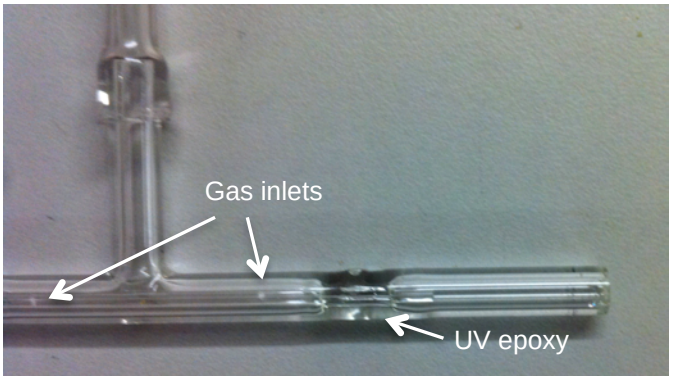

Figure 3.5: Photograph of the 7 cm capillary within the t-piece. The UV curing adhesive used to fix the capillary in place is shown as are the two gas inlets within the capillary itself.

UV curing adhesive was used to fix the capillary in place within the T-piece as it cures rapidly under UV light and does not put extra stress on the capillary itself. The T-piece was then mounted to the vacuum system via two o-ring vacuum feedthroughs mounted on x-y translation stages. A gas inlet tube was attached to the top of the T-piece through which the gas was introduced into the capillary. The full set up is shown in Figure 3.6.

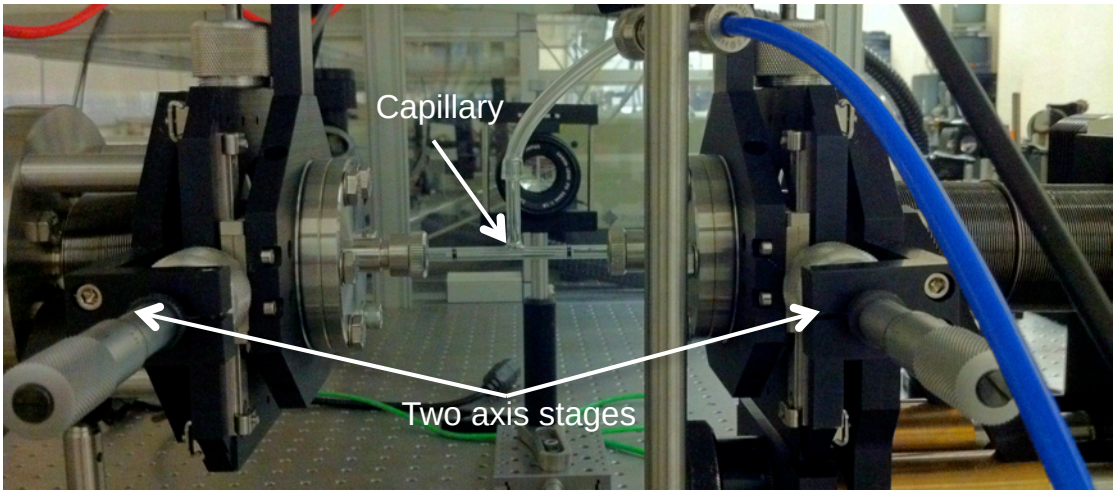

Figure 3.6: Photograph of the 7 cm capillary and T-piece mounted in the vacuum system. The two x-y translation stages are visible on the left and right of the image.

The translation stages allow two axis movement of both ends of the capillary perpendicular to the beam axis whilst the lens is mounted on a translation stage so that the on-axis position of the focus can be placed at the front face of the capillary. Gas is pumped out from both ends of the capillary and in through both inlet holes so that

a flat pressure profile is produced between, with a rapid drop at the holes and linear reduction in pressure to either end. The pressure profile was modelled previously by a different student using ANSYS, a computational fluid dynamics program. The positioning of the holes and the subsequent pressure profile has a dramatic effect on the propagation of the pump pulse as will be discussed and shown in Chapter 5.

3.1.3 Coupling into the capillary

In Section 2.3.4 it was shown that optimum coupling is achieved when the spot size $w_0 = 0.64r_c$ where $r_c = 75$ μm is the radius of the capillary bore. The spot size for optimum coupling is 48 μm. The spot size at the lens and the M^2 of the beam were measured to ensure maximum coupling efficiency. A telescope within the Spitfire Pro amplifier was used to adjust the spot size at the focusing lens to produce a 48 μm focal spot. Initial coupling was carried out at 10 mW to prevent damage to the front face of the capillary. If the initial intensity is greater than the damage threshold of the fused silica the laser will drill into the capillary end, damaging the face and making coupling more difficult in future. An example of this is shown in Figure 3.7.

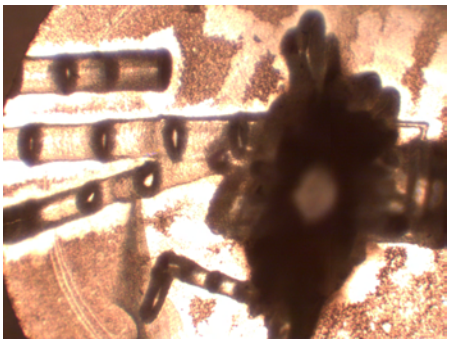

Figure 3.7: Microscope image of a damaged capillary front end. Misalignment of the pump pulse during coupling led to severe ablation of the front face of the capillary. The build up of this damage over time reduced the coupling efficiency and usefulness of the capillary. It was replaced by the 7 cm capillary described in this chapter.

The laser spot was visible on the front face of the capillary and was moved to the core using the front x-y translation stage. When the laser was overlapped with the inner bore a thin red line was seen propagating along the capillary in addition to scattering at the gas inlets. The line was visible due to small scatter from the walls of the capillary. The rear of the capillary was then adjusted until an output mode was observed on IR card. The fully aligned output mode comprises a central spot surrounded by a ring. At low powers the coupling efficiency through the 7 cm capillary was 91% of the theoretical maximum of 72%. This takes into account reflections from lens, input, output window surfaces and loss in the capillary.

The output mode shape does not change as the laser power is increased. All of the experimental results using capillary based HHG discussed in this report use argon as

the target medium. The nonlinearity of argon is large compared to neon and helium which becomes important shortly. Final alignment is carried out at a gas pressure of 150 mbar. At this pressure significant spectral broadening was observed as the pump pulse propagated along the capillary, see Figure 3.8. This is a result of SPM and plasma based

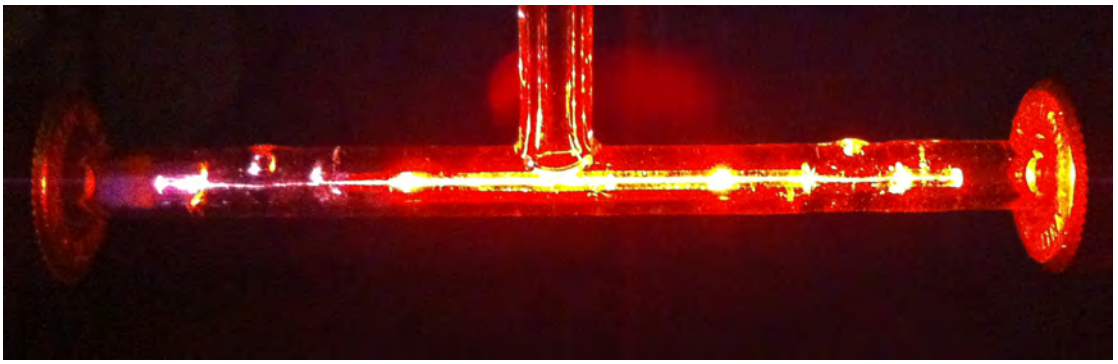

Figure 3.8: Side view of the capillary during experiment. The input power is 805 mW and the gas pressure set to 150 mbar. The pulse enters the capillary from the left, as it propagates along the capillary nonlinear effects broaden the spectrum so that it extends over most of the visible spectrum. Losses from the high order modes within the capillary allow this to be viewed.

broadening within the argon as was discussed in the previous chapter. The emission from the front end of the capillary was dominated by argon ion fluorescence, emitting a blue glow. As the pump pulse propagates down the capillary the spectrum broadens considerably and extensive blue shifting occurs producing green emission near the capillary exit. The emission was observed due to nonlinear mode mixing caused by the plasma generated by the pump pulse. As the front edge of the pulse passes through a region it ionises the gas, the resulting plasma has a lower refractive index than the surrounding neutral gas and so an effective defocusing lens is produced. The trailing end of the pulse sees this refractive index profile and is thus coupled out into higher order, more lossy modes. The laser power used here was 805 mW with a pulse length of 44 fs. The output mode structure in this case had a distinct ring structure as shown in Figure 3.9.

The ring structure is generated by the nonlinear mode mixing to higher order modes within the capillary. At the exit of the capillary these modes propagate out into free space and are observed here in the far field. A piece of white card was placed in the beam path and the photograph was taken through a high pass filter to prevent saturation by the NIR component of the beam. It was realised that the distinct and repeatable ring pattern would provide an excellent analytical tool to test the accuracy of the MM-NLSE propagation model being developed.

The following section of this chapter focuses on analysis of the pump pulse propagation as a means of testing the MM-NLSE propagation model. The summed output spectrum and spatio-spectral output of the beam are measured and compared to the theoretical output predicted by the model. In addition, the argon ion fluorescence is measured and

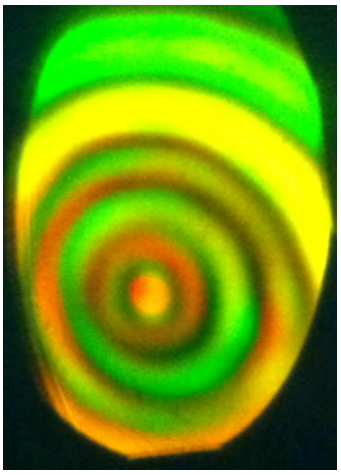

Figure 3.9: Photograph of the capillary output incident on white card. The image was taken through an IR filter to avoid saturating the camera. The ringed structure of the output is clear and extends below 480 nm. The spectral variation of the rings is due to nonlinear mode mixing coupling different parts of the pump pulse into higher order modes. The central two rings contain the majority of the total energy.

compared to the theoretical integrated ionisation of the capillary as a measure of the model's accuracy throughout the length of the capillary.

3.2 Measurement techniques for propagation analysis

The fully three dimensional MM-NLSE propagation model described in Section 2.4 was developed by Dr Peter Horak to better understand how the pump pulse propagates through the capillary. The ultimate aim of this work is to create an efficient and effective HHG source and so knowledge of the evolution of the pump pulse and its interaction with the target gas before, during and after the HHG process is important. The following work describes three methods of experimentally testing the accuracy of the model;

- A summed spectral measurement of the output pulse, which will give an overall look at the spectrum for different pump powers.
- A new spatio-spectral measurement, which is a measure of the spectrum taken across the beam using a fibre coupled spectrometer, providing a complex picture of the output and allowing scrutiny into separate modal contributions.
- Finally, a side image of the argon ion fluorescence at 488 nm is taken and compared to the integrated ionisation profile predicted by the model, to provide insight into the intensity of the pulse along the entire length of the capillary.

The work described here was published in Optics Express [68] in 2010. The majority of the paper was written by myself as was a significant portion of the experimental work carried out, most notably the spatio-spectral measurement.

3.2.1 Experimental set-up

The laser used for these experiments has been described in Section 1.2.1. The power of the system can be varied by adjusting the pump laser to the amplifier to provide pulse energies from 10 μJ to 2.5 mJ. In the following experiments the pulse energies are kept between 500 and 840 μJ. The basic experimental set up is shown in Figure 3.11. The laser is coupled into the 7 cm capillary, 150 μm internal bore diameter with gas inlets placed at 2 and 5 cm from the front face. When no gas is present the vacuum system maintains a constant background pressure of 10^{-3} mbar. Argon can be introduced through the gas inlets and is pumped out from both capillary ends. The gas pressure is regulated by a Tescom ER3000 pressure controller from the background level up to 250 mbar in 1 mbar steps. The gas pressure profile within the capillary is shown in Figure 3.10 and was calculated by a previous student using ANSYS.

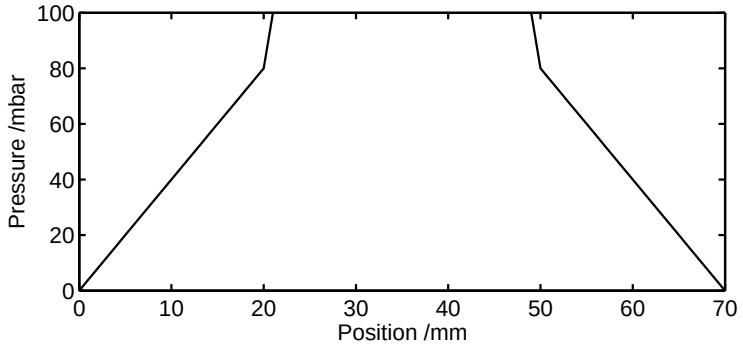

Figure 3.10: Pressure profile within 7 cm capillary for a maximum pressure of 100 mbar. The pressure is constant between the gas inlets, decreasing linearly to the background level from each inlet to the exit. The profile was calculated using ANSYS. The discontinuities within the plot arise from the step size used (1mm).

Figure 3.11 shows the basic layout used for the following experiments. The capillary output is a combination of the pump laser pulse and the generated XUV. The pump laser pulse was reflected out of the vacuum chamber into a fibre-coupled Ocean Optics HR2000 CG-UV-NIR spectrometer mounted on a translation stage. A ground glass diffuser was placed before the fibre input to measure the spectral output of the entire beam. Spatio-spectral measurements were taken by removing the diffuser and placing the 125 μm diameter fibre end at the centre of the output beam and translating it radially outwards across 24 mm of the beam profile. The argon ion fluorescence was imaged using the setup shown in Figure 3.11, consisting of a 35 mm camera lens imaging the capillary from the side onto a Princeton Instruments Pixis: 1024 CCD. A 650 nm high pass and a

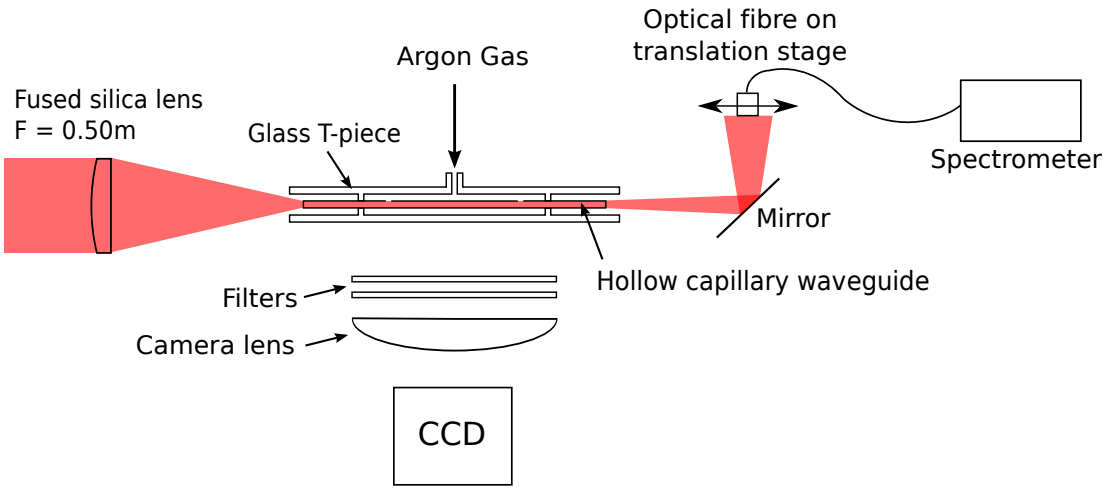

Figure 3.11: Schematic of experimental setup for measuring the output pump pulse spectrum and argon ion fluorescence along the capillary length.

488 nm bandpass filter were used to single out the 488 nm emission line of singly ionised argon in its first excited state.

3.2.2 Summed output spectrum

The total or summed output spectra are compared to the theoretical output to gain an understanding of the processes involved in pump pulse propagation in capillaries. Figure 3.12 shows the theoretical (left) and experimental (right) spectra for three different powers. The gas pressure used was 100 mbar.

The agreement between the three sets of data is excellent, implying at first glance that the model is using the correct physical processes. Blue shifting of the spectrum is observed in both as the power is increased, due to a combination of SPM and self-steepening. At higher powers these effects lead to the more complex spectral structure that is observed. These are described in Section 2.3.1 and in more detail in "Nonlinear Fiber Optics" by G.P Agrawal [53]. The model provides more information than the simple spectrum. The theoretical spectra shown here are the total spectrum (solid line) and the contributions from the two lowest order modes, EH_{11} (red) and EH_{12} (blue). In the lowest power (500 mW) situation the spectrum is dominated by the EH_{11} mode, and the spectrum is simple. As the power is increased to 600 mW the spectrum becomes slightly more complicated, developing a shoulder as well as having a larger contribution from the EH_{12} mode. At 805 mW the spectral broadening is quite extreme, stretching over 100 nm with side peaks on either side of the main peak. The surrounding peaks are a result of the symmetrical broadening of SPM. The greater blue shift is the combination of nonlinear and plasma self steepening of the pulse and subsequent broadening from SPM.

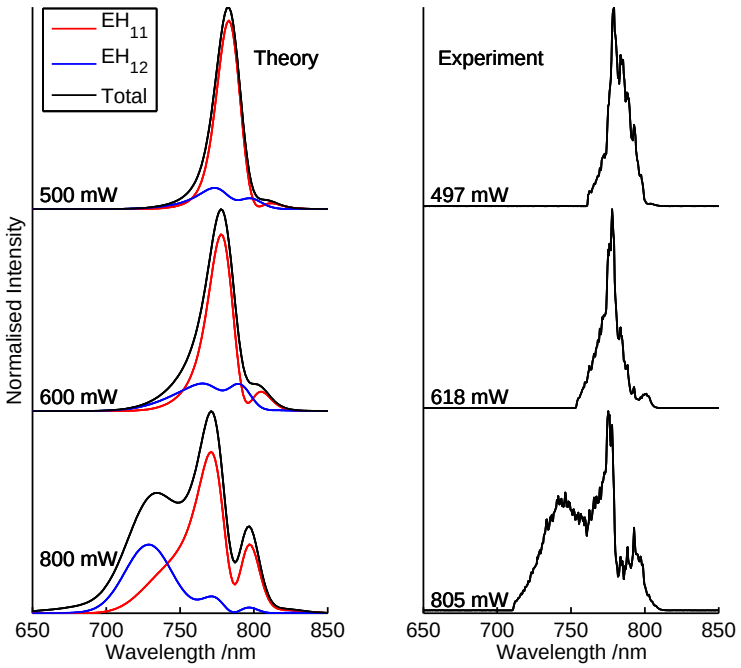

Figure 3.12: Theoretical (left) and experimental (right) output spectra measured at the output for three input powers, shown. The predicted data shows the total spectrum (black), as well as those for the EH_{11} (red) and EH_{12} (blue) modes.

These spectra have been seen before; the interesting point here is the contribution from the modes. At higher power where more extreme blue shifting is observed the contribution from the EH_{12} increases, more precisely, the blue shifted shoulder in the spectrum is dominated by the higher order mode. This can be explained physically when one considers the target gas. As the pump pulse propagates not only does SPM broaden the pulse spectrally, it is also chirps the pulse in addition to the standard GVD. This results in the leading edge of the pulse being red shifted and the trailing edge blue shifted. In addition to this, the leading edge of the pulse ionises the target gas producing a plasma and thus a different refractive index profile, as mentioned in the previous section. As the blue shifted trailing edge of the pulse encounters this new RI profile, it is defocused and coupled into higher order modes. All of this leads to the higher order modes containing a greater portion of the blue shifted spectrum.

To be certain that the blue shifting in the higher order modes is a real effect one must look at the spectrum not simply as a whole, but as contributions from different modes. The next section deals with this problem.

3.2.3 Spatio-spectral output

The pump pulse propagates within the capillary as a set of Bessel modes. The model assumes circularly symmetric modes EH_{11}, EH_{12}, ..., $EH_{1\,20}$. When the pulse reaches the end of the capillary each of these modes propagates out. In the far field the main peak of each of these modes is spatially separated, as shown in Figure 3.13. This is a plot of the first five EH_{1m} modes propagated into the far field from the capillary exit. They are shown scaled linearly to the normalised EH_{11} mode. The EH_{11} mode has a main peak on-axis, with the main peak of each subsequent mode positioned at increasingly greater radii. This means that in the far field it should be possible to see experimental proof of the contribution from the blue shifted higher order modes.

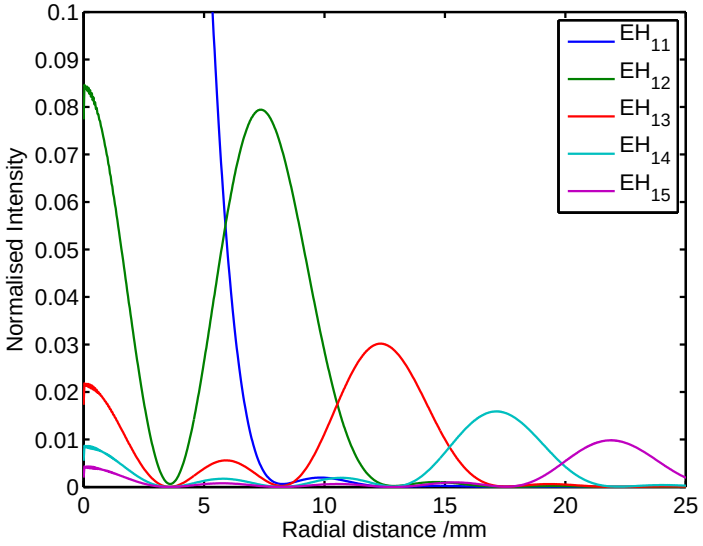

Figure 3.13: The first five $EH_{1\,m}$ modes propagated from the capillary exit to the spectrometer. All five modes have been normalised to the EH_{11} mode (blue line) and the scale limited. The main peak of each successive mode occurs at a greater radial distance from the centre, spatially separating their contribution.

The modal contribution was examined by taking a spatially resolved spectrum for a pump power of 805 mW with a gas pressure of 100 mbar. The spatio-spectral map was built up by measuring the spectrum every 500 μm from on-axis to a radius of 24 mm at a distance of 80 cm from the capillary exit. The spectral intensity is greatest in the first 10 mm so to produce a map out to 24 mm neutral density filters were put in place and removed at greater radial distances. The data was scaled accordingly and combined in Matlab to produce Figure 3.14a. This is a log plot of the spatio-spectral output of the capillary from on axis to 24 mm. The x-axis shows the radial distance while the y-axis shows the wavelength. Figure 3.14b is a sum over the experimentally measured spectrum and shows the summed intensity of all modes over the same radial distance. As a comparison a sum of the first five modes theoretically propagated to the spectrometer are shown in Figure 3.14c. The five main peaks from each mode can be

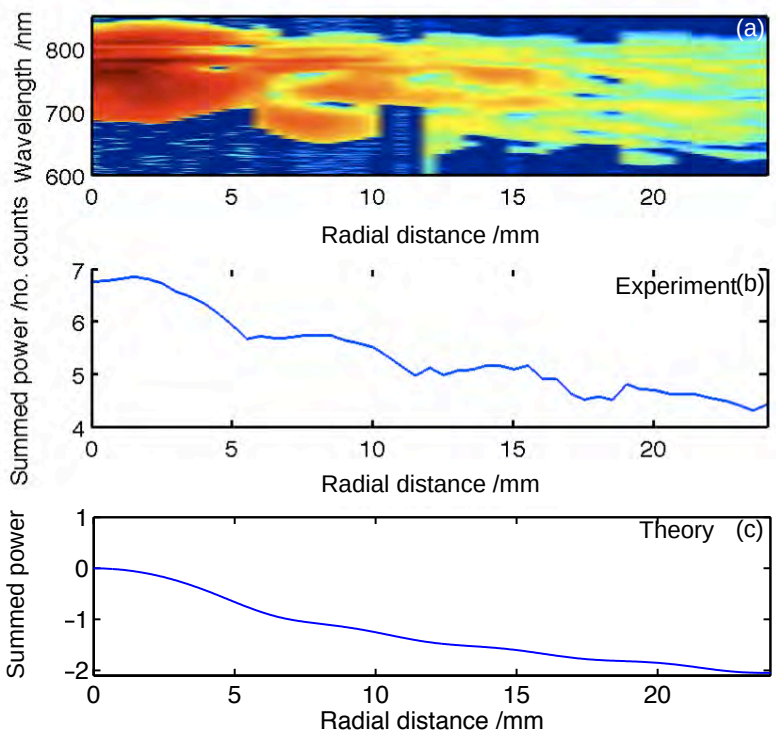

Figure 3.14: Spatio-spectral plot (a) of the output pump pulse. The spectrum (y-axis) at each radial position (x-axis) is shown from on axis to a radius of 24 mm. The spectrally summed intensity (b) is compared to the sum of the first five $EH_{1\,m}$ modes theoretically propagated from the capillary exit to the spectrometer (c). The main peak of each successive mode occurs at a greater radial distance from the centre, spatially separating their contribution. All plots are shown on a log scale

seen in both (b) and (c) and are well aligned with each other spatially. In (a) a clear trend of increased blue shifting at greater radial distances can be seen, as was predicted in the previous section.

To simplify the comparison the theoretical output was limited to a radius of 10 mm and is shown with the corresponding experimental data in Figure 3.15. The calculated (a) and measured (b) spectral intensity distributions are shown on a linear scale as a function of radial distance from the beam axis. The theoretical intensity profiles of the EH_{11} and EH_{12} modes are shown for comparison.

It is clear from both theoretical and experimental distributions that the differences in the intensity distributions of the modes are large. The EH_{11} mode has significant contributions at around 790 and 810 nm, and the blue-shifted components at about 740 nm show the same radial profile as the EH_{12} mode, with an on-axis peak, and another ~8 mm from the axis. This trend is clear in the theoretically modelled intensity distribution. In the measured distributions, the general features of the pattern are repeated. The EH_{11} mode appears at 780 and 810 nm, and the blue-shifted peak at 760nm has the radially narrower distribution of the EH_{12} mode. However, several differences are clear. The first is that more extensive off-axis blue shifting is seen in the experimental data, implying

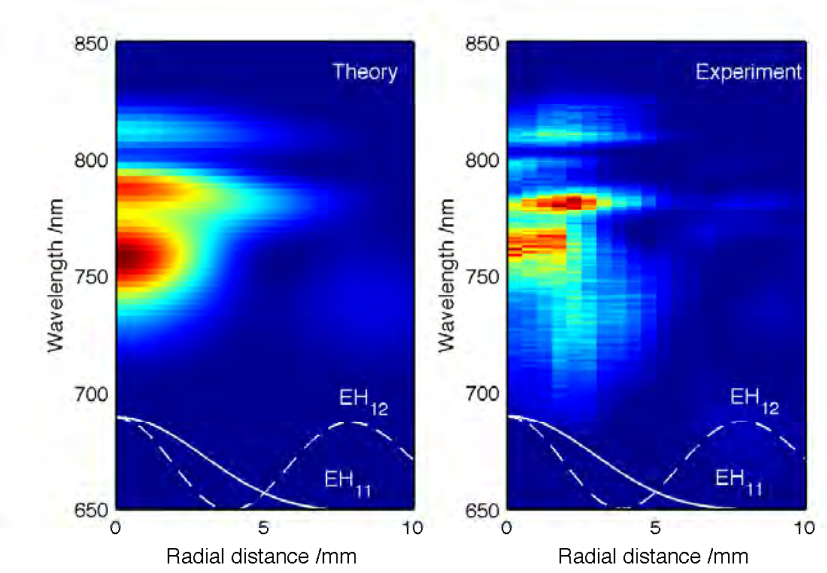

Figure 3.15: Theoretical (left) and experimental (right) spectral intensity plots (linear plot) in the lambda-r-plane. Wavelength is plotted on the y-axis whilst radial position is plotted along the x-axis. The solid and dashed white lines show the far-field profiles of the EH_{11} and EH_{12} modes respectively. The theoretical data was generated by Dr Peter Horak.

greater broadening in the higher order modes than was predicted. Secondly, an extra peak can be seen close to the centre of the beam at ∼800 nm in the experimental data. The shape of the EH_{11} peaks around 790 - 810 nm look similar to the spectral distortion caused by SPM, which produces first a splitting, and then a central peak, rising between the split peaks as the nonlinear phase shift increases. Both of these differences suggest that the nonlinear shifting of the spectrum is slightly stronger in the experiment than predicted by theory.

The simplest reason for the difference in nonlinearity between the model and experiment is that the nonlinearity for argon set in the model was too low and if it was increased would provide a more accurate match. This was discussed and discarded as the nonlinear refractive index for argon ($n_2 = 9.8\times10^{-24}\ m^2W^{-1}$) is well documented [69]. The second possibility was nonlinear propagation prior to entering the capillary. The model assumes a perfect Gaussian pulse at the input to the capillary; however, in the experiment the pulse must propagate through 1 beamsplitter and the 50 cm focal length lens. To check this a pickoff from the beamline was directed into a FROG before the capillary with an equivalent thickness of fused silica in front to replicate propagation of the pulse through the lens. Figure 3.16 shows the temporal and spectral measurement of the pulse at the same laser power used in the spatio-spectral measurement. A partly developed side peak is clearly visible on the red side of the spectrum, which is indicative of nonlinear propagation within the fused silica.

The model was therefore updated to use the real measured pulse as the input to the capillary and the results are shown in Figure 3.17. The plot is set up as in Figure 3.15

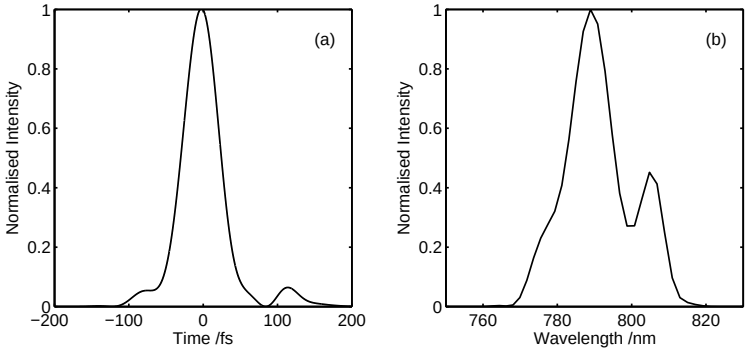

Figure 3.16: Temporal (a) and spectral (b) intensity of an 805 mW pump pulse measured before the capillary. A 3 mm fused silica block was placed in the beamline to simulate nonlinear propagation through the focusing lens.

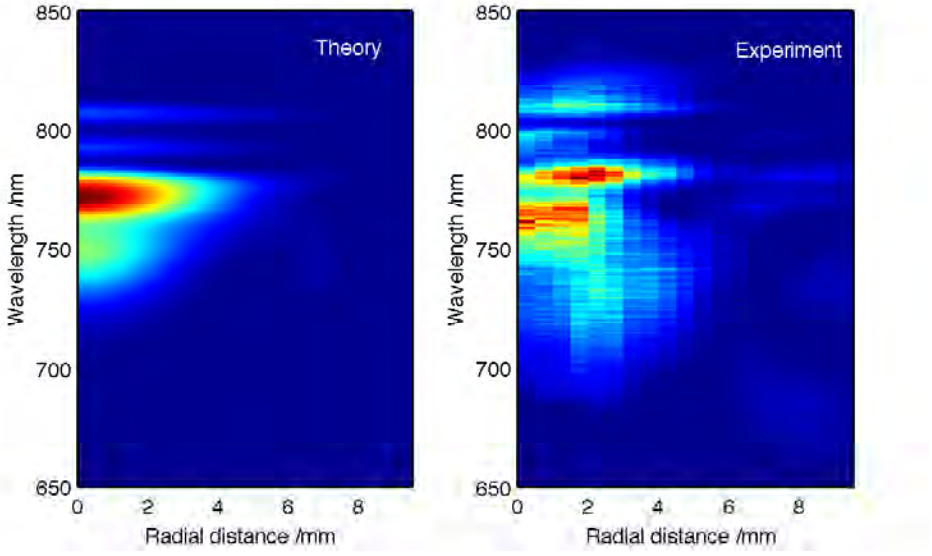

Figure 3.17: Theoretical (left) and experimental (right) spectral intensity plots (linear plot) in the lambda-r-plane. Wavelength is plotted on the y-axis whilst radial position is plotted along the x-axis. The theoretical data was generated by Patrick Anderson.

and one can immediately see the change in the spectrum from the increased nonlinearity, most notably the central peak at ∼800 nm is now visible. The off axis contribution has reduced in this theoretical data set which is attributed to slightly different initial beam parameters being used. The position of the focus with respect to the capillary entrance was not adjusted to match the experiment as accurately. However, this remains a useful result and shows that the initial input to the model is critical to accurately predict the propagation of the pulse within the capillary. From this point onwards, all plots calculated using the MM-NLSE propagation model will use the measured pulse as the input.

3.2.4 Argon ion fluorescence

While spectral measurements at the capillary exit are a good test of the end point of the model, measurement of the argon ion fluorescence along the length of the capillary provides a test of the model along the whole propagation length. An incident pulse of sufficient intensity can ionise a neutral argon atom creating an excited argon ion. The highly excited ion relaxes to its ground state via allowed transitions. For argon ions one of the radiative transmissions is at 488 nm which can be imaged. Experimentally, the fluorescence, produced by excited argon ions created by the pump pulse, is filtered and imaged from the side as shown earlier in Figure 3.11. This fluorescence is proportional to the ionisation in this case as the 488 nm emission line is only produced by excited argon ions, not neutral argon, therefore the fluorescence is dependant on the number of ionised argon ions. The integrated fluorescence from each point along the capillary length can be compared directly to the radially integrated ionisation levels predicted by the propagation model. This experiment was carried out using the same parameters as the spatio-spectral measurement, with an input power of 805 mW and a pressure of 100 mbar.

The integrated argon ion fluorescence and the theoretical integrated ionisation are compared in Figure 3.18. The measured 488 nm argon ion fluorescence should be proportional to the calculated ionisation level within the capillary. To aid comparison, the position of the beating between the EH_{11} and EH_{12} modes calculated for linear propagation is shown as vertical dashed lines. The initial increase in ionisation at the capillary entrance is observed in both theory and experiment and the first two major peaks appear at approximately the same positions within the capillary. The smaller structures within these major peaks do not correlate as strongly but similar trends can be seen. Note that neither the theoretical or experimental peak positions coincide with the peak positions calculated using simple linear mode beating. This highlights the requirement to include nonlinearity in the propagation model, which contributes to the results observed in the previous section. The final peak visible in the theory is not matched well in the experimental results, nor is the overall decrease in ionisation over the length of the capillary that is observed experimentally.

It is useful to remember at this point that the model assumes a perfect waveguide and thus does not include losses due to the gas inlets or other scattering from debris left within the capillary itself. These are the most likely causes for the discrepancies between the two. As the pulse propagates down the capillary small amounts of it will be scattered by any imperfections in the waveguide itself and large amounts by the gas inlets themselves. Strong scattering is not seen at the first hole, as the two plots appear to agree quite well. At the second gas inlet situated at 5 cm there is a clear difference between the two. The theory suggests a continual rise in ionisation producing the third peak, where as the experimental results show a sudden decrease after which

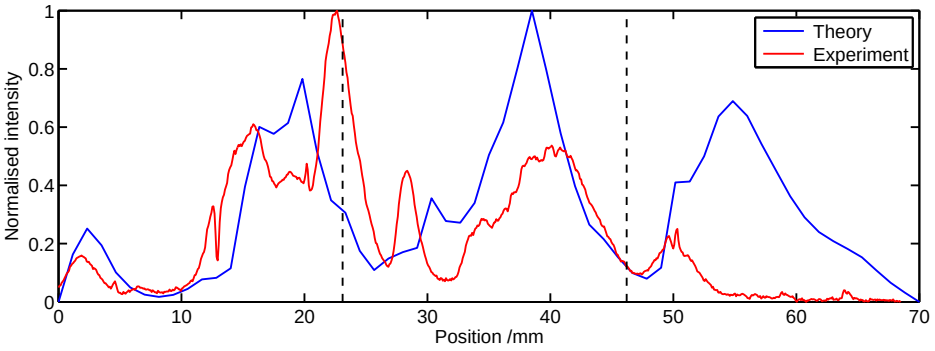

Figure 3.18: Comparison of the summed radial ionisation (blue) and the imaged argon ion fluorescence (red) along the length of the capillary. The vertical dashed lines show the beat positions for linear mode beating between the EH_{11} and EH_{12} modes.

the fluorescence remains low. Scatter from these gas inlets may be greater than expected given the previous descriptions of the capillary manufacture as this particular result is based on an older capillary, whose front face was shown in Figure 3.7. The gas inlets in this case were produced on a laser drilling rig but were larger than those used in the new capillary detailed thus far. These gas inlet holes had a 300 μm diameter which was maintained to the top of the inner bore. Other than this the two capillaries are identical, in length, diameter and output mode shape. This further supports the argument for increased scattering resulting in differences between the model and experiment, but does not detract from the good agreement otherwise, further supporting the model as an accurate representation of pump pulse propagation with capillaries.

3.3 Conclusion and future work

In the first half of this chapter the methods used to manufacture and use a short hollow capillary as a HHG source have been detailed. The method used to cleave and polish the capillary ends was described followed by drilling of the gas inlets using the main beamline of the laser. The symmetrical transmission through the capillary wall was used to accurately align the laser focus with the capillary core prior to drilling. Images of the finished capillary including the end faces, gas inlets and finally mounted within the T-piece were shown for reference. The approach to efficient coupling into the capillary at low power (10 mW) was also described. Finally, the system running at high power with 150 mbar of argon was shown including the extensive spectral broadening and nonlinear mode mixing. This led into the second half of the chapter where the propagation of the pump pulse and the simple observations made thus far were looked at in more detail and used to test the accuracy of the MM-NLSE propagation model being developed.

In Section 3.2 comparisons were drawn between the theoretical and experimental total output spectra (Figure 3.12) and the strong part nonlinear mode coupling has to play was realised. This was further investigated in Section 3.2.3 where a novel method to

spatially resolve the entire output spectrum was used. The initial comparison showed a very strong agreement and proved that the blue shifted part of the spectrum has a large contribution in higher order modes. It was also noted that the total nonlinearity of the model was less than that of the experiment. The cause of this was discovered to be nonlinear propagation prior to the capillary which the model did not take into account. Using the real measured pulse as the input to the model produced a new spatio-spectral output whose comparison to the experimental data was much better. As a result all further theoretical modelling uses the measured field as the input. To ensure the model is accurately predicting the propagation of the pump pulse along the entire length of the capillary and not simply at the end an experiment was devised to compare the theoretical ionisation and experimental fluorescence along the capillary length. The argon ion fluorescence was imaged and compared to the theoretical integrated radial ionisation profile predicted using the model. Agreement between the two was very good accepting that the model assumes a perfect waveguide and does not include losses due to imperfections in the capillary or at the gas inlets.

In summary, a capillary has been manufactured and successfully used to help improve the MM-NLSE propagation model that will ultimately be used to further advance capillary based HHG sources. The model has been shown to be accurate at predicting the spatio-spectral output from a capillary and the overall ionisation hence intensity profile along the length. Whilst this work is an excellent starting point for capillary based HHG it is just that, a starting point. In the next chapter the spectral comparison will be expanded upon by looking at the temporal domain. This allows an extra dimension of accuracy over the spectral intensity comparisons in the form of phase information. The output pulse from the capillary is measured using a FROG under a variety of conditions and compared to the theory. In addition to this the XUV spectra generated under these same conditions will be explored in an effort to understand what is physically happening at the end of the capillary.

Chapter 4

Pulse self-compression and HHG in a short hollow core capillary

The work carried out in this chapter extends the previous chapter's testing of the MM-NLSE propagation model into the temporal domain. This chapter will begin by looking at the initial temporal data from the output of the capillary followed by pulse self-compression. The second half of this chapter focuses on HHG within the capillary and attempts to explain the observed results.

4.1 High intensity pulse self-compression in a short hollow core capillary

The input power and gas pressure within the capillary have a direct effect on the non-linear propagation of the pump pulse and so were considered suitable tests of the model. The initial results will be discussed including the required adjustments to the model and post processing of the experimental data. This was required due to the large bandwidth the pump pulse develops during its propagation and the resultant second order dispersion that it underwent. The final results led to the conclusion that within the capillary the pulse is undergoing self-compression and that dispersion compensation can produce a factor of 3 reduction in pulse length. Further examination of the model indicates in-situ pulse compression down to 10 fs within the capillary, the uses of which are discussed before moving onto the HHG and XUV spectra. Pulse compression of this type opens up a new regime of compression techniques that use high ionisation and higher order modes to self-compress the pulse.

4.1.1 Experimental set up

The experimental set up used to measure the temporal output of the capillary is similar to that used in the previous Chapter. A schematic is shown in Figure 4.1 with the only difference being the replacement of the spectrometer with that of a FROG. Reflective neutral density filters were used to reduce the power of the beam prior to entering the FROG. The internal design of this FROG, a Swamp Optics Grenouille 8-20, becomes important later and has been described in Section 1.2.3. During the first round of experiments the pressure within the capillary was varied from 50 - 200 mbar while the input power ranged from 131 - 947 mW. The variation of input is achieved as before, by changing the pump power to the amplifier. The data collected from the FROG was processed using Matlab.

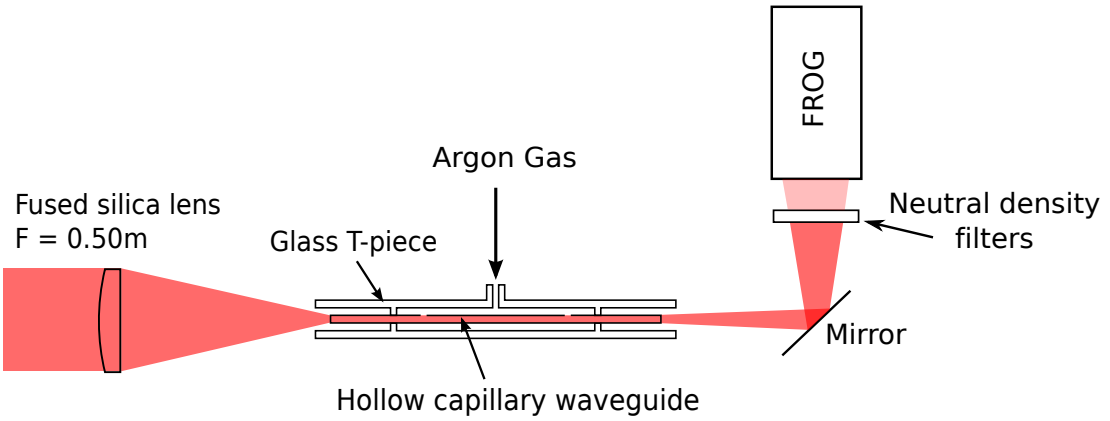

Figure 4.1: Schematic of the experimental setup for measuring the output pump pulse using a FROG. The basic design is the same as in the previous chapter, Figure 3.11, with a FROG device in place of a spectrometer. The pump pulse is directed out of the vacuum chamber into a FROG. Reflective neutral density filters are used to reduce beam power prior to the FROG. The input to the FROG allows only the central 3 mm of the beam, this constitutes the two central rings seen in Figure 3.9.

4.1.2 Temporal measurements of capillary output

Increasing the laser power without affecting the pulse length allows one to vary the intensity of the input pump pulse to the capillary. Given what was learnt in the previous chapter, as the intensity is increased so too will the nonlinear response of the focussing lens to the pump pulse, changing its temporal and spectral distributions. For all of the data modelled here at different powers the correct input pulse was measured and used as the input to the model. As such the model should be able to accurately predict the nonlinear propagation within the capillary and produce an accurate output pulse. The nonlinear length, L_{NL} was given in equation 2.52 and is a guide to how far through a material a pulse must propagate before nonlinear effects become significant. It is inversely proportional to both the pump pulse intensity and the nonlinear refractive

index (n_2) of the of the material. The nonlinear refractive index is scaled by the gas pressure, as a result the nonlinearity observed within the capillary is dependent not only on the laser power but also on the gas pressure. Three power runs and three pressure runs will be discussed in the following pages; the complete data set can be found in Appendix A.

Figure 4.2 shows the reconstructed output pulse as a variation of power for 50 mbar (a), 100 mbar (b) and 150 mbar (c). The temporal (left) and spectral (right) intensity distributions are shown for each case. There is a clear trend to more complex pulses as the power was increased for all of the pressures. At low power the pulse undergoes little spectral broadening, seen on the right hand side, and the pulse shape did not change significantly from those seen previously in Figure 3.16. As the power was increased to 350 mW a small post pulse started to form and by 602 mW the final pulse structure formed. This comprised three separate main peaks and was observed for all pressures above a power of 602 mW. The total spectrum measured by the FROG at the higher powers had the familiar shape of an SPM induced spectrum, with side peaks surrounding the original central peak and a significant blue shift.

Figure 4.3 shows the output pulse as a variation of pressure for 260 mW (a), 476 mW (b) and 805 mW (c). As before the temporal (left) and spectral (right) intensity distributions are shown for each case. At low power (a) little spectral broadening and pulse shaping was observed. A change in pulse shape was observed as the pressure was increased from 50 mbar to 80 mbar, however further increase in the pressure had no effect on the pulse. This was different for the 467 mW (b) input power where the pulse shape at 50 mbar produced a similar pulse shape to the 260 mW, 200 mbar case. This is to be expected as the intensity and pressure both affect the amount of nonlinearity. Above 50 mbar the pulse appears to undergo temporal reshaping, producing the distinctive three peak structure in the 100 mbar case. This becomes more pronounced as the pressure is increased. The 805 mW case is somewhat different. In this case very little change in the temporal or spectral distribution occurs as the pressure is increased. The nonlinear length is inversely proportional to both the intensity and the gas pressure, therefore changing either of these should produce some change in the pump pulse. As this is not the case at high input powers (c) another effect must be contributing to the evolution of the pulse in addition to the nonlinearity of the gas. This is ionisation induced broadening which occurs in conjunction with nonlinear mode mixing. As an intense pulse propagates the leading edge ionises the gas producing a plasma defocusing effect, as described in Section 2.3.3. The trailing edge of the pulse sees this different RI and is defocused leading to the nonlinear mode coupling observed in the previous chapter. The remaining on axis pulse is therefore reduced in length, having lost part of the trailing edge. The loss of the trailing edge steepens the temporal profile of the pump pulse. In the frequency domain this steep edge produces spectral broadening and blue

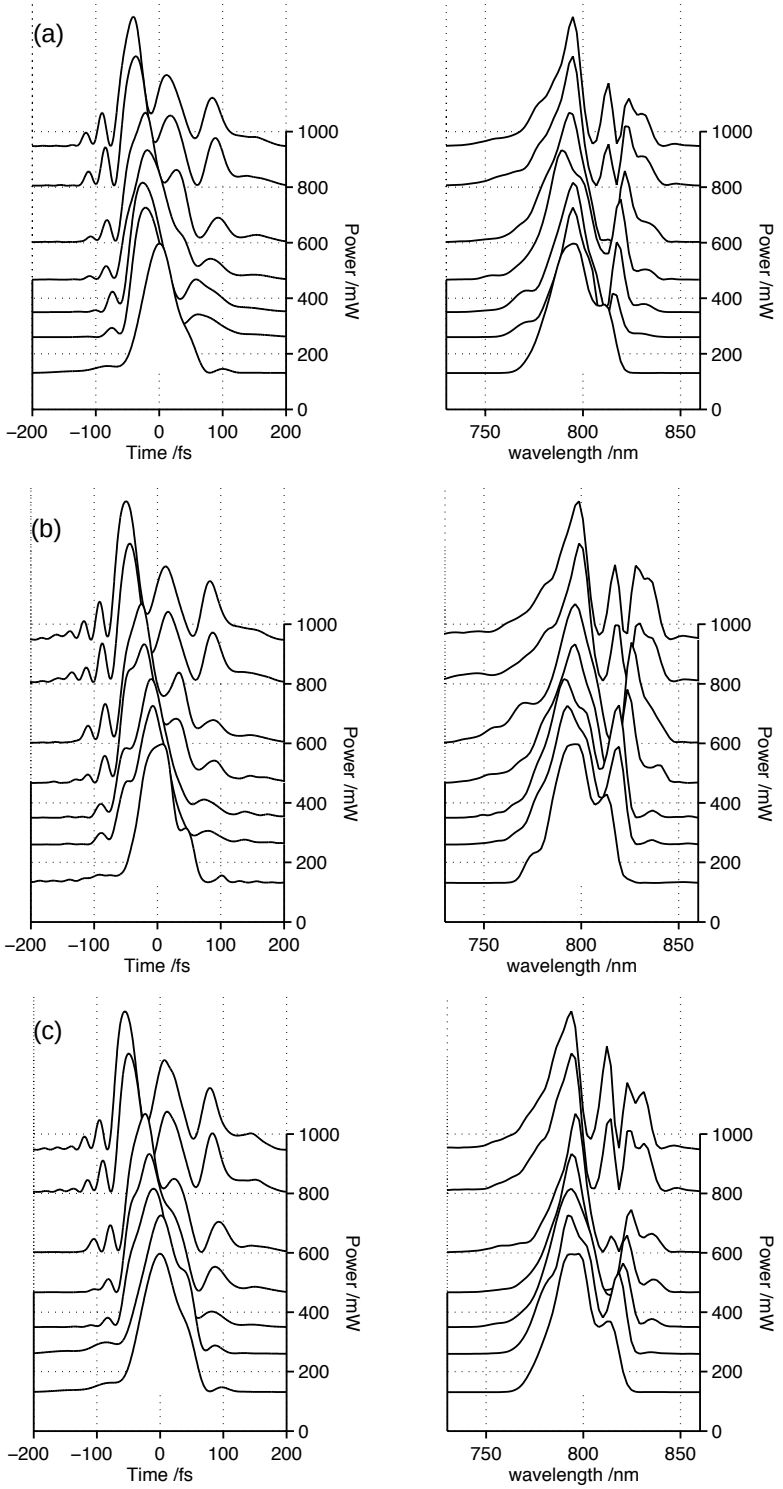

Figure 4.2: FROG reconstructions of output pulses from capillary for a range of powers at 50 mbar (a), 100 mbar (b) and 150 mbar (c). The temporal (left) and spectral (right) intensity distributions are shown for each case.

shifting of the pulse. This effect was not observed at lower input powers as the intensity was not high enough to produce a large plasma based defocusing effect.

A quick comparison of the experimental data to the model was made by theoretically reproducing the 805 mW, 150 mbar case. Figure 4.4 shows the theoretical output pulse propagated to where the FROG is in the experiment. The temporal (left) and spectral (right) distributions for a gas pressure of 150 mbar are shown. The input to the FROG is only 3mm in diameter and so only this portion of the theoretical output beam has been used. The stark difference between the theory and experiment is obvious, immediately showing that something is wrong. The experimental pulse (red line) has three dominant peaks in the time domain whilst the theory (blue line) shows a single 35 fs pulse. In the spectral domain the theory shows the same overall shape shown in Chapter 3, with a blue shifted shoulder and two smaller peaks on the red side of the central peak. The experimental data shown here does not show the same blue shoulder although this is attributed to the FROG device as its measurement of the spectrum is not as accurate as a standard spectrometer. The two red shifted peaks are visible and show greater intensity than the theory. The increased intensity of the side peaks suggest increased nonlinearity.

The model assumes a perfect Gaussian input beam in the same way it originally assumed a perfect Gaussian input pulse. One of the successes of the previous chapter's experiments was the realisation of the need to use more accurate pulse shapes at the input. In exactly the same way the coupling of the beam into the capillary is heavily dependent on the spatial input mode. The laser has an M^2 of around 2, so it was necessary to either, theoretically create a beam with the appropriate M^2 or measure the real wavefront of the beam. The former idea was discarded as there are many combinations of modes that can create an M^2 of 2, with no way of knowing which is correct. A wavefront sensor was built based on work by Jeong et al [70] which measures the field amplitude in the near and far field and uses a phase retrieval algorithm to reconstruct the phase. The measured wavefront was of a collimated beam and so did not show large changes in the phase across the beam width, however, it was not completely featureless as has been assumed thus far in the model. This work was carried out by Patrick Anderson and the wavefront data used in the model. The second problem was with the experimental data.

The spectral broadening that the pulse undergoes has already been discussed. In the previous chapter it was used to describe the coloured ring patterns and the blue shift in the spectrum as the pulse propagated along the capillary at high power and pressure. The pulses measured by the FROG have a FHWM spectral bandwidth of up to 70 nm, the actual bandwidth within the capillary is greater than this given that spectral broadening has been observed to the green at around 530 nm. This means that significant temporal broadening could occur as the pulse passed through the output window, neutral density filters and the components within the FROG itself. The FROG manufacturers

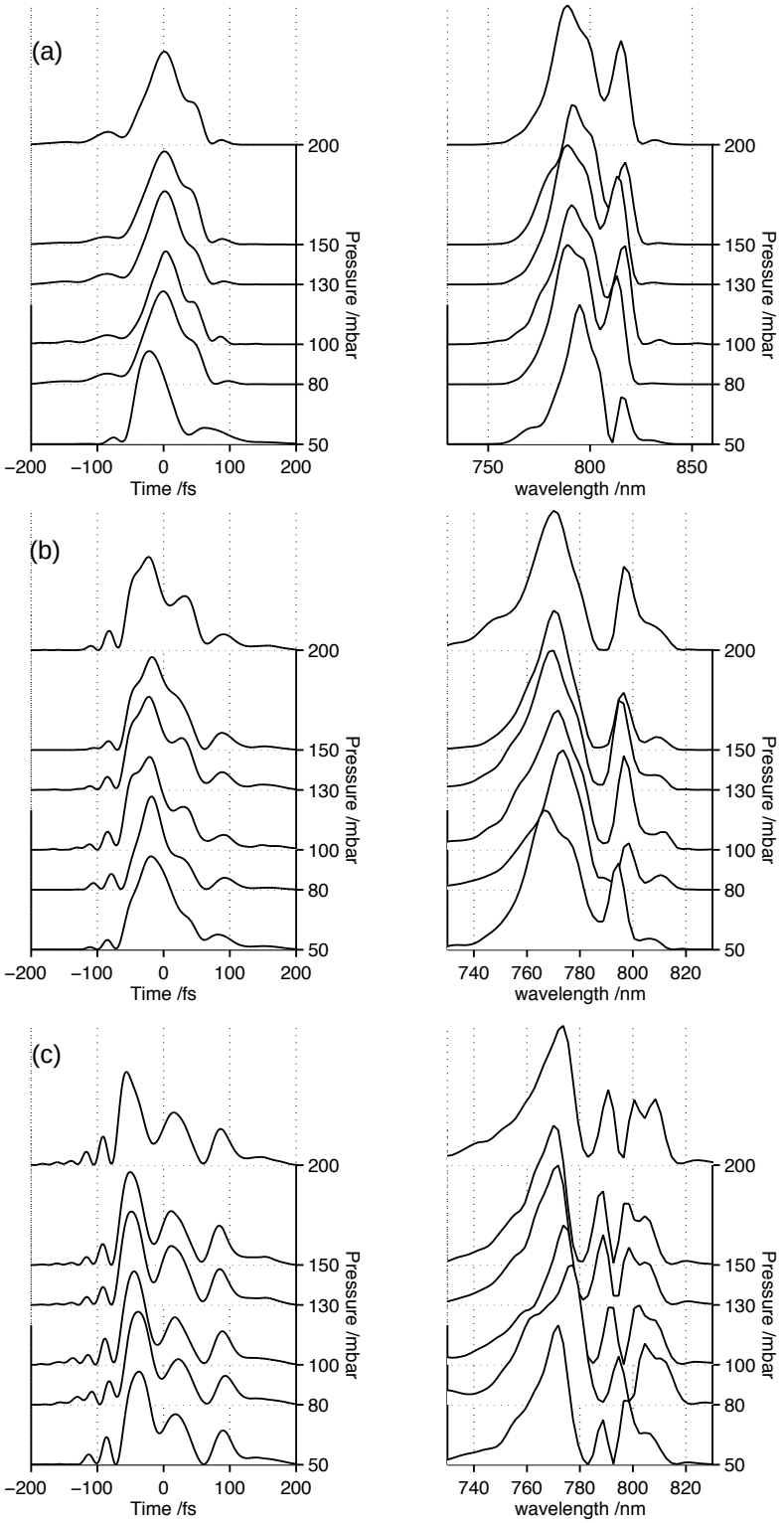

Figure 4.3: FROG reconstructions of output pulses from capillary for a range of pressures at 260 mW (a), 476 mW (b) and 805 mW (c). The temporal (left) and spectral (right) intensity distributions are shown for each case.

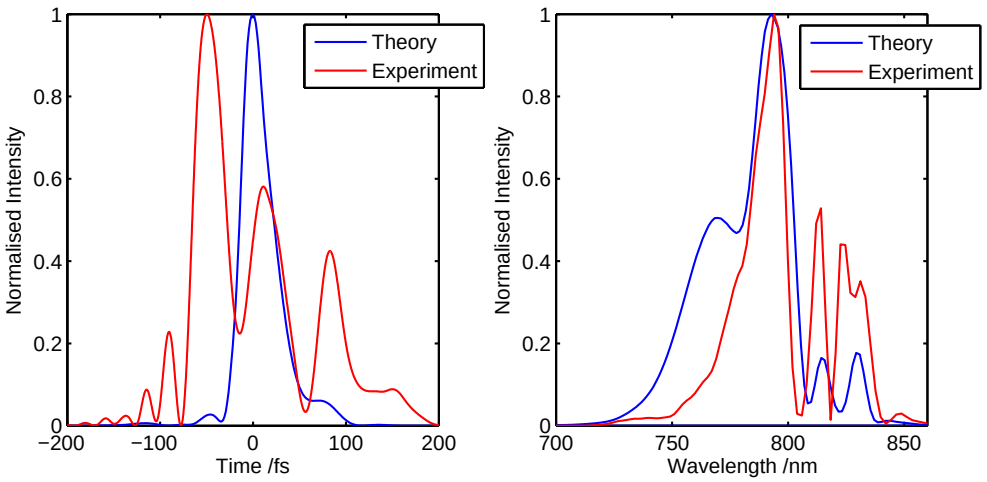

Figure 4.4: Comparison between theoretical (blue line) and experimental (red line) output pulse from the capillary. The input power was 805 mW and the pressure set at 150 mbar. The experimental data was measured using a FROG, the theoretical data was propagated an equivalent distance. The temporal (left) and spectral (right) intensity distributions are shown for each case.

suggest that for large bandwidths it may be necessary to back propagate the pulse to know the pulse length at the input to the FROG device.

Propagation through any material results in a change of the spectral phase of a pulse [53]. The spectral phase, φ, can be written as a Taylor expansion of components shown in equation 2.60. The third term in this equation is the GVD and describes the how the pulse spreads out as it propagates. This is due to the frequency dependence of the group velocity for the individual components comprising the pulse. Higher order dispersion terms also exist but contribute less and so have been ignored for the following calculations. The GVD of most materials is well know, including that of fused silica (36 fs^2mm^{-1} at 800 nm), which makes up the majority of the components used here. If one multiplies this by the length travelled the GDD is given. The FROG is described in Section 1.2.3 where the thickness of all optical components the pulse passes through before the nonlinear crystal has been noted. The combination of GDD from the FROG, neutral density filters and output window is $\sim$ 440 fs^2. The spectral distribution of a pulse can be written as

$$E_\omega = E_\omega^0 e^{i\varphi} \tag{4.1}$$

where E_w^0 is the amplitude of the field and φ is the spectral phase. To back propagate and change the spectral phase of the pulse one simply needs to multiply equation 4.1 with $e^{i\varphi_{prop}}$ where φ_{prop} is given by

$$\varphi_{prop} = \frac{1}{2}k''(\omega - \omega_0)^2 \tag{4.2}$$

where $k'' = 440$ fs^2, ω_0 is the central angular frequency and ω is the instantaneous angular frequency. The FROG reconstructions include the complex field data and so

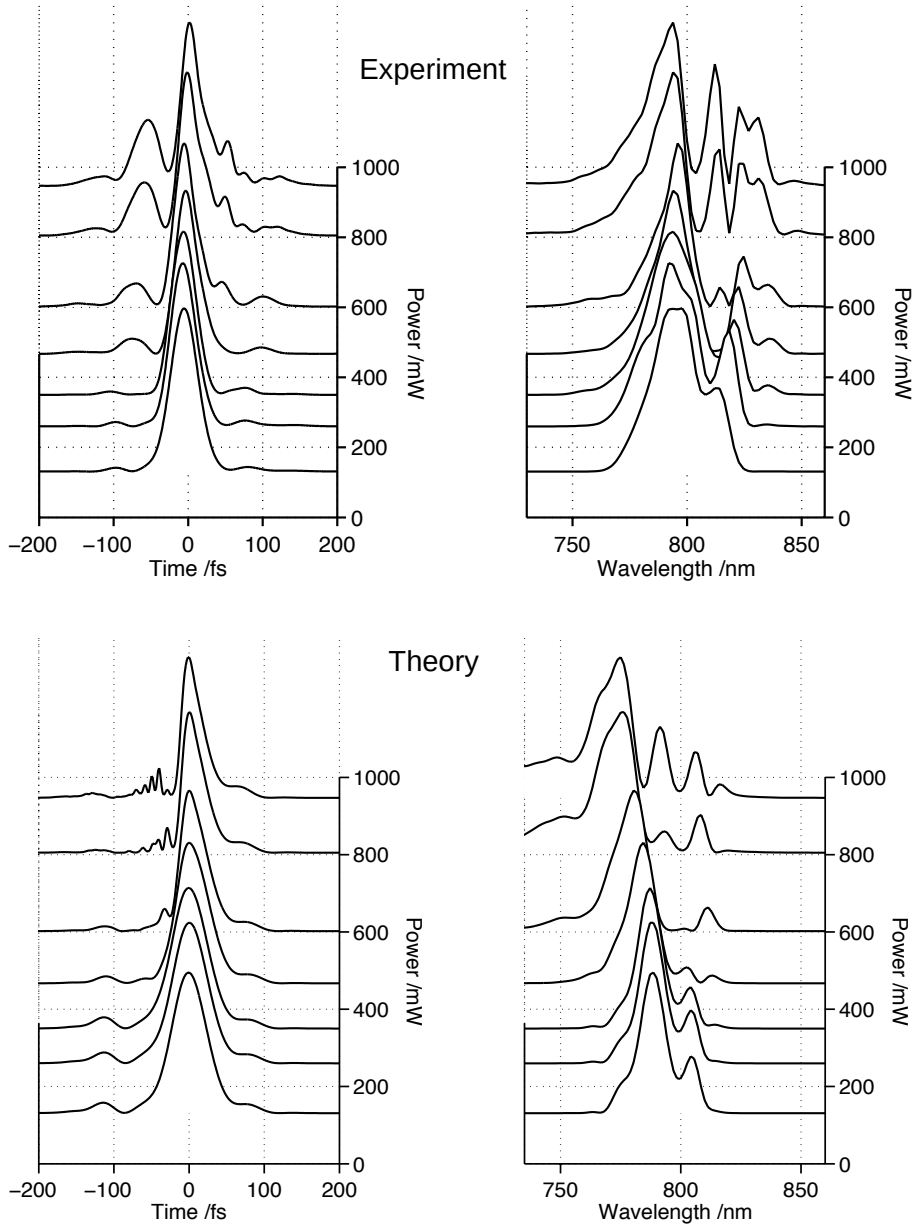

Figure 4.5: Comparison between experiment and theory of output pulses from capillary for a range of powers with gas pressure set at 150 mbar. The temporal (left) and spectral (right) intensity distributions are shown for each case. The experimental data comprises FROG reconstructions that have had 440 fs^2 second order dispersion removed to account for propagation to and through the FROG device. The theory uses experimentally measured input pulse and beam shapes.

the back propagation detailed above was carried out using Matlab. The GDD adjustment was carried out on the 150 mbar power scan experimental data originally shown in Figure 4.2c. The results of this and the new theoretical plots for the same parameters are shown in Figure 4.5.

The experimental results (a) are significantly changed from the original measurements,

which show a single dominant peak with a shoulder on the trailing edge and a smaller pre-pulse forming at higher powers. The theoretical data (b) which now closely resembles the experimental, shows the same dominant peak and shoulder on the trailing edge. The pre-pulse is greatly reduced in the theory, however the overall agreement is very good. The inclusion of the real wavefront to the propagation model has reduced the pulse length after propagation to the FROG device making the minimum pulse length for both data sets 28 fs. This is a very exciting result as the input pulse length for this data was measured at 53 fs, meaning almost a factor of 2 pulse self-compression achieved in a 7 cm capillary.

Pulse compression is a large area of research and many ultrafast research labs use pulse compressors. The two main methods for pulse compression are filamentation [71] and hollow capillary/fibre compression [72–74]. Both of these methods require distances in excess of 1-3 m to achieve spectral broadening and compression. In particular, hollow capillary compression requires post compression in the form of chirped mirrors. Filamentation trades the efficiency of hollow capillary compression (67%) [54] for ionisation induced pulse self-compression. A mixture of SPM and plasma broadening increases the spectral bandwidth of the pulse, however this occurs only in a small region at the centre of the beam. Spatial filtering is required to achieve the shortest pulses reducing the efficiency to 20%. The efficiency of the 7 cm capillary compression was measured as 37%, the losses are due to the scattering at the gas inlets and high ionisation leading to coupling of power into higher order modes. The compression shown here is part of a new regime of pulse compression where ionisation is used to broaden the spectrum and couple the pulse into higher order modes. Capillary compression techniques typically avoid ionisation and use only SPM over long distances to broaden the pulse but show little or no self-compression.

A similar effect in short capillaries has been observed before by Wagner et al [75] where a pulse was compressed in a 2.5 cm capillary. The quoted compression was from 39 fs down to 19 fs. However, the initial Fourier transform limited pulse length was actually 24 fs implying very little spectral broadening occurred. The pressure used was also much lower than that used in these experiments (15 mbar) so one would expect greatly reduced nonlinearity. This work was later extended to very high pressures (10 Torr) [76] where doubly ionised argon produced a cut-off energy over 500 eV, however, the degree of pulse self-compression observed was similar to Wagner et al. The result shown here has a number of benefits over this other short capillary compression. The use of nonlinear propagation allows for much greater spectral broadening, in turn producing far greater compression factors and hence shorter, in-situ pulses. The peak intensity of the two experiments is also quite different, with Wagner et al and Arpin et al using a peak intensity of $2.2\times10^{15}\ Wcm^{-2}$, over an order of magnitude greater than that used here. This means that the technique described here with the longer capillary and different

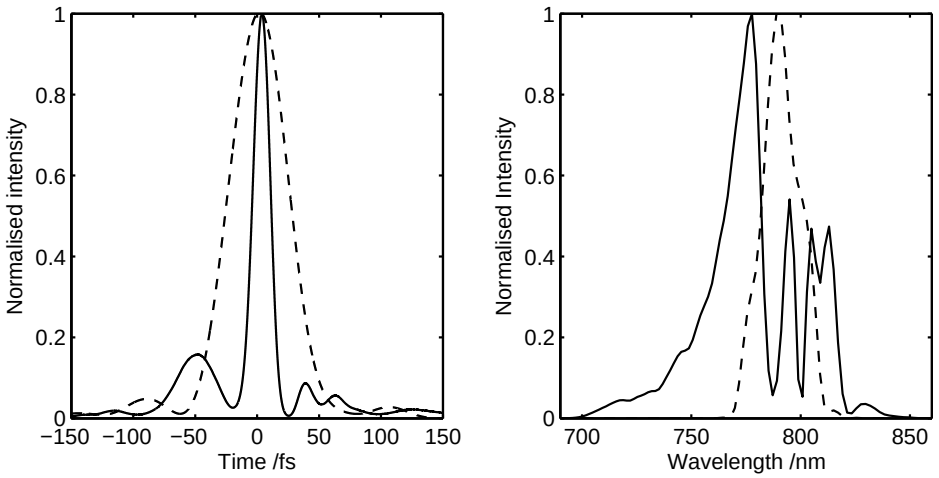

Figure 4.6: Temporal (left) and spectral (right) comparison of input (dashed line) and output (solid line) pump pulse from 7 cm capillary. The input power was 805 mW and gas pressure set at 150 mbar. The output pulse has been dispersion compensated to remove the $440fs^2$ second order dispersion gained during propagation to and through the FROG device, and an additional $150fs^2$ to reduce it to a pulse length of 15 fs. The input pulse length was 53 fs.

gas pressure regime can be more easily replicated by groups that do not possess such powerful lasers, thus indicating a different regime of pulse compression.

During the work compensating for the GDD acquired by the pulse a second discovery was made. The code used to calculate the new pulse lengths allowed any amount of negative dispersion to be applied to the pulse. In real terms this would constitute reflecting the pulse off of chirped mirrors that use a multilayer coating to apply negative chirp, a technique used in hollow capillary compression. The amount of negative GDD applied to the pulses was varied to find the shortest pulse length possible using second order dispersion compensation. It was found that removing a further 150 fs^2 of GDD produced the shortest pulse. This technique was applied to all the pulses in the 150 mbar data set, with the 805 mW case proving to have the greatest potential for compression. Figure 4.6 shows the temporal (left) and spectral (right) distributions of the input pulse (dashed) and output pulse (solid line).

The output pulse has had an extra 150 fs^2 of second order dispersion removed, which reduced the pulse length down to just 15 fs. The extra compression is the equivalent of three reflections from a chirped mirror pair and reduces the 53 fs pulse by a factor of 3.5. The outcome from this research is that a new regime of pulse compression has been opened up with a compression factor of 3.5 and a transmission efficiency of nearly 40%. This is comparable to filamentation and hollow capillary compression and future work on the subject may further improve the compression and size. To that end the following section looks more closely at the pulse within the capillary itself using the updated model.

4.1.3 In-situ pulse self-compression

Up to this point the pulses that have been either measured or theoretically plotted have been outside the capillary in the far field, i.e. after a significant amount of propagation in free space. While this is useful and necessary for many applications if one wants to use compressed pulses, it is important to remember the original purpose of this work, to develop an efficient capillary based HHG source. For this, it is the pulse within the capillary that is critical. The work thus far has served to improve upon the original model and prove a high degree of accuracy in both the spatio-spectral and temporal modelling of the pulse. The propagation of the pulse into the far field requires only a Fourier transform of the pulse at the capillary exit. Given the accuracy of the model in the far field one can assume a certain level of accuracy in the near field also, i.e. within the capillary. Figure 4.7 shows a spatio-temporal plot of the pulse at the start (a), middle (b) and end (c) of the capillary for the 150 mbar, 805 mW case. The line plots show the temporal distribution of the pulse on-axis. The input pulse here uses the measured wavefront data at the focussing lens, this results in a beam at the entrance to the capillary that does not have a maximum intensity on-axis, however the pulse energy redistributes itself during the propagation.

The colour maps are spatio-temporal plots of the pulse, with time on the y-axis and radial position on the x-axis. Zero on the x-axis is the centre of the capillary inner bore. The input pulse has an on-axis peak intensity of around 1.3×10^{14} Wcm^{-2} and a 53 fs pulse length. All of the energy exists within the single pulse which spatially extends out to 30 μm before reducing. When the pulse reaches the middle of the capillary it has undergone extensive spectral broadening and temporal restructuring. The pulse here consists of three narrow peaks, the shortest of which is less than 10 fs in length with a peak intensity of 5.8×10^{14} Wcm^{-2}, 4.5 times higher than at the start of the capillary. The radial structure is quite complex, with the short <10 fs pulses contained within the inner 10 μm. At the exit of the capillary the pulse shape has become yet more complex and now exists as a series of short pulses. The peak intensity at this point has dropped to 5.5×10^{14} Wcm^{-2}. This intense pulse is still contained within the inner 10 μm of the capillary.

It is the longer peak centred at -25 fs that becomes the main pulse in the far field that is measured by the FROG. This pulse remains whilst the shorter, more intense pulse is lost due to diffraction. As the short pulse exists within a 10 μm radius in the near field as it propagates into the far field it diffracts more rapidly than the longer, radially larger pulse. After just 1 cm of propagation from the capillary end the short, intense pulse has diverged to such an extent that it is no longer visible on a linear plot.

Experimentally measuring these pulses is very difficult due to the rapid diffraction upon leaving the capillary. Ideally one would place a collecting optic immediately after the

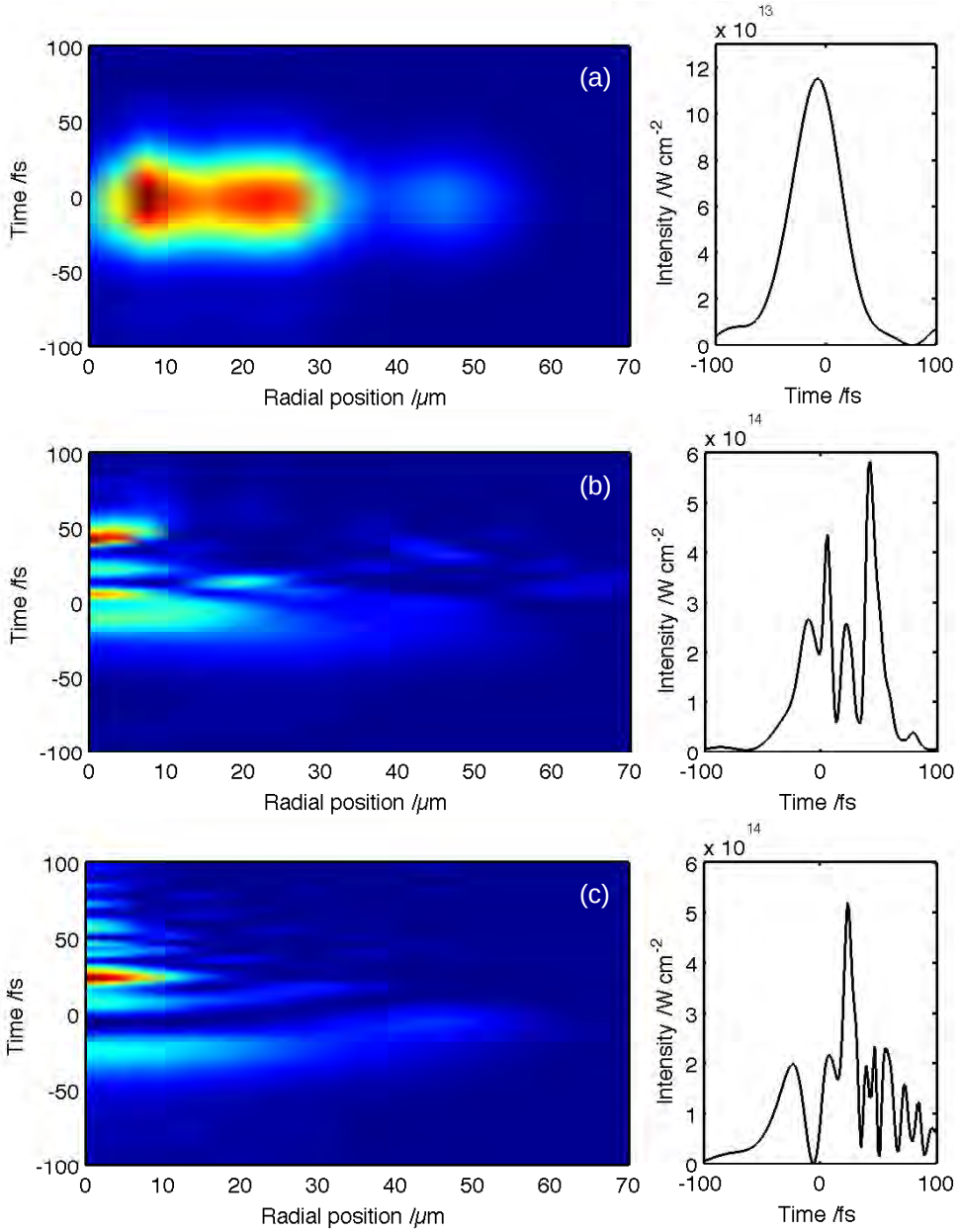

Figure 4.7: Theoretically modelled spatio-temporal distribution of pump pulse shown at the start (a), middle (b) and end (c) of the capillary. The spatio-temporal distribution (left) shows the temporal distribution (y-axis) of the pulse as a function of radial distance from the central axis (x-axis). A plot of the on-axis temporal distribution is shown on the left. Significant pulse splitting and compression is observed as the pulse propagates along the capillary. The intensity colourmap is displayed on a linear scale, scaled to a maximum of $6{\times}10^{14}\ Wcm^{-2}$.

capillary to re-image the capillary end and thus maintain the pulse structure. Unfortunately the high intensity of the pulse prevents this, as any material placed this close to the capillary exit is destroyed. At present these pulses have not be experimentally measured and this remains an area of current and future research. It would be ideal if one could collect the entire output from the capillary and re-image it without damaging the collector. Such an advance would make the capillary compression much more useful, as it may also remove the need for post compression entirely. If the model is correct and the pulse is undergoing self-compression to this extent it makes the capillary a very useful and effective "in-situ" pulse compressor, boasting a compression factor of 4.5 with no need for post compression following spectral broadening.

Short hollow capillary compression provides an ideal method to compress and use pulses within the capillary, as is the case for HHG where the increased intensity leads to higher energy cut-offs and the reduced pulse length improves phase-matching. The usefulness of this method cannot be stressed enough. One of the main objectives for many groups in the HHG field is higher harmonics, pushing the cut-off towards the water window. The cut-off is proportional to the intensity of the driving pulse, and here it has been shown that this can be increased by a factor of 4.5 in 7 cm of propagation and within the target medium used for HHG, removing the need for expensive optics to bring such a short pulse to the target. It is a pulse compressor and XUV source in one.

At this stage the propagation of the pump pulse within the capillary has been studied and tested in some length and the nonlinear propagation model has been shown to be accurate at predicting the pulse evolution in both the time and frequency domains. The following section will look at the XUV spectra produced by some of these pulses.

4.2 Pressure dependence of pump pulse and XUV spectra

high-harmonic generation is a complex process that depends strongly on the pump pulse and the target gas. The pulse wavelength and intensity determine the maximum energy harmonics that can be generated, given by equation 2.4. As a result the laser power used for HHG in the following experiments was kept at 805 mW, as this power has thus far shown the highest compression. To efficiently generate high-harmonics one must consider the phase-matching of the process. phase-matching has been discussed in Section 2.2. The basic premise is to match the phase velocity of the fundamental wavelength and any generated harmonics. Perfect phase-matching is very difficult to achieve in such highly nonlinear conditions due to the number of terms that require balancing. In a capillary one must balance the phase mismatch due to the waveguide (equation 2.34), the atomic phase (equation 2.42), the neutral gas atoms (equation 2.31) and the free electrons (equation 2.27). The waveguide mismatch varies with mode, varying as energy is coupled into different modes. The atomic phase depends on the intensity gradient of

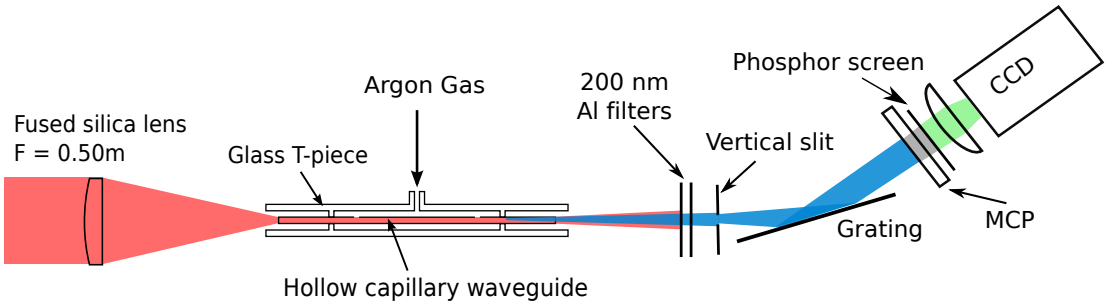

Figure 4.8: Schematic of experimental setup to measure the XUV spectrum generated within capillary. The pump pulse is filtered out using two 200 nm freestanding aluminium filters. The XUV beam passes through these filters to a grazing incident spectrometer. It is spatially sliced by a vertical slit before reflecting off of a 300 lines/mm grating. From here the XUV beam meets an MCP which converts the XUV to electrons, these then collide with a phosphor screen producing visible light that is imaged onto a CCD.

the pump pulse. The neutral gas and free electron terms can be varied by changing the gas pressure and ionisation fraction. The ultimate limit to the amount of XUV one can generate is the absorption of the XUV by the neutral gas. In the following section the dependence of the HHG process within the capillary to gas pressure will be explored showing some interesting effects which will be discussed and explained.

4.2.1 Experimental set up

The experimental set up to measure the output pump pulse includes a 45 degree silvered mirror to direct the beam out of the vacuum chamber. If this mirror is removed the beam can continue to an XUV spectrometer. Aluminium filters were used to separate the pump beam from the XUV beam. Two 200 nm free standing filters were used for these experiments. A grazing incidence spectrometer was used to record the high-harmonic spectra. This consisted of a 0.5 mm wide vertical slit followed by a 300 lines / mm grating at glancing incidence. A micro-channel plate (MCP) detector collected the XUV photons and converted them to electrons which collide with a phosphor screen. The screen is imaged onto a Princeton Instruments Pixis 400 CCD camera using a 35 mm camera lens. The wavelength range of the spectrometer in this configuration is 20 - 60 nm. A schematic of this part of the experiment is shown in Figure 4.8. For this data set the XUV spectrum was collected for a pump input power of 805 mW and argon gas pressure varied in 5 mbar steps from 50 mbar up to 140 mbar and 10 mbar steps from there to 240 mbar. The associated pump pulse data that will be discussed in this section refers to the data set shown in Figure 4.3c.

4.2.2 XUV spectra variation with pressure

To put the following work into context it is useful to think about what one expects to see in a high-harmonic spectrum. The basic structure was described in Section 2.1.1 and consists of a perturbative region at low energies, followed by a plateau and finally the cut-off region at higher energies. The cut-off region is defined by the wavelength and intensity of the input pulse and can be calculated using equation 2.4. The intensity at the end of the capillary is predicted to be $\sim 5.5 \times 10^{14}\ Wcm^{-2}$ which gives a cut-off wavelength around 10 nm. This high energy cut-off cannot be observed in this experiment for several reasons. The aluminium filters used to separate the pump from the XUV have a high absorption between 10 - 18 nm. In addition to this the spectrometer can only measure 20 - 60 nm. For argon there is also an effect known as the Cooper minimum [77] which causes a dip in the harmonic spectrum with a minimum at 25 nm. As a result one would expect to see a harmonic spectrum with an apparent cut-off towards 25 nm. As the gas pressure is varied the harmonic spectrum should retain its shape but the relative intensity between peaks may change as the phase-matching of each harmonic varies.

The full set of CCD images of the XUV spectra are shown in Appendix B. A select few, at the pressures coinciding with the pulse measurements of the previous section are shown in Figure 4.9, these range from 50 mbar (a) through to 200 mbar (f). The curved feature in the top left corner of the images is the edge of the phosphor plate. The wavelength is given along the x-axis while the y-axis shows a slice through the beam.

The change in the spectrum with gas pressure was not anticipated. At 50 mbar (a) the harmonic spectrum does indeed show harmonics spreading towards the expected 25 nm cut-off, the intensity distribution is also shifted as one would expect, however, the spectrum is far from well defined. Off-axis one can see faint lines at the points between spectra, and on axis the harmonics are broad, some showing multiple peaks. This odd structure becomes more apparent as the pressure is increased to 80 mbar (b) where the individual harmonics appear to broaden into each other. The maximum peak intensity has also increased. At 100 mbar (c) the spectrum changes once more, with narrower distinct peaks forming at the higher harmonics. At this point however, the maximum harmonic intensity has reduced to below that seen in the 50 mbar case. More change is observed at 130 mbar (d) where the spectrum is becoming more clearly defined, the inter harmonic peak structures are becoming less obvious and the peak intensity is increasing once again. This trend is continued at 150 mbar (e), with the spectrum appearing more orderly and again an increase in the peak intensity is observed. At 200 mbar (f) the harmonic spectrum appears well defined with a set of narrow peaks. The peak intensity has increased further still and a maximum was observed at 180 mbar (see Appendix B). There are two aspects of this data set that require explanation beyond what has already been mentioned. These are the change of the spectrum from complex to well defined and the variation in harmonic peak intensity as the gas pressure is increased.

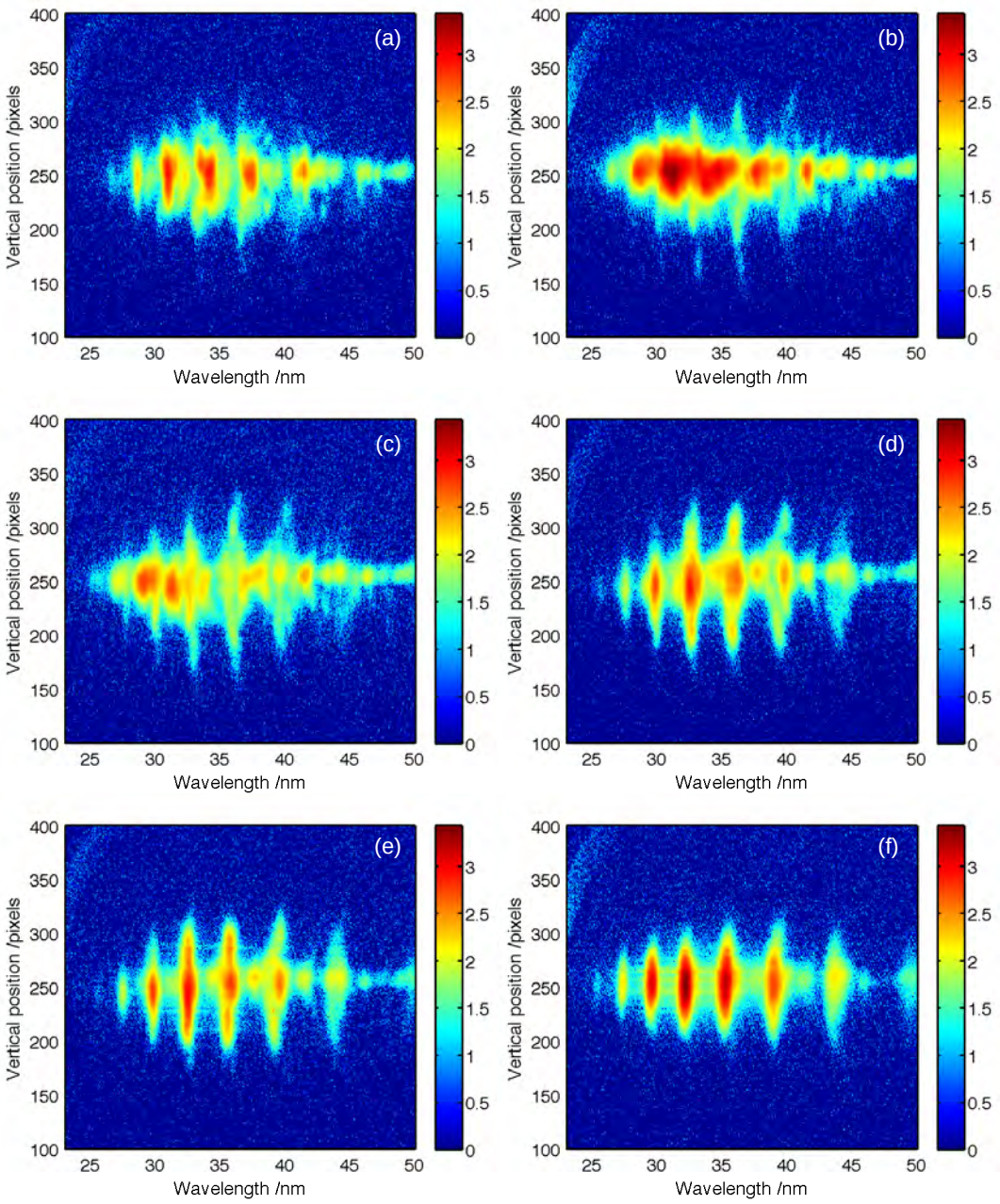

Figure 4.9: XUV spectra imaged using the setup shown in Figure 4.8 at different gas pressures within the capillary. The spectra were taken for pressures of 50, 80, 100, 130, 150 and 200 mbar and are shown here (a - f) respectively. The wavelength is shown on the x-axis and a vertical slice through the beam is shown on the y-axis. The colourmap is a log plot of the intensity in no. counts.

4.2.3 XUV absorption within the capillary

Before further analysis of the data it is necessary to look at the XUV absorption within the capillary. In a waveguide the pump pulse intensity can be maintained over long distances, if perfect phase-matching can be maintained the XUV flux would increase exponentially along the entire capillary length. This is not the case due to absorption of the XUV by the neutral argon gas within the capillary. As such the XUV spectra shown in Figure 4.9 are not representative of the XUV generated throughout the entirety of the capillary. The large majority of XUV photons will be reabsorbed and thus not contribute to the output spectrum. To understand the changes in the spectrum that have been observed, it is necessary to know where in the capillary the generation that is observed is occurring.

The refractive index of all materials in the x-ray range is close to 1 and all absorb. The refractive index of a material in this range can be written as

$$\tilde{n}(\omega) = 1 - \delta(\omega) + i\beta(\omega) \tag{4.3}$$

where $\delta(\omega)$ is the real and dispersive part of the refractive index and $\beta(\omega)$ is the absorptive. All data regarding the refractive index of the XUV used in this report has been taken from the CXRO database [78]. The CXRO database uses this data to provide information on the transmission of XUV through many gases and solids. The transmission data was used to create an integrated transmission for every point within the capillary. This was written using the predicted pressure profile within the capillary shown in Figure 3.10. The data set for a maximum pressure of 100 mbar is shown in Figure 4.10.

This plot shows the capillary position along the x-axis, the wavelength of light transmitted along the y-axis and the transmission percentage from that position to the capillary exit in the colourmap. As one would expect, the transmission increases to 1 at the exit where the gas pressure reduces to zero as does the required propagation distance. This data set shows the furthest distance within the capillary that a significant portion of XUV can be generated and used. The XUV transmission through argon depends strongly on the wavelength. For wavelengths longer than 30 nm absorption becomes strong, reducing transmission. This can be observed in the full data set shown in Figure 4.10, the contribution from wavelengths above 30 nm comes only from the very end of the capillary. For a maximum pressure of 100 mbar and 30 nm XUV one can expect more than 10% transmission from each point only in the final 1 cm of the capillary. In the same conditions one can expect the same transmission from the final 2 cm for 25 nm XUV. This situation becomes more complex when one remembers that XUV can only be generated where argon is present and that the XUV flux scales with the square of the pressure [79]. This was included in the model by multiplying the transmission data set by the normalised, squared pressure profile and is shown in Figure 4.11. This

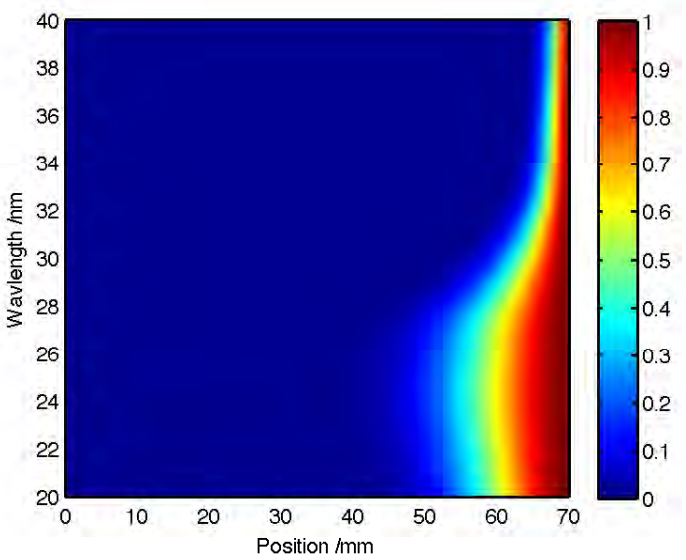

Figure 4.10: XUV transmission for every position within the 7 cm capillary. The x-axis shows the XUV generation position within the capillary, the y-axis shows the wavelength ranged from 20 - 40 nm and the normalised transmission is shown by the colour bar.

figure represents the limit within which XUV can be both generated and transmitted and overlays pulse intensity and phase matching conditions. This absorption produces the longer wavelength cut-off observed in the spectra shown in Figure 4.9. It is also worth remembering the Cooper minimum here. The data shown in Figure 4.11 shows the highest transmission at 25 nm, however, the Cooper minimum will shift this to longer wavelengths.

4.2.4 Pressure dependent XUV spectra; the plot thins

To understand why the spectrum becomes more orderly as the pressure is increased one can look at two things, the pump pulse and the absorption. The measured pulses shown in Figure 4.3c have been adjusted for second order dispersion and are shown in Figure 4.12. This shows the pulse used to generate the XUV spectra in Figure 4.9.

As was mentioned in the previous section, the temporal variation of the pulse with pressure at higher powers is very small. There is a slight change between the 50 mbar and 80 mbar cases, however above these the pulse at the exit of the capillary does not appear to change. The XUV spectra associated with each pulse measurement (Figure 4.9) has been spatially summed and plotted as a function of pressure, see Figure 4.13. The spectra shown here were made by vertically summing the full CCD images. Here the x-axis shows the wavelength, y-axis the intensity and z-axis the pressure the spectrum was taken at. As the pressure is increased from 50 to 100 mbar the individual harmonics broaden and in some cases gain an extra peak. Further increase in the pressure narrows

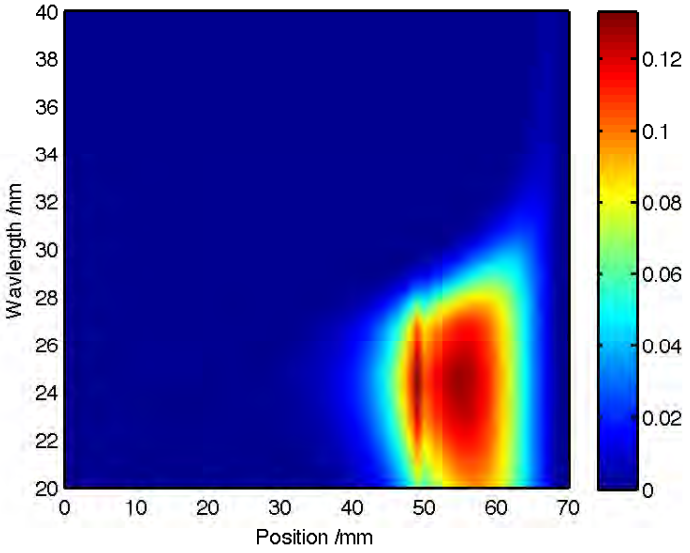

Figure 4.11: XUV generation and transmission for every position within the 7 cm capillary. The pressure profile has been included to account for the fact that the XUV intensity scales with the square of the pressure. The x-axis shows the XUV generation position within the capillary, the y-axis shows the wavelength ranged from 20 - 40 nm and the normalised transmission is shown by the colour bar. Note: the discontinuity of the feature at 50 mm is due to the step size used.

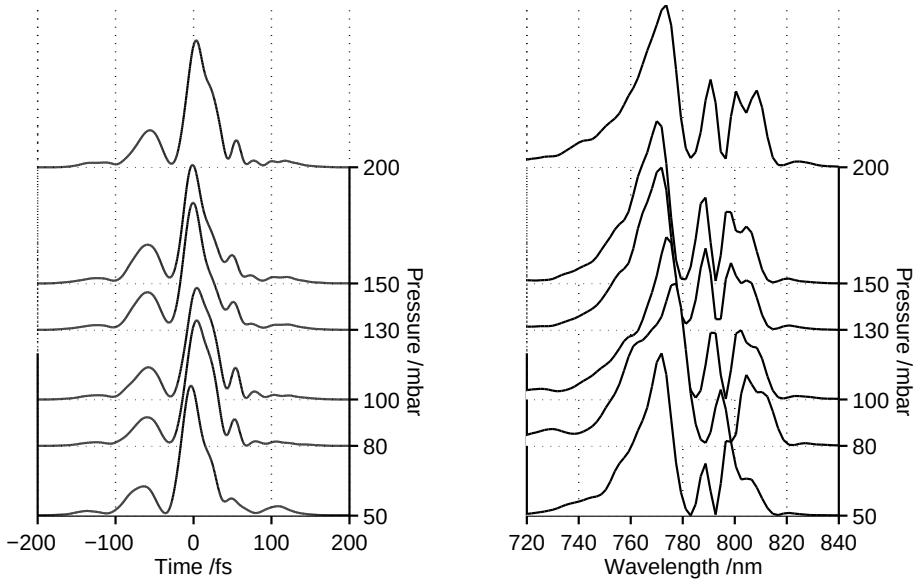

Figure 4.12: Temporal (left) and spectral (right) distributions of output pulse for a range of pressures. The input power was set at 805 mW and the pressure varied from 50 mbar to 200 mbar. The pulses have had 440 fs^2 of second order dispersion removed to account for propagation to and through the FROG.

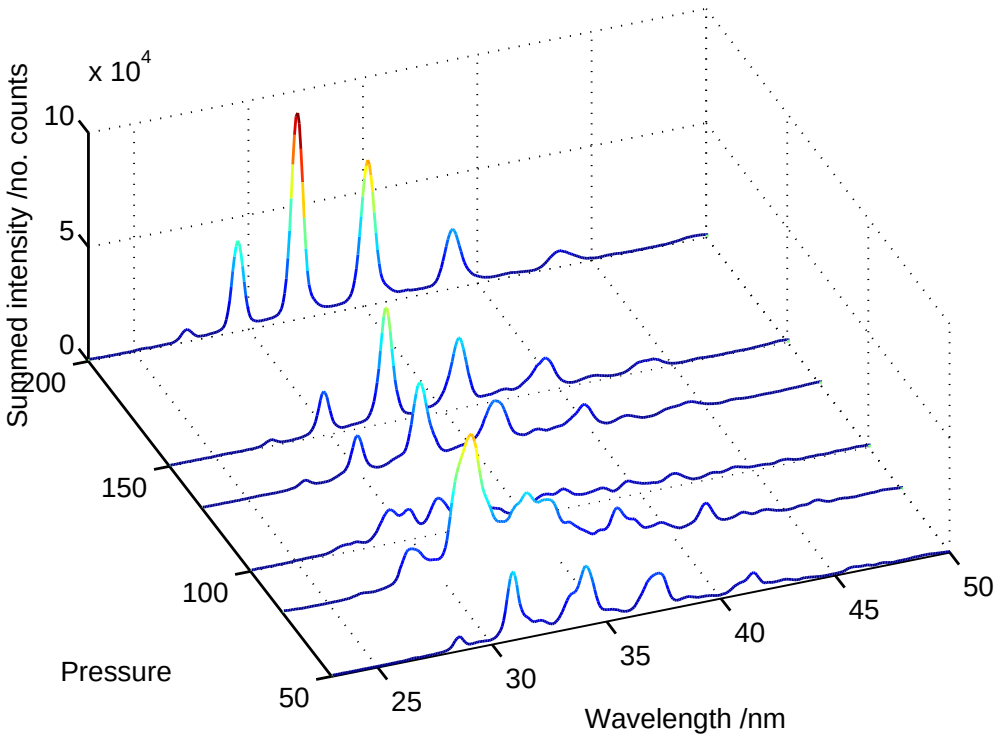

Figure 4.13: Plot of the summed XUV spectra shown in Figure 4.9. The wavelength is shown on the x-axis, the pressure on the z-axis and summed intensity on the y-axis.

the individual harmonics and raises the peak intensity. By 200 mbar the harmonic spectrum is well defined, with a peak intensity 4 times greater than at 50 mbar.

The results shown here are not fully understood and the following is the current explanation I am working with, further work in the future will be required on this subject. To explain these results one must return to the XUV transmission and generation within the capillary. As the maximum pressure within the capillary increases, 50, 80, 100 mbar etc, the length over which XUV can be generated and transmitted decreases. The transmission plots for all six pressures shown above are given in Figure 4.14 while Figure 4.15 shows a plot of the same data for 27 nm radiation only. The spike at 50 mm is a result of the rapid drop in pressure at the second gas inlet reducing the amount of HHG that can occur. It has been shown that the generation and transmission region for 25 nm extended twice the distance into the capillary than for 30 nm radiation. If one considers a single wavelength, 27 nm for example, the same is achieved by a change in pressure. The transmission scales linearly with pressure, therefore 27 nm radiation can be generated and transmitted from 20 mm into the capillary at 50 mbar but only from 45 mm at 200 mbar. This effect coupled with the pressure profile within the capillary results in a narrowing of the generation and transmission region within the capillary as the gas pressure is increased and is shown clearly in Figure 4.15.

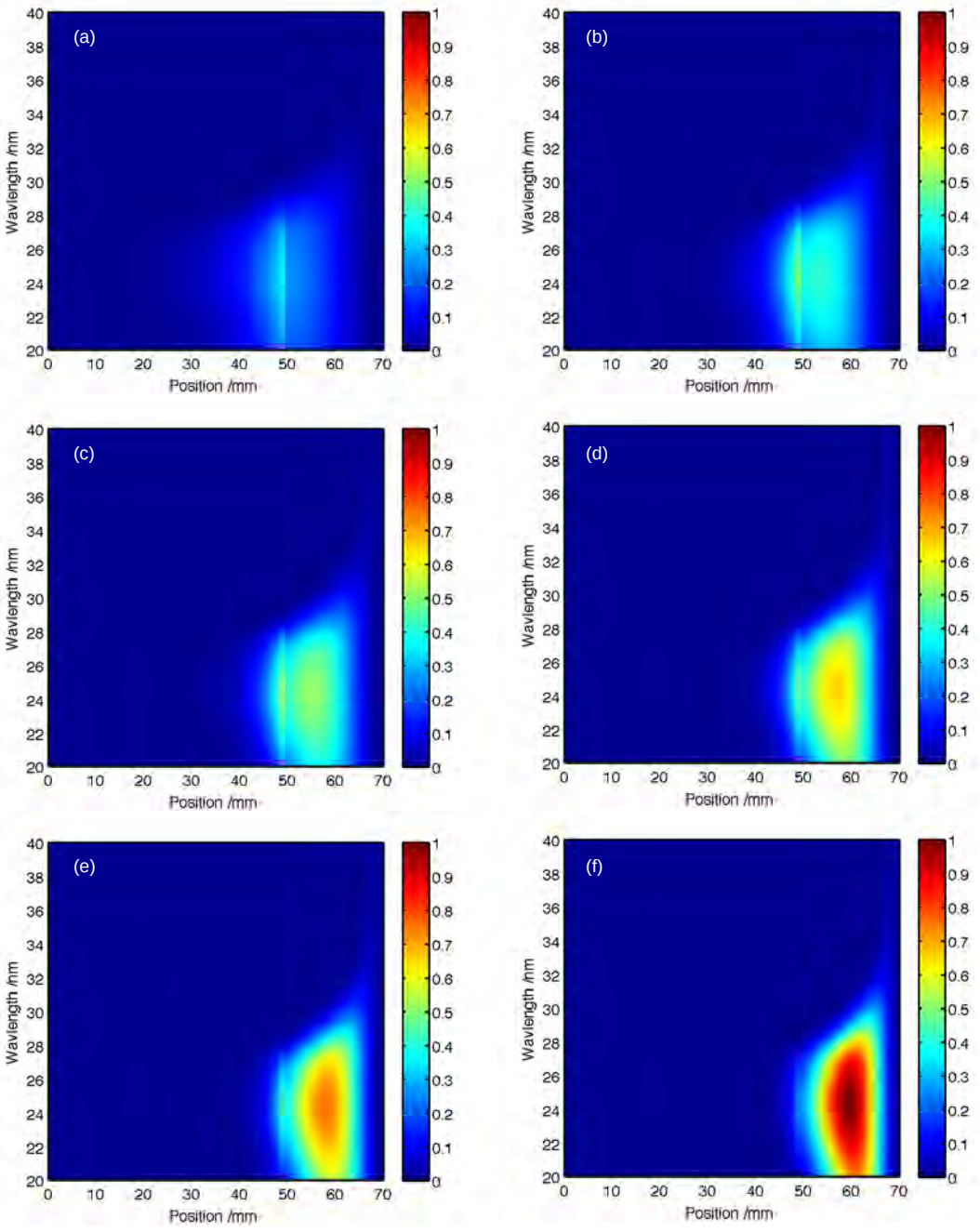

Figure 4.14: XUV generation and transmission for every position within the 7 cm capillary for a range of pressures. The maximum pressure within the capillary is calculated for 50, 80, 100, 130 150 and 200 mbar shown as (a - f) respectively. The pressure profile has been included, taking into account the fact that the XUV intensity scales with the square of the pressure. The x-axis shows the XUV generation position within the capillary, the y-axis shows the wavelength ranged from 20 - 40 nm and the normalised log transmission is shown by the colour bar. The width and maximum of the generation region decreases as the pressure is increased. Note: the discontinuity of the feature at 50 mm is due to the step size used.

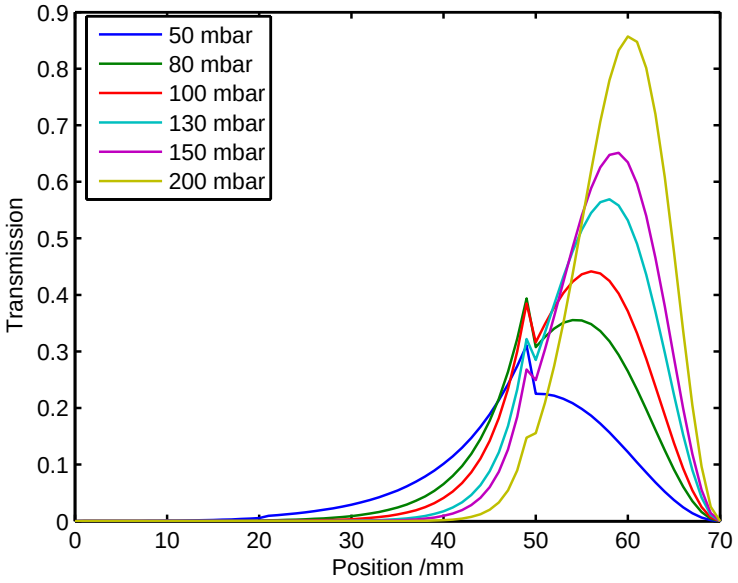

Figure 4.15: 27 nm generation and transmission within the 7 cm capillary for a range of pressures. The maximum pressure within the capillary is shown in the legend and varies from 50 mbar to 200 mbar. The transmission (y-axis) for every position within the capillary (x-axis) is a measure of the relative flux expected from each point. Note: the discontinuity of the feature at 50 mm is due to the step size used.

Although the temporal shape of the pulse at the output does not change with pressure it is changing whilst propagating through the capillary. As the pulse propagates it will undergo spectral broadening, blue-shifting and temporal reshaping. In other words the pulse shape at 4 cm through the capillary will not be the same as it is at 5 or 6 cm. The high-harmonic spectrum generated depends on the pulse shape and spectrum and so the harmonic spectrum generated at 4, 5 or 6 cm along the capillary will not be the same. When the pressure within the capillary is set to 50 mbar, the total XUV spectrum that is generated and transmitted is based on a region within the capillary that is close to twice the length than that at 200 mbar. As a result the spectrum measured and shown in Figure 4.9 is a sum of a larger number of different spectra generated by each different pulse shape. At 200 mbar the generation region is smaller, thus the total summed spectrum will consist of spectra from a similar pulse shape, producing a well defined spectrum. The increase in pressure would also explain the increase in peak intensity, as the region of generation scales linearly with pressure but the flux scales quadratically.

Another possible contributor to the complex harmonic spectral shape is intra-pulse interference. The MM-NLSE model predicts quite complicated temporal distributions within the capillary seen in Figure 4.7. The XUV field generated by different parts of the same pulse can interfere and generate complex spectral shapes, the simplest example being a double pulse producing a spectrum containing interference fringes with spacings defined by the pulse separation. In this case the pulse shape would have to change from a complicated structure at low pressure to a more simple structure at higher pressure which is

not observed as the pulse has been shown to propagate similarly at different pressures. However, HHG is a highly nonlinear process and thus requires a high intensity. If the pulse structure changes such that only a single peak can produce HHG the resulting spectrum would be ordered. An example of this can be seen in Figure 4.7 where the pulse half way down the capillary has two large peaks while at the capillary exit only a single high peak exists. At lower pressures pulses further within the capillary contribute to the final spectrum, thus making it more complex. It is likely that a combination of the narrowing generation region and intra pulse interference are the cause of the spectral changes.

Intra pulse interference and absorption can be used to explain the change in the spectral shape but not dip in harmonic flux observed between 80 - 130 mbar. A reduction in intensity means that something other than simple absorption and pressure scaling is the cause for the flux variation.

Whilst the pressure variation does not affect the pump pulse propagation the combination of absorption and the temporal reshaping that occurs as the pulse propagates will lead to a change in the phase-matching at different pressures. Variation in pressure does not affect the phase mismatch due to the waveguide which remains constant. The contribution from the neutral gas is negligible compared to other contributions and so is not considered. The contribution from the atomic phase and the free electrons will be affected differently. The free electron phase mismatch scales linearly with the number of free electrons, this is dependent on both the pressure and the intensity of the pulse. The atomic phase scales linearly with the pulse intensity but is not dependent on pressure. The intensity of the generating pulse changes as it propagates and thus so will the atomic and free electron phase mismatch contributions. In the same way that a different harmonic spectrum is generated at each point within the capillary, each section of the capillary will have a unique phase mismatch, given by the contributions of the waveguide, free electrons and atomic phase. As the generation and transmission region changes with pressure so too will the total phase mismatch and therefore the final flux of each harmonic, thus producing a more complex harmonic flux dependence on pressure than would exist in a gas cell or jet.

4.3 Conclusion and future work

In a continuation of the previous chapter's work the experimental pump pulse propagation is compared to the theory predicted by the nonlinear propagation model being developed by Dr Peter Horak. In this chapter the testing is extended from the spectral regime to the temporal regime where not only the intensity distribution but also the phase distribution of the pulse was compared upon exiting the capillary. The power of the input pulse and the argon pressure within the capillary were used as variables.

Comparison of the pump pulse temporal output as a function of input power showed major differences between the experiment and theory. This lead to two discoveries. The large degree of spectral broadening that the pulse has undergone means second order dispersion of the pulse after exiting the capillary was important and had to be compensated for in the results taken. The complex pulse data was adjusted to remove the 440 fs^2 of dispersion added to each pulse. Additionally the importance of the input pulse spatial mode was realised. In an analogy to the need for a real temporal pulse input seen in the last chapter, it was realised that using a perfect Gaussian as the input mode is not accurate and leads to different pulse outputs. As a result a wavefront sensor was produced and the real measured beam wavefront was used as the input. These two changes produced excellent results, that not only showed good agreement but also showed pulse self-compression from 53 fs to 28 fs in the 7cm capillary. An additional 150 fs^2 of GDD was removed from the spectral phase of the 805 mW, 150 mbar pulse theoretically, reducing its length to 15 fs. Propagation within a short 7 cm hollow core capillary under the correct conditions has been proven to produce a pulse compression factor of 4.5, and can act as an XUV source, removing the need for further expensive optics or unintentionally increasing the pulse length whilst directing the pulse to the target chamber.

Following the discovery of pulse self-compression within the capillary, the use of it as an XUV source was investigated. In the second section of the chapter the dependence of the harmonic spectrum on gas pressure within the capillary was explored. This decision was made due to the strong dependence of the pump pulse to input power variation, but that at higher powers (805 mW) the dependence on pressure was small. phase-matching within a capillary depends on the waveguide, pulse intensity, neutral gas pressure and free electron density. Adjusting the gas pressure changes the not only the phase-matching but the absorption length of the XUV. The XUV spectrum generated for 805 mW input power and a variety of gas pressures was measured. The data showed a distinct and unexpected difference as the pressure was increased. The XUV spectrum at 50 mbar was quite complicated, with the individual harmonics broadening out, and extra peaks appearing between them, but as the pressure was increased it became more orderly until at 170 mbar a well defined harmonic spectrum was produced. In addition to this the harmonic peak intensity was observed to reduce between 80 -130 mbar before climbing again, a result that cannot be explained without a change in the phase-matching. It was shown that a combination of absorption and gas pressure profile lead to a reduction in the length of capillary HHG could occur and be transmitted in as the gas pressure was increased. The different pulse temporal and spectral distributions at each point in the capillary would generate different harmonic structures. At low pressures the generation length is large, giving rise to a large number of different harmonic structures contributing to the final, complicated output XUV spectrum. At high pressure the short generation length means the different harmonic structures are generated from similar pulses and so the total output XUV spectrum was well defined. The change in generation length

also changed the total atomic and free electron phase mismatch contributions causing the variation in harmonic intensity. To fully understand this the 1-D QM HHG model will be combined with the MM-NLSE model to produce a theoretical XUV spectrum.

This chapter has shown that to produce the most orderly harmonic spectrum with the highest harmonic intensity one must use both high gas pressure, > 150 mbar, as well as high input power, 805 mW. This combination of pressure and power leads to a high compression factor of the pump pulse itself as well as the phase-matching and absorption length required for well defined, high flux harmonics. The next chapter makes use of results from both of the previous chapters. The reliability of the MM-NLSE propagation model is used to help design a new capillary based on two observations that have been made; The argon ion fluorescence from Chapter 3 and the generation region within the capillary based on the gas pressure profile. This results in a shorter capillary with over an order of magnitude increase in the total flux.

Chapter 5

Capillary optimisation for improved flux and energy

The thesis up to this point has looked at the manufacture, operation and modelling of a 7 cm capillary. Within this work the MM-NLSE propagation model has been improved and the importance of the initial conditions were highlighted. Experimentaly, it has been shown that the capillary can be used to generate a harmonic spectrum up to the Cooper minimum using argon as a target gas whilst simultaneously acting as a high intensity pulse compressor. All of these results are excellent steps forward in the understanding of capillary based HHG and can be used to further improve performance. In the following chapter these advances in understanding are used to optimise the capillary design. The arguments for a new capillary design will be discussed in the following section, after which the process of optimisation itself will be described. The observations that have been made thus far in the report are used as an overall structure for the new capillary design and the constraints the design required. The use of the MM-NLSE propagation model to finalise the design was carried out by Patrick Anderson under my supervision. Following the final design and theoretical comparison of the two capillaries the manufacture of the capillary and the subsequent experimental results will be shown and discussed.

5.1 Why design a new capillary?

To understand why a new capillary design may be beneficial one needs to think about the aim of this research. Initial work was a series of tests to improve the MM-NLSE propagation model but that in itself was for a larger purpose, to create an efficient, high energy, high flux source for use in XUV microscopy. At the beginning of the thesis it is mentioned that to make a better microscope, to look at smaller details, one may use shorter wavelengths, hence the use of XUV. The two properties of this source that are the most important for microscopy are shorter wavelengths, i.e. a higher energy cutoff,

and high flux, to reduce the required integration time and improve the SNR. Increasing the cutoff energy has already been discussed in Section 2.1.1 where equation 2.4 shows that one can increase either the wavelength or intensity of the driving pulse to increase the cutoff energy. The cutoff scales with the square of the wavelength which has led many groups to opt for longer wavelength driving lasers [28,80] in order to reach shorter wavelengths.

The previous chapter has shown that increasing the intensity is possible with capillary pulse self-compression, the reduction in pulse length increases the pulse peak intensity within the capillary. The shorter pulse also improves the phase-matching for the higher energy harmonics as the pulse intensity peaks before the ionisation increases significantly. Improving the flux of the source is achieved by this method, as improved phase-matching leads to a greater XUV yield, however, reducing the absorption of the generated XUV is also important for flux increase.

In Chapter 3 argon ion fluorescence was compared to the integrated ionisation profile predicted by the MM-NLSE propagation model, Figure 3.18. The experimental data showed good agreement with the theory and both showed a very similar trend at the end of the capillary, i.e. low levels of ionisation. It has already been mentioned that the ionisation within the capillary is linked with the peak intensity of the pump pulse, yet the experimental data and theory both show a reduction towards the end of the capillary, the experimental data even more so. The cause of this is twofold; a reduction in pressure and hence fewer ions, and a reduction in peak intensity towards the end of the capillary due to losses.

The ionisation profile can be used to estimate where the highest energy XUV can be generated with the largest yield. The ionisation profile results from a combination of gas pressure and pulse intensity. The gas pressure profile between the gas inlets is flat, therefore an increase in the ionisation profile within this region is an indication of an increase in the pulse peak intensity. The high intensity may extend to the end of the capillary. However as the pressure decreases at the capillary exit, so too will the free electron density, shown in Figure 3.18. However, a region of high ionisation is a good indication that both the gas pressure and pulse peak intensity are high. The high peak intensity leads to the generation of higher energy harmonics, given by equation 2.4, whilst the harmonic intensity scales with the pressure squared. Thus, regions within the capillary that have high ionisation should generate larger yields of greater energy high-harmonics.

Figure 5.1 is a comparison of two plots that have previously been shown. The top figure (a) is that of the argon ion fluorescence and ionisation profile from Chapter 3. The bottom figure (b) shows the transmission from each point within the capillary taking into account the pressure profile, as was seen in Chapter 4. The length scale along the y-axis of both have been scaled together to show where the generation within the capillary

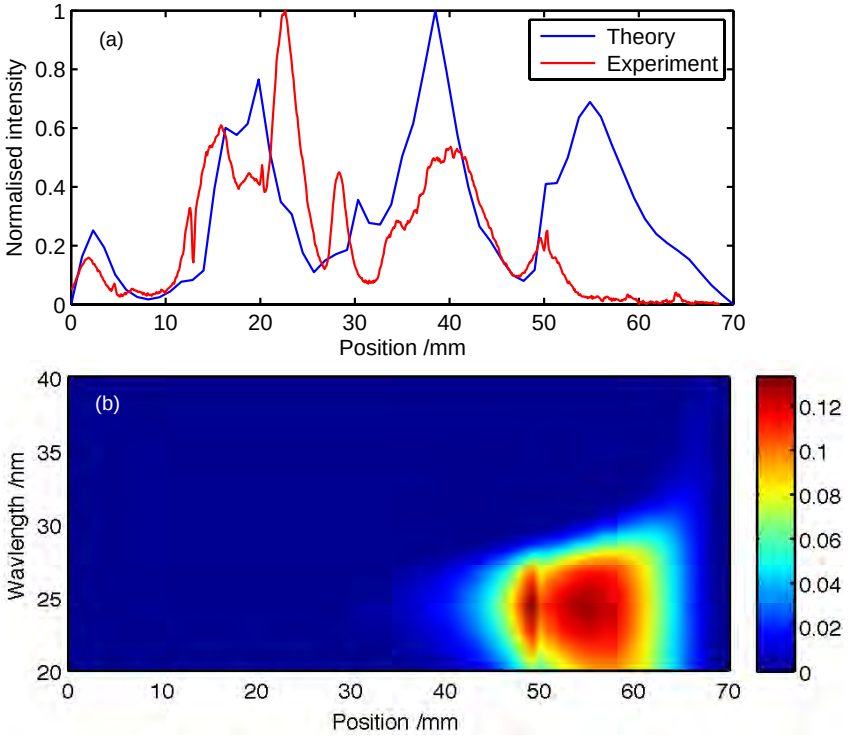

Figure 5.1: Comparison of the ionisation within the 7 cm capillary and the calculated XUV transmission from within the capillary. (a) shows the experimental and theoretical ionisation within the capillary shown previously in Figure 3.18. (b) shows the calculated transmission from each point within the capillary. The position within the capillary (x-axis) is scaled for both plots.

can be achieved and transmitted. It is clear to see from this that the first three peaks in the ionisation profile do not contribute at all to the XUV output of the capillary. The final peak shown in the theory, but not observed as strongly in the experimental data does contribute. However, from the peak ionisation at 55 mm only 9% of the 27 nm radiation will be transmitted out of the capillary. A similar trend can be seen for most wavelengths generated in this region.

The ideal solution here would be for the capillary to end at the apex of the highest ionisation peak, thus generating the highest energy harmonics with the highest transmission possible. This is not possible as the pressure will always decrease towards the exit; however it is possible to get close to this. The position of the final gas inlet must be as close to the back of the capillary as possible. This would produce a constant high pressure up to the end, followed by a rapid decrease in pressure, thus allowing generation to occur followed by the minimum amount of absorption. In addition to this, the back end of the capillary should be shortened to move it closer to the third peak in the ionisation profile. This has the highest ionisation and the shortest pulse, shown in Figure 4.7b. Without the help of the nonlinear propagation model these would be the only changes made to the design, however, using the model it is possible to arbitrarily change the capillary length and pressure profile to produce the best possible pressure

and hence ionisation profile. In this way the nonlinearity within the capillary can be used and controlled by design to produce the best capillary. The next section looks at the capillary optimisation, the final design and a comparison between the old (7 cm) and new (4.5 cm) capillaries.

5.2 Optimising the capillary design

The same capillary cross section was used for the new design and so the inner and outer diameters remain the same at 150 μm and 1.6 mm respectively. The overall constraints around which the new capillary was designed are those mentioned above. The second gas inlet must be as close to the capillary end as possible, in this case 3 mm, and the ionisation profile must peak at the rear of capillary. The MM-NLSE propagation model was run by Patrick Anderson. The following ionisation and spatio-temporal plots shown in this section use the data that he obtained from the model.

Within the model one can simply choose how long the capillary is and what the pressure profile is. The first step in the optimisation process was to look at where the capillary should be stopped, followed by improving the ionisation profile. The nonlinear mode mixing that occurs within the capillary defines how the ionisation profile changes. It was discovered that although the heights and general shapes within ionisation peaks can be changed by the pressure profile, their overall position is the same for a given input pulse and capillary core diameter. It has already been shown that high ionisation results in coupling into higher order modes which is a necessary component to the pulse self-compression techniques. The attenuation constant of the capillary modes, equation 2.70, was shown to scale with u_{nm}^2, therefore coupling to higher order modes makes the capillary more lossy. It was also shown in Chapter 3 that extra loss was observed in the real experiment not included in the model. As a result the capillary design should be shorter to maximise the final intensity of the pump pulse. The ionisation peak at 4 cm was chosen as the target for further development, as it shows the highest ionisation and thus the highest intensity for a given pressure.

The position of the second gas inlet is fixed by manufacturing limitations; however the same is not true of the first gas inlet. Adjustment of the first gas inlet defines how soon within the capillary the pressure increase occurs. At the gas inlet there is a sharp pressure decrease of 20% followed by a linear decrease to the capillary end. The high intensity of the pump pulse causes ionisation of the gas and therefore nonlinear mode mixing within the capillary, in addition to the spectral broadening and subsequent compression of the pulse. If the gas inlet is placed close to the entrance the nonlinear propagation will begin more quickly. The effect of the first gas inlet position on the ionisation profile is shown in Figure 5.2. A series of pressure profiles are shown on the left, where the position of the first gas inlet is shifted towards the front of the capillary, starting at 20 mm

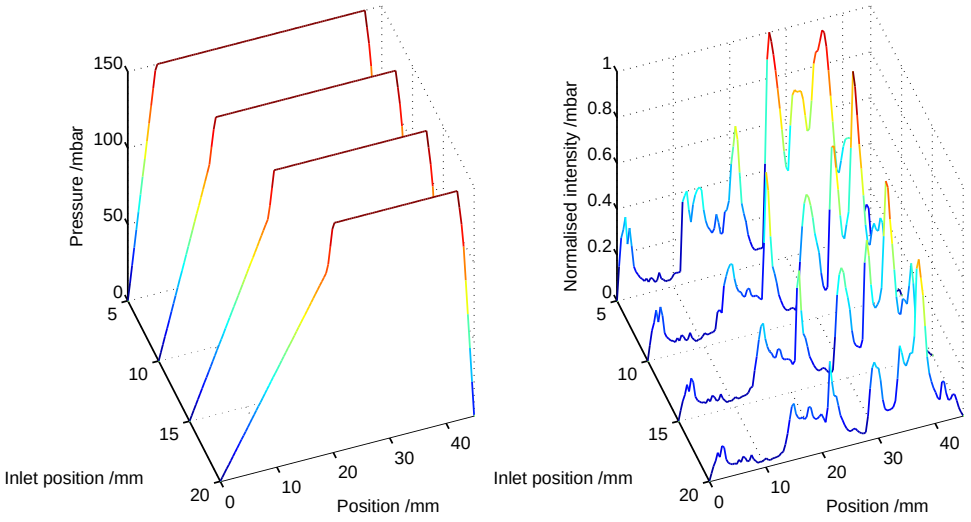

Figure 5.2: Comparison of different first gas inlet positions (left) and the associated theoretical ionisation (right) within the 4.5 cm capillary for each one. The plots are shown for a gas pressure of 150 mbar and inlet positions 20 mm, 15 mm, 10 mm and 5 mm from the front of the capillary.

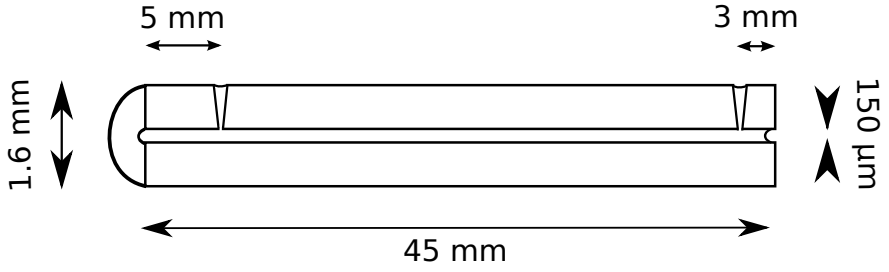

Figure 5.3: Schematic of 4.5 cm capillary. The capillary is 1.6 mm in diameter with an inner bore diameter of 150 μm. Gas inlets passing through the capillary wall are positioned 5 and 3 mm from the front and rear respectively.

and ending at 5 mm. The associated ionisation profile for each is shown on the right. The x-axis for both shows the position along the capillary, while the y-axis shows the normalised pressure (left) and ionisation (right) for each. The z-axis shows the distance of the gas inlet from the front of the capillary. It is clear to see that as the gas inlet is brought closer to the capillary entrance, the height of the final ionisation peak increases. This is a result of the extra nonlinear propagation through the gas up to that point. Longer propagation lengths lead to greater spectral broadening, mode mixing and pulse self-compression. Placing the gas inlet at 3 mm instead of 5 mm made no significant difference to the ionisation profile and having it at 5 mm made it easier to tell which was the front end of the capillary.

The final design of the capillary is shown in Figure 5.3. It is 4.5 cm in length with gas inlets at 5 and 3 mm from the front and back of the capillary respectively. A comparison of the old (7 cm) and new (4.5 cm) capillaries is shown in Figure 5.4. The 7 cm capillary

data is shown on the left, whilst the 4.5 cm data is shown on the right. The comparison is broken into three sections and shows the pressure profile (top), the ionisation profile (middle) and the transmission from within the capillary (bottom). All of the data is scaled together.

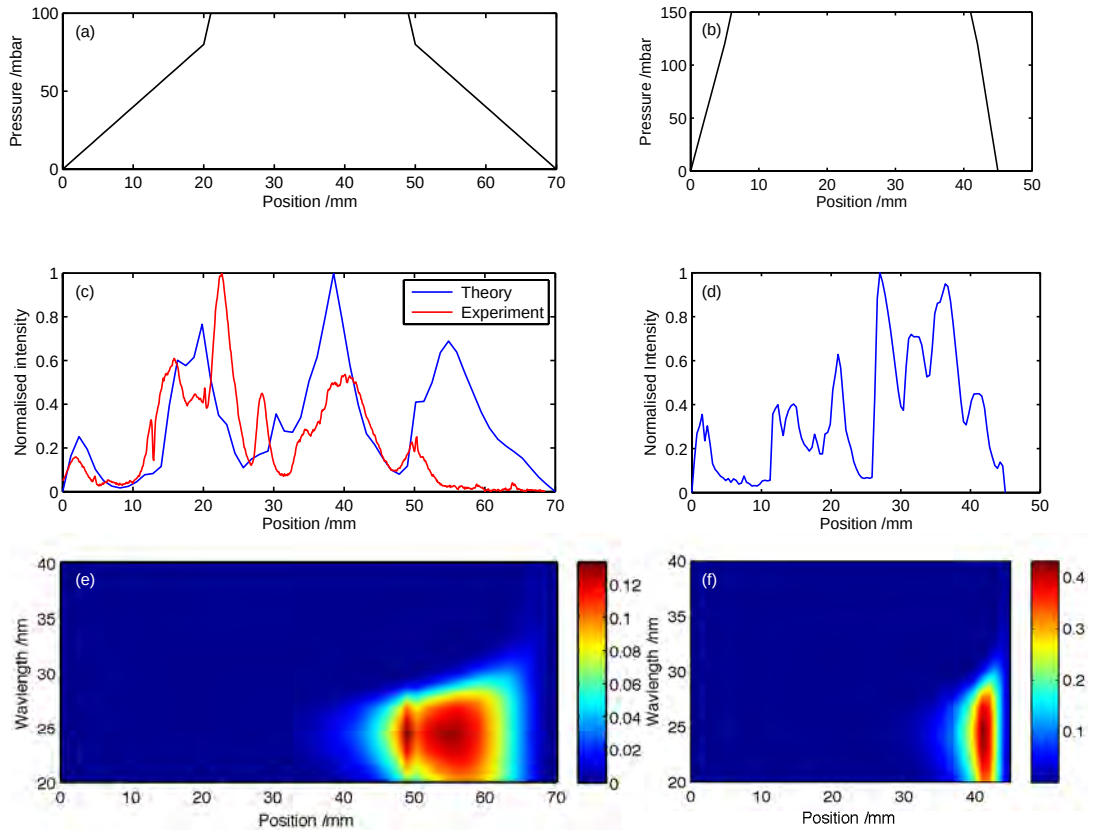

Figure 5.4: Comparison of the pressure profile (top), ionisation profile (middle) and transmission (bottom) between the 7 cm and 4.5 cm capillaries. The 7 cm capillary data is shown on the left whilst the 4.5 cm capillary data is on the right. The capillary position (x-axis) of all the plots is scaled together. The transmission data shows the relative transmission of the capillaries. As expected the 4.5 cm capillary shows a higher transmission.

The lower two comparisons show where the transmission region and ionisation peaks overlap. The new capillary design has higher ionisation at the capillary exit than the old and the overlap between that and the transmission region is greater. The generation and transmission region comparisons shows that simply by pushing the second gas inlet towards the capillary exit the maximum transmission has more than doubled. The increased ionisation peak also indicates that the XUV that is generated will be of higher energy and flux.

The temporal compression in the new capillary is also greater than that in the old capillary, this is shown in Figure 5.5. As before the old and and new capillary data is shown left and right respectively. The plots show the spatio-temporal distribution of the pulse at the exit of the capillary (top) and a line plot of the on axis distribution

(bottom). In the short capillary case the pulse compression has resulted in two sub 5 fs intensity spikes separated by 20 fs. These two features are significantly more intense than the surrounding pulse train of the original, broad pulse. The model thus shows a factor of 10 compression in just 4.5 cm of propagation.

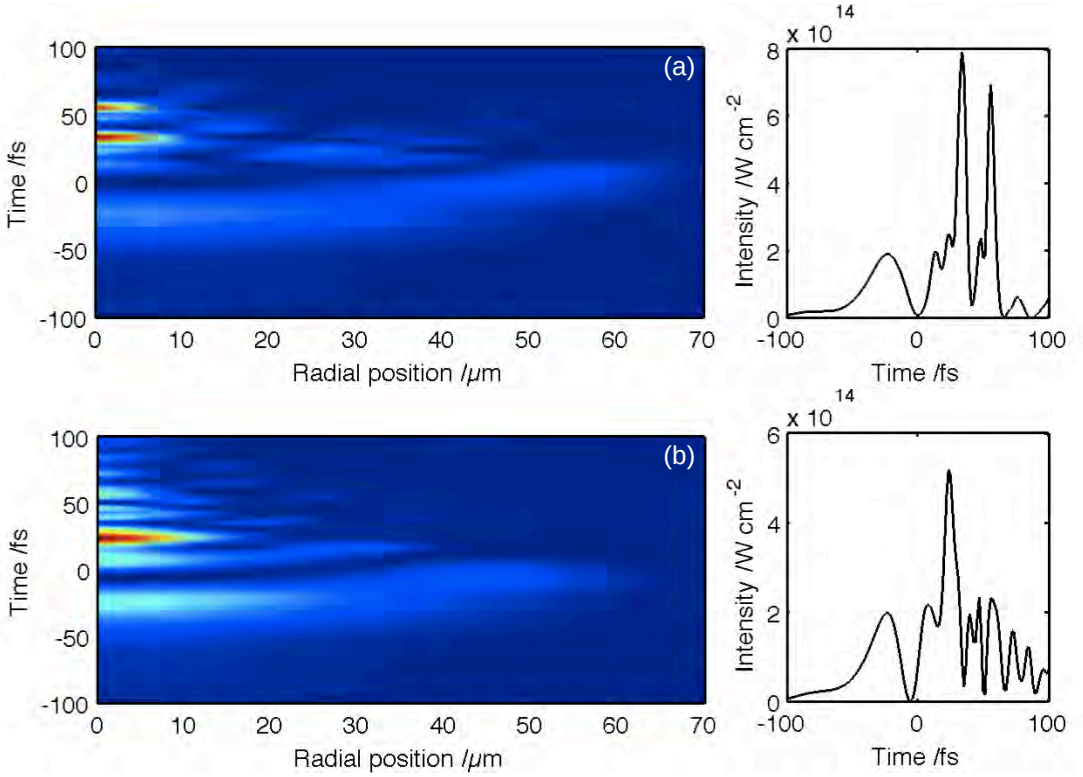

Figure 5.5: Theoretically modelled spatio-temporal distribution of pump pulse at the exit of the 4.5 cm (a) and 7 cm (b) capillaries. The spatio-temporal distribution (left) shows the temporal distribution (y-axis) of the pulse as a function of radial distance from the central axis (x-axis). A plot of the on-axis temporal distribution is shown on the left. Significant pulse splitting and compression is observed as the pulse propagates along the capillaries.

The comparisons give a strong indication that the new capillary can outperform the old in both energy and flux. The next section will describe briefly the manufacture of the new capillary and its transmission.

5.3 Manufacture of 4.5 cm capillary

The manufacture of the new capillary was carried using the same methods as the 7 cm capillary. The ends were cleaved and polished to create a capillary 4.5 cm in length. Images of the front and rear ends of the capillary are shown in Figure 5.6. After cleaning the capillary the gas inlets were drilled, again using the same methods as before, described in Section 3.1.2. Microscope images of the gas inlets are shown in Figure 5.7. Both the first (left) and second (right) inlets show a cleanly drilled hole at the top (a,

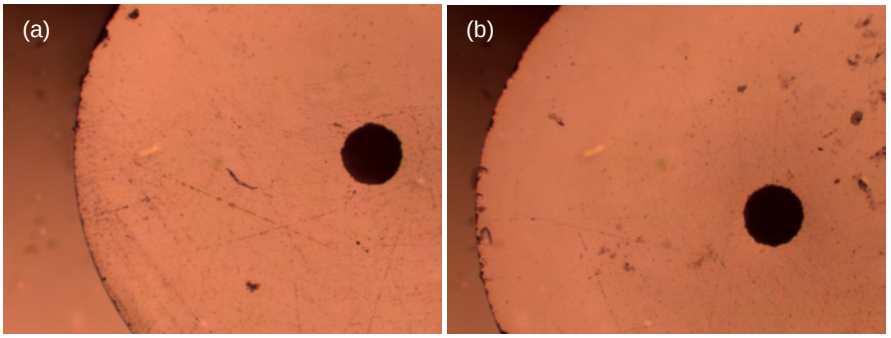

Figure 5.6: Microscope images of the final capillary end faces. Both have been polished to a to a surface roughness of < 300 nm.

b) of the capillary and when focused on core itself (c, d) show that the hole is central to the core. The side images (e, f) show that the first hole appears to hit the core cleanly whilst the second hole has surrounding damage to the core. After cleaning the capillary in acetone and de-ionised water there was still a small amount of debris visible within the capillary. Due to time constraints the capillary was washed several more times before moving onto coupling, with debris inside. The debris does not stop gas flow through the capillary and the combination of gas flow and laser has removed such problems before. The capillary was mounted using x-rings, not UV curing adhesive due to the proximity of the gas inlets to the capillary ends. The adhesive is difficult to contain in a small volume and the risk of it blocking the capillary ends was deemed too high. The x-rings are small rubber rings with an X shaped cross-section. This extra point pushing against the capillary and the glass T-piece reduces the background pressure by more than an order of magnitude over a standard o-ring. An image of the mounted capillary is shown in Figure 5.8. The T-piece holding the 4.5 cm capillary is slightly shorter than that holding the 7 cm capillary, however the front face of both capillaries is placed at the same distance from their T-piece end. In this way the two capillaries can be quickly switched over without the need for extensive realignment of the beamline. The process of switching capillaries and realigning can take less than 5 minutes, including pumping up and down as a gate valve was inserted to separate the front end of the vacuum system from the filters and main chamber.

Although care was taken in the manufacture of this capillary the transmission is not as great as that in the 7 cm capillary. The low power, zero pressure transmission is only 63%. As the power is increased this does not reduce, however, there is a greater interaction between the laser and gas inlets. The output mode is a combination of EH_{11} and EH_{12} comprising a large central mode surrounded by a narrower ring. At high power, supercontinuum generation from within the glass is also observed at the output in the form of two separate coloured ring patterns overlaying the mode structure. Adjustment of the capillary alignment showed that these are caused by the laser passing through glass at the gas inlets, implying that damage of the material around them extends into the inner bore. The light scattered from these gas inlets is more intense

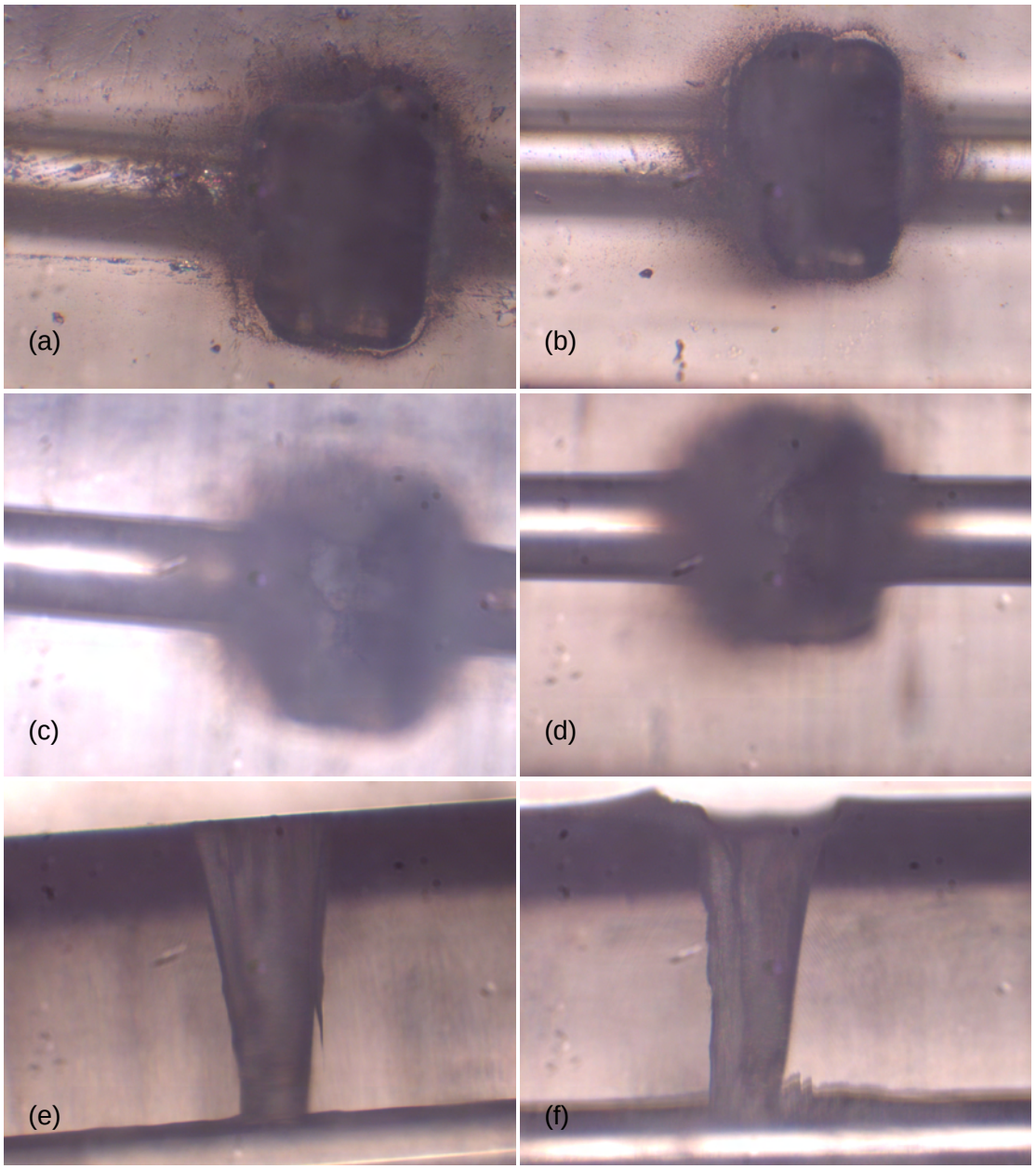

Figure 5.7: Microscope images of gas inlet holes laser drilled through capillary wall. The top images show the outer surface of the first (left) and second (right) gas inlets. The focus is translated through to the core for the middle image. The hole passing through to the open core can be seen in the centre of each image. The bottom image shows a side view of each gas inlet.

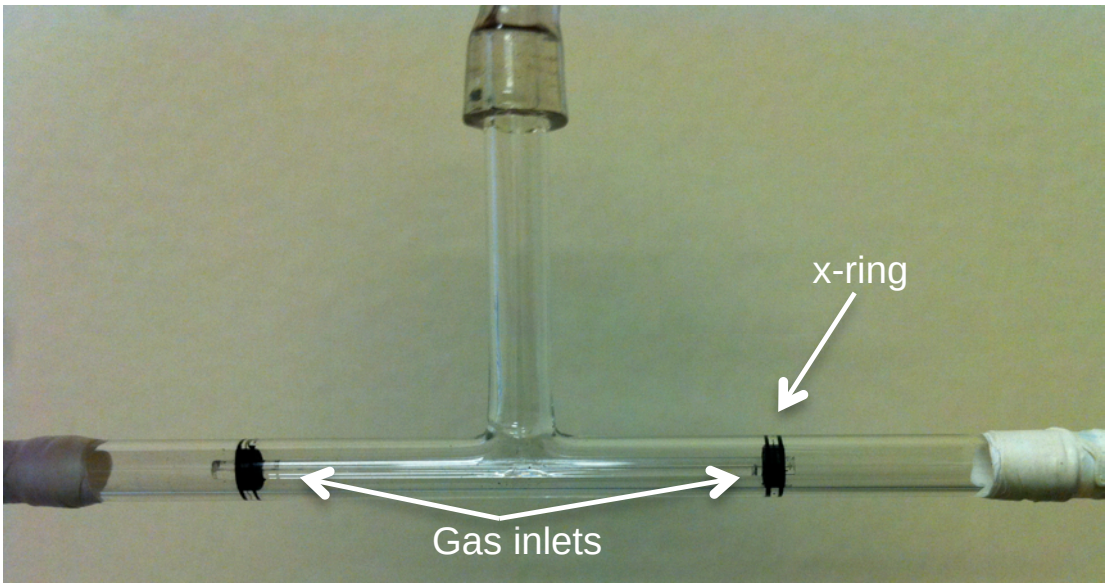

Figure 5.8: Image of the completed 4.5 cm capillary mounted within a glass T-piece. The capillary is held in place by two x-rings which also ensure the gas is introduced into the capillary by two gas inlets.

than the 7 cm capillary and is assumed to be the cause for the reduced transmission. A new capillary was not made but should be in future to remove this problem and further improve the capillary.

5.4 Experimental set up

The experimental set up for this comparison experiment is similar to that used in the previous chapter to measure the XUV spectrum, the difference here being that a flux measurement is being taken. With the spectrometer configuration, shown in Figure 4.8, it is difficult to accurately work back to the total flux of the source, as there are many more mechanisms of loss. In order to not only compare but also to calculate the absolute XUV yield of this new source an Andor XUV CCD camera was used. The only change to the basic layout is that the Andor camera is placed in the beam path on a 2-axis translation stage so that it could be moved whilst the system was under vacuum. Using this it was possible to move the Andor camera out of the beam path so that the XUV spectrometer could be used, as is shown in Figure 5.9.

Images of the XUV beam generated by each capillary were taken. The input power when using the 7 cm capillary was 850 mW, during the course of the experiment the power dropped slightly so that after the 4.5 cm capillary was installed the power had reduced to 810 mW. This difference was smaller than the step change in power possible by adjusting the pump to the amplifier, so could not be changed. Images of the XUV beam from each capillary were taken at pressures of 0, 50, 100, 150 and 200 mbar. The 0 mbar cases were used to remove the background from the images and ensure there was

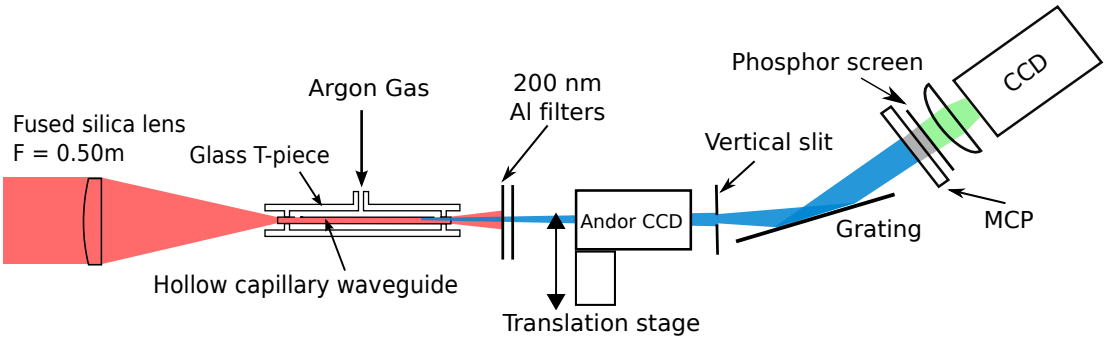

Figure 5.9: Schematic of experimental setup used to measure the XUV flux and spectrum of the 4.5 cm capillary. The basic layout here is the same as that used in Chapter 4 with the addition of an extra vacuum chamber. The chamber (not shown in schematic) contains an Andor XUV CCD camera mounted on a translation stage. This can be placed in the beamline for XUV flux measurements or moved sideways to allow the beam into the grazing incidence spectrometer. The inclusion of the new chamber increases the distance between the capillary and spectrometer by approximately 50 cm.

no pump laser breakthrough. In addition to this the XUV spectrum was measured for the new capillary with an input power of 880 mW, at the same pressures.

The experimental data for the comparison of the flux was taken at the same time to remove the possibility of varying laser conditions or changes in the transmission. The spectral measurements that are also discussed in this section were not taken on the same day. Due to time constraints on the day the spectra for the 4.5 cm capillary were taken the following day, resulting in a slight power difference. In addition, prior to the work carried out in this chapter the beamline was moved and rebuilt to accommodate a large chamber between the capillary and XUV spectrometer for other projects. As a result the XUV spectrometer was moved further from the XUV source and a useable harmonic spectrum from the 7 cm capillary could not be obtained. The spectrum of previous experiments was between 25 and 35 nm. The Cooper minimum of argon means that the high energy cutoff remains at 25 nm, however the longer wavelength cutoff may move to higher energies as the larger peak intensity shifts the entire spectrum to higher energies. The harmonic spectrum should exist between 25 - 35 nm.

5.5 Comparison of 4.5 and 7 cm capillaries

In the data that was collected from the two capillaries there is a difference between the XUV beams that complicates the simple comparison of which capillary has a greater flux, this is the height of the beams. The 7 cm capillary beam is 1-2 mm lower than the 4.5 cm beam when they pass through the aluminium filter mount. The mount is designed to slide left/right so that different filters can be put in place but the height cannot be changed. This meant that the 7 cm capillary beam was clipped slightly by the edge of

the 5 mm hole through which the beams pass. This clipping is present on all of the following images that were taken of the two beams but is stronger in the 7 cm case. The capillary alignment was changed in an attempt to bring the beam up but the coupling was too critical and any adjustments to that end stopped the HHG process altogether. As such one must remember that the flux calculations for the 7 cm capillary will be slightly lower than they are in actuality; that being the case, the difference between the two data sets is so large that this does not account for the majority of the difference. In the worst case scenario the beam has been clipped by half which, as will be shown, is small in comparison to the overall flux difference.

The background subtracted image data from the 7 cm capillary is shown in Figure 5.10. The full CCD images (left) are shown as linear plots and are scaled together. A vertical line section through the most intense region of each image is shown on the left. The pressure is indicated in the top left corner of each image ranging from 50 to 200 mbar. The clipping of the filter mount is most obvious in the 50 mbar case (a-b) where the line section through shows at most half of the beam has been clipped. The clipping is much less extensive in the other cases with the 200 mbar case (g-h) showing no clipping. The FWHM of the beam in all four cases is $\sim$ 150 pixels. The peak number count within this data set is 705, shown in (b).

Figure 5.11 shows the background subtracted data for the 4.5 cm capillary. Again the full CCD images are shown on the left and the line plots through the most intense region are shown on the right. The difference in beam heights is immediately obvious with the 4.5 cm capillary images showing little or no clipping. The magnitude of the signal is also very different. The plots are all scaled linearly as before however in this case the limit is set at 19000 counts instead of 700. The 4.5 cm capillary output beam is slightly larger than the 7 cm output beam, with a FWHM of $\sim$ 200 pixels. It is not unreasonable to expect different sized beams from the two capillaries given how the beams are produced. The mode structure within the capillary will differ between the two as will the point where the XUV beam imaged here is generated. The beam at this point is in the far field, therefore the generation region for the 4.5 cm capillary must have been smaller radially than that of the 7 cm capillary and thus diffracted more quickly.

To show the difference between the two capillaries more explicitly Figure 5.12 shows the vertical line plots through the most intense part of each image overlayed. The similar pressure cases are plotted within the same figure starting with 50 mbar (a) and ending with 200 mbar (d). From this, one can see the variation of flux of each capillary as the pressure is increased. The 7 cm capillary shows a high flux at 50 mbar ($\sim$ 700 counts) which decreases for the 100 ($\sim$500 counts) and 150 mbar($\sim$450 counts) cases before increasing again at 200 mbar ($\sim$600 counts). This trend is similar to that observed previously in Chapter 4 as the pressure was increased. The data here is a summation of all harmonics generated and so the broad intense harmonics observed in Figure 4.13 at 50 mbar will contribute more than the lower ones that exist as the pressure is increased.

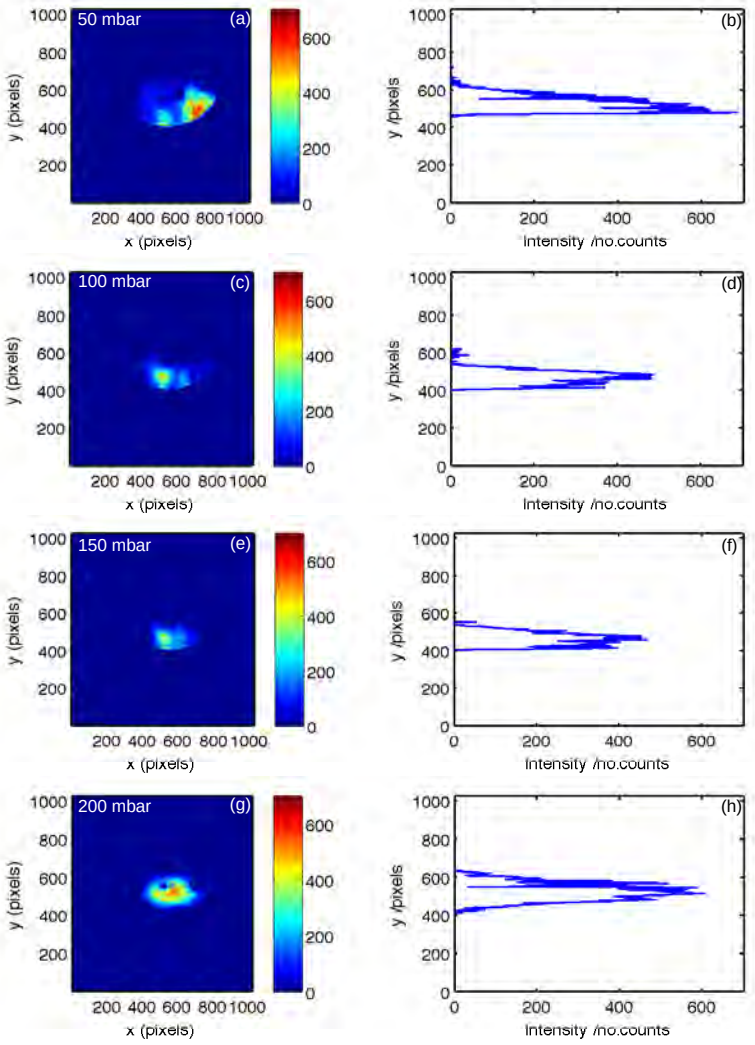

Figure 5.10: Images (left) and line plots (right) of the XUV beam generated by the 7 cm capillary at four different gas pressures. The images were taken using a the setup shown in Figure 5.9. The pressure within the capillaries was set at 50 mbar (a-b), 100 mbar (c-d), 150 mbar (e-f) and 200 mbar (g-h). The colour-map indicates the no. counts of each pixel and is shown on a linear scale. The circular cutoff surrounding the lower half of some beams is created by the filter mount used to separate the XUV from the pump beam.

One would also expect to see an increase as the pressure reached towards 200 mbar when the harmonic peak intensity increased once again.

The reverse is observed in the 4.5 cm case. The peak height at 50 mbar is ∼2500 counts, this increases to ∼7000 counts at 100 mbar and again to ∼18000 counts at 150 mbar. Beyond this the flux decreases with a peak height of ∼6000 counts at 200 mbar. The difference in flux between the two capillaries is both clear and significant. The new 4.5 cm capillary has in the worst case (50 mbar) 3.5 times greater peak count and in the best case (150 mbar) a 46 times greater peak count. In short, the data shows that the new capillary does indeed outperform the old as expected.

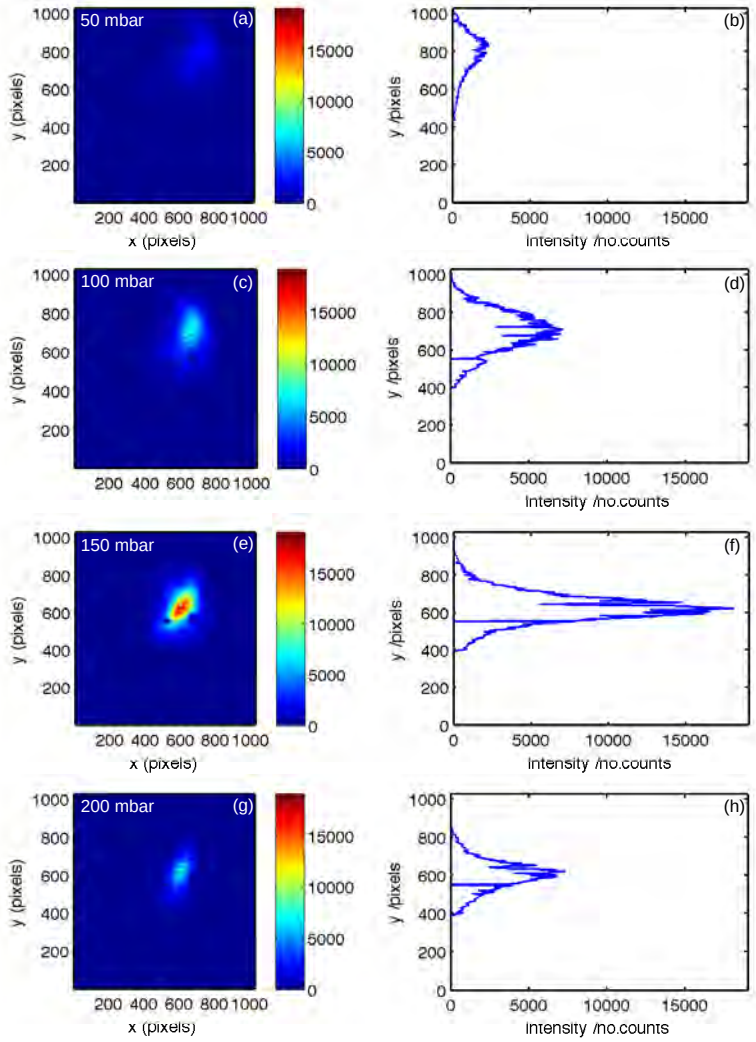

Figure 5.11: Images (left) and line plots (right) of the XUV beam generated by the 4.5 cm (right) capillary at four different gas pressures. The images were taken using the setup shown in Figure 5.9. The pressure within the capillary was set at 50 mbar (a-b), 100 mbar (c-d), 150 mbar (e-f) and 200 mbar (g-h). The colour-map indicates the no. counts of each pixel and is shown on a linear scale. The circular cutoff surrounding each beam is created by the filter mount used to separate the XUV from the pump beam.

Whilst the line plot comparisons of Figure 5.12 show an increased flux from the 4.5 cm case one cannot use those numbers as the difference in flux. Whilst the peak height at each pressure does provide an insight into the peak number of photons at a given point within the beam, it does not give us either the real number or the total number of photons within the beam i.e. the flux. To calculate this one must go back to the image data. A Matlab script was written to calculate the flux hitting the Andor camera for each image and the results are shown in Table 5.1.

Table 5.1 shows the calculated flux of each capillary for all four pressure cases, providing a more accurate comparison of the two data sets. The increase in flux between the two capillaries for each pressure ranges between one and two orders of magnitude. These are

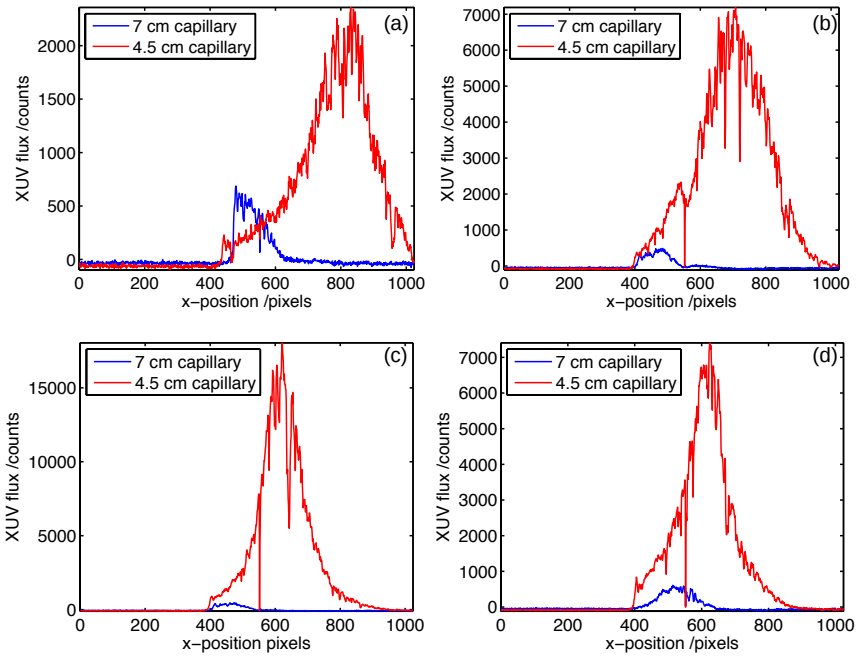

Figure 5.12: Comparison of the most intense part of the XUV beam generated by the 7 cm (blue lines) and 4.5 cm (red lines) capillaries for pressures of 50, 100, 150 and 200 mbar (a-d respectively). The data is a line plot through the most intense region of each image shown in Figures 5.10 and 5.11 with similar pressures plotted together.

Table 5.1: Calculated XUV flux for 7 and 4.5 cm capillaries

Pressure /mbar	7 cm capillary flux /ph s^{-1}	4.5cm capillary flux /ph s^{-1}
50	4.89×10^{8}	0.52×10^{10}
100	2.10×10^{8}	1.06×10^{10}
150	1.65×10^{8}	1.54×10^{10}
200	3.80×10^{8}	0.50×10^{10}

greater than the actual difference, given the clipping of the 7 cm capillary beam for the lower three pressures, but are still significant. The greatest difference is still seen at 150 mbar where the 4.5 cm capillary flux is calculated to be almost 100 times greater than that of the 7 cm capillary. Comparing the best results from each capillary however, one must return to the 50 mbar case for the 7 cm capillary and the 150 mbar case for the 4.5 cm capillary. Here the flux was calculated as being 4.89×10^{8} phs^{-1} and 1.54×10^{10} phs^{-1} respectively, giving a ratio of ~31 in favour of the new capillary. This may reduce to a ratio of 15 or so if the beam was not clipped but still shows a large increase in the overall flux. In addition to that the XUV spectrum produced by the 7 cm capillary at 50 mbar (Figure 4.9a) is not one that one would want to use for the purpose of imaging, where well defined, narrow harmonics are desired. As such this new data shows that not only has the overall flux been improved greatly, but that the pressure where it is greatest should have a cleaner spectrum. To test the truth of this the XUV spectrum of

the 4.5 cm capillary was measured and will be shown following the flux calculations.

The flux for both capillaries measured at the CCD has been calculated but this is not the total flux generated by the capillary. The filters and intermediate argon gas absorb the XUV and so to get a true value of the flux that the new capillary can generate one must take these absorptions into account. The absorption by the argon gas is the simplest to calculate and is done using the CXRO database as in Chapter 4. Between the capillary exit and the Andor camera there are two main regions of differing pressure, before and after the filters. The filters and their mount must remain light tight and thus there is not much space for gas to flow between the two sides, however, enough can pass to prevent the pressure differential from damaging them. The pressure measured between the capillary and the filters while the gas was flowing was 0.23 mbar. The pressure in the main chamber was measured at 1.2×10^{-4} mbar. The respective distances are both about 40 cm. The absorption within the chamber at the lower of the two pressures is negligible and thus transmission is given as 1. The absorption through the first section is greater and for ∼27 nm the transmission given by the CXRO database is 60%.

The transmission of the filters is not easy to calculate given the aluminium oxide layer that exists on each surface. The transmission through 200 nm of aluminium is fixed, however, each surface of the filter has a layer of aluminium oxide. The total absorption of the filter is mainly due to these layers and so the thickness is very important. The thickness of the oxide layers quoted in the literature varies greatly from 4 - 40 nm [81,82] depending on the author. This constitutes a transmission of 80% or 13% per oxide layer for 4 and 40 nm respectively. As this would lead to such a large difference in the calculated flux the literature was not used. To remove this unknown it was necessary to measure the transmission of a single filter, so that the transmission of two such filters could be known. To do this 5 filters were used. Two were placed in one slot of the filter mount and three were placed in another. The Andor camera was used to capture the image of an XUV beam using both of these filter sets, with only a few seconds between exposures one can be confident that the flux of the beam did not change. The flux of each of these cases was calculated in the same method as above. The difference between them was a factor of 0.13, which is the transmission through the single extra filter. Therefore the total transmission between the capillary exit and the Andor camera is 1%. The flux at the capillary is 2 orders of magnitude greater than that measured by the CCD. Table 5.2 shows the updated flux calculations for the two capillaries. The maximum flux is generated by the 4.5 cm capillary at 150 mbar and is 1.54×10^{12} phs^{-1}. This maximum flux is likely to be larger than this. There is a small amount of oil on the surface of the CCD which can be seen as dark spots on the all the images in Figures 5.10 and 5.11. This oil absorbs the XUV reducing the measured flux of all beams. In addition to this Figure 5.11f shows that the beam is being clipped slightly, further reducing the measured flux.

Table 5.2: Adjusted XUV flux for 7 and 4.5 cm capillaries

Pressure /mbar	7 cm capillary flux /ph s^{-1}	4.5cm capillary flux /ph s^{-1}
50	4.89×10^{10}	0.52×10^{12}
100	2.10×10^{10}	1.06×10^{12}
150	1.65×10^{10}	1.54×10^{12}
200	3.80×10^{10}	0.50×10^{12}

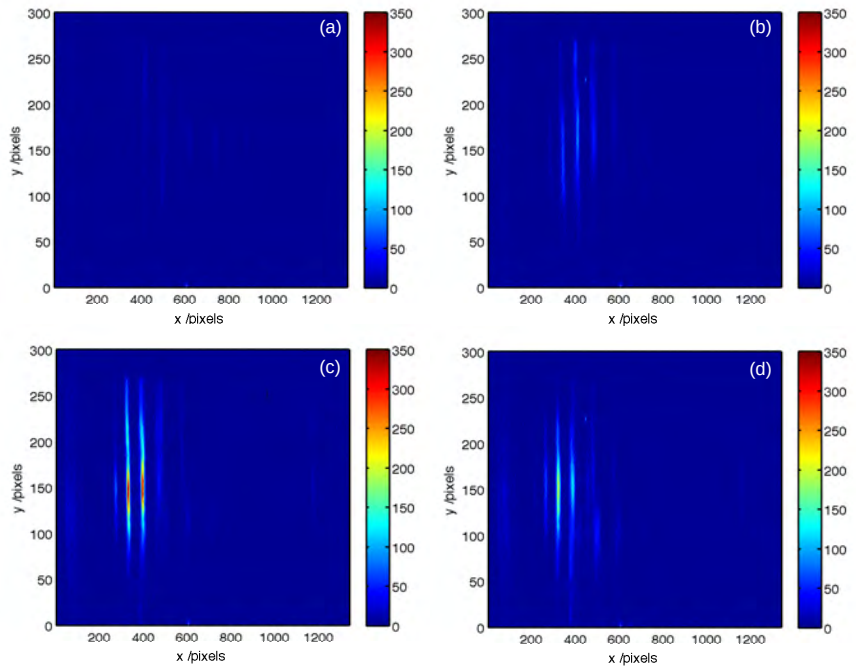

Figure 5.13: XUV spectra imaged using the setup shown in Figure 5.9 at different gas pressures within the capillary. The spectra were taken for pressures of 50, 100, 150 and 200 mbar and are shown here (a - d) respectively. The uncalibrated wavelength is shown on the x-axis and a vertical slice through the beam is shown on the y-axis. The colourmap is a linear plot of the intensity in no. counts.

In order to compare this new XUV source against the sources used by other groups one final piece of information is required, the spectrum. The flux of a high-harmonic source is usually quoted in photons per second per harmonic (ph $harm^{-1}$ s^{-1}) as generally only one harmonic is used for imaging. The XUV spectrum produced by the 4.5 cm capillary was measured for an input power of 880 mW at 50, 100, 150 and 200 mbar of argon. The results are shown in Figure 5.13.

As was mentioned in the discussion of the experimental set up, due to the greater distance between the source and the XUV spectrometer in this experimental configuration the photon losses are greater. As a result the spectrum for the 50 mbar case is not clearly visible, however, the 150 mbar case again shows the highest flux. To make the spectra easier to see Figure 5.14 shows the spectra summed over the spatial axis (y-axis) of the image. The plot shows the uncalibrated wavelength scale along the x-axis and the gas

pressure along the z-axis. The wavelength regime is similar to that of the 7 cm capillary, however, the cut-off has been increased towards the 25 nm Cooper minimum.

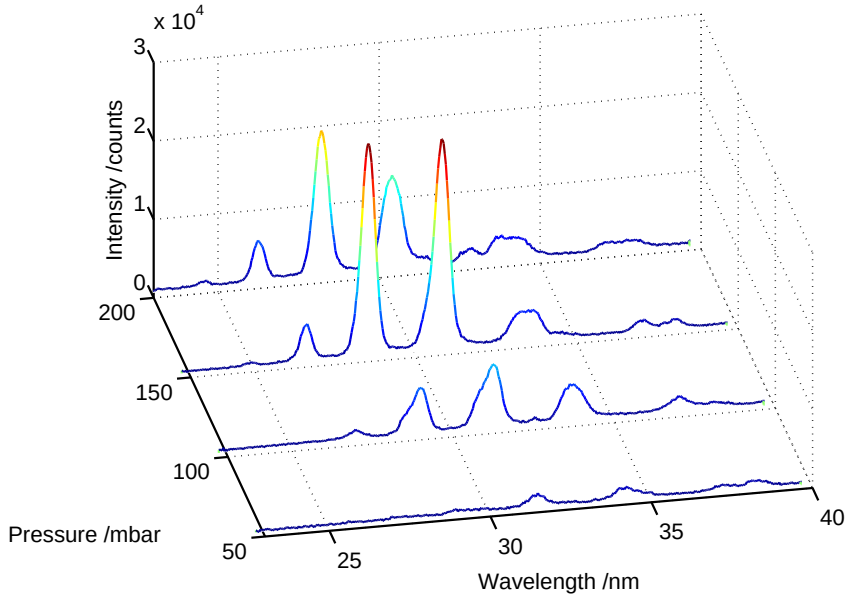

Figure 5.14: Plot of the summed XUV spectra shown in Figure 5.13. The wavelength is shown on the x-axis, the pressure on the z-axis and summed intensity on the y-axis.

The 50 mbar spectrum can be seen in Figure 5.14, as can the blue shift of the overall spectrum as the pressure is increased. This effect was also observed in the 7 cm capillary spectrum, see Figure 4.13. The harmonic peak intensity increases as the pressure is increased up to 150 mbar, after which it decreases again. This trend follows that observed in the flux data taken using the Andor camera. At 150 mbar two peaks dominate over all others, these two peaks contain $\sim 75\%$ of the detected signal. From this one can say that one of these harmonics will contribute to 37.5% of the total flux, giving a final flux of 5.78×10^{11} ph $harm^{-1}$ s^{-1} or 5.3×10^{12} ph $harm^{-1}$ s^{-1} cm^{-2}. This is a conservative estimate given the loss of photons due to the oil on the CCD. This is the highest flux HHG source in the world in this wavelength range.

5.6 Conclusions and future work

Based on observations from the previous two experimental chapters the work described in this chapter detailed the successful improvement of the capillary based HHG source. It was shown from previous work that the area within the 7 cm capillary where the highest harmonics are generated and the volume where the generated harmonics are transmitted out of the capillary did not overlap entirely. This was observed using the 7 cm capillary's ionisation profile both measured and calculated in Chapter 3, and the calculated transmission from within the capillary from Chapter 4. Using this knowledge

a basic redesign for the capillary was outlined. The highest ionisation peak within the capillary occurs at 4 cm down the capillary, whose position is fixed by the input spatial mode and the core diameter of the capillary. The capillary length was reduced to put this peak at the exit of the capillary. In addition to this the position of both gas inlets was moved. The rear gas inlet was moved as far back as possible to 3 mm from the exit, whilst the position of the first gas inlet was allowed to vary in the model to maximise the final ionisation peak structure. The total amount of nonlinear propagation within the capillary is controlled by the position of the first gas inlet. It was shown that the closer this is placed to the front of the capillary the greater the nonlinearity, spectral broadening and subsequent pulse compression. This led to the placement of the first gas inlet 5 mm from the capillary entrance. The final design of the new capillary therefore consisted of a 4.5 cm long capillary with a 150 μm inner bore and a 1.6 mm outer diameter. Gas inlets were laser drilled into the capillary 5 and 3 mm from the entrance and exit of the capillary respectively. The newly manufactured capillary was fixed into a glass T-piece mount using x-rings as the close proximity of the gas inlets to the ends may have resulted in UV curing adhesive entering the capillary bore. A theoretical comparison of the two capillaries is shown in Figures 5.4 and 5.5. These show the improved overlap between the peak ionisation and the transmission regions of the new capillary as well as the increase in transmission simply by reducing the absorption by the argon towards the rear of the capillary. The spatio-temporal comparison of the pump pulse shows increased pulse self-compression in the new capillary, with features of less than 5 fs in length. All this supports an improved capillary design with reduced absorption and improved phase-matching.

The experimental results immediately agree with what was expected. The flux of both capillaries was measured at 50, 100, 150 and 200 mbar using an XUV CCD camera for comparison. The flux data from the 7 cm capillary followed a similar trend to that observed in Chapter 4, with the flux decreasing at 100 and 150 mbar before increasing again at 200 mbar. This was different from the 4.5 cm capillary where the flux increased up to 150 mbar before decreasing afterwards. The maximum flux from the 7 cm capillary was more than an order of magnitude lower than that of the 4.5 cm capillary and at 150 mbar the difference in flux between the two capillaries was almost two orders of magnitude. The maximum flux measured at the CCD for the new capillary was 1.54×10^{10} $ph\ s^{-1}$. The XUV transmission through the aluminium filters was then measured and added to the calculated transmission through the remaining argon gas to provide a value for the flux generated at the capillary exit. This was calculated to be 1.54×10^{12} $ph\ s^{-1}$. Finally the XUV spectrum from the 4.5 cm capillary was measured in order to know the flux per harmonic. The spectrum was measured for the same gas pressures as above, with the 150 mbar case proving to be the best. This was shown in Figure 5.14 where the spectrum was dominated by two harmonics containing 75% of the total flux. The final flux measurement was then calculated to be 5.78×10^{11} ph $harm^{-1}\ s^{-1}$, one of the highest yields of an HHG source in the world.

Further improvement and characterisation of the new source is planned. The transmission of the new capillary was only 60% compared to 80% for the old. This is attributed to excess damage to the inner capillary bore during the gas inlet drilling process. A newly manufactured capillary of the same design with more care taken during the drilling will improve the XUV yield. It is worth noting the large improvement over the old capillary even with this issue.

In addition to remaking the new capillary, the beam height will be adjusted or the filter diameter increased to avoid clipping of the XUV beam and subsequent loss of flux. Looking further on, the aluminium filters will be replaced by Zr or Nb filters as the transmission bandwidth of these lies between 10 - 20 nm. This would allow the true XUV cutoff to be measured, which according to the peak intensities calculated within the capillary should push past 10 nm. Pushing further down towards the water window will require replacing the argon gas with either neon or helium, however both of these are lower nonlinear refractive index values than argon. As such a combination of gases could be used to both allow pulse compression and nonlinear mode mixing from the argon and a higher energy cutoff from the neon or helium which both possess higher ionisation potentials. The final stage of improvement to the project would be the inclusion of the HHG process to the nonlinear propagation model. Inclusion of this, which is being worked on, would allow one to take an extra step forward in future capillary designs. The phase-matching conditions, expected flux and XUV beam profile could be predicted before a capillary was even manufactured, leading to some potentially exciting designs. Needless to say, the area of capillary based HHG is currently, and will be for some time to come, rather exciting.

Chapter 6

High-harmonic generation using a fibre-based CPA laser

The information that one can derive from a scattering experiment is limited by the signal-to-noise ratio. Noise levels can easily 'wash out' the diffracted higher orders, which contain information on smaller structures. An increase in the overall flux will increase the signal-to-noise and can thus allow more information on smaller structures to be obtained in shorter times. The fibre laser was designed with this in mind. Fibre lasers have the potential to run at much higher average powers than bulk lasers due to the different geometry of their gain medium. The fibre laser used in this experiment was designed and built at the University of Southampton by Dr Jonathan Price and will be briefly described in the following sections. The original intention was to create a pulsed fibre laser capable of generating 130 W average power at a repetition rate of 100 kHz. This goal has not yet been achieved, but the laser can produce enough power for HHG whilst running at 33 kHz.

This Chapter will look at the work carried out using a chirped pulse amplifier (CPA) based fibre laser for HHG. The experimental set up will be discussed as will the detection methods used. This is followed by the successful detection of XUV and characterisation of the source. Following the characterisation of the source the possibility of improving the signal further using an interesting focusing geometry is briefly discussed before finishing with flux estimations.

6.1 System design and experimental setup

The available space was small in comparison to the main Ultrafast X-ray laboratory and so a much more compact and simple system was required. The following sections

describe the basic design of the fibre laser used during these experiments as well as the vacuum system, filter and detection systems that were built.

6.1.1 Fibre laser design

6.1.1.1 Fibre laser with integrated phase-based pulse shaping

The schematic of the phase-controlled polarization maintaining (PM) Yb-doped fiber CPA system is shown in Fig. 6.1. The seed laser pulses ($\sim$ 150 fs, λ =1055 nm, $\Delta\lambda \sim$ 12 nm) were reduced in repetition rate from 50 MHz to 100 kHz using an electro-optic modulator. The pulses were then stretched to a duration of $\sim$1 ns using a bulk grating stretcher before being phase-shaped with a computer controlled pulse shaper. Core-pumped Yb-doped fibre pre-amplifiers increased the average power to $\sim$0.1 W, then two cladding-pumped amplifiers were used to achieve high pulse energies and average powers. The first cladding-pumped amplifier comprised a 3.5 m length of double-clad PM Yb-doped large-mode-area fibre (core diameter 20 μm, NA 0.06; inner cladding diameter 240 μm, NA 0.5) pumped by a 6 W fiberised 915 nm diode. The final amplifier comprised a 2 m length of double-clad Yb-doped PCF (core diameter 40 μm , NA 0.03; inner cladding diameter 170 μm, NA 0.6) pumped by a 20 W fiberised 975 nm diode. For the high energy results, acousto-optic modulators prevented ASE build-up, and reduced the final repetition rate to 16.67 kHz. A dielectric grating compressor with 65% overall transmission efficiency re-compressed the pulses.

The pulse shaper used a telescope to expand the input beam-waist and a diffraction grating with a groove density of 1100 lines/mm oriented at 10 degree incidence angle. A cylindrical lens (f=200 mm) focussed the beam and a 128 pixel phase-only liquid crystal spatial light modulator (SLM) was placed at the Fourier plane of the folded 4f setup [83]. The pixilation implies that the spectrum could be manipulated in blocks of width 0.078 nm. The control loop was approached as a global optimisation problem, using a differential evolution algorithm [34]. Following initial trials, the search algorithm typically ran for 3000 iterations and took $\sim$5 minutes to optimise the autocorrelation peak. The inclusion of the pulse shaper allows the system to run at an average power of 1.65 W. Using the phase shaper reduces the pulse length at 1.65 W from 500 fs to 380 fs. The energy per pulse is 99 μJ.

The power and size of the system are limited by the core size and damage threshold of the fibres used in the final amplifiers. At this point, increasing the energy, i.e. the intensity within these fibres leads to nonlinear propagation and subsequent degradation of the pulse shape. Degradation of the pulse results in a reduction in intensity due to pulse broadening and the occurrence of pre- and post-pulses. A bulk compressor is required for similar reasons, the intensity of the compressed pulses is above the damage

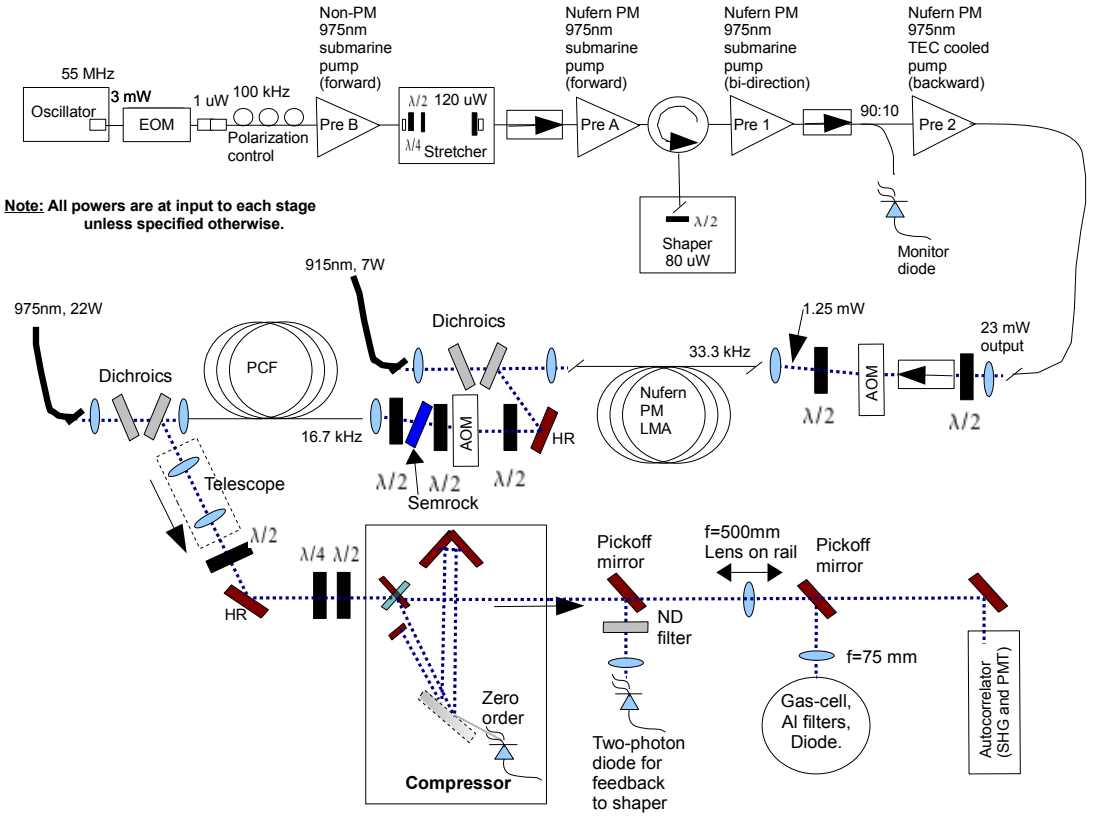

Figure 6.1: Schematic of fibre laser design including basic layout of HHG experiment at the output.

threshold of available fibre designs which would result in material damage and failure of the laser.

6.1.1.2 Filtering and detection system

In Section 5.5 the XUV transmission of aluminium filters is was shown to be dependant on the thickness of both the aluminium and aluminium oxide layers. The thickness of the aluminium layer is 200 nm, whilst that of the oxide layer is typically accepted as being between 4-40 nm. When calculating the total transmission of a filter one must account for two oxide layers, each reducing the signal, for example, at 40 nm by 80%. A simple solution to improve the signal is to remove these oxide layers. This is not possible on a free standing filter, however, if one were to coat the front surface of a photodiode with aluminium only a single oxide layer will grow on the front surface providing a five fold increase in signal. As such, an aluminium coated photodiode (International Radiation Detectors AXUV20AA1) was purchased. A single 200 nm aluminium filter was still required to provide sufficient reduction of the fundamental and was placed at the front of the custom made detector mount (Figure 6.2).

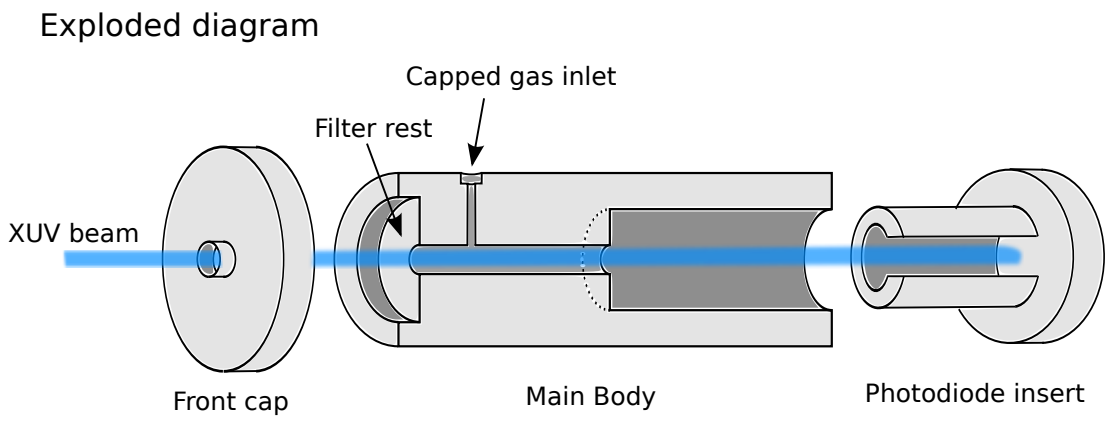

Figure 6.2: Diagram of the new photodiode mount. The diode mount is made of three main components. The front cap is designed to reduce high angle scattering onto or around the single aluminium filter. The central hole is 5 mm in diameter. The main body has a rest for the filter with a 5 mm diameter hole through the centre. A gas inlet has been drilled through to allow pressure regulation around the filter, this is capped to prevent light entering. The rear of the main body has a larger diameter hole to house the diode mount itself. The photodiode sits within the tube and when inserted, is pressed against a rubber ring to prevent light scattering around the edge of the diode itself.

A recess in the front of the mount is occupied by a free standing aluminium filter, the inner diameter of the tube following this is 5 mm, the same as the diode mounted within. A right angled chimney within this section allows the regulation of the pressure around the filter to prevent it from breaking when pumping down. The diode itself presses against a rubber ring to prevent light scattering around the back giving a false signal. It is held in place by an insulating back plate made light tight with carbon tape. The signal cable from the diode is coupled out of the chamber through a BNC adapter to a voltage preamplifier (the manufacturer design and specifications are shown in Appendix C).

6.1.2 Experimental setup

A top down schematic of the setup is shown in figure 6.3. A gas cell is used for the generation. It consists of a short flattened section of $\frac{1}{4}$ inch copper pipe with an interior depth of 500 μm. This is capped at one end for mounting and connected to a gas line at the other. Two 500 μm holes drilled through the cell allow the laser to pass through. It is mounted as close to the input window as is allowed by the length of the copper tube comprising the cell. The gas input feed comes in through the right hand KF40 input and is removed by a KF40 ribbed tube attached to the left hand input on a T-piece with a Leybold pressure gauge to measure background pressure in the chamber. The photodiode mount is placed at the rear of the chamber, again as close to the back as possible to reduce the strain on the aluminium filter from both the gas and fundamental

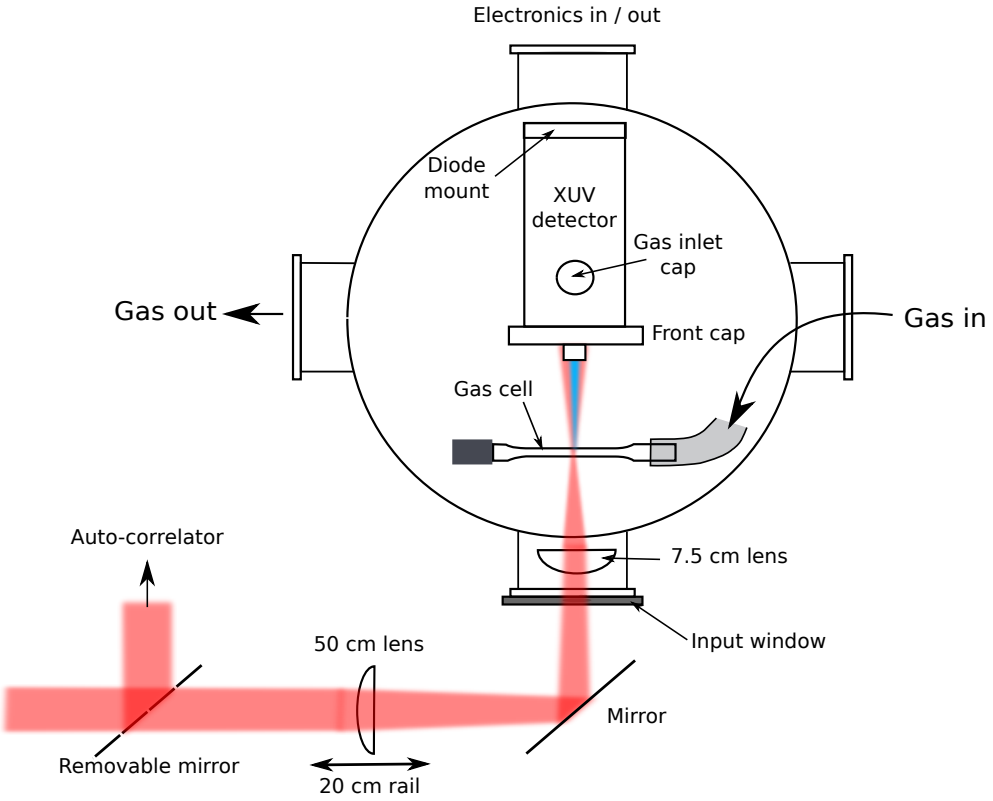

Figure 6.3: Top down diagram of the setup used. The final lens has a focal length of 7.5 cm and is mounted within the KF40 input to the chamber. A 50 cm lens is mounted on a 20 cm rail prior to the vacuum chamber to allow movement of the focus through the gas cell. Xenon and argon gas is fed in through the left port to the gas cell. The gas is pumped out of the chamber through the right port using the same pump and tubing as before. The laser is focused through the gas cell and is filtered by a single 200 nm aluminium filter at the front the of the XUV detector. The aluminium coated XUV photodiode is mounted within. The signal is fed out the back of the vacuum chamber via a BNC adapter directly into the preamp.

laser. The separation of the cell and the front of the detector mount, shown in figure 6.4 is 3 cm.

A 7.5 cm focal length lens is used to focus the laser through the gas cell. The vacuum chamber has a diameter of 15 cm so to accommodate the lens, gas cell and detector whilst avoiding damaging the filters with the fundamental beam. The lens was mounted within the KF40 inlet tube to the chamber in a custom designed mount. In addition to this a 50 cm plano-convex lens was mounted on a rail outside the chamber to provide a means of scanning the focus through the gas cell for improved phase-matching.

6.1.3 Optimisation of vacuum system

The XUV photodiode is situated 7 cm from the generation region inside the gas cell, Figure 6.5 shows the x-ray transmission through this distance of argon for three pressures. From this it is clear that maintaining a low background pressure is critical in

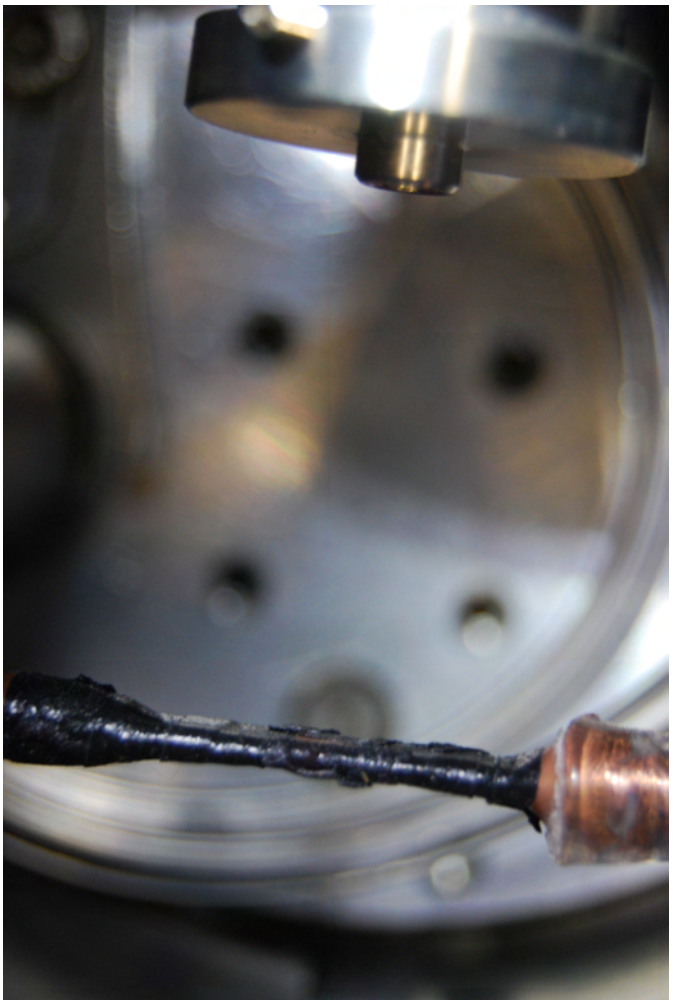

Figure 6.4: Photograph of the gas cell and front of the detector mount. The distance between the two is 3 cm. The laser is incident from the right hand side. The cell is wrapped in carbon tape to absorb laser scatter from the filter. The front of the detector has an aluminium lid placed over the end to reduce high angle scattering onto or around the filter.

detection of harmonics generated with wavelength greater than 30 nm.

Results of the measurement of the background pressure are shown in figure 6.6. The chamber pressure scales linearly with cell pressure but is reduced by two orders of magnitude. This means that for a typical gas cell pressure of 50 mbar the backing pressure of 0.5 mbar will absorb only a few percent of the XUV at 30 nm.

6.2 HHG and XUV results

This section follows a similar pattern to the previous with the addition of successful XUV detection and analysis. The successful detection of an XUV signal using xenon as the target noble gas will be discussed followed by analysis of the signal to ensure it is a result of HHG and to understand the limitations. Possible improvements in the XUV signal

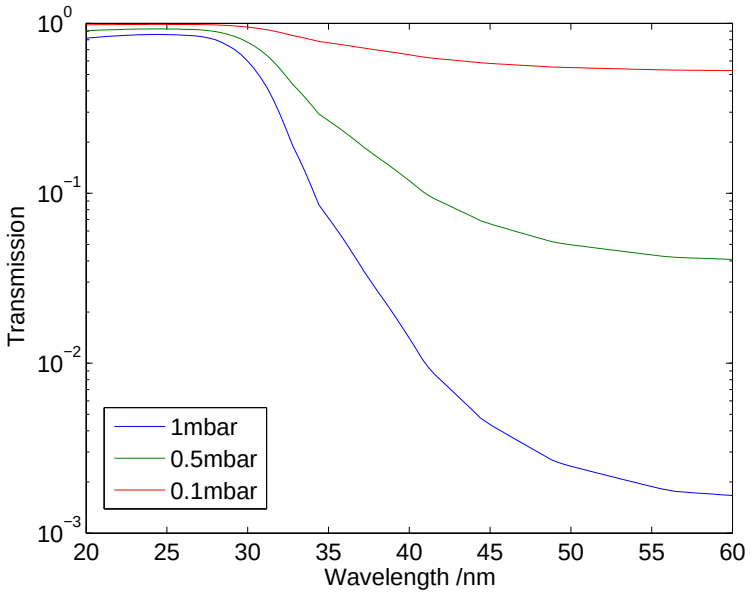

Figure 6.5: Plot showing x-ray transmission from gas cell to photodiode through argon at three different gas pressures. Actual transmission is $\sim$ 1% of these values due to the absorption of both 200nm Al filters. (Data taken from CXRO website [78])

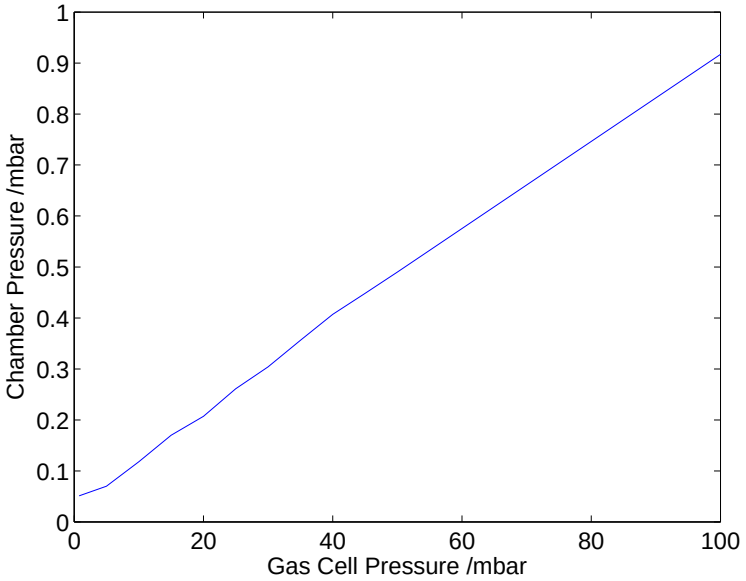

Figure 6.6: Chamber background pressure as a function of cell pressure. The background pressure scales linearly with cell pressure reduced by two orders of magnitude.

based on some interesting observations in the focussing conditions are briefly discussed followed by calculating the maximum flux of this system compared to the Ti:Sapphire based laser used in Chapters 3 - 5.

6.2.1 Analysing the XUV signal

Initial experiments with argon gas showed a small, faint plasma ball at gas cell pressures above 30 mbar. The existence of a plasma ball shows that the intensity is high enough for HHG, however no XUV was detected. The small size of the plasma ball made it possible to use its position to calibrate the relative distance between the gas cell with the calculated position of the focus. The peak intensity of the pulse in this configuration is $1.02\times10^{14}\ Wcm^{-2}$. To calculate the peak intensity and relative position of the focus with respect to the gas cell an ABCD propagation code was written in Matlab. This assumed a flat phase front at the 50 cm lens, and could propagate the beam through both lenses for different separations, with a peak intensity calculation for each separation included. Figure 6.7 shows the change in spot size and the position of the focus for different separations between the first and final focusing lenses, whilst figure 6.8 shows the peak intensity on the same plot. The position of the gas cell's inner and outer walls are shown as dashed and solid lines respectively. Figure 6.8 shows that the intensity drops off rapidly, with an average Rayleigh length of 260 μm and spot size of 9.3 μm. It was decided to switch to xenon as the target gas. This was done for two reasons: the first is that xenon is more easily ionised than argon, it has an ionisation potential of 12.13 eV compared to 15.76 eV for argon. The second is that at the lower harmonics, 40 - 60 nm where one would expect to generate using this setup, xenon is less absorbing than argon, improving the SNR. Argon was initially chosen as it is much cheaper and due to the higher ionisation potential provides a higher energy cutoff than xenon, however, as no XUV was detected it made sense to change to xenon.

The following sections look at the analysis of using xenon as a target gas for HHG. This was immediately successful with results showing a SNR of 100:1. A range of experiments were carried out, firstly to make certain that the signal was as a result of HHG and then to characterise the source itself. The following sections look at whether the signal was HHG induced, the power and pressure dependance of the signal and how changing the position of the focus can affect the signal. Accompanying the data are photographs taken through the top viewing port during the experiments showing the purple plasma of the ionised xenon gas.

6.2.1.1 Is it really HHG?

The simplest and most obvious test of HHG is whether or not a signal exists when no gas is present in the cell. The background signal was 3 mV, which was attributed to laser

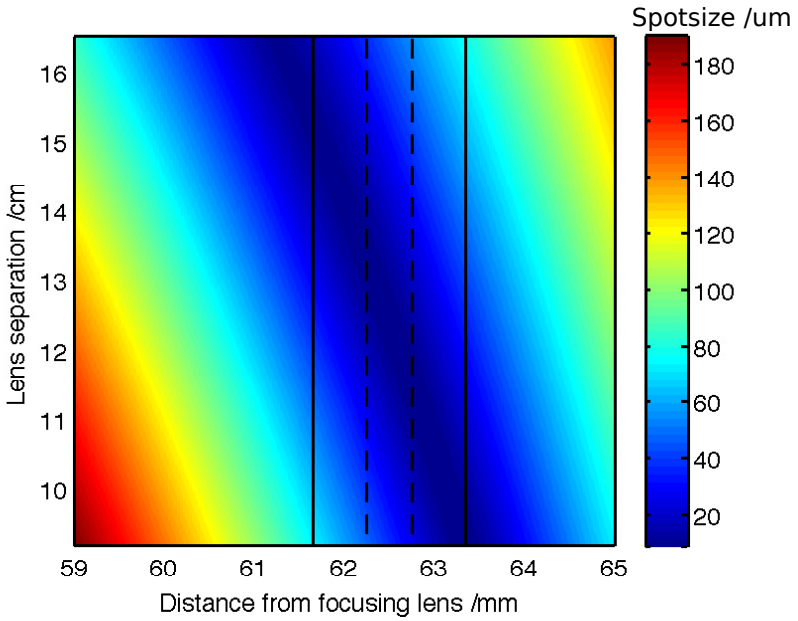

Figure 6.7: Beam spot size w (colormap) through focus as a function of lens separation. The lens separation is shown on the y-axis, the distance from the final focusing lens is shown on x-axis. The position of the gas cell outer walls (solid line) and inner walls (dashed lines) are also shown. A lens separation of 10 cm was used for the majority of the experiments.

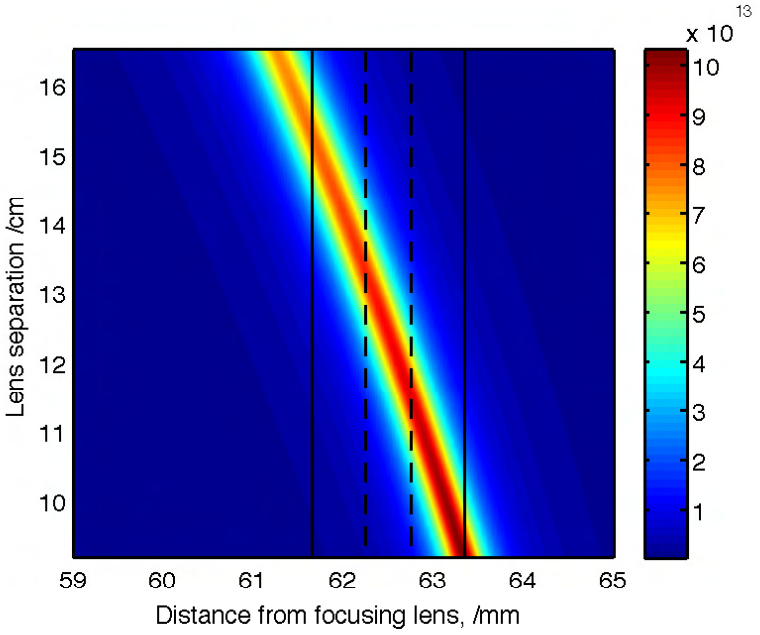

Figure 6.8: Pulse intensity (colormap) through focus as a function of lens separation. The lens separation is shown on the y-axis, the distance from the final focusing lens is shown on the x-axis. The position of the gas cell outer walls (solid line) and inner walls (dashed lines) are also shown.

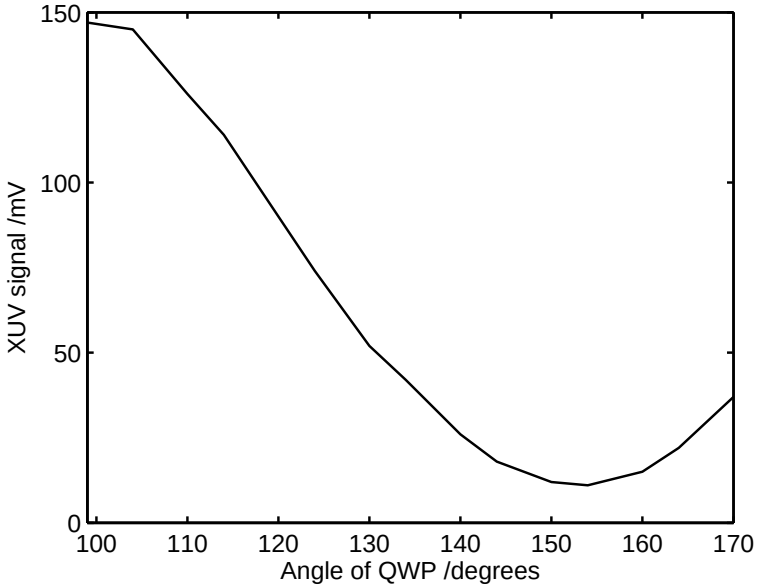

Figure 6.9: Plot of the XUV signal detected as a function of QWP angle in degrees. The maximum coincides with the QWP on axis to the laser polarisation producing a linear polarisation of the beam. As the QWP is rotated the output laser polarisation becomes more circular until it reaches a minimum with almost circular polarisation.

leakage through the filters. When gas was introduced to the cell the peak signal voltage, based on focal position, cell pressure and input power was 360 mV. This maximum varied over the course of the experiments from 140 mV to 370 mV, dependent on the stability of the laser. This initial result shows that the signal is not due to the laser but due to the interaction between the laser and the xenon gas.

A quarter waveplate (QWP) was also used to test whether the signal was caused by HHG. HHG is greatly suppressed if the driving laser is circularly polarised. This is due to the trajectory the ionised electron takes during acceleration. In a linearly polarised field the electron can return to the parent ion, but in a circularly polarised beam the electron does not. HHG can still occur if the wavefunction of the ionised part of the full electron wavefunction can overlap with that still at the ion, however this is reduced to near zero for a circularly polarised driving field. As the ellipticity is increased, the overlap of these wavefunctions is reduced resulting in suppression of HHG. The results of this experiment are shown in figure 6.9. The variation shows a sinusoidal dependence on the QWP angle, ranging from a maximum of 147 mV to a minimum of 11 mV. The signal does not reduce to the background or reach the absolute maximum, as such the polarisation never becomes perfectly circular or remain perfectly linear when the QWP is introduced into the beamline. The dependence on angle is strong evidence that HHG is occurring, however, it is not definite proof, as one would expect a greater dependence on the angle of the QWP. In addition to suppression of HHG, the ellipticity of the driving field also affects the peak intensity and the tunnelling rate. The Keldysh parameter discussed in Section 2.3.3 is less than, but close to one, meaning that whilst

tunnelling ionisation dominates, multi-photon ionisation may still have an effect on the total ionisation. The result is that both the intensity and ionisation [84] decrease with increasing ellipticity, and so one would expect to see a change in the ionisation. This is indeed observed, as shown in figure 6.10. The fluorescence within the xenon gas jet for the linear (left) and circular (right) polarisations of driving field show a reduction in brightness for the circularly polarised field. The laser power had reduced from 1.59 W to 1.49 W by the end of the measurement. For both linear and circular cases the laser power was the same and the focal position required for maximum signal did not change, showing that any change was due to the change in polarisation.

The question remains, is the signal due to HHG or fluorescence? This is difficult to answer with certainty until a spectrum of the generated XUV can be taken. The QWP angle dependence gives more support to fluorescence than HHG, however, one must also look at the filtering system. This consists of a single aluminium filter and an aluminium coating on the photodiode. The reflectivity of aluminium across the visible spectrum is very high, hence the reason it is used as a filter in these experiments. The main xenon fluorescence lines are between 365 and 400 nm. At these wavelengths the transmission of thin aluminium films is still very low. It has been shown that the transmission of a single 200 nm thick aluminium filter in this spectral region is between 6-9% [85]. Therefore the transmission through two such filters is less than 0.1%. In addition to this, two filters were used over the course of the experiments, a 200 nm filter and a 500 nm filter. The transmission of the 500 nm filter is less than 0.1% [85], which should result in a large decrease in the detected signal if fluorescence is the source. This was not the case, with only a slight variation in signal observed, as one would expect if the signal is a result of HHG. It should be noted here that this does not make HHG a certainty, merely the most likely source, in my opinion. Characterisation of the source by focal position, pressure and intensity dependence strengthens the case for HHG, which will be answered fully in the future work planned.

6.2.1.2 Focal position dependence

Working on the basis that the signal was due to HHG, it was necessary to ascertain how the XUV signal could be controlled, improved and studied. As was mentioned in section 2.2 the successful build up of an XUV signal is due to phase-matching the fundamental pump wavelength and the high-harmonics generated. A phase-matching model based on the work by Balcou [50] was used to calculate the phase-matching for the 21st harmonic of the fibre laser. It includes contributions from the Gouy phase and atomic phase discussed in section 2.2. The model calculates the phase mismatch due to both the Gouy phase using equation 2.35 and the atomic phase, equation 2.42 and converts this using equation 2.22 into an overall coherence length at all points through the focus. The hard cutoff surrounding the focus is the minimum intensity required

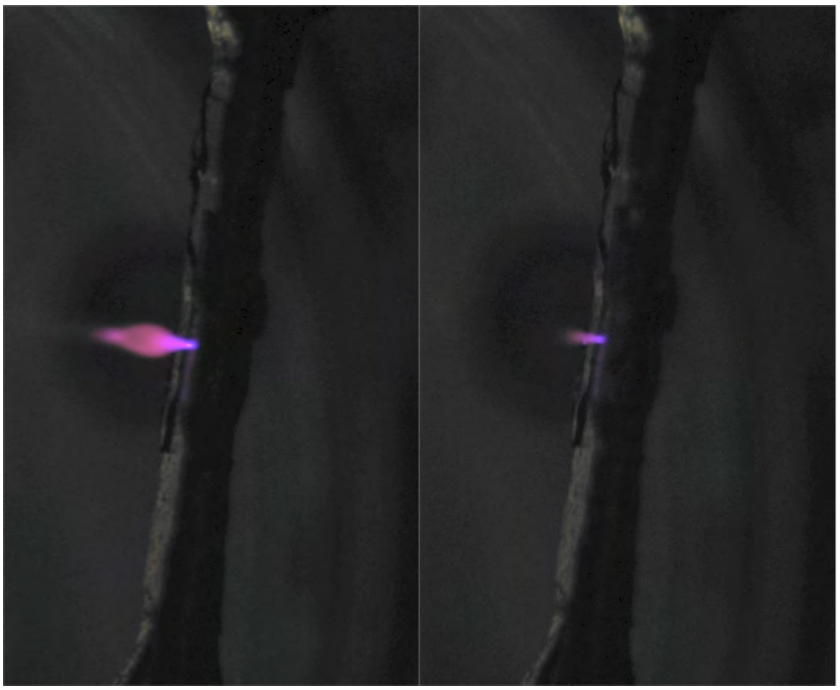

Figure 6.10: Photograph of the plasma generated by the pump-pulse at the focus for linear polarisation (left) and circular polarisation (right). The difference between the two plasma channels is due to the inability of circular polarised light to perform odd number multi-photon ionisation, reducing the total ionisation

to generate the 21st harmonic using the fibre laser, calculated from equation 2.4. The code to calculate the phase-matching was originally written by Dr W.S Brocklesby and adapted by myself for this experiment. Figure 6.11 shows the phase-matching plot for this HHG set up.

The calculation shows that the best phase-matching and hence longest coherence lengths are positioned after the focus. The coherence length increases to a maxmimum of ~ 100 μm at ~ 260 μm from the focus. Positioning of the focus within the the gas cell is critical to maximising the measurable signal produced by the HHG process. The focus should be positioned such that the end of the outer wall should coincide with the furthest point from the focus that HHG can still occur. In this case the focus should be around one Rayleigh length prior to the outer wall so that the best phase-matching region is just inside the gas cell. Such an arrangement has the benefit of maximising the amount of XUV generated and minimising the absorption due to higher pressure gas. At the exit of the cell the gas will become a jet with an associated zone of silence immediately afterwards where the pressure is greatly reduced compared to the pressure within the cell. This zone of silence is clearly visible in Figure 6.10. To test the theory the focus was moved through the gas cell and the associated XUV signal was measured. The results of this are shown in Figure 6.12 where the gas cell position is shown using the dashed (inner walls) and solid (outer walls) lines. The agreement between the theory and the experimental data is strong, showing little signal with the focus before or well inside the gas cell followed by a steep increase in the signal as the focus reaches the back

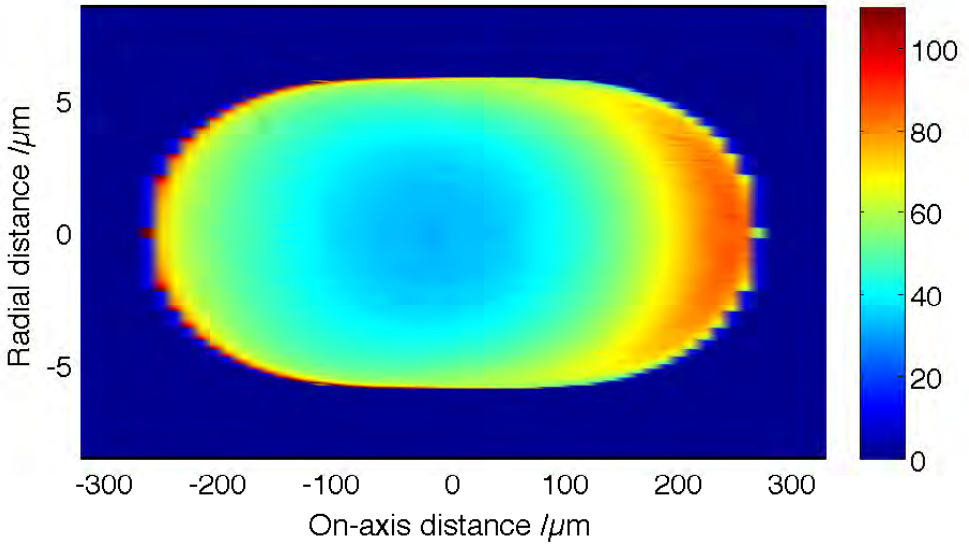

Figure 6.11: Plot of coherence length for the short trajectory of the 21st harmonic on the fibre laser system. The colourbar shows the coherence length through the focus calculated using phase mismatch contributions from the Gouy and atomic phases.

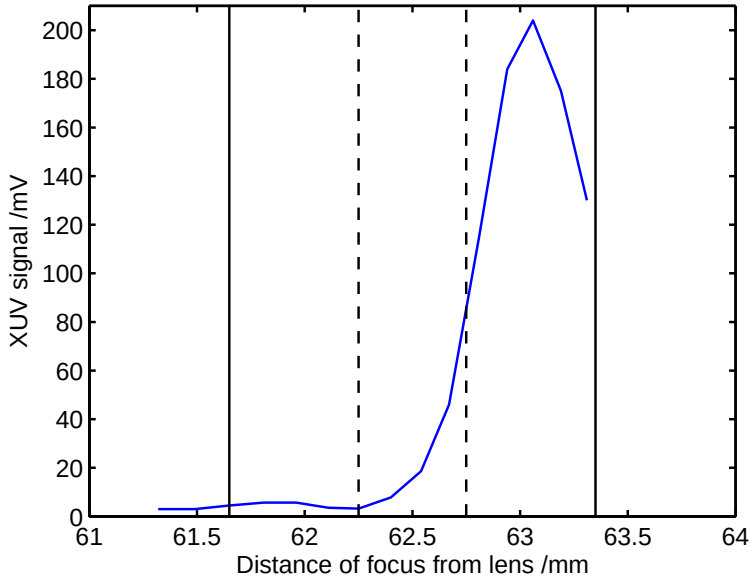

Figure 6.12: Plot of the XUV signal detected as a function of focal position within the gas cell. The gas cell position is shown using the solid (outer walls) and dashed (inner walls) lines. The gas pressure is assumed to be constant between the outer walls and is set at 8mbar.

end of the cell. It is important to note that the signal does not keep rising but begins to reduce once the focus passes to within roughly one Rayleigh length of the outer wall as the overlap between the generation medium and the phasematched region becomes less.

The gas cell position from this point onward was fixed at 63 mm, the point at which the XUV signal detected was greatest.

6.2.1.3 Pressure and power dependence

The pressure dependence of HHG was discussed briefly in Chapter 4 with regards to the change in XUV spectrum with pressure. If the generation region is shorter than both the coherence and absorption lengths the XUV signal measured by the photodiode scales with the square of the pressure. The XUV field is dependant on the number of coherent generation centres, i.e. the number of atoms. As such the field scales linearly with pressure while the intensity scales quadratically. In section 6.2.1.2 it was shown that the generation region is on the order of one Rayleigh length, or $\sim$ 260 μm. For xenon at 1 atm the attenuation coefficient at 40 nm given by the CXRO database is 5.56×10^{-5}. The attenuation length L_{abs} is the distance over which the intensity drops by $1/e$.

$$I = I_0 \exp[-\beta(\omega)k(\omega)z] \tag{6.1}$$

$$\frac{1}{e} = \exp[-\beta(\omega)k(\omega)L_{abs}] \tag{6.2}$$

$$L_{abs} = \frac{1}{\beta(\omega)k(\omega)} \tag{6.3}$$

This gives an attenuation length of 114 μm which scales linearly with pressure. At 100 mbar L_{abs} = 1.14 mm, almost four times the Rayleigh range where generation occurs in this experiment, removing absorption within the gas cell as a major factor in these experiments. The phase-matching varies with pressure due to the contribution of the gas and free electron terms, and so one would expect to observe saturation of the signal as a function of pressure at some point, as is also shown by Constant et al [86]. However, if the signal is not due to HHG but rather the fluorescence discussed previously one would not expect to see a saturation point.

The input power was set at 1.6 W for the duration of this measurement and did not vary. The pressure was varied from 0 to 16 mbar in 1 mbar steps and the corresponding XUV signal was recorded. This data is shown in Figure 6.13.

At low pressure where the free electron density is low the XUV signal increases as expected, rising quadratically to a peak of 162 mV at 6 mbar after which the XUV signal slowly reduces with increased pressure. As the pressure and so the number of coherent emitters increases so does the XUV signal. This continues to a point where the ionisation becomes significant enough to reduce the coherence length and thus saturate the signal. The free electron phase mismatch is linearly dependant on the pressure and so its contribution to the total phase mismatch is also linear with pressure. After the free electron contribution becomes a limiting factor one would therefore expect to see a linear decrease in the signal with pressure, as is shown in Figure 6.13. The pressure dependence of the XUV signal for this experiment shows that for optimal XUV generation the pressure should be set between 5 - 8 mbar. The following work in this section looks at the variation of XUV signal as a function of power.

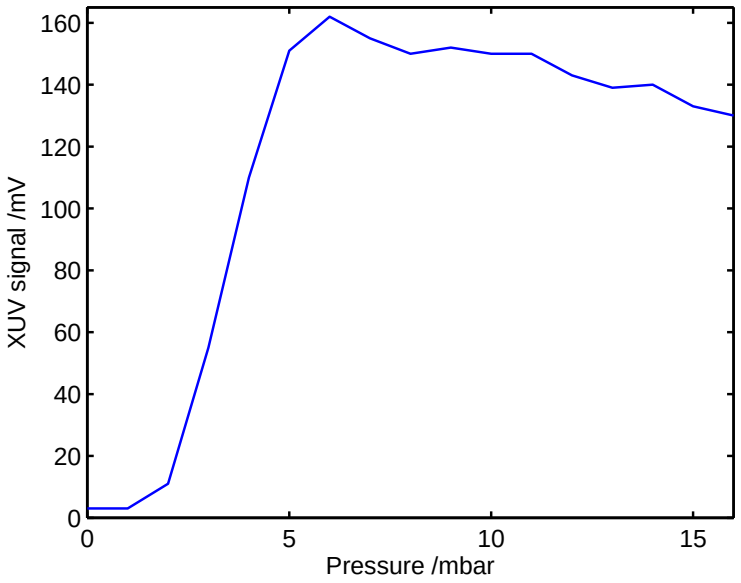

Figure 6.13: Plot of the XUV signal detected as a function of gas cell pressure. There is a rapid increase in the signal up to a pressure of $\sim$ 8 mbar above which it linearly decreases. The position of the maximum is a combination of the XUV absorption and phase-matching conditions

In low order harmonic generation, i.e. second, third order harmonic generation, the intensity of the harmonic scales with the fundamental by a power law. The scaling follows an I^q power law where q is the harmonic order. In HHG the system is more complex and so a simple I^q power law cannot describe it. The intensity and hence power dependence of HHG was examined in detail by L'Huillier et al in 1992 [87]. In that work they looked at the amplitude response of individual harmonics up to the 21st, using xenon as a target gas. They found within the perturbative regime, the low harmonic orders, an I^q dependence on the pump intensity, however, in the plateau regime the power law remains fairly constant at about I^5. What this implies is that a log-log plot of input power vs XUV signal should be linear, with the gradient of the line around 5. A pressure of 7.8 mbar was set for this experiment as this provided the greatest XUV signal. Figure 6.14 is a log-log plot of the XUV signal as a function of power. The power was varied from 0.85 W below which no signal was observed, to 1.53 W.

A linear fit of the data has been added to the figure as has the equation for the fitted line. The data shows a linear dependence on the log-log plot and so follows a power law. The XUV signal measured here follows an $I^{6.63}$ power law. This is higher than that observed by L'Huillier et al, but is not unexpected. This signal is not an individual harmonic but a sum of all the harmonics generated. In this experiment as the power and hence intensity of the pump pulse increases so too will the cutoff energy of the HHG process. This will act to shift the harmonic spectrum to higher energies and hence shorter wavelengths where the absorption of both xenon and aluminium decreases. The increase in intensity will also increase the ionisation fraction and thus change the phase-matching conditions

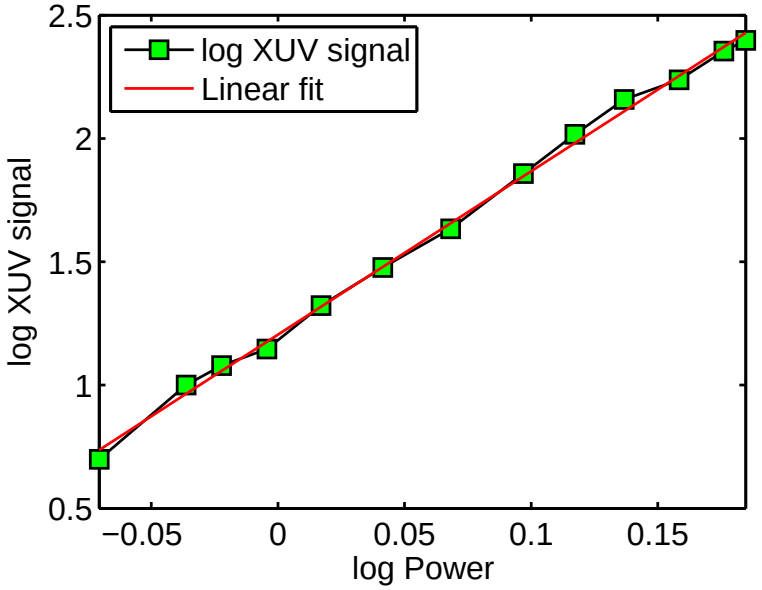

Figure 6.14: Plot of the XUV signal detected as a function of pump laser power. The graph shows a nonlinear dependence on the power which is expected for such a highly nonlinear process. For an average power of less than 0.88 W the signal drops below the noise, however a plateau is not reached at the upper level indicating that it may be possible to increase the flux still further if the laser power can be increased. The gradient of the linear fit is 6.63.

within the gas cell, providing another possibility for a larger power law dependence here. Finally, by increasing the intensity one changes the effective volume within which HHG can occur. As the power is increased the intensity in the wings of the beam will become great enough to generate high-harmonics, thus increasing the harmonic yield further. The XUV signal does not saturate with increased pump power, which one would expect to see when the ionisation fraction becomes too large and the phase-matching is reduced. As such the XUV signal can be increased by further improvements to the laser system that increase the average power.

The experiments that have been described above provide the conditions for maximising the XUV signal with the laser in its current state. Changes to the laser that increase the average power and reduce the pulse length would lead to further improvement of the XUV signal. In the near future it is also useful to look at methods of improving the XUV signal without making changes to the laser system itself. The following section details preliminary observations of a method to improve the XUV signal simply by twisting the first focusing lens, resulting in a doubling of the XUV signal.

6.2.2 Improving the XUV signal

The observation discussed in the following section was made towards the end of the experimental run that has been explained thus far in this chapter, as such it is only

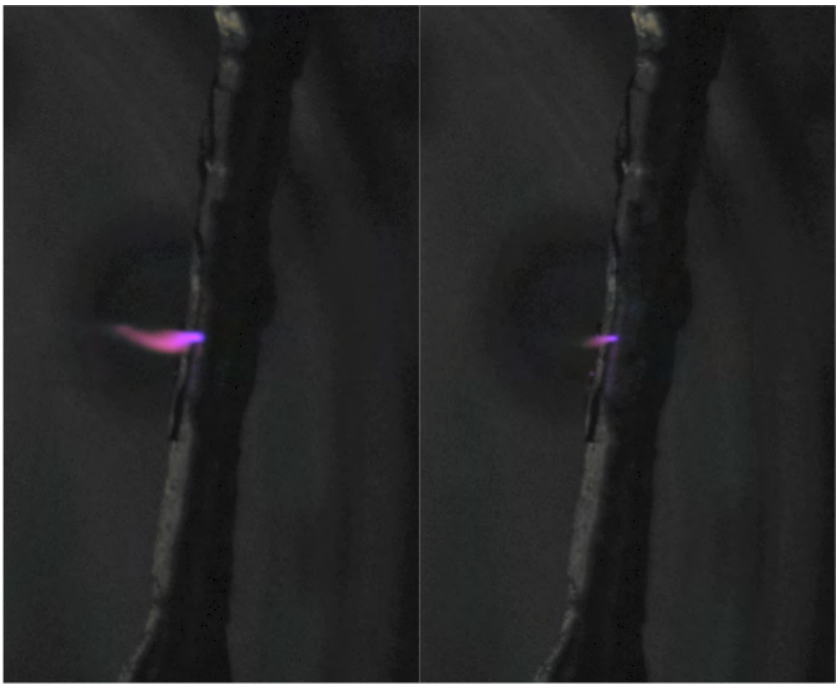

Figure 6.15: Photograph of the plasma generated by the pump-pulse at the focus for linear polarisation (left) and circular polarisation (right). In this case the 50 cm focal length lens has been slightly twisted resulting in a shift in the focal position. This is clearly visible in the shape of the plasma channel observed coming out of the gas cell, as only the lower half of the gas jet exiting the cell has been excited by the pump-pulse.

preliminary and not well understood. It has been included because it is an interesting result which may help to improve free space HHG geometries. The experimental set up used here includes two focusing optics, 50 cm and 7.5 cm plano-convex lenses. The 50 cm lens is located outside the main chamber on a rail to enable scanning of the focus through the gas cell. It was noticed that occasionally whilst moving the lens along the rail the XUV signal detected would peak suddenly. After some investigation it was realised that this peak was induced by slightly twisting the 50 cm lens. The rotation was on the order of 5 - 10 degrees and resulted in a signal increase from 145 mV to 360 mV. The power and pressure remained constant. This increase in signal could be induced for any power, pressure or focal position combination, to different extents. To ensure that this signal was still due to HHG a QWP was placed in the beamline and rotated between linear and circular polarisations. The XUV signal changed accordingly and Figure 6.15 shows a photograph of the gas cell for the linear (left) and circular (right) polarisation states.

The image of the jet exiting the gas cell is intriguing. It shows only half of the jet structure, which is observable thanks to the fluorescence of the xenon gas. The change in the fluorescence is similar to the normal case shown in Figure 6.10. For such an image to be recorded the focus within the gas cell must be changed by the twisting of the lens. Furthermore it implies that the only gas particles interacting with the laser are on the

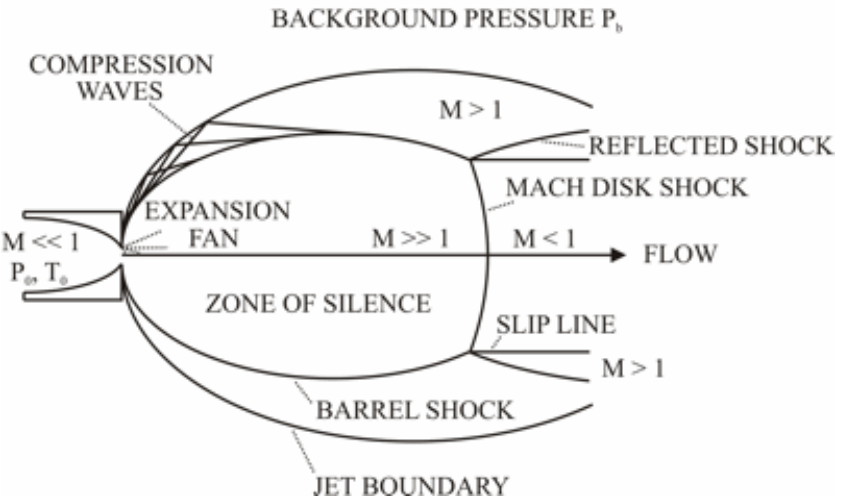

Figure 6.16: Diagram of supersonic jet structure. The low pressure zone of silence can be seen immediately after the nozzle extending towards the Mach disk where the pressure rises. Surrounding the zone of silence is the barrel shock, where the pressure is similar to that of the Mach disk.

left hand side of the cell and thus contribute to that side of the jet only. The focal spot size is on the order of 10 μm, 25 times smaller than the holes through which the beam passes. The outer lens is not moved and so the longitudinal position of the focus should not change. It is possible that rotating the lens causes the focus to shift laterally, which is supported by observation. This may explain the change in the appearance of the gas jet but not the increase of the signal. Absorption effects have been ruled out as the attenuation length at 8 mbar exceeds 12 cm. This leaves only generation region and phase-matching as possible causes of the increase in XUV signal.

A schematic of the jet structure is shown in Figure 6.16. The area immediately after the exit is known as the zone of silence and has been mentioned previously. The gas pressure in this region is very low compared to the gas cell due to the rapid expansion of the jet into vacuum. This is the region that the laser and hence XUV beam passes through under normal conditions. It is surrounded on both sides by a barrel shock region where the gas pressure increases again as the gas slows and collides. These two barrel shock regions meet at the Mach disc directly after the zone of silence. All of these features can be seen in the normal jet structure shown in Figure 6.10. In this twisted lens case only one side of the jet can be seen, namely the left hand barrel shock region. The gas pressure profile that the fundamental and XUV beams will see is different to the normal case. Instead of a region of high pressure (inside the cell) followed by a rapid decrease (zone of silence) the pressure will remain high, as the pulse passes through the barrel shock. This could effectively increase the length of the generation region, but such a change does not explain why this effect was not observed with the focus placed within the gas cell which has a similar pressure to the barrel shock region.

The increase in signal could also be due to a change in the phase-matching conditions

brought about by a change in the focusing geometry. It is possible that all of the phase-matching contributions have been affected by the lens twist. In an ideal set up the Gouy phase is given by equation 2.35. However, the system is no longer on axis and thus the contribution from the focusing geometry may be more complicated. The change in the focusing geometry will also have an effect on the peak intensity of the pulse and hence both the atomic and free electron contributions. Further experiments will be required to fully understand what is the true cause of this signal increase and whether it can be used as a general tool.

6.2.3 Calculating the XUV flux

The flux calculation carried out here is based on the highest signal measured thus far, 370 mV. The XUV spectrum has not been measured but is assumed to exist between 40 - 80 nm, due to the cutoff energy and aluminium transmission respectively. The XUV field generated by each pulse is collected by the photodiode. Each photon generates ∼2 electrons which are then collected within the capacitor, resulting in a voltage step proportional to the number of photons incident on the photodiode per pulse. This voltage step is then amplified and fed into an oscilloscope where the signal is averaged to reduce random noise fluctuations. The signal, S, measured by the photodiode and voltage amplifier combined and connected to a 50 Ω load, was given by the amplifier manufacturer as

$$S = \frac{q}{C_{det} \cdot 4600} \tag{6.4}$$

where q is the total charge collected by the photodiode capacitor and C_{det} is the capacitance of the photodiode, 2 nF. The largest signal measured was $S = 370$ mW. The number of electrons generated per pulse can be calculated by rearranging equation 6.4.

$$no.\,electrons = \frac{C_{det}S}{4600} 1.6 \times 10^{19} \tag{6.5}$$

where $1.6{\times}10^{19}$ converts the charge q to number of electrons. This gives $2.58{\times}10^{6}$ electrons per pulse, which corresponds to $1.29{\times}10^{6}$ photons per pulse. The repetition rate of the laser is 16.67 kHz and so the number of photons per second is $2.15{\times}10^{10}$ phs^{-1}. This is the number of photons that are detected every second by the photodiode but as before does not represent the total number of photons generated. Transmission through the aluminium filter for 50 nm radiation is ∼ 10%, whilst transmission through the 150 nm aluminium coating of the photodiode is 70%. An aluminium oxide layer will exist on the coating. A conservative thickness of 10 nm corresponds to a transmission of 40% at 50 nm. The resulting total transmission through the filters is 2.8%. In addition to this the XUV must travel through 8 cm of background xenon which for a cell pressure of 8 mbar was 0.1 mbar. Transmission through this is 70% giving a total transmission of 1.96%. When this is factored in the XUV flux generated at the gas cell is given

as 1.1×10^{12} phs^{-1}. This is comparable to the maximum flux generated by the 4.5 cm capillary described in Chapter 5, which was calculated as 1.54×10^{12} phs^{-1} and greater than that by produced by other fibre laser systems [88, 89]

Of the two generation methods both have merits. The Ti:Sapphire and capillary based system has a much higher cutoff and so can generate shorter wavelengths. If one wants to achieve water window wavelengths, 2 - 5 nm, in the near future the bulk system must be used, however, the fibre laser has shown that having a increased repetition rate can counter some of the drawbacks of lower energy and longer pulses. In fact, when run at its current maximum repetition rate of 33.3 kHz it can double the maximum flux to 2.2×10^{12} phs^{-1}, above that of the Ti:Sapphire laser.

6.3 Conclusions and future work

Moving away from work on capillary based HHG this chapter has explored the possibilities of HHG, using a fibre laser and the high average powers they run at as a means to increase the XUV flux. To that end a custom built high-harmonic generation and detection system was constructed. A gas cell was chosen as the generation geometry due to the small space within which to work and the ability to maintain low background pressure. A short 7.5 cm focal length lens was used to focus the 1055 nm, 380 fs, 99 μJ pulses into the centre of the gas cell. In addition to this a second lens was placed outside the chamber on a rail to allow control over the focal position within the chamber whilst under vacuum. An aluminium coated XUV photodiode was mounted within the chamber inside a light tight mount using a 200 nm aluminium filter, to separate the fundamental pump pulse from the generated XUV. The photodiode was connected via a voltage preamp to a digital oscilloscope with averaging functionality.

Initial experiments with argon showed no XUV signal although the laser was sufficiently intense to create a small amount of ionisation. The argon was replaced by xenon. This has a lower ionisation potential making HHG possible at lower intensities, but also reduces the cutoff energy. The harmonic spectrum generated using xenon could not extend below 40 nm; however, the absorption at longer wavelengths is reduced.

Using xenon as a target gas a signal was observed. A QWP was placed in the beam to switch the linearly polarised beam to circularly polarised. The signal reduced as the ellipticity of the driving field was increased however the dependence on angle was more in line with xenon fluorescence than HHG. This lead to a discussion of the filtering system and the conclusion that the aluminium filters should block the xenon fluorescence, although this is not a certainty. The dependence of the signal on focal position, gas pressure and power was explored. It was found that the signal peaked when the focus was placed a Rayleigh length within the final wall of the cell, a fact which was corroborated by

phase-matching calculations. The pressure dependence was shown to be quadratic until a saturation point was reached, a feature that would not be expected for fluorescence, lending strength to the HHG argument. The saturation point can be explained by an increase in the phase-matching contribution from the free electrons in the HHG case. The power dependence was observed to follow the expected power law dependence first examined by L'Huillier et al with an increase in the power law dependence as the signal is a measure of the total harmonic spectrum. Further work showed that a change in the focusing conditions brought about by twisting the external lens led to a doubling of the signal, which is still not well understood. Flux calculations of the maximum signal obtained thus far showed an XUV flux of 1.1×10^{12} phs^{-1} which can be extended easily to 2.2×10^{12} phs^{-1} by increasing the repetition rate of the laser.

Future work with this system will aim to measure the spectrum of the generated XUV, which is still required to fully characterise the signal as XUV, and continue the research in improving the flux. To that end phase shaping of the driving pulse using the XUV signal as feedback is planned, as is continuation of the twisted lens research. Finally improvement of the fibre laser itself will allow the use of argon and open the system up to higher cutoff energies.

Chapter 7

Conclusions

The work carried out in this report began in chapter 3 with the manufacture and use of a 7 cm hollow capillary waveguide. The methods used to cleave and polish the capillary ends were described followed by drilling of the gas inlets using the main beamline of the laser. The approach to efficient coupling into the capillary at low power (10 mW) was described including the beam shape to expect at the output. The finished product was a 7 cm long capillary with an outer diameter of 1.6 mm and a core diameter of 150 μm. Gas inlets were placed 2 cm from either end. Once a working capillary had been constructed the output mode structure immediately became of interest. Extensive spectral broadening was observed within the capillary, visible due to lossy higher order modes, and in the output mode structure which consisted of concentric circles of different colours. This output led to the second part of the chapter where the MM-NLSE propagation model developed by Dr Peter Horak was compared against experimental data both as a test of the model and to understand the processes affecting the pump pulse.

In section 3.2 comparisons were drawn between the theoretical and experimental total output spectra which lead to the discovery of the large part nonlinear mode coupling plays within the propagation. This was further investigated in section 3.2.3 where a novel method to spatially resolve the entire output spectrum was used. The initial comparison showed a strong agreement and proved that the blue shifted part of the spectrum has a large contribution in higher order modes. It was also noted that the total nonlinearity of the model was less than that of the experiment. The cause of this was discovered to be nonlinear propagation prior to the capillary which the model did not take into account. Using the real measured pulse as the input to the model produced a new spatio-spectral output whose comparison to the experimental data was much better. As a result all further theoretical modelling used the measured field as the input. To ensure the model was accurately predicting the propagation of the pump pulse along the entire length of the capillary and not simply at the exit, an experiment was devised to compare the integrated ionisation along the capillary length. The argon

ion fluorescence along the capillary length was imaged and compared to the theoretical integrated radial ionisation profile predicted using the model. Agreement between the two was very good accepting that the model assumes a perfect waveguide and does not include losses due to imperfections in the capillary or at the gas inlets.

Chapter 4 focused on two aspects, the temporal evolution of the pump pulse within the capillary and the HHG process and resulting XUV spectra. In section 4.1.2 the output pulse from the capillary was measured for a number of input powers and gas pressures. A comparison of this data to the theoretically predicted output pulse showed major differences. The differences were caused due to errors in both data sets. The experimental pulse had a significant positive chirp due to propagation through neutral density filters and the optical components within the FROG measuring device. Removing this chirp changed the temporal shape from a three peak structure to a single 28 fs pulse. The model was also enhanced by using the pulse's real spatial input at the beginning instead of a perfect Gaussian distribution. This changed the nonlinear mode mixing during the propagation and led to the prediction of a 28 fs output pulse. The agreement between the two new data sets was excellent, and in addition to that showed a pulse self compression from 53 fs to 28 fs. It was also noted that by applying a further 150 fs^2 of negative chirp the output pulse could be reduced to 15 fs, a factor of 4.5 reduction in pulse length. Finally the theory was used to show that at the exit of the capillary the pulse length was in fact sub 10 fs.

The XUV spectrum was measured for an input power of 805 mW over a range of gas pressures. The spectrum was observed to clean up as the pressure was increased. At low pressures (50 - 100 mbar) the XUV spectrum was complicated. A harmonic structure could be seen however some of the harmonics were made of two smaller peaks and each harmonic was quite broad. As the pressure was increased the harmonic structure became more ordered until at 170 mbar and above the XUV spectrum consisted of a set of sharp well defined spikes. To understand this process a generation and transmission profile of the capillary was created. This used the transmission of argon over the 18 - 40 nm range coupled with the known pressure profile within the capillary to calculate the absorption limited area within the capillary where HHG could occur and the subsequent XUV be transmitted. It was shown that as the pressure was increased this region was reduced in length. Due to the change in pulse shape during propagation within the capillary different harmonic spectra are generated at different points. At low pressures more of these are summed together, thus creating a more complicated total spectrum. At higher pressures fewer different spectra can be summed producing a simple well defined spectrum.

In Chapter 5 a new capillary was designed and manufactured to replace the original 7 cm capillary. The design changes were made with two aims in mind; To maximise the ionisation peak at the capillary exit and to change the pressure profile so that the transmission overlapped well with the ionisation peak. This led to a new 4.5 cm capillary

with gas inlets 5 and 3 mm from the front and back of the capillary respectively. Based on the transmission calculations for the new capillary it was expected to outperform the old and boast a greater in-situ pulse compression. The XUV flux from both capillaries was measured using an Andor X-ray CCD camera at 50, 100, 150 and 200 mbar. The results showed an increase in flux ranging from 30 to 100 times depending on the gas pressure. The XUV spectrum of the new capillary was measured and using this the maximum flux of the new capillary was calculated as 0.58x10^{12} $ph\ harm^{-1}s^{-1}$.

The final chapter moved away from capillary based HHG and explored the possibility of using a high repetition rate CPA based fibre laser to produce a high flux XUV source. To that end a custom built high harmonic generation and detection system was constructed. A gas cell was chosen as the generation geometry due to the small space within which to work and the ability to maintain low background pressure. The fibre laser runs at a repetition rate of 16.67 kHz, with a pulse length of 380 fs at 1055 nm and a pulse energy of 99 μJ. The detector was an XUV photodiode coated with 150 nm of aluminium to act as a second filter. This reduced the total absorption improving the SNR. The photodiode and filters were held in a custom built, light tight mount situated 5 cm from the gas cell. An XUV signal was detected using xenon as the target gas. Xenon was chosen due to its lower ionisation potential, increasing the likelihood of HHG. The XUV signal strength was measured as a function of QWP angle, gas pressure, input power and focal position to characterise the source and determine its maximum flux. This was calculated as being 1.1x10^{12} phs^{-1}. The spectrum could not be measured at the time due to space limitations and so the per harmonic flux is not known at this point. If the fibre laser is run at its current maximum capacity of 99 μJ at 33.3 kHz then it is possible to double the flux to 2.2x10^{12} phs^{-1}, greater than that of the 4.5 cm capillary.

Future development of both the Ti:Sapphire based system and the CPA fibre laser system could take the form of capillary based HHG. Looking to the future of the Ti:Sapphire laser system first, the 4.5 cm capillary represents an excellent step forward in the development process, however, the work from Chapter 5 suggests that the capillary could be shortened by 3 - 5 mm to produce a better overlap between transmission and ionisation peaks. The pump pulse has been used shown here with a maximum energy of 947 μJ however the laser has the capability of producing 3 mJ pulse energies. This will allow neon to replace argon as the target gas and push the cutoff energy closer to the water window.

The fibre laser based system has one current weakness, the pulse length. This problem may be solved by the use of a xenon filled short hollow core capillary for pulse compression and HHG. Xenon is ten times more nonlinear and easier to ionise than argon and so the lower intensity pulses may be able to self-compress. This work will be studied theoretically at first using the MM-NLSE propagation model. This should enable the flux and energy of both systems to be improved over the next couple of years.

To summarise, two different systems for a high flux XUV source were developed during the course of the work discussed in this thesis. A capillary based XUV source was tested against a MM-NLSE propagation model and improved to generate over an order of magnitude more flux than previous versions. In addition to that, the short hollow core capillaries were shown to be useful for high intensity pulse compression in a small area, opening a possible alternative to long hollow fibre compression techniques. Finally a CPA based fibre laser designed and built at the ORC was used to generate XUV from xenon. The maximum flux measured from both of these sources exceeded 10^{12} phs^{-1} putting them amongst the highest flux HHG sources in the world. Further work and development should improve both of these systems, giving the ORC at Southampton two useable high flux coherent XUV sources.

Appendix A

FROG measurements of output pulse

The following are the FROG measurements in the time (left) and frequency (right) domains of the output pulse from the capillary for a range of pressures and powers. The data is shown as a power run at each pressure, 50, 80, 100, 130 150 and 200 mbar.

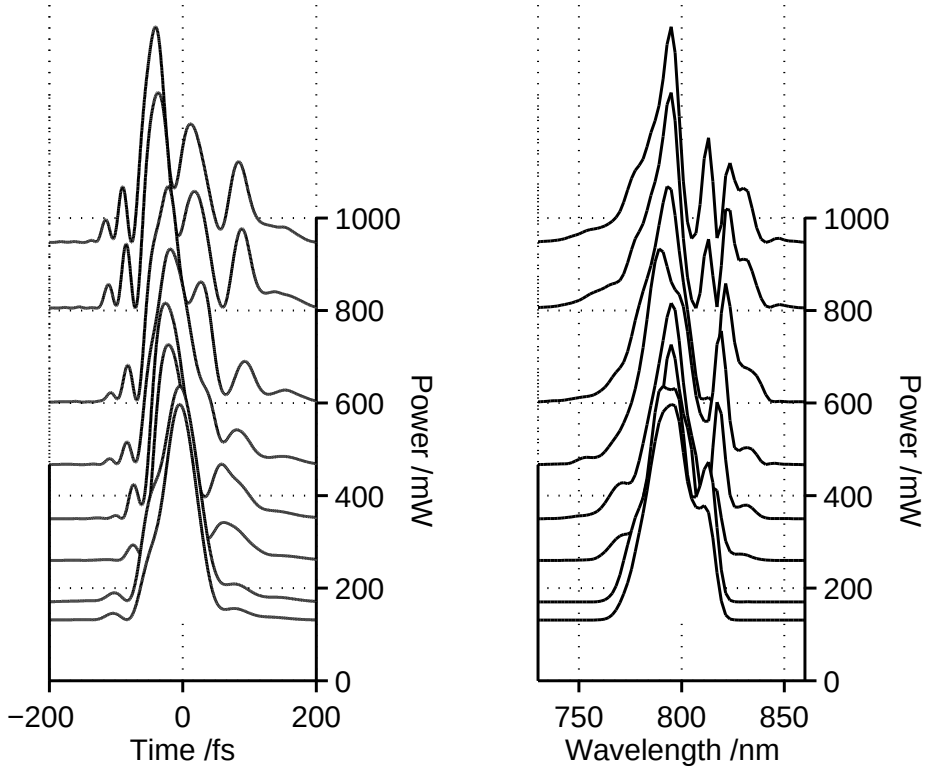

Figure A.1: FROG measurements of output pulse for a range of powers at 50 mbar

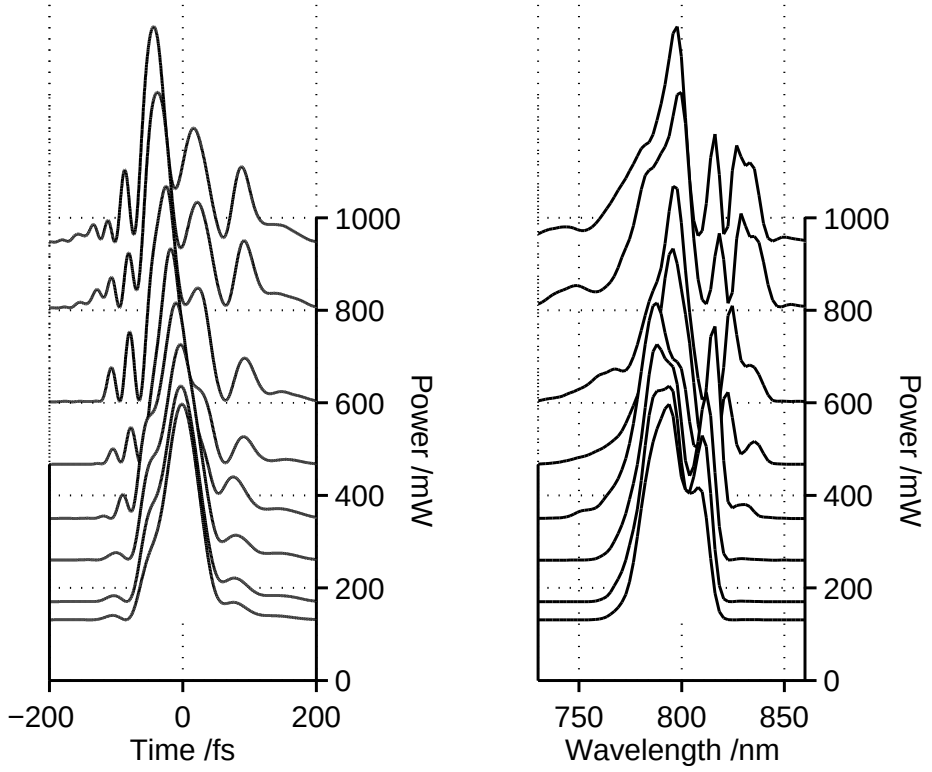

Figure A.2: FROG measurements of output pulse for a range of powers at 80 mbar

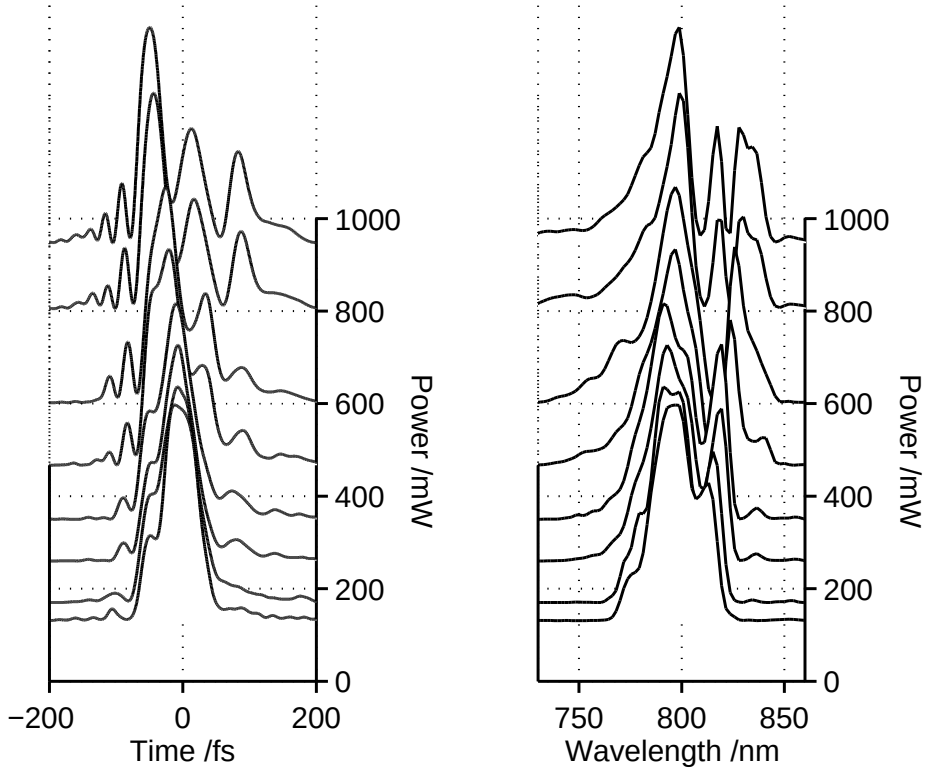

Figure A.3: FROG measurements of output pulse for a range of powers at 100 mbar

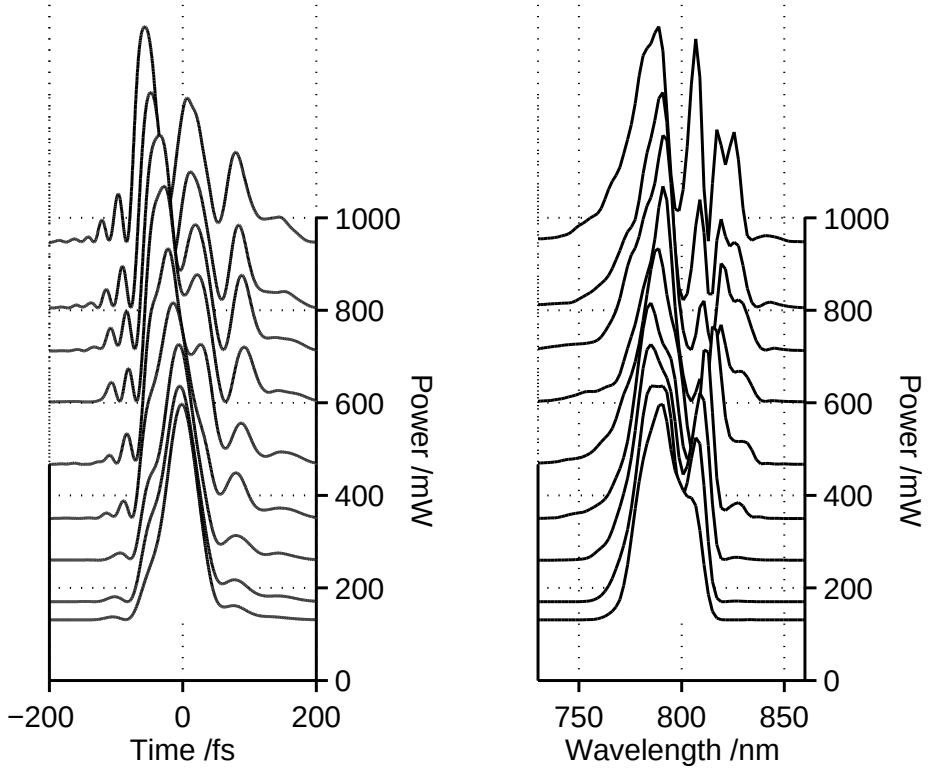

Figure A.4: FROG measurements of output pulse for a range of powers at 130 mbar

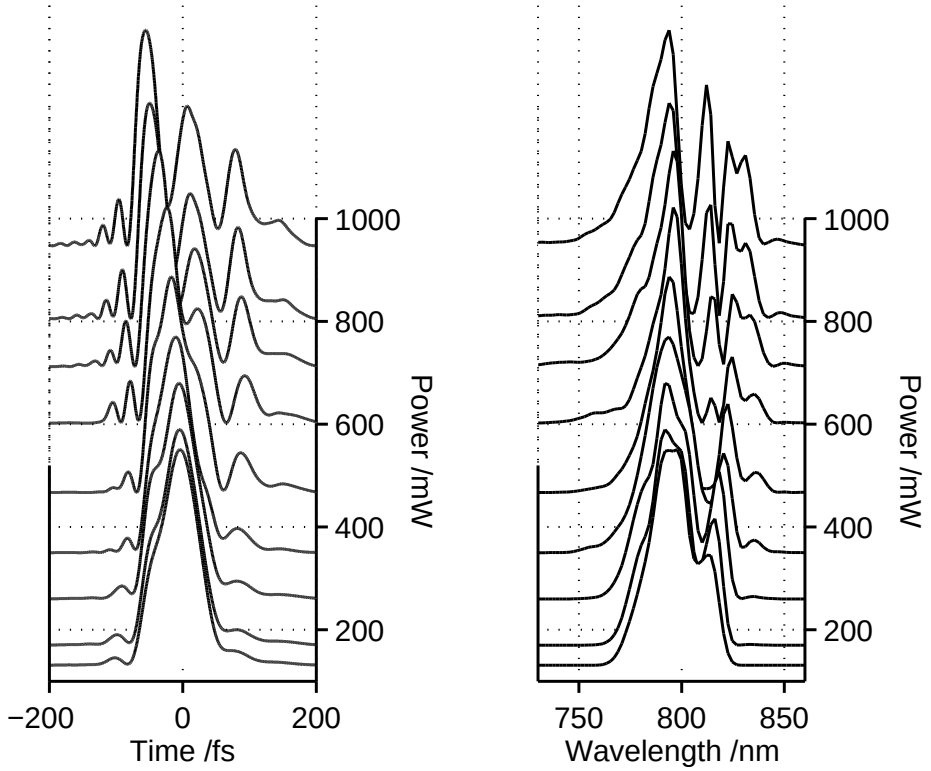

Figure A.5: FROG measurements of output pulse for a range of powers at 150 mbar

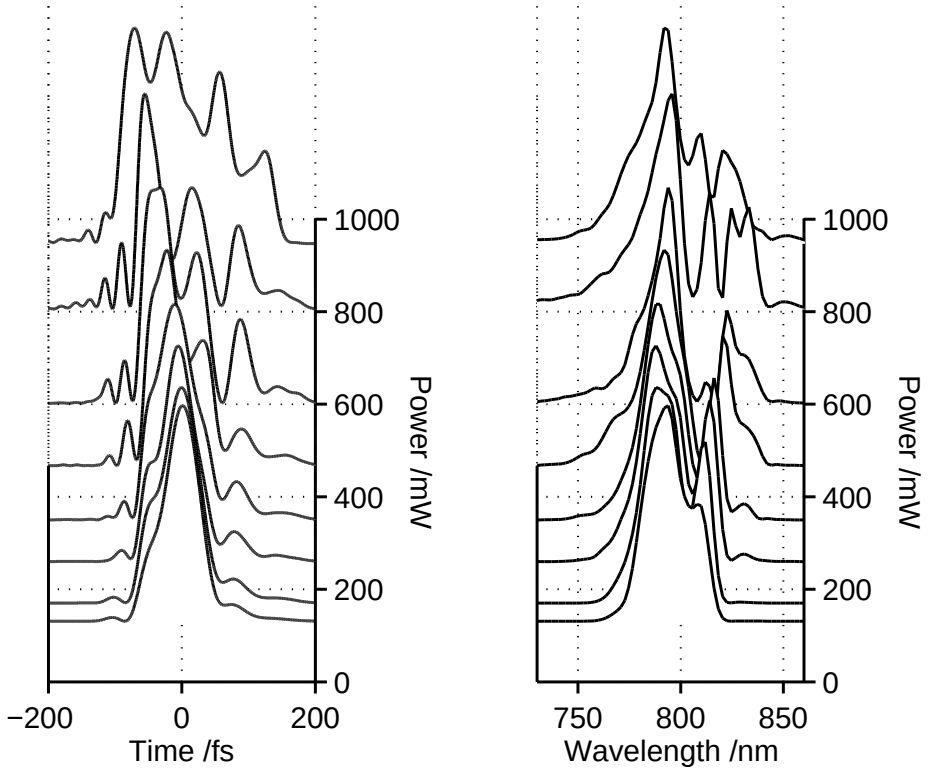

Figure A.6: FROG measurements of output pulse for a range of powers at 200 mbar

Appendix B

XUV spectra as a function of pressure

The following sets of images contain the full set of spectra recorded during the work discussed in Chapter 4. The gas pressure was varied from 50 mbar to 240 mbar, all data is shown on a log scale and which is scaled to the maximum of the data set. The experimental setup used is shown below.

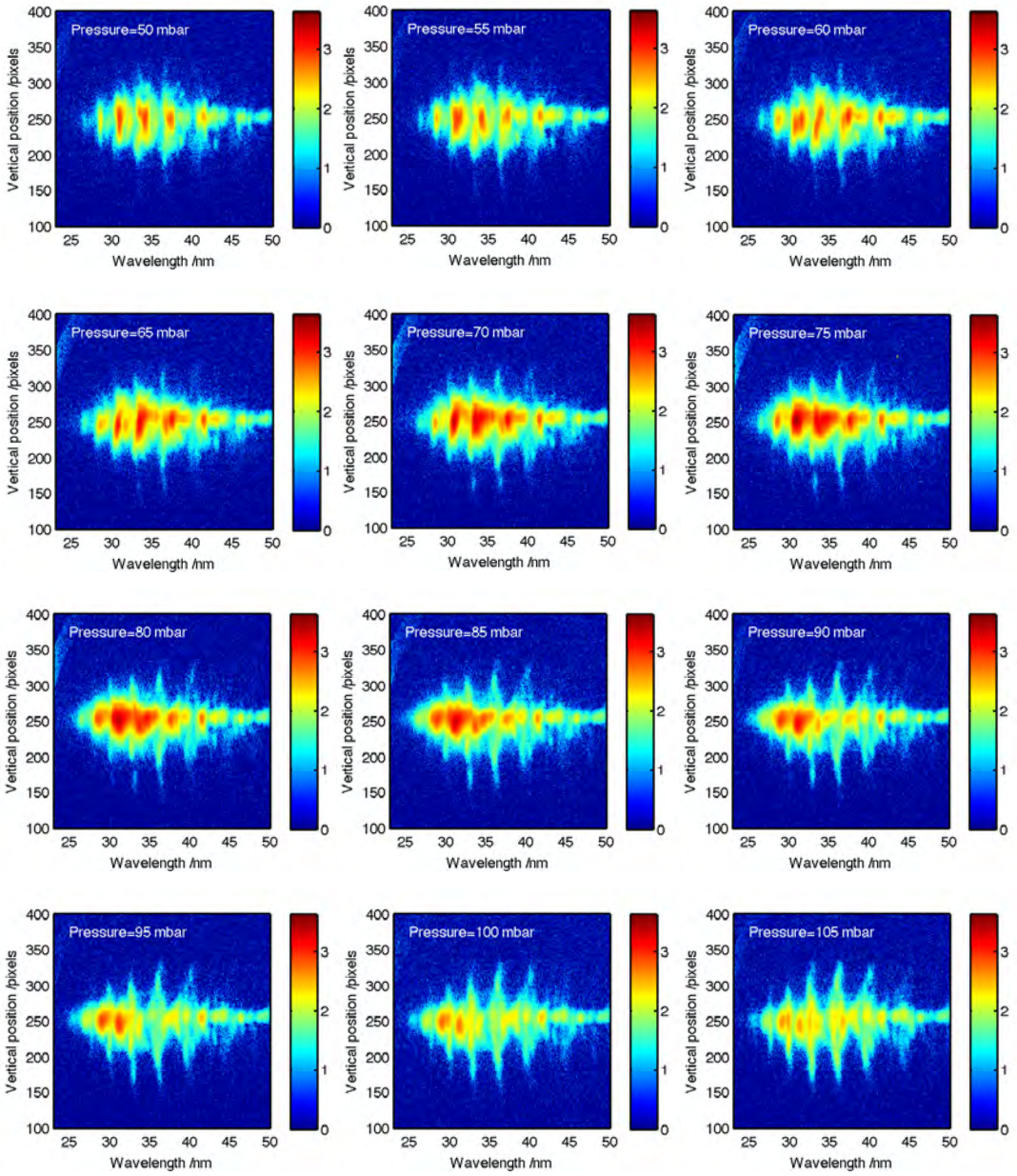

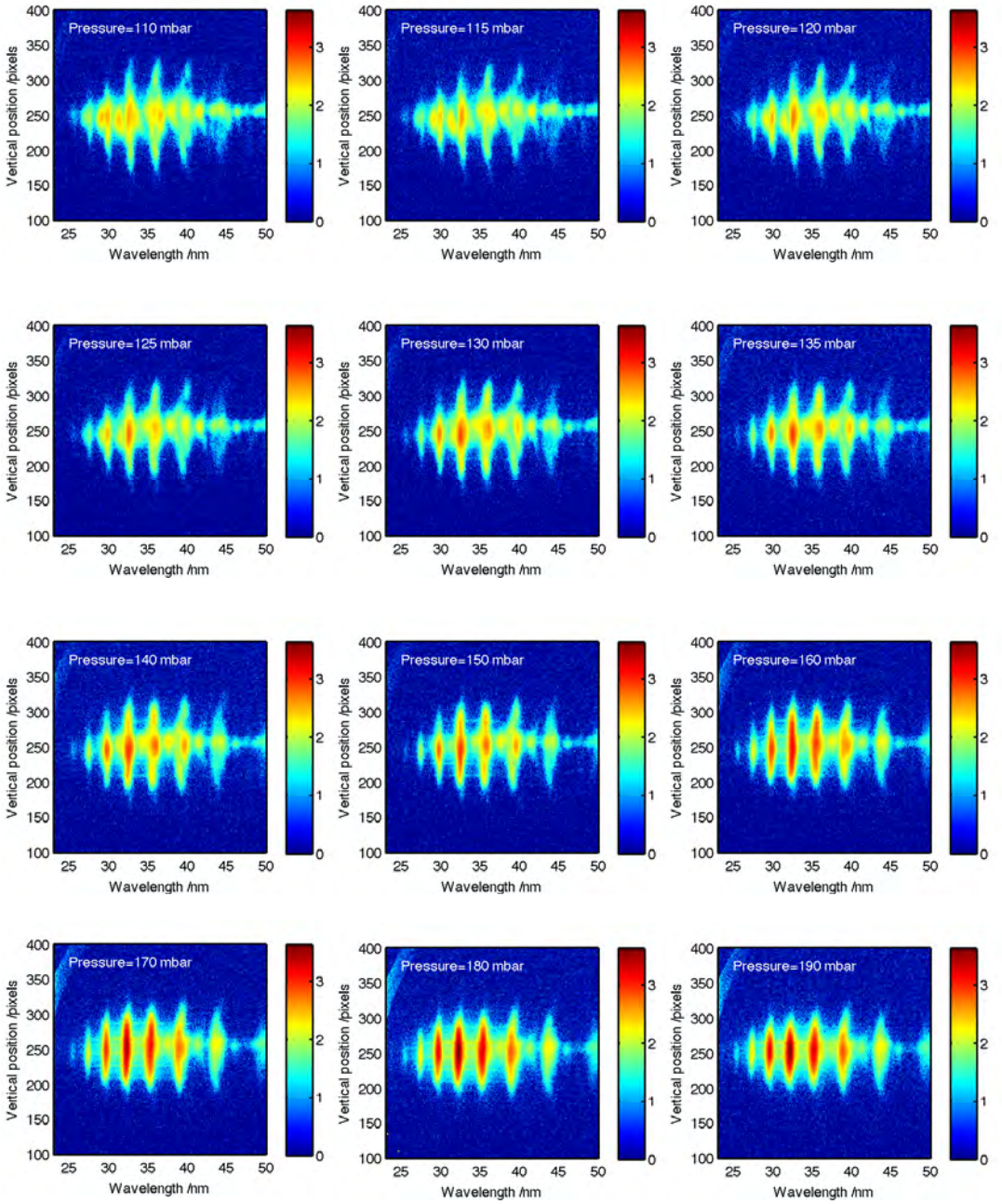
Pressure=110 mbar
Pressure=115 mbar
Pressure=120 mbar
Pressure=125 mbar
Pressure=130 mbar
Pressure=135 mbar
Pressure=140 mbar
Pressure=150 mbar
Pressure=160 mbar
Pressure=170 mbar
Pressure=180 mbar
Pressure=190 mbar
Vertical position /pixels
Wavelength /nm

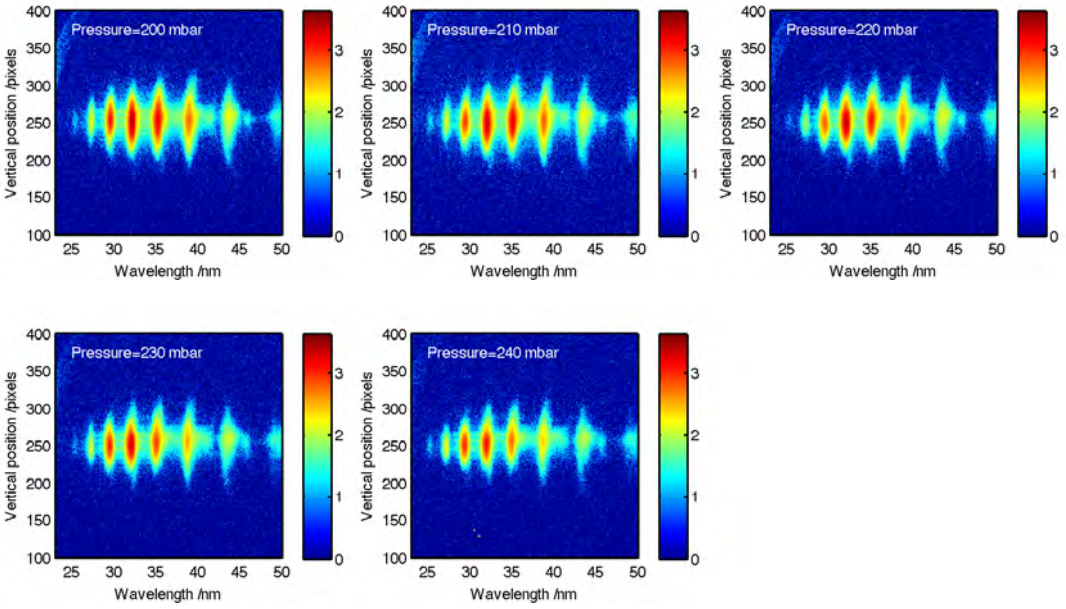
Pressure=200 mbar
Pressure=210 mbar
Pressure=220 mbar
Pressure=230 mbar
Pressure=240 mbar
Vertical position /pixels
Wavelength /nm

Appendix C

Amplifier design

Robert Theobald
15 Briary
Gardens
Tel: 01207 502 522
Shotley Bridge
E-mail: rct@theoptics.co.uk
Consett
www.theoptics.co.uk
County Durham
DH8 0RE

Soft X_ray detector, design approach

For Jonathan Price at ORC, Southampton 29 January 2011

The simplest approach would be to couple the detector into a 50R load. With 2 nF detector, this would roll off the high frequencies with a 100 nS time constant - equivalent to 1.6 MHz. The noise current contribution of the 50R would be very high - about 18 pA per root Hz. Equivalent to shot noise of a massive 1 mA average detector current.

The approach of using the detector capacitance to "remember" the charge from the detector, holds the most promise. The repeating component of the waveform can only contain fundamental and harmonics of the repetition rate.

Each time the soft Xray signal is detected, a packet of charge q will be delivered to the detector, with capacitance C_det. This will cause a voltage step v = q/C_det. For a JFET amplifier, this is a low impedance source at the frequencies we require, so we need to minimise voltage noise.

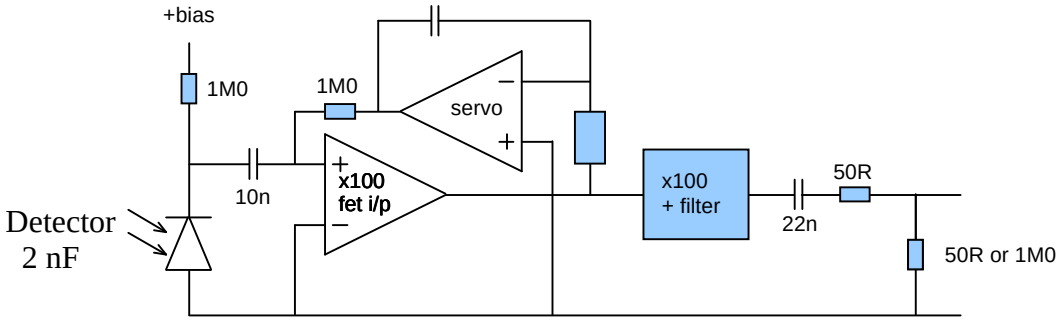

The circuit above shows the general arrangement. The servo adjusts to the d.c. offset at the output of the fet/transistor input amplifier - setting up the gate-source voltage for approximately 0V at the output. It reaches a steady state when the steady current into the detector node balances the average input current (approx. q x repetition frequency). When it has settled - after a few cycles - this results in a sawtooth voltage with a fast step, when q arrives, followed by a linear ramp to the beginning of the next fast step.

Noise: Note that the detector current isn't very amenable to noise analysis! Most of the time there is no current flow so no shot noise. L.F. noise comes from the 1M0 resistors. As frequency is increased, the decreasing detector reactance shunts this until it is reduced below the voltage noise of the following amplifier.

Looking at this more closely:

Noise current of two x 1M0 will be 179 fA/root(Hz).
Noise voltage of preamp is about 800pV/root(Hz).
Ratio is reactance at change-over frequency = 4K5. With 2 nF this occurs at about 18 kHz.
With smaller capacitance detector this frequency will be higher in inverse proportion. A high-pass filter is needed to remove this L.F noise.

Preamp requirements:
1) Pulse-by-pulse operation, where it is possible to see the amplitude of each pulse. The signal needs to have rise-time fast enough to trigger an oscilloscope and recovery time short enough to have minimal effect on the next pulse. Faster rise-time means more bandwidth and therefore noise.
2) Averaging oscilloscope, or spectrum analyser operation. Here, most of the energy is close to the repetition rate. The detector capacitance always appears in any attempt to calibrate sensitivity.
To summarize: Charge from the detector is integrated by the detector capacitance, converting it from an impulse to a step. A steady current from the servo ramps the voltage back in time for the next step, producing a sawtooth waveform. Subsequent amplification and filtering is aimed at converting this to an output pulse proportional to the step height, whilst ignoring the steady ramping of the sawtooth. The output is a pulse which is shorter than the repetition period, so pulses don't run into one another.

Waveforms:

Above shows spice response to pulses starting after 30 µs. By 200 µs it has established a steady baseline at 5 mV (This 5 mV is spice-modelled input offset voltage of servo amplifier).

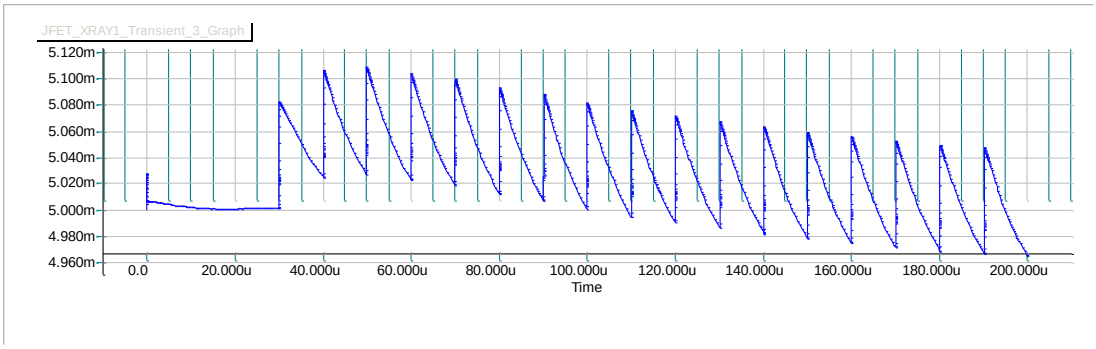

After high and low pass filtering. 10 to 90% risetime is about 200 ns. Half height width is 1.4 µs. Note that after 2 or 3 pulses, it has established a baseline. The steady (-50 mV due to op-amp offset) won't pass through the final d.c. blocking capacitor.

The following shows the waveform difference into 1M0 and 50R loads. With 1M0 load one high-pass pole is moved to a much lower frequency. Also the output is double when it is not loaded by the 50R load.

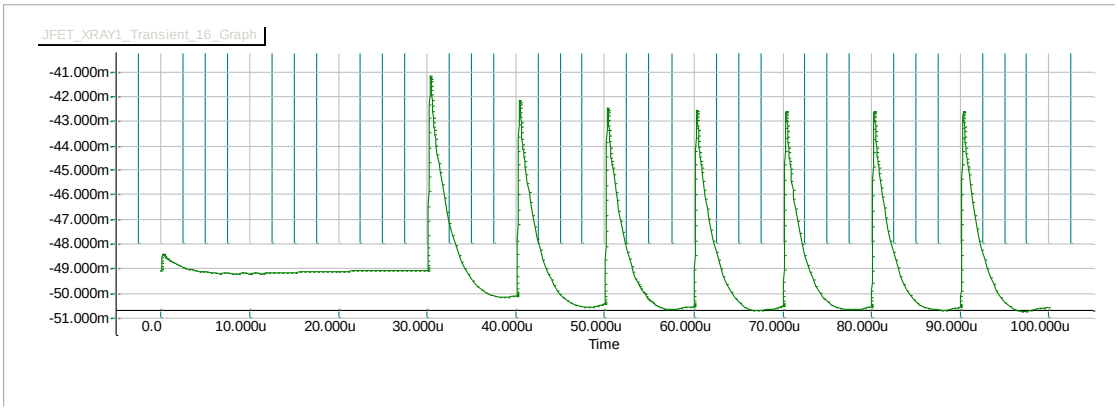

Graph above is output into 1M0. Below into 50R.

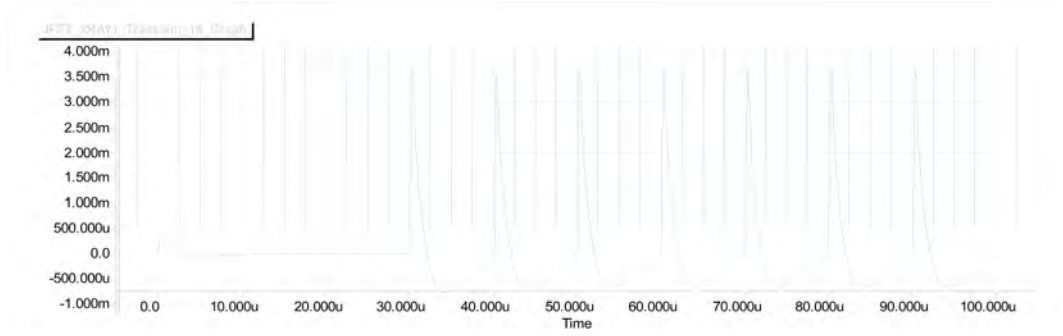

The following graph shows frequency response when driven by 10 mVrms = - 40 dB(V) in series with the detector. The Y-axis is dB relative to 1Vrms. So -40 to nearly +40 dB is just under 10,000:

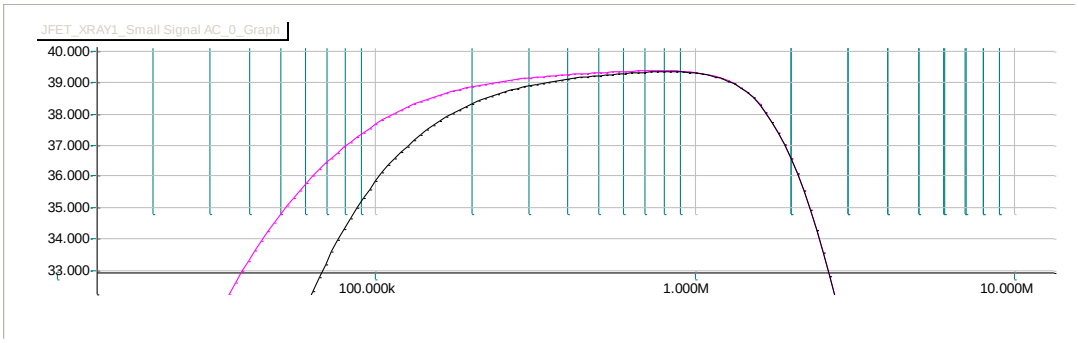

The curves are before and after the output blocking capacitor. So double the output seen, if a 50R load is attached.
When driving a 1M0 scope input, both curves have the wider LF bandwidth. The -3 dB points above are: 66 kHz, 110 kHz and 2.0 MHz. This needs some explanation for lower rep rates:
The aim is to pass on the trigger edge, and maintain a good S/N ratio. This is accomplished for lower rep rates. It maintains the same rise-time and pulse shape, but because this is a shorter duty cycle, the rep rate component becomes less.

High and low pass filter sections and x100 amplifier:

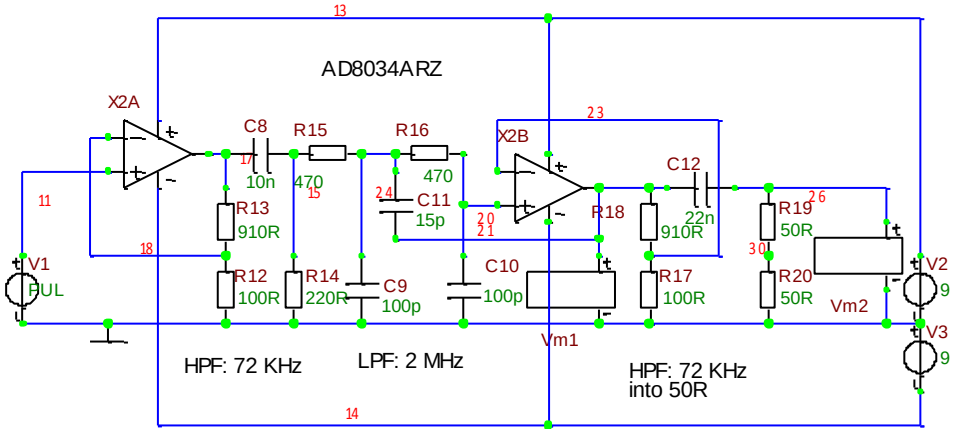

The amplifier above follows the low voltage noise input stage. That stage has input noise of less than 1 nV/~ with gain approaching 100. Noise output will be just under 100 nV/~. The op-amp above is a "fast-fet" type with typically 11 nV/~. Although the data sheet claims 80 MHz at unity gain, this does not translate to a gain-bandwidth figure. With feedback for a gain of ten, the bandwidth is about 4 MHz.

Input stage is a simple x10 gain block, with gain 1 + R13/R12
C8 and R14 form a single pole high-pass at 72 kHz
R15/16 and C9/10 define a 2nd order low-pass at around 2 MHz.
R17/18 define second stage gain, as before.
C11 increases h.f. gain near the cut-off frequency, for close to critical damping (Bessel).

C12 acts with the 50R output resistor and matched 50R load. Together they have a 2.2 µs TC, which is the same as C8 and R14. Using a 2 pole high-pass causes undershoot after the pulse. It seemed useful to offer the choice, as explained with waveforms on the previous page.

Overall gain of the above op-amp stages is therefore x100 into a high impedance, or x50 into 50R.

Overall gain of the whole detector, preamplifier and fillter is q/C(det) x 9200 into high impedance, or q/C(det) x 4600 into 50R.
Example 1 pC and 2 nF gives 2.3 V into 50R. Note that this is the amplitude of the fast trigger edge excursion which has about 160 ns rise-time. Noise levels seen during testing, should allow operation down to around 10 fC.

Appendix D

Publications

D.1 Optics Express paper based on the work from Chapter 3

Modal effects on pump-pulse propagation in an Ar-filled capillary

Richard T. Chapman,[1] Thomas J. Butcher,[2] Peter Horak,[2,*] Francesco Poletti,[2] Jeremy G. Frey,[1] and William S. Brocklesby[2]

[1] *School of Chemistry, University of Southampton, Southampton SO17 1BJ, United Kingdom*
[2] *Optoelectronics Research Centre, University of Southampton, Southampton SO17 1BJ, United Kingdom*
** peh@orc.soton.ac.uk*

Abstract: Accurate three-dimensional modelling of nonlinear pulse propagation within a gas-filled capillary is essential for understanding and improving the XUV yield in high harmonic generation. We introduce both a new model based on a multimode generalized nonlinear Schrödinger equation and a novel spatio-spectral measurement technique to which the model can be compared. The theory shows excellent agreement with the measured output spectrum and the spatio-spectral measurement reveals that the model correctly predicts higher order mode contributions to spectral broadening of the pulse. Fluorescence from the excited argon is used to verify the predicted ion distribution along the capillary.

OCIS codes: (190.7110) Ultrafast nonlinear optics; (080.1510) Propagation methods;

References and links

1. A. L'huillier and P. Balcou, *High-Order Harmonic Generation in Rare Gases with a 1-ps 1053-nm Laser.* Phys. Rev Lett. **70**, 774-777(1993).
2. I. Christov, H. Kapteyn, and M. Murnane, *Quasi-phase matching of high-harmonics and attosecond pulses in modulated waveguides.* Opt. Exp. **7,** 362-367 (2000).
3. I.P. Christov, M.M. Murnane, and H.C. Kapteyn, *High-Harmonic Generation of Attosecond Pulses in the "single-cycle" Regime*. Phys. Rev Lett. **78**, 1251-1254 (1997).
4. I.P. Christov, *Control of high harmonic and attosecond pulse generation in aperiodic modulated waveguides.* J. Opt. Soc. Am. B **18**, 1877-1881 (2001).
5. C. Courtois, A. Couairon, B. Cros, J. R. Marquès, and G. Matthieussent, *Propagation of intense ultrashort laser pulses in a plasma filled capillary tube: Simulations and experiments.* Phys. Plas. **8,** 3445-3456 (2001).
6. M. Nurhuda, A. Suda, M. Hatayama, K. Nagasaka and K. Midorikawa, *Propagation dynamics of femtosecond laser pulses in argon.* Phys. Rev. A **66**: p. 1-8 (2002).
7. R.K. Nubling and J.A. Harrington, *Launch conditions and mode coupling in hollow-glass waveguides.* Opt. Eng. **37**, 2454-2458 (1998).
8. C.A. Froud, R.T.Chapman, E.T.F.Rogers, M.Praeger, B.Mills, J.Grant-Jacob, T.J.Butcher, S.L.Stebbings, A.M. de Paula, J.G.Frey and W.S.Brocklesby, *Spatially resolved Ar * and Ar +* imaging as a diagnostic for capillary-based high harmonic generation.* J. Opt. A **11**, 054011 (2009).
9. F. Poletti and P. Horak, *Description of ultrashort pulse propagation in multimode optical fibers.* J. Opt. Soc. Am. B **25,** 1645(2008).
10. E.A.J. Marcatili and R.A. Schmeltzer, *Hollow Metallic and Dielectric Waveguides for Long Distance Optical Transmission and Lasers.* Bell Tech. Syst. J. **43**, 1783-1809 (1964).
11. F. Poletti and P. Horak, *Dynamics of femtosecond supercontinuum generation in multimode fibers.* Opt. Exp. **17**, 6134-6147 (2009).
12. V.S. Popov, *Tunnel and multiphoton ionization of atoms and ions in a strong laser field (Keldysh theory).* Physics-Uspekhi **47**, 855-885 (2004).

1. Introduction

High-power ultrashort laser pulses at near-infrared wavelengths propagating in gas-filled capillaries can form a compact source of extreme ultraviolet (XUV) and soft X-ray radiation by high-harmonic generation (HHG) [1]. Maximisation of the frequency conversion efficiency

requires a detailed understanding of the radiation-atom interaction mechanism as well as the propagation properties of both the near-infrared pump in the presence of a partially ionized gas, and of the generated XUV. Previous theoretical studies of capillary-based HHG by Christov et al. [2] have used numerical solutions of the 3-dimensional version of the scalar wave equation. This work focused on understanding attosecond pulse generation [3] and quasi phasematching within waveguides [4]. Experimentally measurable predictions of these theories have typically centred on the temporal profile of the pump and the harmonics generated. In this work, we focus on understanding the spectral and spatial distribution of the pump. We introduce a numerical model of pump pulse propagation based on a multimode generalized nonlinear Schrödinger equation. This model is verified firstly by simple measurement of the total output spectrum, a commonly used procedure [5, 6] which only tests the summation over all modes. More stringent testing of the model is then demonstrated by measuring the spatio-spectral distribution of the output power in the far field, and by measuring the evolution of the ionization along the capillary length. Both of these are much more sensitive to nonlinear mode coupling than the summed spectral output.

2. Experimental configuration

The experimental setup is shown in Fig. 1. A 40 fs laser pulse centred at 790 nm, with a 1 kHz repetition rate, was coupled into a 70 mm long hollow capillary with internal diameter 150 µm using a 0.5 m plano-convex lens. The ratio of beam spot size, w, to capillary radius, a, was 0.64, giving optimum coupling into the lowest order, EH_{11}, mode [7]. The input pulse energy was varied between 378 and 840 µJ (corresponding to an intensity range of 2.8–6.3 $x10^{14}$ Wcm^{-2}) by inserting reflective neutral density filters into the beam.

The central region of the capillary was filled with argon gas via a pair of 300 µm holes drilled 20 mm from either end of the 70 mm long capillary. Argon gas at pressures up to 200 mbar could be introduced into the system from a pressure-regulated supply. The capillary was mounted within a vacuum chamber kept at ~ 10^{-4} mbar. The overall gas pressure profile was calculated using computational fluid dynamics and can be approximated by a central 30 mm flat region with linear pressure gradients in the 20 mm regions at each end of the capillary.

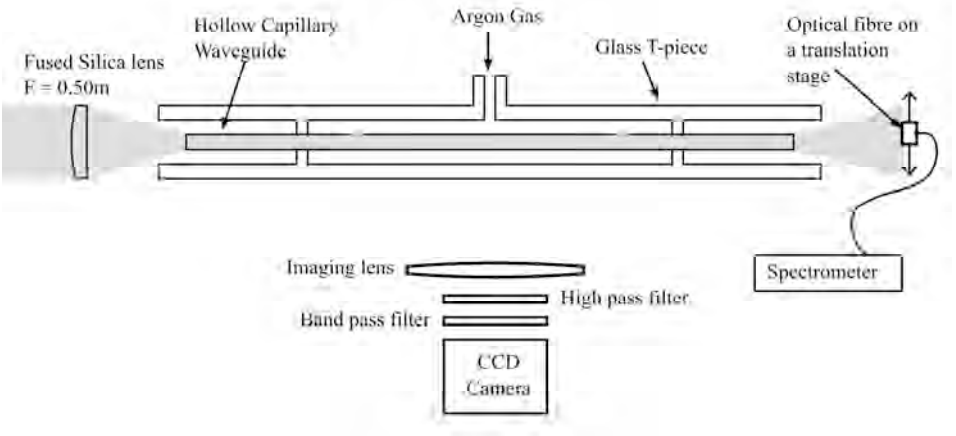

Fig. 1. Schematic for measuring the spatio-spectral output and argon ion fluorescence from a capillary running in a HHG regime.

The capillary output is a combination of the pump laser pulse and the generated XUV. The pump laser pulse was reflected out of the vacuum chamber into a fibre-coupled spectrometer mounted on a translation stage. The 125-µm diameter fibre end was placed at the centre of the beam and translated radially outwards across the whole beam profile. The argon ion

fluorescence was imaged using the setup shown in Fig. 1, consisting of a 35 mm focal length lens imaging the capillary from the side onto a CCD. A high pass and bandpass filter were used to single out the 488 nm emission line that is emitted by singly ionised argon [8].

3. Numerical model

For the accurate theoretical description of the pump pulse propagation we developed a numerical model based on a multimode generalized nonlinear Schrödinger equation [9] which we extended to include ionization and plasma effects [5]. To this end, the electric field of the laser pulse is written as a sum over modal contributions

$$E(r,z,t)=\frac{\sqrt{2Z_0}}{2\pi}\sum_n\frac{1}{2}F_n(r)A_n(z,t)e^{i(k_0z-\omega_0t)}+c.c. \tag{1}$$

where $Z_0=\sqrt{\mu_0/\varepsilon_0}$, $F_n(r)$ is the transverse mode function of the EH_{1n} mode of the capillary [10] normalized to $\int rdr\left|F_n(r)\right|^2=1$, and A_n is the pulse envelope such that the modal power is given by $\left|A_n\right|^2/(2\pi)$ in units of Watt, and the temporal dependence of the carrier wave has been factored out. Note that in writing Eq. (1) we have restricted the analysis to circularly symmetric modes only, assuming a symmetric pump laser mode and preferential coupling between modes of the same symmetry [9, 11].The modal evolution of the pulse along the capillary is then given by

$$\begin{aligned}\frac{\partial A_n}{\partial z}&=iD_n+in_2(z)k_0\sum_{k,l,m}Q_{nklm}A_kA_lA_l^*+\frac{i}{2}k_0\int rdrF_n(r)S(r,z,t)n_{pl}^2(r,z,t)\\&-\frac{1}{2}\int rdrF_n(r)S(r,z,t)\frac{\rho_0(r,z,t)W(r,z,t)U}{\left|S(r,z,t)\right|^2/(2\pi)}\end{aligned} \tag{2}$$

Here, $S=\sum F_nA_n$, D_n describes modal dispersion and losses, including high-order dispersion, and the subsequent terms model the gas nonlinearity, plasma refractive index, and ionization losses of the pump, respectively. In Eq. (2), $n_2(z)$ is the nonlinearity of the neutral Ar gas as a function of the local pressure, k_0 is the propagation constant at the pump frequency, $Q_{nklm}=\int rdrF_nF_kF_lF_m$ are the mode overlap integrals, n_{pl} is the refractive index of the local plasma density resulting from ionization of the neutral gas by the propagating pulse, ρ_0 and W are the neutral gas density and ionization rate, respectively, and U is the ionization potential [5, 9].The ionization rate W is calculated using the Keldysh theory [12].For the results presented in this work, the set of equations (2) was solved by a Fourier split-step method for typically 20 modes, which we found sufficient for an accurate description of our experimental parameters. We emphasize that this model is capable of describing the full temporal dynamics of the propagating light in three dimensions, including modal effects such as group velocity mismatch. Therefore, as will be discussed in the following sections, the model allows us to investigate detailed spatial and spectral correlations, beyond what was possible with a simpler, earlier model [8].

4. Comparison of experimental results with numerical model

The predicted and measured total output spectra for three different input powers are shown in figure 2. The theoretical and experimental spectra show excellent agreement with not only the

degree of blue shifting observed, but also the complex spectral shapes that occur at higher powers. We believe this is the first evidence that the blue-shifted shoulder of the spectrum is primarily located in higher order modes.

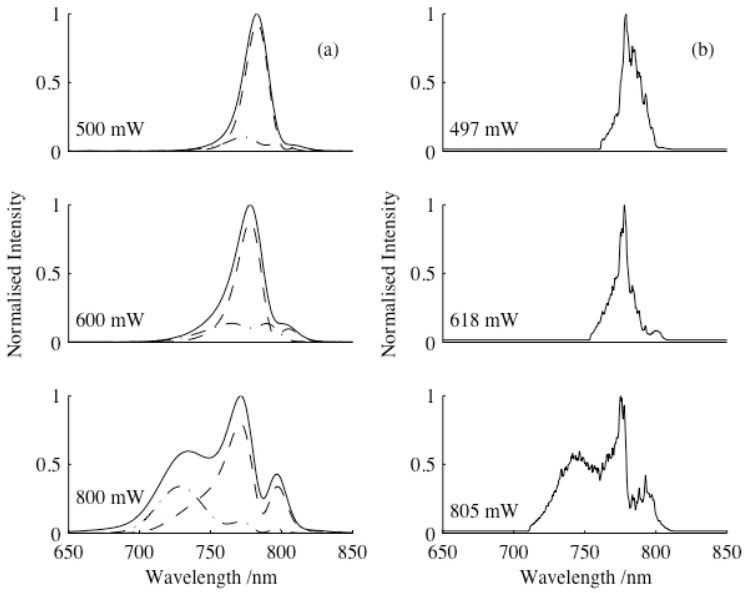

Fig. 2. Predicted (a) and experimental (b) output spectra measured for three input powers, shown. The predicted data shows the total spectrum (solid), as well as those for the EH_{11} (dashed) and EH_{12} (dot dashed) modes. At each laser power, the summed spectral intensity of the modes is normalised to a peak level of 1, as is the experimental data.

Figure 2 shows that at lower powers the EH_{11} mode dominates the spectrum as nonlinear mode coupling is small. The model also predicts a walk-off between the modes, this is calculated to be 8 fs between the EH_{11} and the EH_{12} modes along the 7 cm of the capillary. As the power is increased, more energy is coupled into the EH_{12} and other higher modes. The theoretical model indicates that nonlinear mode coupling is greater at the trailing edge of the pulse due to plasma defocusing, which leads to the observed blue shifted spectra in the higher order modes. Experimentally, the modal distribution cannot be directly determined from a summed spectrum of the kind shown in figure 2, although the agreement between theory and experiment allows us to infer that the modal distribution is correct.

In order to test whether the model correctly predicts the distribution of intensity in high order modes, we make use of the fact that as the modes propagate into the far field their spatial divergence is strongly dependent on their order, with higher order modes showing significantly greater angular spread. This means that the radial distribution of the spectral intensities has contributions from different modes at different radii (although the modes are not completely separated). Thus the spatio-spectral intensity distribution in the far field is very sensitive to any variation in the intensities of individual modes, and its measurement can provide a sensitive test of the ability of the numerical model to correctly predict the modal distribution.

Figure 3 shows the calculated (a) and measured (b) spectral intensity distribution as a function of radial distance from the beam axis. The theoretical intensity profiles of the EH_{11} and EH_{12} modes are shown for comparison. It is clear from both theoretical and experimental distributions that the differences in the intensity distributions of the modes are large. The EH_{11}

mode has significant contributions at around 790 and 810 nm, and the blue-shifted components at about 740 nm show the same radial profile as the EH_{12} mode, with an on-axis peak, and another ~8 mm from the axis. This distribution is clear in the theoretically modelled intensity distribution. In the measured distributions, the general features of the pattern are repeated. The EH_{11} mode appears at 780 and 810 nm, and the blue-shifted peak at 760 nm has the radially narrower distribution of the EH_{12} mode. However, several differences are clear. The first is that more extensive off-axis blue shifting is seen in the experimental data, implying greater broadening in the higher order modes than was predicted. Secondly, an extra peak can be seen close to the centre of the beam at ~800 nm in the experimental data. The shape of the EH_{11} peaks around 790-810 nm look similar to the spectral distortion caused by SPM, which produces first a splitting, and then a central peak, rising between the split peaks as the nonlinear phase shift increases. Both of these differences suggest that the nonlinear shifting of the spectrum is slightly stronger in the experiment than predicted by theory.

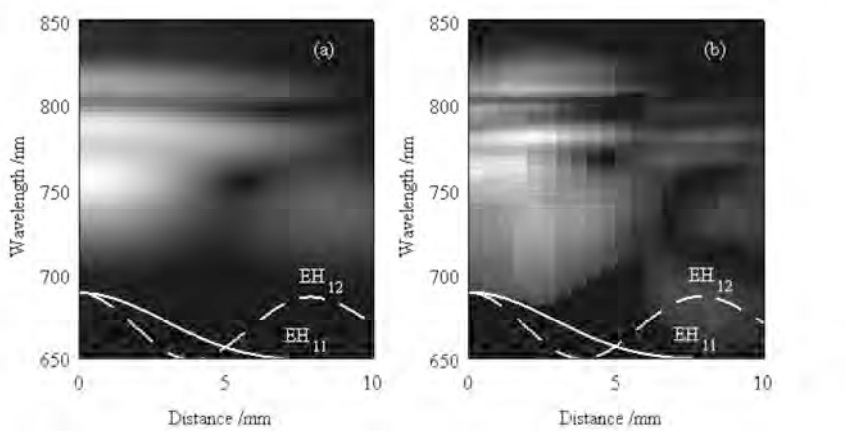

Fig. 3. Predicted (a) and experimental (b) spectral intensity plots in the lambda-r-plane. The solid and dashed white lines show the far-field profiles of the EH_{11} and EH_{12} modes respectively.

While spectral measurements at the capillary exit are a good test of the end point of the model, measurement of the Ar ion fluorescence along the length of the capillary provides a test of the model along the whole propagation length. Experimentally, the fluorescence, produced by excited Ar ions created by the pump pulse, is filtered and imaged from the side. The integrated fluorescence from each point along the capillary length can be compared directly to the ionisation levels predicted by the propagation model.

The integrated argon ion fluorescence and the theoretical integrated ionisation are compared in figure 4. The measured 488 nm argon ion fluorescence should be proportional to the calculated ionisation level within the capillary. The beat positions for the EH_{11} and EH_{12} modes calculated for linear propagation are shown as vertical dashed lines; as expected, both experimental and calculated beat positions are clearly shifted from these positions by the effects of nonlinear propagation. The initial increase in ionisation at the capillary entrance is observed in both theory and experiment and the first two major peaks appear at approximately the same positions within the capillary. The smaller structures within these major peaks do not correlate.

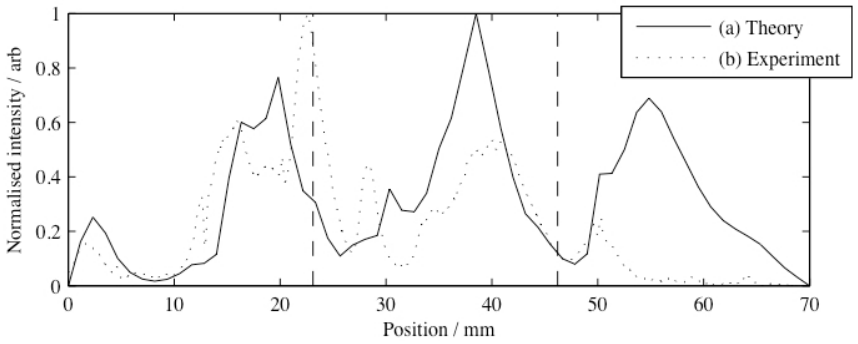

Fig. 4. Comparison of the summed radial ionisation (a) and the imaged argon ion fluorescence (b) along the length of the capillary. The vertical dashed lines show the beat positions for linear mode beating between the EH_{11} and EH_{12} modes.

The final major peak predicted by the numerical model is observed at the same point in the capillary but is significantly smaller in length and size. The discrepancy may be due to losses at the gas inlets within the capillary wall. These have been observed as increased scattering during experiments and are not included within the numerical model.

Conclusion

In this paper we have introduced a new method for numerically modelling nonlinear propagation within a capillary used for HHG. We have compared this model to the spectral output of the capillary and observed strong correlation. The model predicts the modal variation of the pulse shape, and the spatio-spectral measurement technique allows detailed comparison of not just the integrated spectrum, but also the individual modal contributions, because of the differences in the far-field mode patterns, validating the model and the coupling terms chosen. Understanding the modal distribution will allow modelling of XUV phase matching in the presence of nonlinear mode mixing, which is important for XUV generation at high intensities. It will also allow better understanding of the spatial profiles of the compressed pump pulses predicted by the model, providing a route to their exploitation.

Acknowledgments

This research was supported by Research Councils UK Basic Technology Research Programme, Engineering and Physical Sciences Research Council and the University of Southampton.

D.2 CLEO Europe posters based on work from Chapters 4 and 5

The following pages show the Abstracts and scaled down posters that were presented at CLEO Europe, May 2011. The work is based on chapters 4 and 5 and covers the pulse self-compression and new capillary design respectively.

High intensity pulse self-compression in short hollow core capillaries

***Thomas J. Butcher*[1], *Patrick N. Anderson*[1], *Peter Horak*[1], *Jeremy G. Frey*[2], *William S. Brocklesby*[1]**

1. Optoelectronics Research Centre, University of Southampton, Highfield, Southampton, SO171BJ, UK

2. School of Chemistry, University of Southampton, Highfield, Southampton, SO171BJ, UK

The drive for shorter pulses for use in techniques such as high harmonic generation and laser wakefield acceleration requires continual improvement in post-laser pulse compression techniques. The two most commonly used methods of pulse compression for high intensity pulses are hollow capillary compression via self-phase modulation (SPM) [1] and the more recently developed filamentation [2]. Both of these methods can require propagation distances of 1-3 m to achieve spectral broadening and compression. Additionally, hollow capillary compression requires post compression of the broadened pulse by chirped mirrors. Filamentation trades the efficiency of hollow capillary compression (67%) for ionisation-induced pulse self-compression. A mixture of SPM and plasma generation increases the spectral bandwidth of the pulse; however this occurs only in a small region at the centre of the beam. Spatial filtering is required to achieve the shortest pulses, reducing the efficiency to 20%. Although the majority of hollow core capillary compression requires long propagation distances, compression in short capillaries [3] with significant plasma generation has been demonstrated to be a promising technique.

Here we present pulse self-compression in a 7 cm hollow core capillary with a reduction in pulse length from 53 fs to 16 fs shown in figure 1. The efficiency of this process (37%) is greater than that of filamentation, whilst maintaining the benefits of pulse self-compression, removing the need for post-capillary compression.

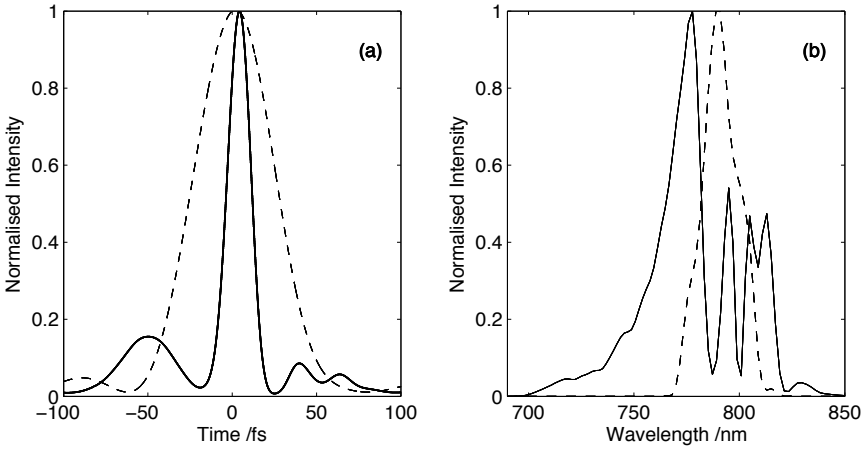

Fig. 1 Comparison of the temporal (a) and spectral (b) distributions of the pulse prior to (dashed) and following (solid) compression within the capillary. The output pulse has a FWHM of 16fs compared to 53fs for the input pulse.

A 53 fs, 600 μJ pulse centred at 790 nm was coupled into a 7 cm hollow core capillary with a core radius of 75 μm. Argon gas was injected into the capillary through two holes drilled 2 cm from either end Typical pressures were between 50 and 200 mbar. The time profile of the measured 16 fs output pulse and its corresponding spectrum are shown in figure 1 in comparison with the input pulse. Propagation of the pulse is modelled using a multimode nonlinear Schrödinger equation, including the effects of ionization. The observed spectral broadening due to both SPM and plasma generation matches that predicted by the model. The measured efficiency of this process is 37%.

We have observed similar spectral and temporal changes in capillaries as short as 4.5cm, with scaleable pressures and powers. Unlike both filamentation and traditional hollow capillary compression the propagation distance required for significant spectral broadening is small, reducing the bench space required. In addition the self-compression of the pulse can save both space and money by removing the need for post compression. Thus we have produced an efficient and compact alternative for compressing high intensity pulses.

References

[1] S. Bohman, A. Suda, T. Kanai, S. Yamaguchi, K. Midorikawa, "Generation of 5.0 fs, 5.0 mJ pulses at 1kHz using hollow-fiber pulse compression", Opt. Lett. **35**, 1887-1889 (2010)

[2] O. Varela, B. Alonso, I. J. Sola, J. San Román, A. Zair, C. Méndez and L. Roso, "Self-compression controlled by the chirp of the input pulse", Opt. Lett. **35**, 3649-3651 (2010)

[3] N. L. Wagner, E. A. Gibson, T. Popmintchev, I. P. Christov, M. M. Murnane and H. C. Kapteyn, "Self-Compression of Ultrashort Pulses through Ionization-Induced Spatiotemporal Reshaping", Phys. Rev. Lett. **93**, 173902 (2004)

High intensity pulse self-compression in short hollow core capillaries

Thomas J. Butcher[1], Patrick N. Anderson[1], Richard T. Chapman[2], Peter Horak[1], Jeremy G. Frey[2], William S. Brocklesby[1]

1. Optoelectronics Research Centre, University of Southampton, Highfield, Southampton, SO171BJ, UK
2. School of Chemistry, University of Southampton, Highfield, Southampton, SO171BJ, UK

UNIVERSITY OF Southampton
Optoelectronics Research Centre
School of Chemistry

Experimental work

- We have successfully shown pulse self-compression within a 7 cm capillary from 53 fs to 27 fs without dispersion compensation, and compression to 16 fs with.
- The nonlinearity observed generates a spectrum that can support sub 10 fs pulses, however these very short pulses have not yet been observed in the far field due to divergence of the beam. More on this at the bottom of the page!
- We hope to use this technique and our model to develop a new, more compact high energy pulse compressor.

Experimental Set-up

A 50fs pulse centered at 790nm is coupled into the 75μm core of our 7 cm capillary. The laser repetition rate is 1kHz and the pulse energy is varied from 170μJ to 805μJ. Argon gas is injected into the capillary through two 500μm holes and can be varied from 0 mbar to 240 mbar. The output pulse is directed out of the vacuum and into a *Swamp Optics 8-20-USB Grenouille FROG* for characterisation.

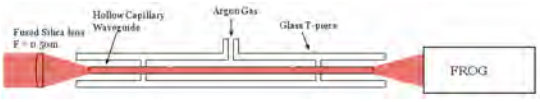

Theoretical work

- We have developed a three dimensional nonlinear propagation model for pump-pulse propagation within hollow core capillaries [1].
- The model is based on a multimode nonlinear Schrödinger equation, shown below.
- We have previously tested the model against experimental output spectra using a novel spatio-spectral measurement technique [2].
- The model has undergone improvements and now uses a real input pulse and beam wavefront measured prior to the capillary showing a marked improvement in the experimental and theoretical agreement.

Modal dispersion and losses; Gas nonlinearity; Plasma refractive index

$$\frac{\partial A_n}{\partial z} = iD_n + in_2(z)k_0 \sum_{k,l,m} Q_{nklm} A_k A_l A_m^* + \frac{i}{2} k_0 \int r\,dr F_n(r) S(r,z,t) n_{pl}^2(r,z,t)$$

Ionisation losses

$$-\frac{1}{2} \int r\,dr F_n(r) S(r,z,t) \frac{\rho_0(r,z,t) W(r,z,t) U}{|S(r,z,t)|^2 / (2\pi)}$$

Experimental results

- Below we show the experimental temporal and spectral shape of the output pulse for a range of powers. These are matched by the equivalent theoretical results on the far right. The agreement between the two is excellent.
- The output pulses measured by our FROG were back propagated to remove the dispersion encumbered by the output window, ND filters and focusing optics within the FROG device itself. Further compression with chirped mirrors can reduce these 27 fs pulses down to 16 fs. Shown in figure 1 in the center.
- Interestingly a similar pattern is not observed as readily for a variation in pressure. At the higher powers the output pulse shapes and spectra do not vary significantly with pressure, ranged between 30-200 mbar.

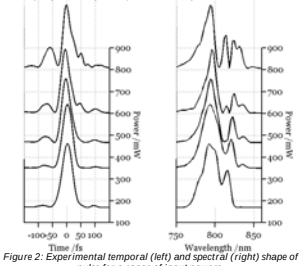

Figure 2: Experimental temporal (left) and spectral (right) shape of pulse for a range of input powers.

Summary

We show pulse compression using a 7 cm hollow core capillary from an input pulse of 53 fs reduced to 16 fs. High levels of ionisation, similar to those present in filamentation allow spectral broadening and spatio-temporal reshaping. The compression observed is greater than has previously been achieved using such short capillaries [3]. In addition to this we show the excellent agreement of these results with our theoretical model, and the exciting conclusions this allows us to draw, namely, in situ pulse self-compression within the capillary from 53 fs to 7 f.

The amount of nonlinearity within the system and hence the degree of compression depends on both the intensity of the input pulse and the pressure of the gas within the capillary. The figure below shows the output pulse measured using a FROG for the optimal pump power (805 mW) and gas pressure (150 mbar) we used, here we apply dispersion compensation to the experimental data theoretically. A power scan can be seen to the left and right showing the strong agreement between the experimental and theoretical work respectively.

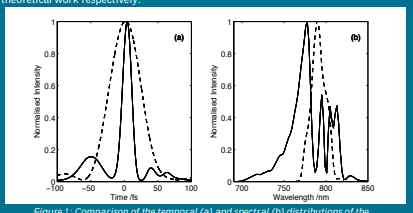

Figure 1: Comparison of the temporal (a) and spectral (b) distributions of the pulse prior to (dashed) and following (solid) compression within the capillary and post compression optics. The output pulse has a FWHM of 16fs compared to 53fs for the input pulse.

Theoretical results

- Below we show the theoretical temporal and spectral shapes of the output pulse for a range of powers. These are matched by the equivalent experimental results on the far left. The agreement between the two is excellent.
- The spectral structure shows blue shifting of the main peak and the emergence of one and then two smaller peaks as the input power and thus nonlinearity is increased.
- The pulse self-compresses and a self-steepened leading edge is observed, due to the plasma dispersion.

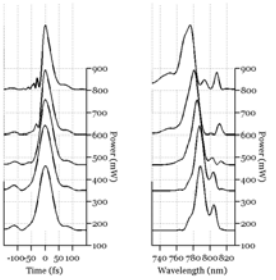

Figure 3: Theoretical temporal (left) and spectral (right) shape of pulse for a range of input powers.

In-situ pulse compression

- Nonlinear pulse propagation leads to sub 10 fs pulses within the capillary!.
- Capillary design can shift where this occurs, a recent capillary we have made has sub 7 fs pulses at the end.
- Here we see 6 fold increase in intensity, ideal for high harmonic generation.

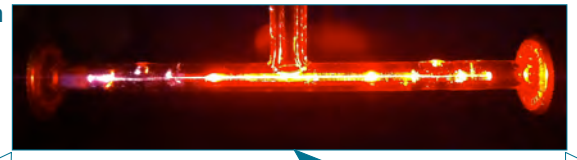

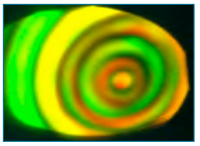

Output of capillary imaged through IR filter. Ring pattern spectrum extends to the blue at high powers.

Beginning

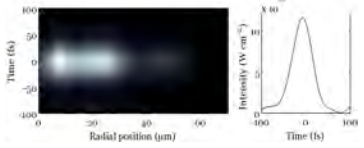

Figure 4: (left) Theoretical spatio-temporal plot of pulse at beginning of capillary, pulse is ~50 fs. (right) On-axis plot of pulse in time.

~53 fs

Middle

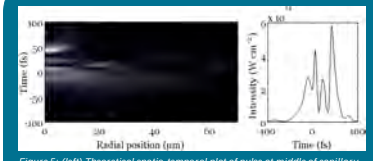

Figure 5: (left) Theoretical spatio-temporal plot of pulse at middle of capillary, individual pulses are sub 10 fs. (right) On-axis plot of pulse in time.

<10 & 10-20 fs

End

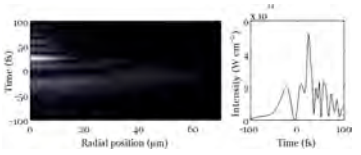

Figure 4: (left) Theoretical spatio-temporal plot of pulse at end of capillary, individual pulses are 10-20 fs. (right) On-axis plot of pulse in time.

10-20 fs

Theoretical spatio-temporal profiles

References

[1] F. Poletti and P. Horak, "Description of ultrashort pulse propagation in multimode optical fibers", J. Opt. Soc. Am. B 25, 1645(2008)
[2] R.T.Chapman, T.J.Butcher, P.Horak, F.Poletti, J.G.Frey, W.S.Brocklesby, "Modal effects on pump-pulse propagation in an Ar-filled capillary", *Optics Express* 18 pp.13279 (2010)
[3] N. L. Wagner, E. A. Gibson, T. Popmintchev, I. P. Christov, M. M. Murnane and H. C. Kapteyn, "Self-Compression of Ultrashort Pulses through Ionization-Induced Spatiotemporal Reshaping", Phys. Rev. Lett. 93, 173902 (2004)

High-flux capillary based XUV source via the direct engineering of a laser induced ionization profile

Patrick N. Anderson[1], Thomas J. Butcher[1], Peter Horak[1], Jeremy G. Frey[2], William S. Brocklesby[1]

1. Optoelectronics Research Centre, University of Southampton, Southampton SO17 1BJ, United Kingdom

2. School of Chemistry, University of Southampton, Southampton SO17 1BJ, United Kingdom

High harmonic generation (HHG) has proven to be a fascinating and incredibly useful nonlinear optical phenomenon and has led to the realization of tabletop sources of coherent extreme ultraviolet (XUV) radiation. Capillary based geometries in particular have attracted a great deal of attention due to the lengthy regions over which HHG can occur and the potential to phase match the HHG process leading to a large increase in XUV flux [1]. Until now reabsorption of XUV radiation has been a major problem when designing high-flux sources, in both capillary and other geometries. In this work we have used computational modelling to optimize our original capillary design in an effort to minimize the absorption of the generated XUV. Subsequent experimental work has shown a flux increase of almost 50 times over our existing capillary-based source, regardless of the maximum gas pressure.

Our three dimensional model [2] is based on a multimode-generalized nonlinear Schrödinger equation and includes effects such nonlinear mode mixing and ionization induced nonlinear effects. Using the model we adjusted both the capillary length and gas density profile with two aims: to maximize the radially integrated ionization fraction at the capillary exit coupled with a rapid decrease in gas pressure. This has the effect of increasing not only the XUV flux but also pushes the cut-off limit of the generated harmonics to higher energies as more ionization is a result of higher pump-pulse intensity. The XUV range that we can generate within presently is restricted to between 18-40 nm by the Cooper minimum and argon absorption respectively. For our 75 µm radius capillary we found the optimum design to be 45 mm long with gas inlets 5 mm and 3 mm from the input and output respectively. The theoretical gas density and integrated ionization profiles are given in Figures 1(a) and 1(b).

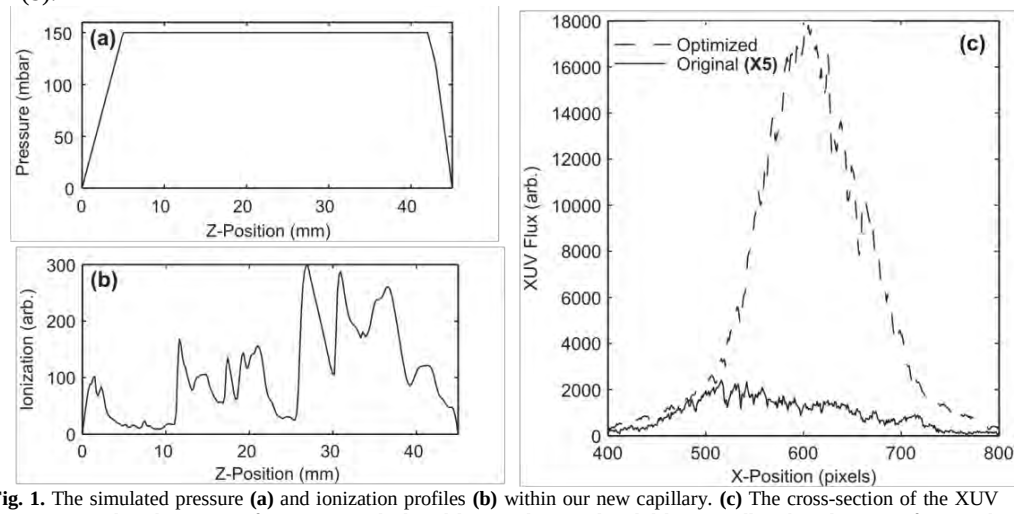

Fig. 1. The simulated pressure **(a)** and ionization profiles **(b)** within our new capillary. **(c)** The cross-section of the XUV beam measured at the output of our optimized (dotted line) and original (solid line) capillary based sources for a peak pressure of 150 mbar. Note that the cross-section data for the original source has been multiplied by a factor of five.

Based on this theoretical work several of these new capillaries were manufactured and integrated into our existing apparatus [2]. The output XUV flux was measured on an X-ray CCD camera situated behind an aluminium filter. Figure 1(c) shows the comparison between the capillary optimized for a high integrated ionization and low reabsorption (dotted line) with the original 70 mm capillary design (solid line). This shows an increase in the XUV flux of almost 50 times when compared to a non-optimized source and we have observed similar increases throughout our experimental pressure range of 0-200 mbar.

We have used our theoretical model to dramatically increase the output XUV flux of a capillary based high harmonic source by reducing the reabsorption of the generated XUV whilst simultaneously increasing the final intensity and flux of the pump laser at the capillary exit.

References

[1] A. Rundquist, C. Durfee, Z. Chang, C. Herne, S. Backus, M. Murnane and H. Kapteyn, "Phase-Matched Generation of Coherent Soft X-Rays," Science **280**, 1412 (1998)

[2] R. T. Chapman, T. J. Butcher, P. Horak, F. Poletti, J. G. Frey, W. S. Brocklesby, "Modal effects on pump-pulse propagation in an Ar-filled capillary" Optics Express **18**, 13279 (2010)

High-flux capillary based XUV source via the direct engineering of a laser induced ionization profile

Patrick N. Anderson[1], Thomas J. Butcher[1], Peter Horak[1], Jeremy G. Frey[2], William S. Brocklesby[1]

1. Optoelectronics Research Centre, University of Southampton, Southampton SO17 1BJ, United Kingdom

2. School of Chemistry, University of Southampton, Southampton SO17 1BJ, United Kingdom

Summary

- The output XUV flux of a capillary based high harmonic source has been increased by a factor of 50
- This has been achieved by using a numerical model to simultaneously reduce XUV absorption and increase pump pulse intensity at the capillary exit
- Once constructed the new source was characterized experimentally
- The XUV flux of this optimized source has been calculated as ~10^{12} photons s^{-1}

Using this model to design better XUV sources

- Adjust the capillary length and gas density profile within the model to produce a rapid pressure drop and high ionization fraction at the capillary exit
- Thus minimizing XUV absorption and shifting the harmonic cut-off to higher energies (as a high ionization fraction is indicative of a high intensity pump)
- Modelling suggests this is due to nonlinear self-compression being enhanced by a high gas density early in the capillary

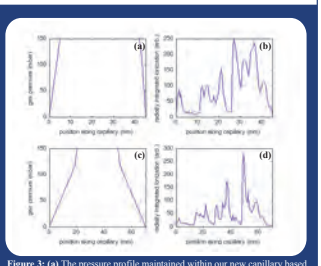

Figure 3: (a) The pressure profile maintained within our new capillary based source (computed by COMSOL). **(b)** The radially integrated ionization profile that we have selected. **(c) and (d)** The corresponding plots for our previous capillary based source.

Why model the nonlinear propagation dynamics of the pump beam within the capillary?

- Numerous nonlinear interactions are observed when pulses with intensities greater than 10^{14} Wcm^{-2} propagate through gas filled capillaries
- These lead to phenomena such as extreme spectral blue-shifting, nonlinear self-compression [1] and even filamentation (some of these processes are illustrated in figure 1)
- If the propagation dynamics of the pump pulse can be accurately modelled then we can use these nonlinear effects to enhance the HHG process.
- Thus developing more elegant sources of sub-30 nm radiation for imaging applications

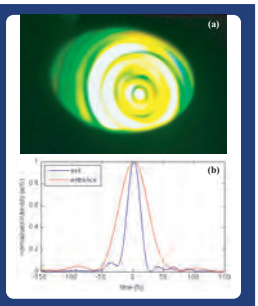

Figure 1: (a) The observation of spectral blue-shifting in the far-field ring pattern of our capillary. **(b)** An illustration of the nonlinear self-compression of an input pulse (red) as it propagates through a 7 cm capillary filled with Argon.

The model

- We based our model [2] on a multimode-generalized nonlinear Schrödinger equation (MM-GNLSE) [3]:

$$\frac{\partial A_p}{\partial z} = D(A_p) + N(\{A_n\}) + I(\{A_n\}) + L(\{A_n\}). \quad (1)$$

- *(D)*ispersion, *(N)*onlinearity, *(I)*onization effects and *(L)*osses
- Allows for the study of a great number of fascinating phenomena such as nonlinear mode mixing and plasma induced nonlinear effects
- Solved via a split-step Fourier algorithm within MATLAB

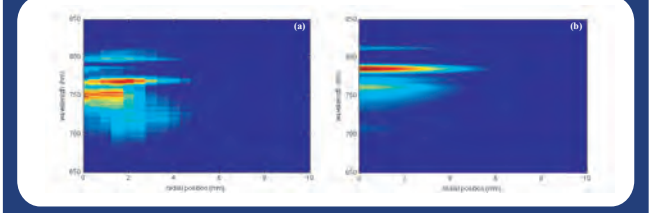

Figure 2: The experimental **(a)** and theoretical **(b)** spatio-spectral distributions after the capillary's exit.

Experimental results

The capillary described above was manufactured and integrated into our existing experiment (figure 4). The results are compared with our previous source in figure 5.

- XUV flux increased by a factor of 50
- Photon flux calculated to be ~10^{12} photons s^{-1}
- Three dominant XUV harmonics

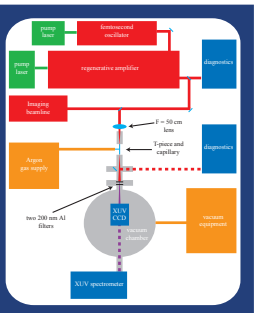

Figure 4: The experimental apparatus used to characterize our capillary based XUV sources [2].

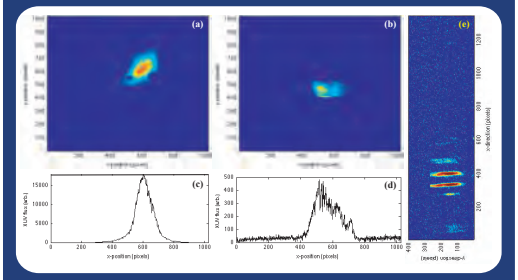

Figure 5: (a) The XUV beam profile produced by our new source. **(b)** The XUV profile produced by our existing source under similar experimental conditions. **(c) and (d)** The cross-sections of these two beams. **(e)** An image of our spectrometer's MCP plate when illuminated by our optimized source.

Conclusions and future work

Figure 5 demonstrates an increase in XUV flux of almost 50 times when compared to a non-optimized source and we have observed similar increases throughout our experimental pressure range of 0-200 mbar. Preliminary calculations have shown a photon flux of at least 10^{12} photons s^{-1}.

Our current work involves linking this propagation model to a quantum mechanical model describing the HHG process. We are also working on developing XUV filters with a high transmission in the 10-20 nm spectral region. This will allow us to confirm the shift to higher cut-off energies predicted by this work.

REFERENCES

[1] N. L. Wagner, E. A. Gibson, T. popmintchev, I. V. Christov, M. N. Murnane, H. C. Kapteyn, "Self-Compression of Ultrashort Pulses through Ionization-Induced Spatiotemporal Reshaping," Phys. Rev. Lett. **93**(17), 3902-3905 (2004).

[2] R. T. Chapman, T. J. Butcher, P. Horak, F. Poletti, J. G. Frey, W. S. Brocklesby, "Modal effects on pump-pulse propagation in an Ar-filled capillary," Opt. Express **18**(12), 13279-13284 (2010).

[3] F. Poletti, P. Horak, "Description of ultrashort pulse propagation in multimode optical fibers," J. Opt. Soc. Am. B **25**(10), 1645-1654 (2008).

Bibliography

[1] T. H. Maiman, "Stimulated Optical Radiation in Ruby," *Nature*, vol. 187, pp. 493–494, Aug. 1960.

[2] P. A. Franken, A. E. Hill, C. W. Peters, and G. Weinreich, "Generation of Optical Harmonics," *Phys. Rev. Lett.*, vol. 7, pp. 118–119, Aug. 1961.

[3] P. Corkum, "Plasma perspective on strong field multiphoton ionization," *Physical Review Letters*, vol. 71, no. 13, pp. 1994–1997, 1993.

[4] M. Lewenstein, P. Balcou, M. Ivanov, and P. Corkum, "Theory of high-harmonic generation by low-frequency laser fields," *Physical Review A*, vol. 49, no. 3, p. 2117, 1994.

[5] M. Ferray, A. L'Huillier, X. F. Li, L. A. Lompre, G. Mainfray, and C. Manus, "Multiple-harmonic conversion of 1064 nm radiation in rare gases," *Journal of Physics B: Atomic, Molecular and Optical Physics*, vol. 21, pp. L31–L35, Feb. 1988.

[6] A. McPherson, G. Gibson, H. Jara, U. Johann, T. S. Luk, I. A. McIntyre, K. Boyer, and C. K. Rhodes, "Studies of multiphoton production of vacuum-ultraviolet radiation in the rare gases," *Journal of the Optical Society of America B*, vol. 4, p. 595, Apr. 1987.

[7] E. Seres, J. Seres, and C. Spielmann, "X-ray absorption spectroscopy in the keV range with laser generated high harmonic radiation," *Applied Physics Letters*, vol. 89, p. 181919, Nov. 2006.

[8] M. Born and E. Wolf, *Principles of Optics: Electromagnetic Theory of Propagation, Interference and Diffraction of Light*. Cambridge University Press, 1999.

[9] J. W. S. Hearle, *Use of the Scanning Electron Microscope*. Pergamon Press, 1972.

[10] S. J. Pennycook and P. D. Nellist, *Scanning Transmission Electron Microscopy: Imaging and Analysis*. Springer, 2011.

[11] D. B. Williams and C. B. Carter, *Transmission Electron Microscopy: A Textbook for Materials Science*. Springer, 2009.

[12] R. Neutze, R. Wouts, D. van der Spoel, E. Weckert, and J. Hajdu, "Potential for biomolecular imaging with femtosecond X-ray pulses.," *Nature*, vol. 406, pp. 752–7, Aug. 2000.

[13] C. Spielmann, N. Burnett, S. Sartania, and R. Koppitsch, "Generation of coherent X-rays in the water window using 5-femtosecond laser pulses," *Science*, vol. 278, p. 661, 1997.

[14] Diamond Website, "http://www.diamond.ac.uk/."

[15] FLASH Website, "http://hasylab.desy.de/facilities/flash/index_eng.html."

[16] J. Dunn, J. Nilsen, A. L. Osterheld, Y. Li, and V. N. Shlyaptsev, "Demonstration of transient gain x-ray lasers near 20nm for nickellike yttrium, zirconium, niobium, and molybdenum.," *Optics Letters*, vol. 24, no. 2, pp. 101–103, 1999.

[17] P. X. Lu, T. Kawachi, M. Suzuki, K. Sukegawa, S. Namba, M. Tanaka, N. Hasegawa, K. Nagashima, H. Daido, T. Arisawa, Y. Kato, and H. Fiedorowicz, "Demonstration of a transient high gain soft X-ray laser for neon-like argon," *Japanese Journal of applied physics part 2-letters*, vol. 41, pp. L133–L135, Feb. 2002.

[18] P. Neumayer, B. Aurand, M. Basko, B. Ecker, P. Gibbon, D. C. Hochhaus, A. Karmakar, E. Kazakov, T. Kuhl, C. Labaune, O. Rosmej, A. Tauschwitz, B. Zielbauer, and D. Zimmer, "The role of hot electron refluxing in laser-generated K-alpha sources," *Physics of Plasmas*, vol. 17, p. 103103, Oct. 2010.

[19] C. Cerjan, "Spectral characterization of a Sn soft x-ray plasma source," *Journal of Applied Physics*, vol. 76, p. 3332, Sept. 1994.

[20] D. Salzmann, C. Reich, I. Uschmann, E. Förster, and P. Gibbon, "Theory of K(alpha) generation by femtosecond laser-produced hot electrons in thin foils.," *Physical review. E, Statistical, nonlinear, and soft matter physics*, vol. 65, p. 036402, Mar. 2002.

[21] K. J. Schafer, B. Yang, L. F. DiMauro, and K. C. Kulander, "Above threshold ionization beyond the high harmonic cutoff," *Phys. Rev. Lett.*, vol. 70, pp. 1599–1602, Mar. 1993.

[22] S. X. Hu and L. A. Collins, "Attosecond pump probe: exploring ultrafast electron motion inside an atom," *Physical review letters*, vol. 96, no. 7, p. 073004, 2006.

[23] S. Baker, J. S. Robinson, C. A. Haworth, H. Teng, R. A. Smith, C. C. Chirila, M. Lein, J. W. G. Tisch, and J. P. Marangos, "Probing proton dynamics in molecules on an attosecond time scale.," *Science (New York, N.Y.)*, vol. 312, pp. 424–7, Apr. 2006.

[24] J.-F. Adam, J.-P. Moy, and J. Susini, "Table-top water window transmission x-ray microscopy: Review of the key issues, and conceptual design of an instrument for biology," *Review of Scientific Instruments*, vol. 76, p. 091301, Aug. 2005.

[25] S. Marchesini, H. Chapman, and S. Hau-Riege, "Coherent X-ray Diffractive Imaging; applications and limitations," *Optics Express*, vol. 11, no. 19, pp. 2344–2353, 2003.

[26] J. Miao, D. Sayre, and H. N. Chapman, "Phase retrieval from the magnitude of the Fourier transforms of nonperiodic objects," *Journal of the Optical Society of America A*, vol. 15, p. 1662, June 1998.

[27] J. R. Fienup, "Reconstruction of an object from the modulus of its Fourier transform," *Optics Letters*, vol. 3, p. 27, July 1978.

[28] Matthew D. Seaberg, Daniel E. Adams, William F. Schlotter, Yanwei Liu, Carmen Menoni, Margaret Murnane, and Henry C. Kapteyn, "Sub-30nm Spatial Resolution Imaging Using a Tabletop 13nm High Harmonic Source - OSA Technical Digest (CD)," in *CLEO:2011 - Laser Applications to Photonic Applications*, p. CTuH3, Optical Society of America, May 2011.

[29] R. A. Dilanian, B. Chen, G. J. Williams, H. M. Quiney, K. A. Nugent, S. Teichmann, P. Hannaford, L. V. Dao, and A. G. Peele, "Diffractive imaging using a polychromatic high-harmonic generation soft-x-ray source," *Journal of Applied Physics*, vol. 106, p. 023110, July 2009.

[30] J. M. Rodenburg, A. C. Hurst, A. G. Cullis, B. R. Dobson, F. Pfeiffer, O. Bunk, C. David, K. Jefimovs, and I. Johnson, "Hard-X-Ray Lensless Imaging of Extended Objects," *Phys. Rev. Lett.*, vol. 98, p. 34801, Jan. 2007.

[31] G. Sansone, E. Benedetti, J. P. Caumes, S. Stagira, C. Vozzi, M. Nisoli, L. Poletto, P. Villoresi, V. Strelkov, I. Sola, L. B. Elouga, A. Za\"\ir, E. Mével, and E. Constant, "Shaping of attosecond pulses by phase-stabilized polarization gating," *Phys. Rev. A*, vol. 80, p. 63837, Dec. 2009.

[32] T. Sekikawa, A. Kosuge, T. Kanai, and S. Watanabe, "Nonlinear optics in the extreme ultraviolet.," *Nature*, vol. 432, pp. 605–8, Dec. 2004.

[33] L. Misoguti, I. P. Christov, S. Backus, M. M. Murnane, and H. C. Kapteyn, "Nonlinear wave-mixing processes in the extreme ultraviolet," *Phys. Rev. A*, vol. 72, p. 63803, Dec. 2005.

[34] J. Prawiharjo, N. K. Daga, R. Geng, J. H. Price, D. C. Hanna, D. J. Richardson, and D. P. Shepherd, "High fidelity femtosecond pulses from an ultrafast fiber laser system via adaptive amplitude and phase pre-shaping," *Optics Express*, vol. 16, p. 15074, Sept. 2008.

[35] F. He, H. S. S. Hung, J. H. V. Price, N. K. Daga, N. Naz, J. Prawiharjo, D. C. Hanna, D. P. Shepherd, D. J. Richardson, J. W. Dawson, C. W. Siders, and C. P. Barty, "High energy femtosecond fiber chirped pulse amplification system with adaptive phase control," *Optics Express*, vol. 16, p. 5813, Apr. 2008.

[36] D. Kane and R.Trebino, "Characterisation of arbitrary femtoseconds pulses using frequency-resolved optical gating," *IEEE J. Quantum Electronics*, vol. 29, no. 571, 1993.

[37] A. E. Siegman, "New developments in laser resonators," in *Proceedings of SPIE*, vol. 1224, pp. 2–14, SPIE, June 1990.

[38] R. Trebino, *Frequency-Resolved Optical Gating: The Measurement of Ultrashort Laser Pulses*. Springer, 2002.

[39] M. Kimmel, X. Gu, and R. Trebino, "Highly simplified device for ultrashort-pulse measurement," *Optics Letters*, vol. 26, no. 12, pp. 932–934, 2001.

[40] L. Van Dao, S. Teichmann, J. Davis, and P. Hannaford, "Generation of high flux, highly coherent extreme ultraviolet radiation in a gas cell," *Journal of Applied Physics*, vol. 104, no. 2, p. 023105, 2008.

[41] S. L. Stebbings, E. T. F. Rogers, A. M. de Paula, M. Praeger, C. A. Froud, B. Mills, D. C. Hanna, J. J. Baumberg, W. S. Brocklesby, and J. G. Frey, "Molecular variation of capillary-produced soft x-ray high harmonics," *Journal of Physics B: Atomic, Molecular and Optical Physics*, vol. 41, p. 145602, July 2008.

[42] H. J. Wörner, J. B. Bertrand, D. V. Kartashov, P. B. Corkum, and D. M. Villeneuve, "Following a chemical reaction using high-harmonic interferometry.," *Nature*, vol. 466, pp. 604–7, July 2010.

[43] A. L'Huillier, M. Lewenstein, P. Salieres, P. Balcou, M. Ivanov, J. Larsson, and C. Wahlström, "High-order harmonic-generation cutoff," *Physical Review A*, vol. 48, no. 5, pp. 3433–3436, 1993.

[44] Q. Chang, "Difference Schemes for Solving the Generalized Nonlinear Schrödinger Equation," *Journal of Computational Physics*, vol. 148, pp. 397–415, Jan. 1999.

[45] A. Paul, R. A. Bartels, R. Tobey, H. Green, S. Weiman, I. P. Christov, M. M. Murnane, H. C. Kapteyn, and S. Backus, "Quasi-phase-matched generation of coherent extreme-ultraviolet light.," *Nature*, vol. 421, pp. 51–4, Jan. 2003.

[46] J. Seres, V. S. Yakovlev, E. Seres, C. Streli, P. Wobrauschek, C. Spielmann, and F. Krausz, "Coherent superposition of laser-driven soft-X-ray harmonics from successive sources," *Nature Physics*, vol. 3, pp. 878–883, Nov. 2007.

[47] C. Durfee, A. Rundquist, S. Backus, C. Herne, M. Murnane, and H. Kapteyn, "Phase matching of high-order harmonics in hollow waveguides," *Phys. Rev. Lett*, vol. 83, no. 11, pp. 2187–2190, 1999.

[48] A. Naumov, A. Zheltikov, A. Fedotov, D. SIDOROV-BIRYUKOV, A. TARASEVITCH, P. ZHOU, and D. VON DER LINDE, "Ionization and absorption effects in high-order harmonic generation in gas-filled hollow fibers," *Laser and Particle Beams*, vol. 19, pp. 75–79, Jan. 2001.

[49] T. Brabec and F. Krausz, "Intense few-cycle laser fields: Frontiers of nonlinear optics," *Reviews of Modern Physics*, vol. 72, no. 2, p. 545, 2000.

[50] P. Balcou, P. Salieres, A. L'Huillier, and M. Lewenstein, "Generalized phase-matching conditions for high harmonics: the role of field-gradient forces," *Phys. Rev. A*, vol. 55, pp. 3204–3210, 1997.

[51] F. Lindner, G. Paulus, H. Walther, A. Baltuska, E. Goulielmakis, M. Lezius, and F. Krausz, "Gouy phase shift for few-cycle laser pulses," *Physical Review Letters*, vol. 92, no. 11, p. 113001, 2004.

[52] F. Lindner, W. Stremme, M. Schätzel, F. Grasbon, G. Paulus, H. Walther, R. Hartmann, and L. Strüder, "High-order harmonic generation at a repetition rate of 100 kHz," *Physical Review A*, vol. 68, pp. 1–8, July 2003.

[53] G. Agrawal, *Nonlinear Fiber Optics, Third Edition (Optics and Photonics)*. Academic Press, 2001.

[54] S. Bohman, A. Suda, T. Kanai, S. Yamaguchi, and K. Midorikawa, "Generation of 5.0 fs, 5.0 mJ pulses at 1 kHz using hollow-fiber pulse compression," *Optics Letters*, vol. 35, no. 11, pp. 1887–1889, 2010.

[55] J. H. Marburger, "Self-focusing: theory," *Progress in Quantum Electronics*, vol. 4, pp. 35–110, 1975.

[56] E. Marcatili and R. Schmeltzer, "Hollow Metallic and Dielectric Waveguides for Long Distance Optical Transmission and Lasers," *Bell Tech. Syst. J.*, vol. 43, pp. 1783–1809, 1964.

[57] O. E. Martinez, J. P. Gordon, and R. L. Fork, "Negative group-velocity dispersion using refraction," *Journal of the Optical Society of America A*, vol. 1, p. 1003, Oct. 1984.

[58] R. L. Fork, O. E. Martinez, and J. P. Gordon, "Negative dispersion using pairs of prisms," *Optics Letters*, vol. 9, p. 150, May 1984.

[59] R. Szipocs, K. Ferencz, C. Spielmann, and F. Krausz, "Chirped multilayer coatings for broadband dispersion control in femtosecond lasers," *Optics Letters*, vol. 19, p. 201, Feb. 1994.

[60] L. V. Keldysh, "Ionization in the field of a strong electromagnetic wave," *JETP*, vol. 20, no. 5, pp. 1307–1314, 1965.

[61] M. Ammosov, N. Delone, and V. Krainov, "Tunnel ionization of complex atoms and of atomic ions in an alternating electromagnetic field," *Sov Phys JETP*, vol. 64, no. 6, pp. 1191–1194, 1986.

[62] V. S. Popov, "Tunnel and multiphoton ionization of atoms and ions in a strong laser field (Keldysh theory)," *Physics-Uspekhi*, vol. 47, pp. 855–885, Sept. 2004.

[63] R. Nubling and J. Harrington, "Launch conditions and mode coupling in hollow-glass waveguides," *Optical Engineering*, vol. 37, p. 2454, 1998.

[64] F. Poletti and P. Horak, "Description of ultrashort pulse propagation in multimode optical fibers," *Journal of the Optical Society of America B*, vol. 25, p. 1645, Sept. 2008.

[65] K. Blow and D. Wood, "Theoretical description of transient stimulated Raman scattering in optical fibers," *IEEE Journal of Quantum Electronics*, vol. 25, no. 12, pp. 2665–2673, 1989.

[66] P. Horak and F. Poletti, "Multimode nonlinear fibre optics: theory and applications," in *Optical Fibers* (Y. Moh, S. W. Harun, and H. Arof, eds.), InTech, Rijeka, book 3 ed., 2011.

[67] C. Courtois, A. Couairon, B. Cros, J. R. Marques, and G. Matthieussent, "Propagation of intense ultrashort laser pulses in a plasma filled capillary tube: Simulations and experiments," *Physics of Plasmas*, vol. 8, p. 3445, July 2001.

[68] R. T. Chapman, T. J. Butcher, P. Horak, F. Poletti, J. G. Frey, and W. S. Brocklesby, "Modal effects on pump-pulse propagation in an Ar-filled capillary," *Optics Express*, vol. 18, p. 13279, June 2010.

[69] G. Tempea and T. Brabec, "Theory of self-focusing in a hollow waveguide," *Optics Letters*, vol. 23, p. 762, May 1998.

[70] T.-M. Jeong, C.-M. Kim, D.-K. Ko, and J.-M. Lee, "Reconstruction of Wavefront Aberration of 100-TW Ti:sapphire Laser Pulse Using Phase Retrieval Method," *Journal of the Optical Society of Korea*, vol. 12, pp. 186–191, Sept. 2008.

[71] A. Couairon and A. Mysyrowicz, "Femtosecond filamentation in transparent media," *Physics Reports*, vol. 441, pp. 47–189, Mar. 2007.

[72] X. Chen, A. Malvache, A. Ricci, A. Jullien, and R. Lopez-Martens, "Efficient hollow fiber compression scheme for generating multi-mJ, carrier-envelope phase stable, sub-5 fs pulses," *Laser Physics*, vol. 21, pp. 198–201, Dec. 2010.

[73] J. Y. Park, J. H. Lee, and C. H. Nam, "Laser chirp effect on femtosecond laser filamentation generated for pulse compression," *Optics Express*, vol. 16, no. 7, pp. 4465–4470, 2008.

[74] M. Nurhuda, A. Suda, M. Kaku, and K. Midorikawa, "Optimization of hollow fiber pulse compression using pressure gradients," *Applied Physics B*, vol. 89, pp. 209–215, Oct. 2007.

[75] N. L. Wagner, E. A. Gibson, T. Popmintchev, I. P. Christov, M. M. Murnane, and H. C. Kapteyn, "Self-Compression of Ultrashort Pulses through Ionization-Induced Spatiotemporal Reshaping," *Physical Review Letters*, vol. 93, no. 17, p. 173902, 2004.

[76] P. Arpin, T. Popmintchev, N. Wagner, a. Lytle, O. Cohen, H. Kapteyn, and M. Murnane, "Enhanced High Harmonic Generation from Multiply Ionized Argon above 500eV through Laser Pulse Self-Compression," *Physical Review Letters*, vol. 103, no. 14, pp. 1–4, 2009.

[77] J. Higuet, H. Ruf, N. Thiré, R. Cireasa, E. Constant, E. Cormier, D. Descamps, E. Mével, S. Petit, B. Pons, Y. Mairesse, and B. Fabre, "High-order harmonic spectroscopy of the Cooper minimum in argon: Experimental and theoretical study," *Phys. Rev. A*, vol. 83, p. 53401, May 2011.

[78] CXRO Website, "http://henke.lbl.gov/optical_constants/."

[79] J. Grant-Jacob, B. Mills, T. J. Butcher, R. T. Chapman, W. S. Brocklesby, and J. G. Frey, "Gas jet structure influence on high harmonic generation," *Optics Express*, vol. 19, p. 9801, May 2011.

[80] Tenio Popmintchev, Ming-Chang Chen, Paul Arpin, Michael Gerrity, Matthew Seaberg, Bosheng Zhang, Dimitar Popmintchev, Giedrius Andriukaitis, Tadas Balciunas, Oliver D. Mücke, Audrius Pugzlys, Andrius Baltuska, Margaret Murnane, and Henry Kapteyn, "Bright Coherent Ultrafast X-rays from mid-IR Lasers - OSA Technical Digest (CD)," in *High Intensity Lasers and High Field Phenomena*, p. HThB5, Optical Society of America, Feb. 2011.

[81] M. Hatayama, H. Takenaka, E. M. Gullikson, A. Suda, and K. Midorikawa, "High-Transmittance Free-Standing Aluminum Extreme Ultraviolet Filter," *Japanese Journal of Applied Physics*, vol. 48, p. 122202, Dec. 2009.

[82] M. Schnürer, Z. Cheng, M. Hentschel, F. Krausz, T. Wilhein, D. Hambach, G. Schmahl, M. Drescher, Y. Lim, and U. Heinzmann, "Few-cycle-driven XUV laser harmonics: generation and focusing," *Applied Physics B: Lasers and Optics*, vol. 70, pp. S227–S232, June 2000.

[83] A. M. Weiner, "Femtosecond pulse shaping using spatial light modulators," *Review of Scientific Instruments*, vol. 71, p. 1929, May 2000.

[84] P. H. Bucksbaum, M. Bashkansky, R. R. Freeman, T. J. McIlrath, and L. F. DiMauro, "Suppression of Multiphoton Ionization with Circularly Polarized Coherent Light," *Phys. Rev. Lett.*, vol. 56, pp. 2590–2593, June 1986.

[85] G. HASS and J. E. WAYLONIS, "Optical Constants and Reflectance and Transmittance of Evaporated Aluminum in the Visible and Ultraviolet," *Journal of the Optical Society of America*, vol. 51, p. 719, July 1961.

[86] E. Constant, D. Garzella, P. Breger, E. Mevel, C. Dorrer, C. L. Blanc, F. Salin, and P. Agostini, "Optimizing high harmonic generation in absorbing gases: model and experiment," *Physical Review Letters*, vol. 82, no. 8, pp. 1668–1671, 1999.

[87] A. L'Huillier, P. Balcou, S. Candel, and K. Schafer, "Calculations of high-order harmonic-generation processes in xenon at 1064 nm," *Physical Review A*, vol. 46, no. 5, pp. 2778–2790, 1992.

[88] S. Hädrich, J. Rothhardt, M. Krebs, F. Tavella, A. Willner, J. Limpert, and A. Tünnermann, "High harmonic generation by novel fiber amplifier based sources.," *Optics Express*, vol. 18, no. 19, pp. 20242–20250, 2010.

[89] J. Boullet, Y. Zaouter, J. Limpert, S. Petit, Y. Mairesse, B. Fabre, J. Higuet, E. Mével, E. Constant, and E. Cormier, "High-order harmonic generation at a megahertz-level repetition rate directly driven by an ytterbium-doped-fiber chirped-pulse amplification system," *Optics Letters*, vol. 34, p. 1489, Apr. 2009.